



**HAL**  
open science

# Study of viscoelastic instability in Taylor-Couette system as an analog of the magnetorotational instability

Yang Bai

► **To cite this version:**

Yang Bai. Study of viscoelastic instability in Taylor-Couette system as an analog of the magnetorotational instability. Fluid Dynamics [physics.flu-dyn]. Université du Havre, 2015. English. NNT : 2015LEHA0015 . tel-01255319

**HAL Id: tel-01255319**

**<https://theses.hal.science/tel-01255319>**

Submitted on 13 Jan 2016

**HAL** is a multi-disciplinary open access archive for the deposit and dissemination of scientific research documents, whether they are published or not. The documents may come from teaching and research institutions in France or abroad, or from public or private research centers.

L'archive ouverte pluridisciplinaire **HAL**, est destinée au dépôt et à la diffusion de documents scientifiques de niveau recherche, publiés ou non, émanant des établissements d'enseignement et de recherche français ou étrangers, des laboratoires publics ou privés.



## **THESE**

Présentée à

**L'UNIVERSITE DU HAVRE**

Pour le grade de

**DOCTEUR DE L'UNIVERSITE DU HAVRE**

Discipline : **Physique**

Spécialité : **Dynamique des Fluides et Energétique**

Par : **Yang BAI**

# **Study of the viscoelastic instability in Taylor-Couette system as an analog of the magnetorotational instability**

le 16 décembre 2015 devant le jury composé de:

Patrice LAURE	Rapporteur	Directeur de Recherche CNRS, Laboratoire de Mathématiques J.-A. Dieudonné, Nice
Oleg KIRILLOV	Rapporteur	Senior Research Scientist, Steklov Mathematical Institute, Moscow, Russia
Caroline NORE	Examineur	Professeur à l'Université Paris-Sud 11 à Orsay
Abdelhak AMBARI	Examineur	Professeur à l'ENSAM, Angers
Innocent MUTABAZI	Directeur de thèse	Professeur à l'Université du Havre
Olivier CRUMEYROLLE	Co-encadrant	Maitre de Conférences à l'Université du Havre

LABORATOIRE ONDES ET MILIEUX COMPLEXES (LOMC), UMR 6294, CNRS-  
Université du Havre

## ACKNOWLEDGMENTS

All of the work presented in this thesis is conducted in the Laboratoire Ondes et Milieux Complexes (LOMC) in the university of le Havre. This thesis project is financed by the administration and supported by the CNRS and Labex.

I would like to thank my director of thesis Innocent Mutabazi and co-encadrant Olivier Crumeyrolle for all their help during the three years of study. Your guidance and help was so valuable, without it I would not have been able to make such progress in the subject.

I would like also to thank all the colleges for your help and inspiring discussions.

I would like to thank the members of my final examination committee for your time and discussions.

Finally thank you so much my dear parents and friends. Even though you are so far away, it is your continuous support and encourage that have kept me on track.

# Table of contents

---

<b>Nomenclature .....</b>	<b>1</b>
<b>Chapter 1: Introduction.....</b>	<b>5</b>
1.1. Accretion disk & magnetorotational instability (MRI) .....	5
1.2. Analogy between MRI and viscoelastic instability.....	6
1.3. The viscoelastic instability.....	7
1.4. Plan of this thesis .....	9
<b>Chapter 2: General equations.....</b>	<b>11</b>
2.1. Hydrodynamic equations of Newtonian fluids .....	11
2.2. Magneto-Hydrodynamic (MHD) equations .....	11
2.3. Hydrodynamic equations of viscoelastic fluids .....	12
2.4. Analogy between MHD fluids and Oldroyd-B fluids.....	13
2.5. Dimensionless form of the Oldroyd-B fluid equations.....	14
2.6. Conclusion .....	15
<b>Chapter 3: Viscoelastic Couette flow .....</b>	<b>17</b>
3.1. The Couette- Taylor system .....	17
3.2. Viscoelastic Couette flow .....	17
a. Base flow velocity profile .....	18
b. Stress tensor components .....	20
3.3. Control parameters for viscoelastic Couette flows .....	21
3.4. Magnetic analogy of the viscoelastic Couette flow.....	23
3.5. Conclusion .....	24
<b>Chapter 4: Stability of viscoelastic Couette flow .....</b>	<b>25</b>
4.1. Rayleigh criterion of stability.....	25
a. Rotational Rayleigh discriminant and epicyclic frequency .....	25
b. Elasto-rotational Rayleigh discriminant .....	26
c. Instability induced by elastic force.....	28
d. Analogy with MHD .....	31
4.2. Linear stability analysis (LSA).....	31
a. Linear stability equations .....	32

b. Numerical methods.....	33
c. Code validations.....	34
4.3. Conclusion .....	37
<b>Chapter 5: Experimental setup &amp; working fluids.....</b>	<b>39</b>
5.1. Experimental setup .....	39
5.2. Working fluids.....	40
5.3. Viscosity measurements.....	42
a. Solvent viscosity.....	42
b. Fluid viscosity .....	43
c. Variation of the viscosity with PEG concentration.....	44
5.4. Relaxation times of the solutions.....	46
a. Three relaxation times.....	46
b. Variation of the relaxation times with the PEG concentration.....	48
5.5. Conclusion .....	51
<b>Chapter 6: Viscoelastic instability in the annulus with one rotating cylinder</b>	<b>53</b>
6.1. Regime $\mu = 0$ .....	53
6.1.1. LSA results.....	53
a. Marginal stability curves.....	53
b. Variation of the critical parameters with $E$ .....	55
c. Effect of the viscosity ratio $S$ on the critical states .....	59
6.1.2. Experimental results.....	64
a. Flow patterns.....	64
b. Comparison with LSA results .....	68
c. Comparison with previous results .....	72
d. Supercriticality or subcriticality .....	73
6.2. Regime $\mu = \infty$ .....	74
6.2.1. LSA results.....	74
6.2.2. Experimental results.....	78
a. Flow patterns.....	78
b. Comparison with LSA results .....	79
c. Comparison with previous results .....	81
6.3. Conclusion .....	82

## **Chapter 7: Viscoelastic instability in Keplerian regime and the MRI analogy 83**

7.1. Keplerian regime .....	83
7.1.1. LSA results.....	83
a. Marginal stability curves.....	83
b. Variation of the critical parameters with $E$ .....	85
c. Effect of the viscosity ratio $S$ on the critical states .....	91
7.1.2. Experimental results.....	94
a. Flow patterns .....	94
b. Comparison with LSA results .....	103
7.2. Anti-Keplerian regime.....	106
7.2.1. LSA results.....	106
7.2.2. Experimental results.....	110
a. Flow patterns.....	110
b. Comparison with LSA results .....	111
7.3. Discussion of the VEI in the Keplerian rotation and MRI analogy .....	113
a. Application of Rayleigh criterion and Velikhov-Chandrasekhar criterion .....	113
b. Condition for ERI : axial field dominates the azimuthal field .....	114
c. Alfvén waves.....	115
d. Comparison with results of Ogilvie & Potter and experiments of Boldyrev .....	116
7.4. Conclusion .....	116

## **Chapter 8: Viscoelastic instability in the intermediate regime of $\mu = \eta^3$ ....119**

8.1. LSA results .....	119
a. Marginal stability curves.....	119
b. Variation of the critical parameters with $E$ .....	121
c. Effect of the viscosity ratio $S$ on the critical states .....	126
8.2. Experimental results .....	128
a. Flow patterns .....	128
b. Comparison with LSA results .....	131
8.3. Conclusion .....	133

## **Chapter 9: Purely elastic instability .....** 135

9.1. LSA results .....	135
------------------------	-----

a. Marginal stability curves for $Re = 0$ .....	135
b. Variation of the critical modes with $S$ .....	137
9.2. Experimental results .....	141
9.3. Conclusion .....	143
<b>General conclusion.....</b>	<b>145</b>
<b>List of references.....</b>	<b>147</b>
<b>List of tables and figures.....</b>	<b>151</b>
<b>Résumé .....</b>	<b>161</b>

# Nomenclature

---

## Subscript

$r$	Radius direction
$\theta$	Azimuthal direction
$z$	Axial direction
$i$	Inner cylinder
$o$	Outer cylinder
$p$	Polymer
$s$	Solvent
$c$	Critic value

## Solution properties

$\rho$	Density
$\nu_s$	Kinematic viscosity of the solvent
$\nu_p$	Polymer contribution to the kinematic viscosity
$\nu$	Total kinematic viscosity of the solution
$\tau_v = \frac{d^2}{\nu}$	Viscous time
$\tau$	Relaxation time
$\tau_e$	Relaxation time measured by elongation rheometer
$\tau_{N_1}$	Relaxation time estimated by $N_1$
$\tau_m$	Relaxation time estimated by molar mass
$C_i$	Polymer concentration
$T$	Temperature
$E = \frac{\tau}{\tau_v} = \frac{\tau\nu}{d^2}$	Elasticity
$S = \frac{\nu_p}{\nu}$	Viscosity ratio
$ES = \frac{\tau\nu_p}{d^2}$	Polymer elasticity

## Magnetic fluid properties

$\nu_m$	Magnetic diffusivity
$R_m$	Magnetic Reynolds number

$\sigma_e$	Electric conductivity
$\mu_0$	Permeability of free space
$\vec{F}_l$	Lorentz force
$\bar{T}_M$	Magnetic stress tensor

### Geometry parameters

$l$	Length of the cylinders
$\Omega_i$	Angular velocity of the inner cylinder
$\Omega_o$	Angular velocity of the outer cylinder
$L$	Angular momentum
$a$	Radius of the inner cylinder
$b$	Radius of the outer cylinder
$r$	Radius
$r_g = \sqrt{ab}$	Geometric mean radius
$r_a = \frac{a+b}{2}$	Arithmetic mean radius
$d = b - a$	Gap length
$\Gamma = \frac{l}{d}$	Aspect ratio
$\Gamma_\theta = \frac{\pi(1+\eta)}{1-\eta}$	Azimuthal aspect ratio
$\eta = \frac{a}{b}$	Radius ratio
$\mu = \frac{\Omega_o}{\Omega_i}$	Angular velocity ratio
$\hat{r} = \frac{r}{d}$	Dimensionless radius

### Flow parameters

$\vec{U} = (U, V, W)^t$	Velocity vector
$A, B$	Coefficients of the base flow
$\Omega = \frac{V}{r}$	Azimuthal angular velocity
$\bar{\Omega} = \Omega(r_g)$	Geometric mean angular velocity
$R_\Omega = \frac{2\bar{\Omega}}{\dot{\gamma}}$	Rotational number
$\langle \omega \rangle = \frac{\int_a^b r\Omega(r)dr}{\int_a^b r dr}$	Mean angular velocity

$\Pi = p + \rho g z$	Generalized pressure
$g$	Gravity acceleration constant
$\vec{\omega}$	Vorticity
$\bar{\bar{T}} = \begin{pmatrix} T_{rr} & T_{r\theta} & T_{rz} \\ T_{r\theta} & T_{\theta\theta} & T_{\theta z} \\ T_{rz} & T_{\theta z} & T_{zz} \end{pmatrix}$	Stress tensor
$\bar{\bar{T}}^s$	Solvent stress tensor
$\bar{\bar{T}}^p$	Polymer stress tensor
$\bar{\bar{T}}_p = \bar{\bar{T}}^p + \frac{\rho v_p}{\tau} \bar{\bar{I}}$	Modified polymer stress tensor
$\vec{B}_{p1}, \vec{B}_{p2}, \vec{B}_{p3}$	Polymer analog of the magnetic field
$B_0 = \sqrt{\frac{\rho v_p}{\tau}}$	Characteristic of the polymer analog of the magnetic field
$\dot{\gamma} = \frac{ \Omega_i a - \Omega_o b }{d}$	Shear rate
$\dot{\gamma}_s = \frac{2 \Omega_i - \Omega_o  ab}{b^2 - a^2}$	Dynamic based shear rate
$N_1 = T_{\theta\theta} - T_{rr}$	First normal stress difference
$N_2 = T_{rr} - T_{zz}$	Second normal stress difference
$Re = \tau_v \dot{\gamma} = \frac{ \Omega_i a - \Omega_o b  d}{\nu}$	Reynolds number
$Re_s = \tau_v \dot{\gamma}_s = \frac{2 \Omega_i - \Omega_o  ab d^2}{(b^2 - a^2)\nu}$	Shear Reynolds number
$R_i = \tau_v \dot{\gamma}_i = \frac{\Omega_i a d}{\nu}$	Reynolds number associated with the inner cylinder
$R_o = \tau_v \dot{\gamma}_o = \frac{\Omega_o b d}{\nu}$	Reynolds number associated with the outer cylinder
$Ta = \sqrt{\frac{2d}{R_i + R_o}} Re$	Taylor number
$Wi = \tau \dot{\gamma} = \tau \frac{ \Omega_i a - \Omega_o b }{d}$	Weissenberg number
$Wi_i = \tau \dot{\gamma}_i = \frac{\tau \Omega_i a}{d}$	Weissenberg number associated with the inner cylinder
$Wi_o = \tau \dot{\gamma}_o = \frac{\tau \Omega_o b}{d}$	Weissenberg number associated with the inner cylinder
$Wi_s = \tau \dot{\gamma}_s = \tau \frac{2 \Omega_i - \Omega_o  ab}{b^2 - a^2}$	Shear Weissenberg number

$$K = \sqrt{\frac{sd}{r_a}} Wi$$

Modified Weissenberg number

$$K_s = \sqrt{\frac{sd}{r_g}} Wi_s$$

Modified shear Weissenberg number

$m$

Azimuthal wave number

$k$

Axial wave number

$$\lambda = \frac{1}{k}$$

Axial wavelength

$$q = 2\pi dk$$

Dimensionless axial wave number

$$s = \sigma + i\omega$$

Complex growth rate

$\sigma$

Growth rate

$\omega$

Angular frequency

$f$

Frequency

### Rayleigh criterion

$\Phi_r$

Rotational Rayleigh discriminant

$\Phi_{er}$

Elasto-rotational Rayleigh discriminant

$$\omega_{ep}^r = \sqrt{\Phi_r}$$

Rotational epicyclic frequency

$$\omega_{ep}^{er} = \sqrt{\Phi_{er}}$$

Elasto-rotational epicyclic frequency

$$\Psi_r = \frac{\Phi_r}{\Omega_i^2}$$

Dimensionless rotational Rayleigh discriminant

$$\Psi_{er} = \frac{\Phi_{er}}{\Omega_i^2}$$

Dimensionless elasto-rotational Rayleigh discriminant

$\Phi_{mr}$

Magneto-rotational discriminant of the Michael criterion

# Chapter 1: Introduction

---

## 1.1 Accretion disk & Magnetorotational instability (MRI)

According to the current accepted Solar Nebular theory, stars are created from dense interstellar clouds of dusts and gases in the space. One interstellar cloud is called a nebula. If the mass of a nebula is greater than certain critical value, the central part of the cloud will collapse to a proto-star while the surrounding part will rotate around it [Woolfson2000]. As more matter collapses into the proto-star, the surrounding cloud rotates faster since the angular momentum is conserved in a nebula; and it flattens to disk shape along the equator. This disk-like structure of the interstellar cloud around a proto-star is known as *an accretion disk* [Hoyle1960, Cassen1981]. The accretion process continues until sufficient mass accretes into the proto-star to initiate thermonuclear fusion leading to the creation of a new star.

However it is not clear how the angular momentum in an accretion disk is transported out of the system in order to allow the dusts and gases collapse into the proto-star [Balbus2011]. Viscous friction could cause kinetic energy dissipation and momentum transportation but it is largely inefficient as the interstellar cloud is too sparse and too cold. Turbulent flow in an accretion disk may cause large momentum transportation, but previous theoretical works indicate that purely hydrodynamic turbulence is inadequate [Pringle1981, Balbus1998]. In 2006 Ji *et al.* [Ji2006] have studied experimentally the Newtonian quasi-Keplerian flow comparable to an astrophysical accretion disk. They have observed no hydrodynamic instabilities that should be responsible for the large angular momentum transportation.

An electrically conducting fluid in an accretion disk could be destabilized with weak axial magnetic field when the Velikhov-Chandrasekhar criterion (angular velocity decreases with the radius) is fulfilled [Chandrasekhar1960]. In 1990's Balbus and Hawley have linked this instability to the momentum transportation of accretion disks and have verified numerically the implication of the MRI in astrophysical accretion disks [Balbus1991]. They have proposed that the MRI in an accretion disk can be explained by the "dumbbell" model represented in figure 1.1. In a perfectly conducting fluid, co-rotating fluid elements attract each other by Lorentz force, which acts as elastic strings. In an accretion disk, the Keplerian velocity distribution  $\Omega(r) \propto r^{-3/2}$  is applied, so that an element on the inner orbit rotates faster than its neighbor on the outer orbit. Being retarded by the "elastic string", the inner element loses angular momentum, then it goes to even inner orbit and rotates faster, while, on the other way, the outer element gains angular momentum and goes outer and then slows down. This process leads to the MRI.

In practice the MRI can be of different types by different dominating magnetic fields. The MRI that appears in the axial magnetic fields is called the *standard MRI* (SMRI) while the MRI that appears in the azimuthal magnetic fields is called the *azimuthal MRI* (AMRI) and the MRI that appears when both axial and azimuthal magnetic fields are present is called the *helical MRI* (HMRI).

The direct experiments to detect the SMRI are found difficult. Until now no positive results have been reported [Ji2013].

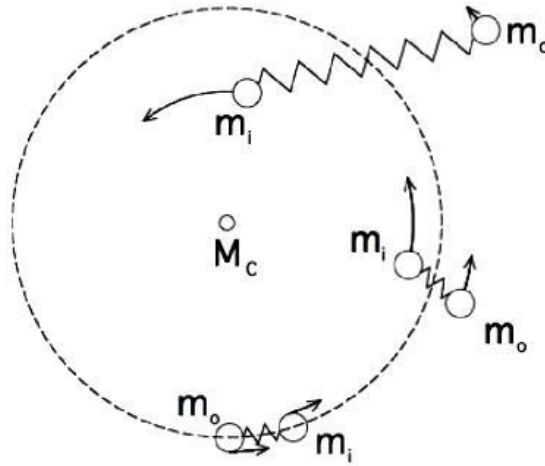


Figure 1.1: The “dumbbell” model to explain the mechanism of the SMRI proposed by Balbus. ([http://www.scholarpedia.org/article/Magnetorotational\\_instability](http://www.scholarpedia.org/article/Magnetorotational_instability))

In 2005 Hollerbach and Rüdiger have suggested through theoretical analyses that the HMRI is easier to realize than the SMRI, and that it might be relevant to cooler astrophysical disks [Hollerbach2005]. A year later the HMRI was observed experimentally with liquid metal alloy GaInSn by Stefani *et al.* [Stefani2006] [Stefani2007] [Stefani2009]. Recently the AMRI was observed experimentally [Seilmayer2014]. But unluckily these observations are not realized in Keplerian regime. Recently several analytical studies [Kirillov2013] [Kirillov2014] and numerical studies [Child2015] have predicted that the HMRI and AMRI could be observed in the Keplerian regime in certain condition. But to our knowledge no experimental observation of HMRI or AMRI in the Keplerian flow is reported till now.

## 1.2. Analogy between MRI and viscoelastic instability

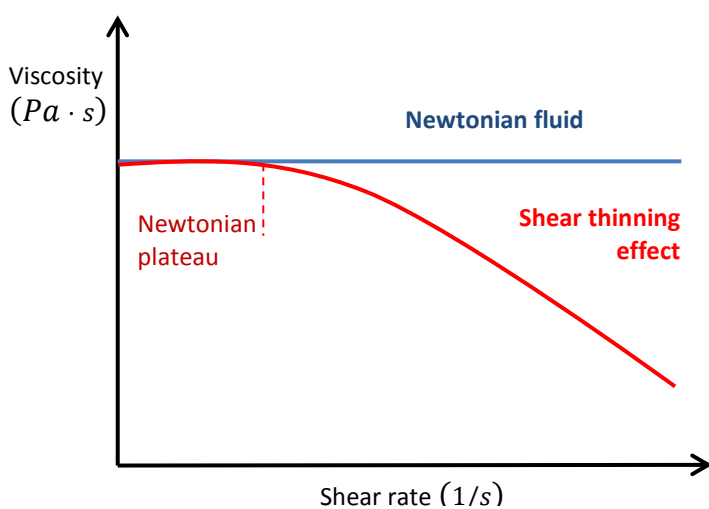
As it is difficult to realize the SMRI in experiments with liquid metals, it looks reasonable to replace the fluid with something easier to control. The dumbbell model that explains the SMRI inspires us of the viscoelastic fluids which can be described by dumbbell models [Bird1977]. Among all the molecular models Ogilvie & Proctor [Ogilvie2003] have suggested that the viscoelastic fluids of Oldroyd-B model can be considered as an analog to the electrically conducting fluids [Ogilvie03]. This analogy was analyzed theoretically and the investigation of the MRI through the study of viscoelastic instabilities (VEI) in the quasi-Keplerian flow was proposed [Ogilvie08]. This analogy leads us to a bypass to know better about the SMRI and the turbulence in accretion disks.

The only experimental research on the analogy between SMRI and VEI was reported by Boldyrev *et al.* [Boldyrev09]. However the viscoelastic solutions of this work were not well characterized and they seem not to fit the Oldroyd-B model. The authors have got only qualitative agreement with the theoretical prediction of Ogilvie & Potter [Ogilvie08].

On the other hand the viscoelastic instabilities are unsolved problems because there are no universal equations to describe the viscoelastic fluids and it is not easy to get fluids that fit perfectly the Oldroyd-B model. Beside these practical difficulties, the complexity of the viscoelastic fluids makes the study of the viscoelastic instability (VEI) a difficult task. So before all, we need to resume the main researches of the VEI available in literature.

### 1.3. The viscoelastic instability

We consider dilute polymer solutions composed of long-chain macromolecules with high molecular weight. These fluids are called viscoelastic fluids because they show not only viscous behaviors but also elastic behaviors. The most significant properties of the viscoelastic fluids are the *shear-thinning effect* and the elastic effects among which the *Weissenberg effect* is the most famous. The shear-thinning effect consists in the decrease in the viscosity in strong shear flows. Illustrated in figure 1.2 (a), the fluid viscosity stays constant at small shear rate which forms the so called Newtonian plateau and it decreases with the shear rate after certain critical value. The Weissenberg effect consists in the fluid climbing through a rotating rod as illustrated in figure 1.2 (b). As the rod rotates in a viscoelastic fluid, it induces shear that stretches the 'spring' that connects the fluid parcels so that the fluid shrinks around the rod and the fluid parcels 'climb' the rod.



(a)

(b)

Figure 1.2: (a) Shear thinning effect, (b) Weissenberg effect.

The most important discovery of the viscoelastic liquids described by the Oldroyd-B model (liquid solutions with constant shear viscosity) is the observation of the *purely elastic instability* by Larson and Shaqfeh [Larson1990]. These authors have shown theoretically and experimentally that a viscoelastic fluid of Oldroyd-B model can be destabilized in a rotating flow by the elastic force with very weak (almost vanishing) shear rate. The figure 1.3 presents the photo of the purely elastic instability when it is fully developed. A drawback of this research is that the authors have used only approximate equations in the limit of small gap and only axisymmetric modes were considered.



Figure 1.3: Photo of the purely elastic instability provided by Larson & Shaqfeh [Larson 1990].

To explain the purely elastic instability, Larson et al. [Larson1990] have proposed a destabilization scenario based on the “dumbbell” model (figure 1.4) which is similar to the model that Balbus has used to describe the mechanism the MRI.

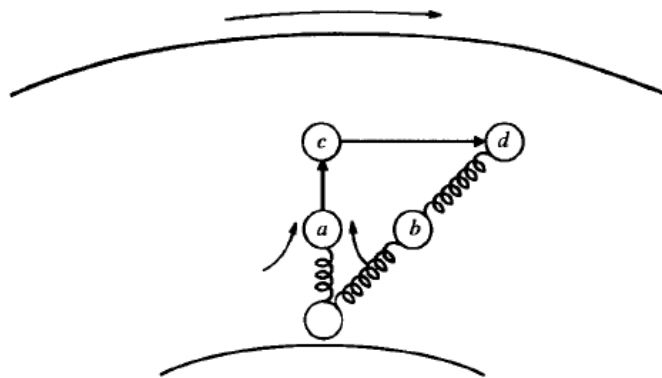


Figure 1.4: “Dumbbell” model proposed by Larson & Shaqfeh [Larson1990].

Later on Joo & Shaqfeh have conducted linear stability analysis of the *inertia-elastic instability* with approximate equations used by Larson-Muller-Shaqfeh [Joo1992]. The competition between the inertial instability and the purely elastic instability was analyzed numerically.

In 1993 Avgousti *et al.* [Avgousti1993] have conducted the linear stability analysis with complete governing equations of the Oldroyd-B model in a Couette-Taylor system. They have predicted that the VEI critical mode could be either axisymmetric or non-axisymmetric depending on the elasticity values.

In 1997 a new dissipative mode has been observed experimentally by Groisman and Steinberg [Groisman1997] when decreasing the shear rate of the destabilized viscoelastic flow of highly elastic polymer solutions. This mode appears as distinct vortex pairs or “diwhirls”.

Different critical modes were observed experimentally by Baumert & Muller [Baumert1997, Baumert1999] with fluids of low and medium elasticity. They have reported also flow patterns of shear rate higher than the critical values in different rotational velocity ratio of the cylinders.

The VEI was also studied experimentally in LOMC where three different critical modes for fluids of different elasticities have been reported by Crumeyrolle Kelai, Latrache [Crumeyrolle2005] [Kelai2011] [Latrache2012]. However despite various situations were investigated, none of them was conducted in the Keplerian or quasi-Keplerian regime

## 1.4. Plan of this thesis

The purpose of this thesis is to study theoretically and experimentally the VEI of Oldroyd-B model in order to get better understanding of the MRI and the momentum transportation in accretion disks.

In chapter 2, we will present the general equations of the Hydrodynamics of the viscoelastic fluids and of the magneto-hydrodynamics (MHD) of electrically conducting fluids, in order to show the conditions of the analogy between the VEI and the MRI. In chapter 3 the properties of the viscoelastic circular Couette flows are analyzed, the polymer analogs of the magnetic fields are presented to prepare the construction of the analogy of VEI with the MRI.

The chapter 4 addresses the revisited theoretical studies of the VEI. First the rotational Rayleigh discriminant is generalized to the elastic-rotational flow which is an analog of the Rayleigh criterion of the rotating flow in the presence of the magnetic field. Then the perturbation equations and the numerical methods of the linear stability analysis are presented together with the validation of our codes. The chapter 5 describes the experimental setup, the working fluids and their rheology, and the measurements of the relaxation time elasticity of polymer solutions.

The following chapters contain the theoretical and experimental results obtained in different rotating regimes and the conclusions drawn from them. In chapter 6, we study the VEI in shear flows by rotating one cylinder of the Couette-Taylor system. The experimental results are compared to the linear stability analysis results and the results of the other authors. In chapter 7 the VEI is studied in quasi-Keplerian flow and anti-Keplerian flow. The analogy between the MRI and VEI is then discussed. The chapter 8 discusses the case of an intermediate rotation regime in which both the centrifugal force and the elasticity force are the driving mechanisms of instability. The chapter 9 is concerned with the special case of the purely elastic instability in the limit of infinite elasticity of polymer solutions. It yields a new insight in this instability which was investigated by Larson *et al* [Larson, JFM 1990] in the 1990's. The thesis ends with a general conclusion and an outlook of further developments of the present work.



# Chapter 2: General equations

---

In this chapter, we introduce the general hydrodynamic equations of the electrically conducting fluids and the viscoelastic fluids of Oldroyd-B model. Then these equations are compared to bring out the analogy between these fluids.

## 2.1. Hydrodynamic equations of Newtonian fluids

An isothermal and incompressible flow is governed by the equations of conservation of mass and momentum:

$$\nabla \cdot \vec{U} = 0 \quad 2.1$$

$$\rho \left( \frac{\partial \vec{U}}{\partial t} + \vec{U} \cdot \nabla \vec{U} \right) = -\nabla \Pi + \nabla \cdot \bar{\bar{T}} + \vec{F} \quad 2.2$$

where  $\bar{\bar{T}}$  is the total stress tensor,  $\Pi = p + \rho g z$  is the general pressure and  $\vec{F}$  is the external force density.

In order to solve these equations, constructive models of the fluids are needed. For a Newtonian fluid, the stress is proportional to the strain. The constitutive equation which connects the stress tensor  $\bar{\bar{T}}$  and the strain tensor  $\bar{\bar{D}} = \nabla \vec{U} + (\nabla \vec{U})^T$  of a Newtonian flow is written as:

$$\bar{\bar{T}} = -\rho \nu \bar{\bar{D}} \quad 2.3$$

where  $\rho$  is the density of the fluid and  $\nu$  is the kinematic viscosity of the fluid. So that the momentum conservation equation of Newtonian fluids (2.2) becomes:

$$\rho \left( \frac{\partial \vec{U}}{\partial t} + \vec{U} \cdot \nabla \vec{U} \right) = -\nabla \Pi + \rho \nu \nabla^2 \vec{U} + \vec{F} \quad 2.4$$

## 2.2. Magneto-Hydrodynamic (MHD) equations

A special class of Newtonian fluids is the electrically conducting fluids in the presence of the magnetic field. The magneto-hydrodynamics (MHD) studies the dynamics of electrically conducting fluids which include plasmas and liquid metals. In an electrically conducting fluid moving with velocity  $\vec{U}$ , the magnetic field  $\vec{B}$  exerts on the charged fluid parcels a Lorentz force  $\vec{F}_l$ :

$$\vec{F}_l = \frac{1}{\mu_0} \nabla \times \vec{B} \times \vec{B} \quad 2.5$$

Where  $\mu_0$  is the permeability. Hence the equation of the momentum conservation becomes:

$$\rho \left( \frac{\partial \vec{U}}{\partial t} + \vec{U} \cdot \nabla \vec{U} \right) = -\nabla \Pi + \rho \nu \nabla^2 \vec{U} + \frac{1}{\mu_0} \nabla \times \vec{B} \times \vec{B} \quad 2.6$$

In a well conducting liquid, the magnetic field obeys the following dynamic equation:

$$\frac{\partial \vec{B}}{\partial t} + \vec{U} \cdot \nabla \vec{B} = \vec{B} \cdot \nabla \vec{U} + \nu_m \nabla^2 \vec{B} \quad 2.7$$

where  $\nu_m = 1/(\sigma_e \mu_0)$  is the magnetic diffusivity,  $\sigma_e$  is the electrical conductivity of the liquid. The equation 2.7 is an analog of the vorticity equation.

Thus, the momentum conservation equation 2.6 and the induction equation 2.7 together with the mass conservation equation 2.1 constitute the MHD governing equations.

### 2.3. Hydrodynamic equations of viscoelastic fluids

In many industrial applications, polymer solutions made of long-chain molecules are involved. These solutions do not satisfy the Newtonian law when they are sheared. Instead, their constitutive laws are much more complicated. These fluids are a class of non-Newtonian fluids. There exist many models to describe the non-Newtonian fluids, depending on their rheology: dependence of the viscosity on shear rate, presence of the elasticity ... The fluids that possess both viscosity and elasticity due to polymer molecules are called viscoelastic fluids.

One of the simplest models used to describe the viscoelastic fluids is the Upper-convected Maxwell (UCM) model. The UCM model considers fluid parcels as Brownian beads connected by an infinitely extensible spring [Bird1977]. The constitutive equation of the UCM model is written as follows, where  $\tau$  is relaxation time of the viscoelastic fluid.

$$\bar{\bar{T}} + \tau \left[ \frac{\partial \bar{\bar{T}}}{\partial t} + \vec{U} \cdot \nabla \bar{\bar{T}} - \left( (\nabla \vec{U})^T \cdot \bar{\bar{T}} + \bar{\bar{T}} \cdot (\nabla \vec{U}) \right) \right] = \rho \nu \bar{\bar{D}} \quad 2.8$$

The UCM model neglects the solvent contribution to the viscosity, it may be suitable to the thick polymer solutions or polymer melts. A better model to describe the dilute polymer solutions is the *Oldroyd-B model* [Oldroyd1950]. In this model, the stress tensor is decomposed into the polymeric stress tensor  $\bar{\bar{T}}^p$  and the Newtonian solvent stress tensor  $\bar{\bar{T}}^s$ :

$$\bar{\bar{T}} = \bar{\bar{T}}^p + \bar{\bar{T}}^s \quad 2.9$$

The viscosity of the total solution  $\nu$  is the sum of the solvent viscosity  $\nu_s$  and the polymer contribution of the viscosity  $\nu_p$ . Both  $\nu_p$  and  $\nu_s$  are assumed to be independent to the shear rate, the fluid viscosity  $\nu$  is independent to shear rate:

$$\nu = \nu_p + \nu_s \quad 2.10$$

So the Oldroyd-B model is used to describe viscoelastic fluids with a constant viscosity.

As the solvent stress tensor  $\bar{\bar{T}}^s$  satisfies the Newtonian constitutive equation 2.3, the momentum conservation equation writes as follows, where  $\nu_s$  is the solvent viscosity.

$$\rho \left( \frac{\partial \vec{U}}{\partial t} + \vec{U} \cdot \nabla \vec{U} \right) = -\nabla \Pi + \nabla \cdot \bar{\bar{T}}^p + \rho \nu_s \nabla^2 \vec{U} \quad 2.11$$

As the polymeric stress tensor  $\bar{\bar{T}}^p$  satisfies the UCM model, we have the constitutive equation of the Oldroyd-B model as follow:

$$\bar{\bar{T}}^p + \tau \left[ \frac{\partial \bar{\bar{T}}^p}{\partial t} + \vec{U} \cdot \nabla \bar{\bar{T}}^p - (\nabla \vec{U})^T \cdot \bar{\bar{T}}^p - \bar{\bar{T}}^p \cdot \nabla \vec{U} \right] = \rho \nu_p [\nabla \vec{U} + (\nabla \vec{U})^T] \quad 2.12$$

Hence the equations 2.11 and 2.12 together with the mass conservation equation 2.1 constitute the governing equations of the viscoelastic fluids of the Oldroyd-B model.

By taking the divergence of the momentum equation 2.11 we obtain the pressure equation as follow, where  $\Omega^2 = \bar{\Omega}\bar{\Omega}, \Sigma^2 = \bar{\Sigma}\bar{\Sigma}$ ,  $\bar{\Omega} = 1/2(\nabla\vec{U} - (\nabla\vec{U})^t), \bar{\Sigma} = 1/2(\nabla\vec{U} + (\nabla\vec{U})^t)$  are the antisymmetric and symmetric parts of the velocity gradient tensor  $\nabla\vec{U}$ .

$$\Delta\Pi = -\vec{\nabla} \cdot [(\vec{U} \cdot \vec{\nabla})\vec{U}] + \vec{\nabla} \cdot (\vec{\nabla} \cdot \bar{T}^p) \quad \text{or} \quad \Delta\Pi = \frac{\rho}{2}(\Omega^2 - \Sigma^2) + \vec{\nabla} \cdot (\vec{\nabla} \cdot \bar{T}^p) \quad 2.13$$

By applying the curl operator to the momentum equation (2.11), the vorticity equation is obtained, where  $\nu_s$  is the kinematic viscosity of the solvent.

$$\frac{\partial\vec{\omega}}{\partial t} + (\vec{U} \cdot \vec{\nabla})\vec{\omega} = (\vec{\omega} \cdot \vec{\nabla})\vec{U} + \nu_s\Delta\vec{\omega} + \frac{1}{\rho}\vec{\nabla} \times (\vec{\nabla} \cdot \bar{T}^p) \quad 2.14$$

The polymer stress tensor  $\bar{T}^p$  yields a supplementary contribution to the pressure and to the vorticity generation.

The Oldroyd-B model gives good predictions for the so called Boger fluids which are fluids with very large solvent viscosity [Mackay1987]. This model has only one relaxation time  $\tau$ , however a real polymer solution displays several distinct time constants [MagdaLarson1988]. Therefore the model will not capture all the features of the real polymer solution dynamics.

## 2.4. Analogy between MHD fluids and Oldroyd-B fluids

In their investigation of the MHD, Ogilvie and Proctor have first discovered the similarity between MHD equations and the viscoelastic equations of Oldroyd-B model [Ogilvie03]. They rewrote the MHD equations (equations 2.1, 2.6, 2.7) by introducing a modified magnetic stress tensor  $\bar{T}_m$ :

$$\bar{T}_m = \frac{\vec{B}\vec{B}}{\mu_0} \quad 2.15$$

Then the MHD equations become:

$$\left\{ \begin{array}{l} \nabla \cdot \vec{U} = 0 \\ \rho \left( \frac{\partial\vec{U}}{\partial t} + \vec{U} \cdot \nabla\vec{U} \right) = -\nabla\Pi + \nabla\bar{T}_m + \rho\nu\nabla^2\vec{U} \\ \frac{\partial\bar{T}_m}{\partial t} + \vec{U} \cdot \nabla\bar{T}_m - (\nabla\vec{U})^T \cdot \bar{T}_m - \bar{T}_m \cdot \nabla\vec{U} = \frac{\nu_m}{\mu_0} (\vec{B}\nabla^2\vec{B} + (\nabla^2\vec{B})\vec{B}) \end{array} \right. \quad 2.16$$

It is possible to rewrite the viscoelastic equations of Oldroyd-B model (equations 2.1 2.11 2.12) by introducing the modified polymeric stress tensor, where  $\bar{I}$  is an identity tensor.

$$\bar{T}_p = \bar{T}^p + \frac{\rho\nu_p}{\tau}\bar{I} \quad 2.17$$

So that the viscoelastic governing equations become:

$$\left\{ \begin{array}{l} \nabla \cdot \vec{U} = 0 \\ \rho \left( \frac{\partial \vec{U}}{\partial t} + \vec{U} \cdot \nabla \vec{U} \right) = -\nabla \Pi + \nabla \bar{T}_p + \rho \nu_s \nabla^2 \vec{U} \\ \frac{\partial \bar{T}_p}{\partial t} + \vec{U} \cdot \nabla \bar{T}_p - (\nabla \vec{U})^T \cdot \bar{T}_p - \bar{T}_p \cdot \nabla \vec{U} = -\frac{1}{\tau} \left( \bar{T}_p - \frac{\rho \nu_p}{\tau} \bar{I} \right) \end{array} \right. \quad 2.18$$

In the limit of small magnetic diffusivity  $\nu_M$  and long relaxation time  $\tau$ , the terms of  $\frac{\nu_m}{\mu_0} (\vec{B} \nabla^2 \vec{B} + (\nabla^2 \vec{B}) \vec{B})$  and  $-\frac{1}{\tau} \left( \bar{T}_p - \frac{\rho \nu_p}{\tau} \bar{I} \right)$  are negligible. The remaining terms of the equations are exactly the same, so that we have a strict analogy between the MHD fluid and the Oldroyd-B fluid. This analogy can be expressed symbolically as follows:

$$\lim_{\nu_m \rightarrow 0} (MHD \text{ fluid}) = \lim_{\tau \rightarrow \infty} (Oldroyd - B \text{ fluid}) \quad 2.19$$

So that the analogy between MHD fluid and Oldroyd-B fluid holds only in the case of an ideally conducting liquid.

## 2.5. Dimensionless form of the Oldroyd-B fluid equations

The characteristic length and velocity are  $d$  and  $U_0$  respectively. The pressure and the stress tensor are scaled by  $U_0^2$ . The resulting dimensionless equations of the Oldroyd-B fluid read:

$$\begin{aligned} \nabla \cdot \vec{U} &= 0 \\ Re \left( \frac{\partial \vec{U}}{\partial t} + \vec{U} \cdot \nabla \vec{U} \right) &= -\nabla \Pi + \nabla \cdot \bar{T}^p + (1 - S) \nabla^2 \vec{U} \\ \bar{T}^p + E Re \left[ \frac{\partial \bar{T}^p}{\partial t} + \vec{U} \cdot \nabla \bar{T}^p - (\nabla \vec{U})^T \cdot \bar{T}^p - \bar{T}^p \cdot \nabla \vec{U} \right] &= S [\nabla \vec{U} + (\nabla \vec{U})^T] \end{aligned} \quad 2.20$$

where we have introduced the following control parameters :

$$Re = \tau_v \dot{\gamma} = \frac{d U_0}{\nu} \quad E = \frac{\tau}{\tau_v} = \frac{Wi}{Re} \quad E Re = \tau \dot{\gamma} = Wi \quad S = \frac{\nu_p}{\nu} \quad 2.21$$

where  $\dot{\gamma} = U_0/d$  is the characteristic shear rate;  $\tau_v = d^2/\nu$  is the diffusion time;  $Re$  is the Reynolds number,  $Wi$  is the Weissenberg number,  $E$  is the elasticity number and  $S$  is the viscosity ratio of the solution. The choice of the shear rate  $\dot{\gamma}$  will depend on the flow configuration under consideration. This will be discussed in the next chapter in the case of the Couette-Taylor flow.

In the case of the MHD, the dimensionless control parameter that estimates the magnetic diffusivity is the magnetic Reynolds number  $R_m = U_0 d / \nu_m$ . So that the expression 2.19 of the analogy between MHD fluids and viscoelastic fluids can be written as:

$$\lim_{R_m \rightarrow \infty} (MHD \text{ fluid}) = \lim_{Wi \rightarrow \infty} (Oldroyd - B \text{ fluid}) \quad 2.22$$

The cylindrical system of coordinates  $(r, \theta, z)$  is suitable for the description of the flow in the Couette-Taylor system. In this case, equations 2.20 read

$$\frac{1}{r} \frac{\partial(rU_r)}{\partial r} + \frac{1}{r} \frac{\partial U_\theta}{\partial \theta} + \frac{\partial U_z}{\partial z} = 0$$

$$\begin{aligned}
Re \left( \frac{\partial U_r}{\partial t} + (\vec{U} \cdot \vec{\nabla}) U_r - \frac{U_\theta^2}{r} \right) &= -\frac{\partial \Pi}{\partial r} - \left( \frac{1}{r} \frac{\partial(rT_{rr})}{\partial r} + \frac{1}{r} \frac{\partial T_{\theta r}}{\partial \theta} + \frac{\partial T_{zr}}{\partial z} - \frac{N_1}{r} \right) + (1-S) \left( \Delta U_r - \frac{2}{r^2} \frac{\partial U_\theta}{\partial \theta} \right) \\
Re \left( \frac{\partial U_\theta}{\partial t} + (\vec{U} \cdot \vec{\nabla}) U_\theta + \frac{U_r U_\theta}{r} \right) &= -\frac{\partial \Pi}{\partial r} - \left( \frac{1}{r^2} \frac{\partial(r^2 T_{r\theta})}{\partial r} + \frac{1}{r} \frac{\partial T_{\theta\theta}}{\partial \theta} + \frac{\partial T_{z\theta}}{\partial z} \right) + (1-S) \left( \Delta U_\theta + \frac{2}{r^2} \frac{\partial U_r}{\partial \theta} \right) \\
Re \left( \frac{\partial U_z}{\partial t} + (\vec{U} \cdot \vec{\nabla}) U_z \right) &= -\frac{\partial \Pi}{\partial r} - \left( \frac{1}{r} \frac{\partial(rT_{rz})}{\partial r} + \frac{1}{r} \frac{\partial T_{\theta z}}{\partial \theta} + \frac{\partial T_{zz}}{\partial z} \right) + (1-S) (\Delta U_z) \\
T_{rr} + ERe \left[ \frac{\partial T_{rr}}{\partial t} + (\vec{U} \cdot \nabla) T_{rr} - \frac{2U_\theta T_{r\theta}}{r} - 2 \left( \frac{\partial U_r}{\partial r} T_{rr} + \left( \frac{1}{r} \frac{\partial U_r}{\partial \theta} - \frac{U_\theta}{r} \right) T_{\theta r} + \frac{\partial U_r}{\partial z} T_{zr} \right) \right] &= 2S \frac{\partial U_r}{\partial r} \\
T_{r\theta} + ERe \left[ \frac{\partial T_{r\theta}}{\partial t} + (\vec{U} \cdot \nabla) T_{r\theta} + \frac{U_\theta (T_{rr} - T_{\theta\theta})}{r} \right. \\
&\quad \left. - \left( \frac{\partial U_r}{\partial r} T_{r\theta} + \left( \frac{1}{r} \frac{\partial U_r}{\partial \theta} - \frac{U_\theta}{r} \right) T_{\theta\theta} + \frac{\partial U_r}{\partial z} T_{\theta z} + \frac{\partial U_\theta}{\partial r} T_{rr} + \left( \frac{1}{r} \frac{\partial U_\theta}{\partial \theta} + \frac{U_r}{r} \right) T_{r\theta} \right. \right. \\
&\quad \left. \left. + \frac{\partial U_\theta}{\partial z} T_{rz} \right) \right] = S \left( \frac{\partial U_\theta}{\partial r} + \frac{1}{r} \frac{\partial U_r}{\partial \theta} - \frac{U_\theta}{r} \right) \\
T_{\theta\theta} + ERe \left[ \frac{\partial T_{\theta\theta}}{\partial t} + (\vec{U} \cdot \nabla) T_{\theta\theta} + \frac{U_\theta}{r} (T_{r\theta} + T_{\theta r}) - 2 \left( \frac{\partial U_\theta}{\partial r} T_{r\theta} + \left( \frac{1}{r} \frac{\partial U_\theta}{\partial \theta} + \frac{U_r}{r} \right) T_{\theta\theta} + \frac{\partial U_\theta}{\partial z} T_{z\theta} \right) \right] &= 2S \left( \frac{1}{r} \frac{\partial U_\theta}{\partial \theta} + \frac{U_r}{r} \right) \\
T_{rz} + ERe \left[ \frac{\partial T_{rz}}{\partial t} + (\vec{U} \cdot \nabla) T_{rz} - \frac{U_\theta}{r} T_{\theta z} \right. \\
&\quad \left. - \left( \frac{\partial U_r}{\partial r} T_{rz} + \left( \frac{1}{r} \frac{\partial U_r}{\partial \theta} - \frac{U_\theta}{r} \right) T_{\theta z} + \frac{\partial U_r}{\partial z} T_{zz} + \frac{\partial U_z}{\partial r} T_{rr} + \frac{1}{r} \frac{\partial U_z}{\partial \theta} T_{\theta r} + \frac{\partial U_z}{\partial z} T_{zr} \right) \right] \\
&= S \left( \frac{\partial U_z}{\partial r} + \frac{\partial U_r}{\partial z} \right) \\
T_{\theta z} + ERe \left[ \frac{\partial T_{\theta z}}{\partial t} + (\vec{U} \cdot \nabla) T_{\theta z} + \frac{U_\theta}{r} T_{rz} \right. \\
&\quad \left. - \left( \frac{\partial U_\theta}{\partial r} T_{rz} + \left( \frac{1}{r} \frac{\partial U_\theta}{\partial \theta} + \frac{U_r}{r} \right) T_{\theta z} + \frac{\partial U_\theta}{\partial z} T_{zz} + \frac{\partial U_z}{\partial r} T_{r\theta} + \frac{1}{r} \frac{\partial U_z}{\partial \theta} T_{\theta\theta} + \frac{\partial U_z}{\partial z} T_{z\theta} \right) \right] \\
&= S \left( \frac{1}{r} \frac{\partial U_z}{\partial \theta} + \frac{\partial U_\theta}{\partial z} \right) \\
T_{zz} + ERe \left[ \frac{\partial T_{zz}}{\partial t} + (\vec{U} \cdot \nabla) T_{zz} - 2 \left( \frac{\partial U_z}{\partial r} T_{rz} + \frac{1}{r} \frac{\partial U_z}{\partial \theta} T_{\theta z} + \frac{\partial U_z}{\partial z} T_{zz} \right) \right] &= 2S \frac{\partial U_z}{\partial z}
\end{aligned} \tag{2.23}$$

where

$$\vec{U} \cdot \nabla = U_r \frac{\partial}{\partial r} + \frac{U_\theta}{r} \frac{\partial}{\partial \theta} + U_z \frac{\partial}{\partial z} \tag{2.24}$$

The boundary conditions are the no-slip conditions at the cylindrical surfaces bounding the fluid in the radial direction.

These equations contain two limit cases: the Newtonian case ( $E = 0, S = 0$ ) and the pure inertialess case ( $E \rightarrow \infty, Re \rightarrow 0$  keeping  $Wi = ERe$  finite). The stability of the latter case has been investigated in details by Larson et al. [Larson1990] and Joo & Shaqfeh [Joo1992].

## 2.6. Conclusion

In this chapter we have presented the general equations governing the dynamics of viscoelastic fluids within the Oldroyd-B model and their analogy with the MHD equations. This analogy will be developed in the next chapters within the linear stability analysis and it will be used to realize experiments that should give insight in the magneto-rotational instability (MRI).



# Chapter 3: Viscoelastic Couette flow

The general equations presented in chapter 2 are independent of the flow configuration. In this chapter, we will solve them for the specific case of the viscoelastic circular Couette flow in the gap between two differentially rotating coaxial cylinders, the so-called Couette-Taylor system.

## 3.1. The Couette- Taylor system

The Couette –Taylor flow consists of a fluid confined in the gap between 2 coaxial cylinders, rotating at different angular velocities (Fig.3.1) The radius of the inner and outer cylinder is denoted by  $a$  and  $b$  respectively, which makes the gap  $d = b - a$ . The length of the cylinders is denoted  $l$ . The two cylinders rotate separately with the angular velocities  $\Omega_i$  and  $\Omega_o$ .

The Couette-Taylor system has been chosen as a hydrodynamic prototype for the investigation of flow instabilities in closed systems because of its large group of symmetries: translation symmetry in the axial and azimuthal directions, rotation symmetry around the axis, reflection symmetry about the plane that passes the central cross section; the system can be invariant in time.

The following dimensionless parameters are widely used to characterize the flow regimes in the Couette-Taylor system: the length aspect ratio  $\Gamma = l/d$ , the radius ratio  $\eta = a/b$ , the angular velocity ratio :  $\mu = \Omega_o/\Omega_i$ . The radius ratio is related to the azimuthal aspect ratio by the expression  $\Gamma_\theta = \pi(1 + \eta)/(1 - \eta)$ .

According to different values of the angular velocity ratio  $\mu$ , we can define different rotational regimes of the Couette-Taylor system. The most investigated regime is the one for which the inner cylinder rotates while the outer cylinder is fixed i.e.  $\mu = 0$ . On the opposite side, we can fix the inner cylinder and rotate the outer cylinder, in this case  $\mu = \infty$ . We can also rotate the two cylinders at the same time with a fixed rotation ratio.

Since the aim of this thesis is to investigate the analogy of viscoelastic instability in the Couette-Taylor with the magneto-rotational instability (MRI) that is supposed to be responsible of turbulence in the accretion disk which rotates in Keplerian distribution of  $\Omega(r) \propto r^{-3/2}$ , we will focus our study to Keplerian regime where the two cylinders rotate with  $\Omega_i/\Omega_o = (a/b)^{-3/2}$  or  $\mu = \eta^{3/2}$ . We may inverse the Keplerian regime to get the anti-Keplerian regime where  $\mu = \eta^{-3/2}$ . Beside these regimes we have also studied the regime of  $\mu = \eta^3$  which lies between  $\mu = 0$  and the Keplerian regime.

## 3.2. Viscoelastic Couette flow

In a Couette-Taylor system with a large aspect ratio ( $\Gamma \gg 1$ ), the boundary effects on the top and bottom can be neglected. Before the flow is destabilized it is laminar and is called circular Couette flow. In the cylindrical coordinates  $(r, \theta, z)$ , it possesses only the azimuthal velocity:

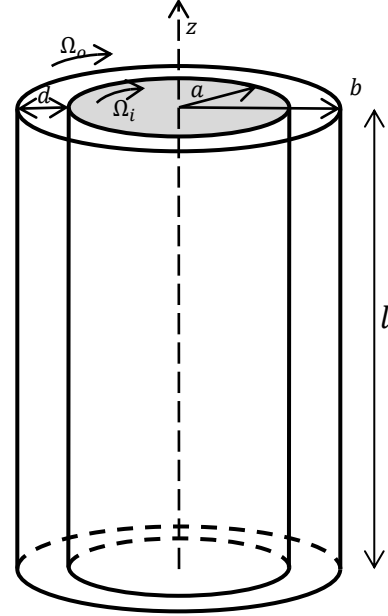


Figure 3.1: A scheme of the Couette-Taylor flow system.

$$\vec{U} = V(r)\vec{e}_\theta \quad 3.1$$

As there is no stress in the  $\theta z$  and  $rz$  planes,  $\bar{T}^p$  is written a priori:

$$\bar{T}^p = \begin{pmatrix} T_{rr}(r) & T_{r\theta}(r) & 0 \\ T_{r\theta}(r) & T_{\theta\theta}(r) & 0 \\ 0 & 0 & T_{zz}(r) \end{pmatrix} \quad 3.2$$

In the Couette flow the velocity and the stress tensor are both invariant in  $\theta z$  planes ( $\frac{\partial V}{\partial z} = \frac{\partial V}{\partial \theta} = 0$ ,  $\frac{\partial \bar{T}}{\partial z} = \frac{\partial \bar{T}}{\partial \theta} = 0$ ) and in time ( $\frac{\partial V}{\partial t} = 0$ ,  $\frac{\partial \bar{T}}{\partial t} = 0$ ).

By substituting the base flow expressions 3.1 and 3.2 to the dimensional Oldroyd-B equations 2.18, the equations of the base flow in a cylindrical annulus of infinite length read:

$$\begin{aligned} \rho \frac{V^2}{r} &= \frac{d\Pi}{dr} - \frac{T_{\theta\theta} - T_{rr}}{r} \Leftrightarrow \frac{d\Pi}{dr} = \rho \frac{V^2}{r} + \frac{N_1}{r} \\ 0 &= \frac{1}{r^2} \frac{d(rT_{r\theta})}{dr} \end{aligned} \quad 3.3$$

The first equation is the balance between the pressure gradient and the centrifugal force reinforced by the elasticity force i.e. the contribution of the first normal stress difference  $N_1 = T_{\theta\theta} - T_{rr}$ . The second one gives the conservation of the momentum in the radial direction.

The Oldroyd-B constitutive equations are simplified to

$$\begin{aligned} T_{rr} &= 0 \\ T_{r\theta} &= \rho v_p \left( \frac{dV}{dr} - \frac{V}{r} \right) \\ T_{\theta\theta} &= 2 \rho v \tau \left( \frac{dV}{dr} - \frac{V}{r} \right)^2 \\ T_{zz} &= 0 \end{aligned} \quad 3.4$$

Note that the second normal stress difference  $N_2 = T_{rr} - T_{zz}$  vanishes identically.

The boundary conditions for cylindrical annulus are

$$V(r = a) = \Omega_i a \quad V(r = b) = \Omega_o b \quad 3.5$$

### a. Base flow velocity profile

The solution of the second equation of the system 3.3 is straightforward and reads

$$V(r) = Ar + \frac{B}{r} \quad A = \frac{\Omega_o b^2 - \Omega_i a^2}{b^2 - a^2} \quad B = \frac{(\Omega_i - \Omega_o) a^2 b^2}{b^2 - a^2} \quad 3.6$$

which is the same velocity profile as the Newtonian Couette flow. The non-vanishing component of  $\dot{\gamma}$  reads:

$$\dot{\gamma}_{r\theta} = \frac{dV}{dr} - \frac{V}{r} \quad \text{or} \quad \dot{\gamma}_{r\theta} = \frac{2B}{r^2} = -\frac{2(\Omega_i - \Omega_o) a^2 b^2}{(b^2 - a^2) r^2} \quad 3.7$$

The velocity profile of the circular Couette flow velocity and the shear strain rate are not affected by the viscosity nor by the elasticity properties.

The angular velocity  $\Omega(r)$  of the Couette flow is then determined as follow:

$$\Omega(r) = \frac{V(r)}{r} = A + \frac{B}{r^2} \quad 3.8$$

The angular velocity depends on the radial position  $r$ , so we can define also the mean angular velocity  $\langle \omega \rangle$  of the base flow as follows:

$$\langle \omega \rangle = \frac{\int_a^b r \Omega(r) dr}{\int_a^b r dr} = A + 2B \frac{\ln(b/a)}{(b^2 - a^2)} \quad 3.9$$

Non-dimensionstionized by  $\Omega_i$ , this mean angular velocity reads:

$$\frac{\langle \omega \rangle}{\Omega_i} = \frac{\mu - \eta^2}{1 - \eta^2} \left[ 1 - \frac{1 - \mu}{\mu - \eta^2} \frac{\eta^2}{1 - \eta^2} \ln(\eta^2) \right] \quad 3.10$$

For the five different regimes studied, the velocity profiles of the circular Couette flow are presented in figure 3.2.

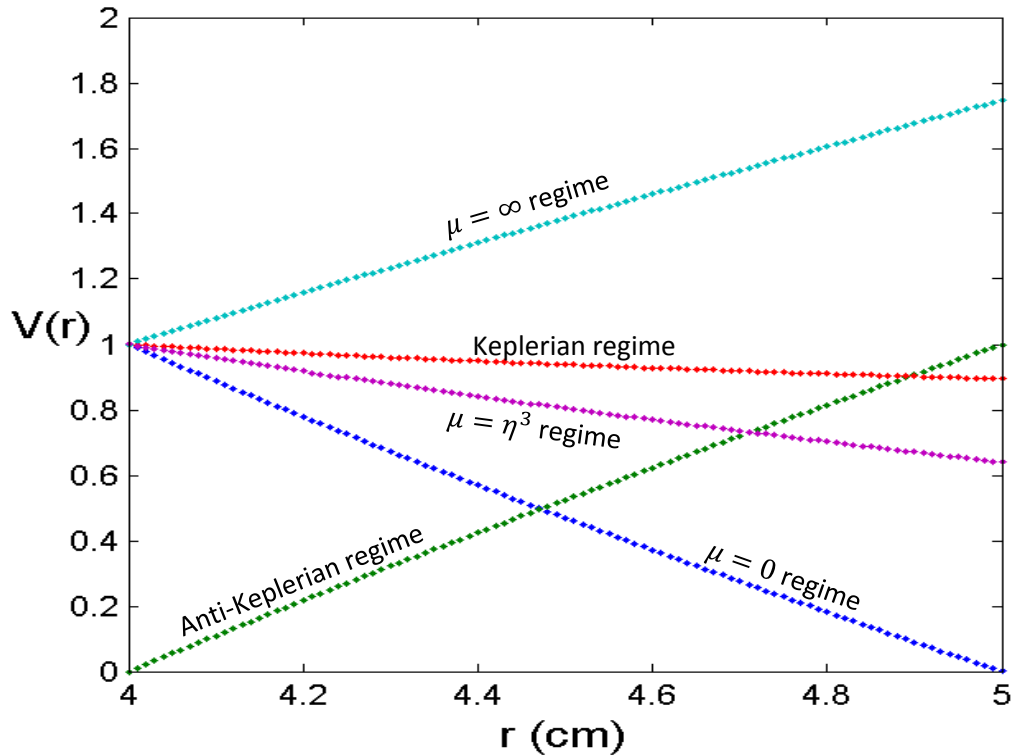


Figure3.2: The velocity of the base flow for five different rotation regimes for  $\eta = 0.8$ .

## b. Stress tensor components

Substituting the base flow profile 3.6 into the Oldroyd-B equations 3.4, we get finally the following result for the relations between stress tensor and strain tensor components in the Oldroyd B model for the circular Couette flow

$$\bar{\bar{T}}^p = \begin{pmatrix} 0 & T_{r\theta} & 0 \\ T_{r\theta} & T_{\theta\theta} & 0 \\ 0 & 0 & 0 \end{pmatrix} \quad \text{with} \quad T_{r\theta} = \frac{-2\rho\nu_p B}{r^2} \quad T_{\theta\theta} = \frac{8\rho\nu_p \tau B^2}{r^4} \quad 3.11$$

Only the component  $T_{\theta\theta}$  contains the elasticity while the shear one is independent of  $\tau$

The first normal stress difference  $N_1$  is given by

$$N_1 = T_{\theta\theta} = \frac{8\rho\nu_p \tau B^2}{r^4} \quad 3.12$$

The radial pressure gradient is then given by

$$\frac{d\Pi}{dr} = \rho \left( A^2 r + \frac{2AB}{r} + \frac{B^2}{r^3} \right) + \frac{8\rho\nu_p \tau B^2}{r^5} \quad 3.13$$

The profile of the pressure gradient from 3.13 is plotted in figure 3.3 for five different rotation regimes for both Newtonian and viscoelastic flows. For all regimes the viscoelastic flows have larger pressure gradients than the Newtonian flows and the contribution from the first normal stress difference  $N_1$  is larger near the inner cylinder than near the outer cylinder.

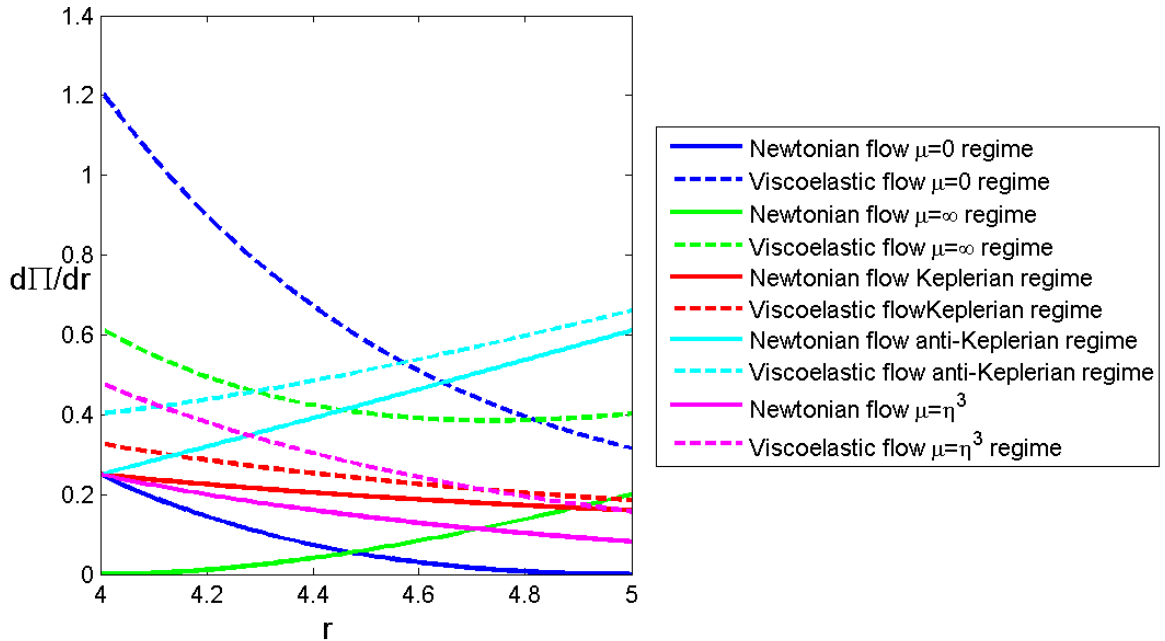


Figure 3.3: Radial profile of the pressure gradient for five rotation regimes for  $\eta = 0.8, ES = 1$ . Solid lines represent the Newtonian flows while dashed lines represent the viscoelastic flows.

### 3.3 Control parameters for viscoelastic Couette flows

Assuming the infinite length of the cylinders, i.e.  $\Gamma \gg 1$ , the geometric parameter of the Couette flow is the radius ratio  $\eta = a/b$ . As seen in the chapter 2, the shear rate  $\dot{\gamma} = U_0/d$  enters the definition of the dimensionless control parameters  $Re$  and  $Wi$ . The characteristic length of the Couette flow is the gap width  $d = b - a$  between the rotating cylinders. Therefore the question is how to choose the characteristic velocity  $U_0$  in the case of two differentially rotating cylinders.

Most of studies use the shear rate at the cylindrical surfaces, therefore defining the Reynolds numbers associated with the rotating cylinders [Andereck1986]:

$$R_i = \frac{\dot{\gamma}_i d^2}{\nu} = \frac{\Omega_i a d}{\nu} \quad R_o = \frac{\dot{\gamma}_o d^2}{\nu} = \frac{\Omega_o a d}{\nu} \quad 3.14$$

and correspondingly the Weissenberg numbers associated with the inner and outer cylinders:

$$Wi_i = \tau \dot{\gamma}_i = \frac{\tau \Omega_i a}{d} \quad Wi_o = \tau \dot{\gamma}_o = \frac{\tau \Omega_o b}{d} \quad 3.15$$

For viscoelastic solutions between differentially rotating cylinders, neither the two Reynolds numbers nor the two Weissenberg numbers are relevant for the dynamics. It is more appropriate to define an average shear rate, and therefore one Reynolds number and one Weissenberg number. There is no unique way to define the mean shear rate. We give some common choices used in literature. The simplest definition of the average shear rate is given by the analogy with the plane Couette flow (Fig. 3.4) and we will call it "traditional":

$$\dot{\gamma} = \frac{|\Omega_i a - \Omega_o b|}{d} \quad 3.16$$

Here  $U_0 = |\Omega_i a - \Omega_o b|$  is the relative velocity of the cylinders. The second control parameter will be then the rotation ratio  $\mu = \Omega_o/\Omega_i$ .

Dubrulle et al. [Dubrulle2005] have defined the shear rate determined at the geometric mean radius  $r_g = \sqrt{ab}$  i.e.

$$\dot{\gamma}_s = \left| r \frac{d}{dr} \left( \frac{V}{r} \right) \right|_{r_g} = \frac{|2B|}{r_g^2} = \frac{2|\Omega_i - \Omega_o|ab}{b^2 - a^2} \quad 3.17$$

Here the characteristic velocity is

$$U_0 = \frac{|\Omega_i - \Omega_o|ab}{(a+b)/2} = |\Omega_i - \Omega_o| \frac{r_g^2}{r_a} = \Omega_i a \frac{2|\mu - 1|}{1 + \eta} \quad 3.18$$

where  $r_a = (a+b)/2$  is the arithmetic mean radius. This definition introduces a second parameter which is the angular velocity of the rotating frame. This angular velocity  $\bar{\Omega}$  is determined at the characteristic radius  $r_g$  i.e.

$$\bar{\Omega} \equiv \Omega(r_g) = \frac{\Omega_i a + \Omega_o b}{b + a} \quad 3.19$$

This angular velocity defines the rotation number

$$R_\Omega = \frac{2\bar{\Omega}}{\dot{\gamma}_s} \quad 3.20$$



Figure 3.4: Average shear rate: (a) traditional definition, (b) dynamic definition [Dubrulle2015].

The table below gives the control parameters defined according these definitions.

Traditional control parameters		Dynamics-motivated parameters	
Shear rate	$\dot{\gamma} = \frac{ \Omega_i a - \Omega_o b }{d}$		$\dot{\gamma}_s = \frac{2 \Omega_i - \Omega_o ab}{b^2 - a^2}$
Reynolds number	$Re = \tau_v \dot{\gamma} = \frac{ \Omega_i a - \Omega_o b d}{\nu} =  R_i - R_o $	Shear Reynolds number	$Re_s = \tau_v \dot{\gamma}_s = \frac{2 \Omega_i - \Omega_o abd^2}{(b^2 - a^2)\nu} = \frac{2}{1 + \eta}  R_i - \eta R_o $
Rotation ratio	$\mu = \frac{\Omega_o}{\Omega_i}$	Rotation number	$R_\Omega = \frac{2\bar{\Omega}}{\dot{\gamma}_s} = \frac{(\Omega_i a + \Omega_o b)(b - a)}{ \Omega_i - \Omega_o ab} = \frac{1 - \eta}{\eta} \frac{\mu + \eta}{ 1 - \mu }$
Weissenberg number	$Wi = \tau \dot{\gamma} = \tau \frac{ \Omega_i a - \Omega_o b }{d}$	Shear Weissenberg number	$Wi_s = \tau \dot{\gamma}_s = \tau \frac{2 \Omega_i - \Omega_o ab}{b^2 - a^2}$
Taylor number	$Ta = \sqrt{\frac{d}{r_a}} Re$	Shear Taylor number	$Ta_s = \sqrt{\frac{d}{r_g}} Re_s$
Modified Weissenberg number	$K = \sqrt{\frac{dS}{r_a}} Wi$	Modified shear Weissenberg number	$K_s = \sqrt{\frac{dS}{r_g}} Wi_s$

Table 3.1: Main control physical parameters of the viscoelastic Couette flow.

The different Weissenberg numbers are related as follows:

$$Wi = \frac{|\eta - \mu|}{\eta} Wi_i \quad Wi = \frac{|\eta - \mu|(1 + \eta)}{2\eta|1 - \mu|} Wi_s \quad 3.21$$

In the present study, we will use the “traditional” definition of the shear rate. The control parameters of the viscoelastic Couette flow are resumed in Table 3.2

	Dimensional form	Dimensionless form
Characteristic velocity	$U_0 =  \Omega_i a - \Omega_o b $	1
Azimuthal velocity $V(r) = Ar + \frac{B}{r}$	$A = \frac{\Omega_o b^2 - \Omega_i a^2}{b^2 - a^2}$ $B = \frac{(\Omega_i - \Omega_o)a^2 b^2}{b^2 - a^2}$	$A = \frac{\mu - \eta^2}{\eta(1 + \eta)}$ $B = \frac{(1 - \mu)\eta}{(1 - \eta)(1 - \eta^2)}$
Shear strain rate	$T_{r\theta} = -\frac{2\mu_p B}{r^2}$	$T_{r\theta} = -\frac{2S B}{r^2}$
Azimuthal strain rate	$T_{\theta\theta} = \frac{8\mu_p \tau B^2}{r^4}$	$T_{\theta\theta} = \frac{8 Wi S B^2}{r^4}$
First Normal stress difference	$N_1 = \frac{8\mu_p \tau B^2}{r^4}$	$N_1 = \frac{8 Wi S B^2}{r^4}$
Pressure gradient	$\frac{d\Pi}{dr} = \rho \left( A^2 r + \frac{2AB}{r} + \frac{B^2}{r^3} \right) + \frac{8\mu_p \tau B^2}{r^5}$	$\frac{d\Pi}{dr} = Re \left( A^2 r + \frac{2AB}{r} + \frac{B^2}{r^3} \right) + \frac{8 Wi S B^2}{r^5}$

Table 3.2: Base flow characteristics in the Couette-Taylor system.

### 3.4 Magnetic analogy of the viscoelastic Couette flow

Following Ogilvie & Proctor [Ogilvie2003], we introduce a set of 3 auxiliary fields  $\vec{B}_i$  ( $i = 1, 2, 3$ ) such that the component of the polymer stress tensor can be written as follows

$$T_p^{ij} = B_{p1}^i B_{p1}^j + B_{p2}^i B_{p2}^j + B_{p3}^i B_{p3}^j \quad 3.22$$

The polymer stress tensor for the base flow 3.2 yields the modified polymer stress tensor  $\vec{T}_p$  for the base flow, the form of which suggests that

$$B_{p3}^1 = B_{p3}^2 = B_{p1}^3 = B_{p2}^3 = 0 \quad \text{and} \quad B_{p3}^3 B_{p3}^3 = \frac{\rho v_p}{\tau} \Rightarrow B_{p3}^3 = B_0 \quad 3.23$$

Here  $B_0 = \sqrt{\rho v_p / \tau}$  is the characteristic polymer analog of the magnetic field.

The remaining components satisfy the following system:

$$\begin{cases} B_{p1}^1 B_{p1}^1 + B_{p2}^1 B_{p2}^1 = \frac{\rho v_p}{\tau} \\ B_{p1}^1 B_{p1}^2 + B_{p2}^1 B_{p2}^2 = \frac{2\rho v_p B}{r^2} \\ B_{p1}^2 B_{p1}^2 + B_{p2}^2 B_{p2}^2 = \frac{8\rho v_p \tau B^2}{r^4} \end{cases} \quad 3.24$$

There are 4 unknowns in the system of three equations; this suggests two choices of these auxiliary fields, either

$$\vec{B}_{p1} = \frac{B_0}{\sqrt{2}} \begin{pmatrix} 1 \\ 0 \\ 0 \end{pmatrix} \quad \vec{B}_{p2} = \frac{B_0}{\sqrt{2}} \begin{pmatrix} 1 \\ \frac{2\tau B}{r^2} \\ 0 \end{pmatrix} \quad \vec{B}_{p3} = B_0 \begin{pmatrix} 0 \\ 0 \\ 1 \end{pmatrix} \quad 3.25$$

or

$$\vec{B}_{p1} = B_0 \begin{pmatrix} 1 \\ \frac{2\tau B}{r^2} \\ 0 \end{pmatrix} \quad \vec{B}_{p2} = B_0 \begin{pmatrix} 0 \\ \frac{2\sqrt{2}\tau B}{r^2} \\ 0 \end{pmatrix} \quad \vec{B}_{p3} = B_0 \begin{pmatrix} 0 \\ 0 \\ 1 \end{pmatrix} \quad 3.26$$

In the dimensionless form, the polymer analog of the azimuthal component of the magnetic fields becomes:

$$\vec{B}_{p2} = B_0 \begin{pmatrix} 1 \\ \frac{(1-\mu)}{(\eta-\mu)(1+\eta)} \frac{\sqrt{2}Wi a^2}{r^2} \\ 0 \end{pmatrix} \quad \text{or} \quad \vec{B}_{p2} = B_0 \begin{pmatrix} 0 \\ \frac{(1-\mu)}{(\eta-\mu)(1+\eta)} \frac{2\sqrt{2}Wi a^2}{r^2} \\ 0 \end{pmatrix} \quad 3.27$$

The axial field  $\vec{B}_{p3} = B_0 \vec{e}_z$  will dominate the azimuthal field if

$$\frac{(1-\mu)}{(\eta-\mu)(1+\eta)} \frac{\sqrt{2}Wi a^2}{r^2} \ll 1 \quad 3.28$$

which yields a critical Weissenberg number  $Wi^*$  defined by:

$$Wi^* \equiv \min_r \frac{(\eta-\mu)(1+\eta)}{(1-\mu)} \frac{r^2}{\sqrt{2}a^2} \quad 3.29$$

For example, for the geometry with  $\eta = 0.8$ , using  $r = a$  we get  $Wi^* \sim 0.76$ .

Therefore, in the case of the Keplerian rotation regime, the destabilization of the viscoelastic Couette flow with  $Wi \ll Wi^*$  may be interpreted as an analog of the standard MRI (SMRI). In the opposite case, when  $Wi \gg Wi^*$ , the dominating polymer analog of the azimuthal component of the magnetic field may lead to the analog of the azimuthal MRI (AMRI) or the Michael instability.

For intermediate values of  $Wi$ , both the axial and the azimuthal components will contribute to the viscoelastic instability which reminds the helical MRI (HMRI).

In the viscoelastic analog, the polymeric analog of the azimuthal magnetic field possesses a profile of  $B_p \propto 1/r^2$ , while current experiments of HMRI with liquid metal [Stefani06] [Stefani07] [Seilmayer2014] have azimuthal magnetic field profile of  $B \propto 1/r$ .

### 3.5 Conclusion

In this chapter we have presented the viscoelastic base flow in the Couette-Taylor system, named viscoelastic Couette flow, with control parameters defined in both dimensional and dimensionless form. The polymer stress tensor of the viscoelastic Couette flow can be expressed in analogy with some effective magnetic fields. Full details of the analogy will be given in section 7.3.

# Chapter 4: Stability of viscoelastic Couette flow

## 4.1. Rayleigh criterion of stability

### a. Rotational Rayleigh discriminant and epicyclic frequency

The stability of a circular Couette flow is predicted by the inviscid condition established by Lord Rayleigh in 1916 and named *circulation Rayleigh criterion*. A rotating flow can be destabilized by axisymmetric perturbations only if the Rayleigh discriminant  $\Phi_r(r)$  is negative somewhere in the flow. The Rayleigh discriminant is given by

$$\Phi_r(r) = \frac{1}{r^3} \frac{d(rV(r))^2}{dr} \Big|_r = \frac{1}{r^3} \frac{dL^2}{dr} \Big|_r \quad 4.1$$

where the subscript  $r$  denotes “rotation”. Otherwise stated, an inviscid rotating flow is stable if the angular momentum  $L = r^2\Omega$  or the circulation increases monotonically outward (positive stratification of the angular momentum or the circulation). We substitute the expression of  $V(r)$  (equations 3.6) into equation 4.1 and we have:

$$\Phi_r(r) = 4A \left( A + \frac{B}{r^2} \right) \quad 4.2$$

Then we scale the Rayleigh discriminant by  $\Omega_i^2$  i.e.  $\Psi_r(\hat{r}) = \Phi_r(\hat{r})/\Omega_i^2$  with  $\hat{r} = r/d$  to get the dimensionless Rayleigh discriminant:

$$\Psi_r(\hat{r}) = \frac{4(\eta^2 - \mu)}{(\eta^2 - 1)^2} \left( (\eta^2 - \mu) + (\mu - 1) \left( \frac{\eta}{1 - \eta} \right)^2 \frac{1}{\hat{r}^2} \right) \quad 4.3$$

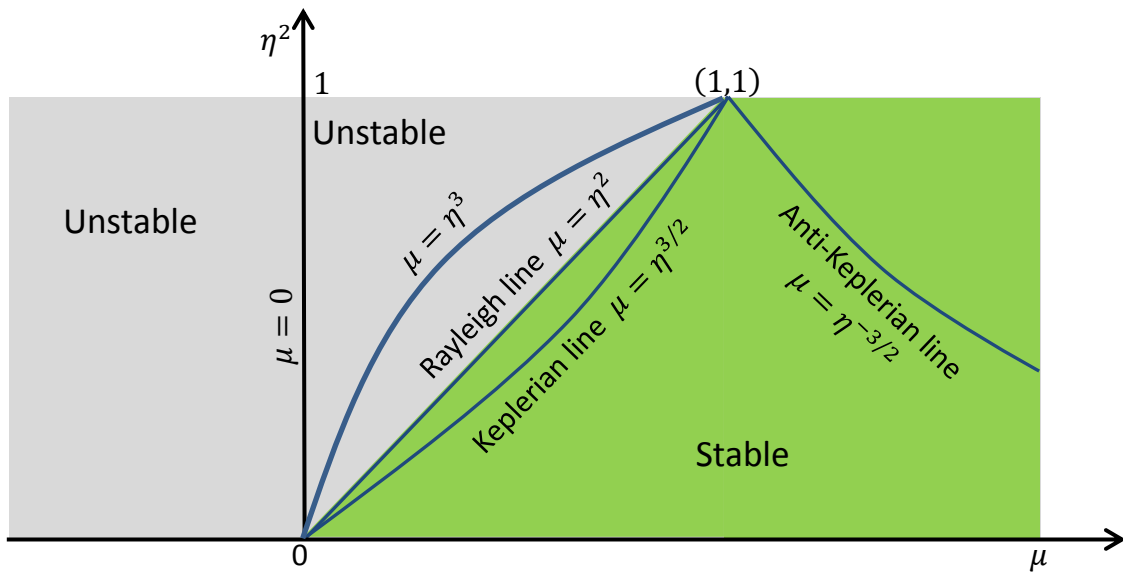


Figure 4.1: Stability diagram of the circular Couette flow according to circulation Rayleigh criterion.

Equation 4.2 Implies that a circular Couette flow is potentially unstable only if  $\mu < \eta^2$ . So that the Keplerian regime, anti-Keplerian regime and  $\mu = \infty$  regime are potentially stable as  $\Psi_r(\hat{r}) > 0$  while the  $\mu = 0$  regime and the  $\mu = \eta^3$  regime are potentially unstable as  $\Psi_r(\hat{r}) < 0$ .

In the potentially stable zone i.e. when the discriminant is positive, the radially displaced particles may oscillate with a frequency called epicyclic frequency  $\omega_{ep}$  in the Astrophysics of the accretion disks assumed to be axisymmetric [Balbus2009]:

$$\omega_{ep}^r(r) = \sqrt{\Phi_r(r)} \quad 4.4$$

The epicyclic frequency is used to determine the boundaries of the accretion disks when the discriminant becomes negative and therefore unstable to small perturbations.

The instabilities of a Newtonian flow in a Couette-Taylor system already have been investigated by many researchers. An experimental diagram of different states observed in circular Couette flow was provided by Andereck in 1986, it gives a clear evidence of the validity of Rayleigh criterion (see figure 4.2). A recent state diagram including high turbulence has been established by the Twente group [Huisman2014].

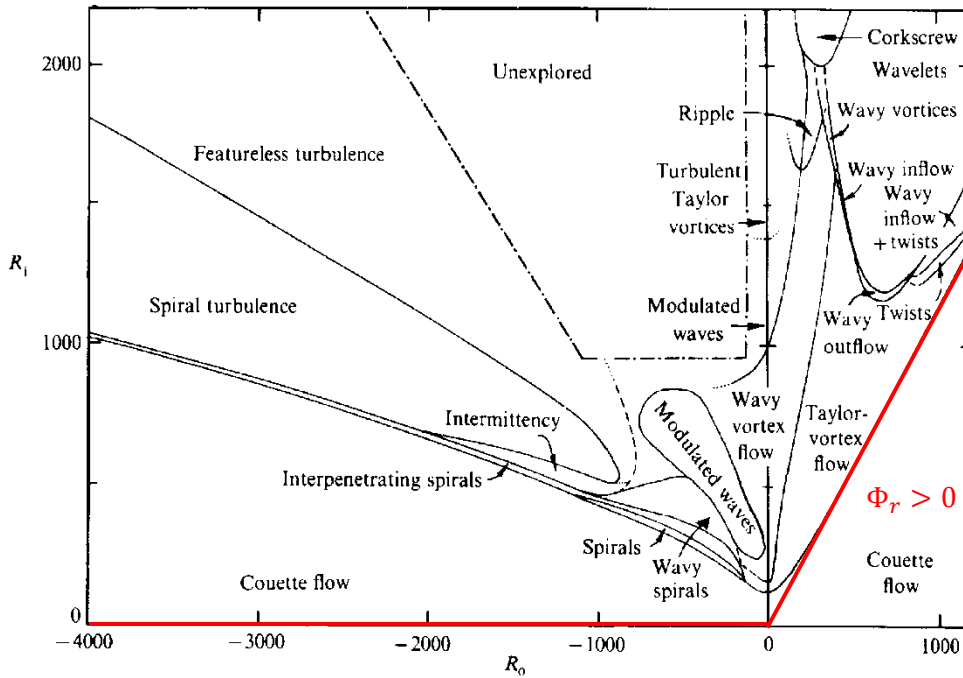


Figure 4.2: State diagram of Newtonian Couette-Taylor instabilities for different rotational regimes with  $\eta = 0.883$ ;  $R_i$  and  $R_o$  are the Reynolds numbers of the inner and outer cylinders respectively [Andereck1986]. The red line represents the condition of  $\Phi_r = 0$ . The flow in the positive  $\Phi_r$  zone is predicted to be stable Couette flow, all states were found in the region where  $\Phi_r < 0$ .

### b. Elasto-rotational Rayleigh discriminant

Following the lead of the circulation Rayleigh criterion, we have made our first step in the study of the elastic instability in the Couette-Taylor system by generalizing the circulation Rayleigh criterion to elastic fluids within the Oldroyd-B model.

We consider a fluid particle in a differential rotating laminar flow. The particle rotates at the orbit of the radius  $r$  because of the balance between the centrifugal force and the pressure gradient modified by the contribution of the first normal stress difference. If this particle is moved from its orbit into a nearby orbit  $r + dr$  so quickly that  $\tau_{disp} \ll (\tau_v, \tau)$ , no dissipation nor relaxation occurs and the momentum of the fluid particle is conserved. The net force acting on the displaced fluid particle at the new orbit  $r + dr$  can be written as follow:

$$df = -\rho\Phi_{er}(r)dr + o(dr^2) \quad 4.5$$

where we have introduced the generalized Rayleigh discriminant  $\Phi_{er}(r)$  that can be called elasto-rotational discriminant where the subscript  $er$  denotes “elasto-rotational” :

$$\Phi_{er}(r) = \Phi_r(r) + \frac{1}{\rho r} \frac{dN_1}{dr} \Big|_r \quad 4.6$$

For the circular Couette viscoelastic flow, the elasto-rotational discriminant is expressed:

$$\Phi_{er}(r) = \Phi_r(r) + \Phi_e(r) = 4A \left( A + \frac{B}{r^2} \right) - \frac{32\mu_p\tau B^2}{\rho} \frac{1}{r^6} \quad 4.7$$

where the elasto-rotational Rayleigh discriminant  $\Phi_{er}(r)$  is composed of the rotation contribution  $\Phi_r(r)$  and the elastic contribution  $\Phi_e(r)$ . Then the non-dimensional elasto-rotational Rayleigh discriminant reads:

$$\Psi_{er}(\hat{r}) = \frac{4(\eta^2 - \mu)}{(\eta^2 - 1)^2} \left( (\eta^2 - \mu) + (\mu - 1) \left( \frac{\eta}{1 - \eta} \right)^2 \frac{1}{\hat{r}^2} \right) - \frac{32ES(\mu - 1)^2}{(\eta^2 - 1)^2} \left( \frac{\eta}{1 - \eta} \right)^4 \frac{1}{\hat{r}^6} \quad 4.8$$

where the product  $ES$  represents the polymer contribution to the elasticity of the solution.

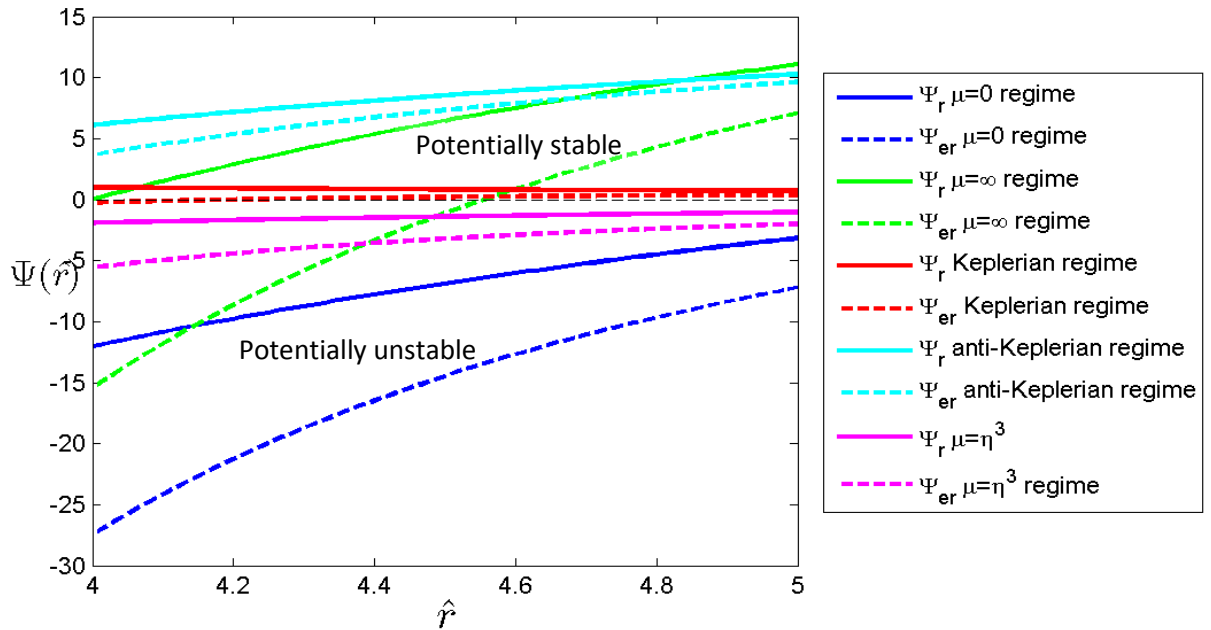


Figure 4.3: Rotational Rayleigh discriminant  $\Psi_r(\hat{r})$  and elasto-rotational Rayleigh discriminant  $\Psi_{er}(\hat{r})$  for flows with  $ES = 1$  in five rotation regimes.

In figure 4.3, we have plotted the rotation Rayleigh discriminant  $\Psi_r(\hat{r})$  and the elasto-rotational Rayleigh discriminant  $\Psi_{er}(\hat{r})$  for a solution with  $ES = 1$  for five rotation regimes. We set  $\hat{r} \in [4,5]$  corresponding to  $\eta = 0.8$ . We can see that the curves of the elasto-rotational Rayleigh discriminant for all regimes are located below the corresponding curves of the rotational Rayleigh discriminant. The contribution from the elasticity force is the enhancement of the potential instability.

The rotational and elasto-rotational epicyclic frequencies  $\omega_{ep}^r(\hat{r})$  and  $\omega_{ep}^{er}(\hat{r})$  corresponding to the rotational and elasto-rotational Rayleigh discriminant are defined by:

$$\omega_{ep}^r(\hat{r}) = \sqrt{\Psi_r(\hat{r})} \quad \omega_{ep}^{er}(\hat{r}) = \sqrt{\Psi_{er}(\hat{r})} \quad 4.9$$

In figure 4.4 the profiles of the rotational epicyclic frequencies  $\omega_{ep}^r$  and the elastic epicyclic frequency  $\omega_{ep}^{er}$  are plotted for solutions of  $ES = 1$  in respect to  $\hat{r}$  for the regimes with positive  $\Psi(\hat{r})$ . In the regimes of  $\mu = \infty$  and  $\mu = \eta^{-3/2}$ , both the  $\omega_{ep}^r(\hat{r})$  and  $\omega_{ep}^{er}(\hat{r})$  increase with  $\hat{r}$ . However in the Keplerian regime,  $\omega_{ep}^r(\hat{r})$  decreases with  $\hat{r}$  while  $\omega_{ep}^{er}(\hat{r})$  increases with  $\hat{r}$ .

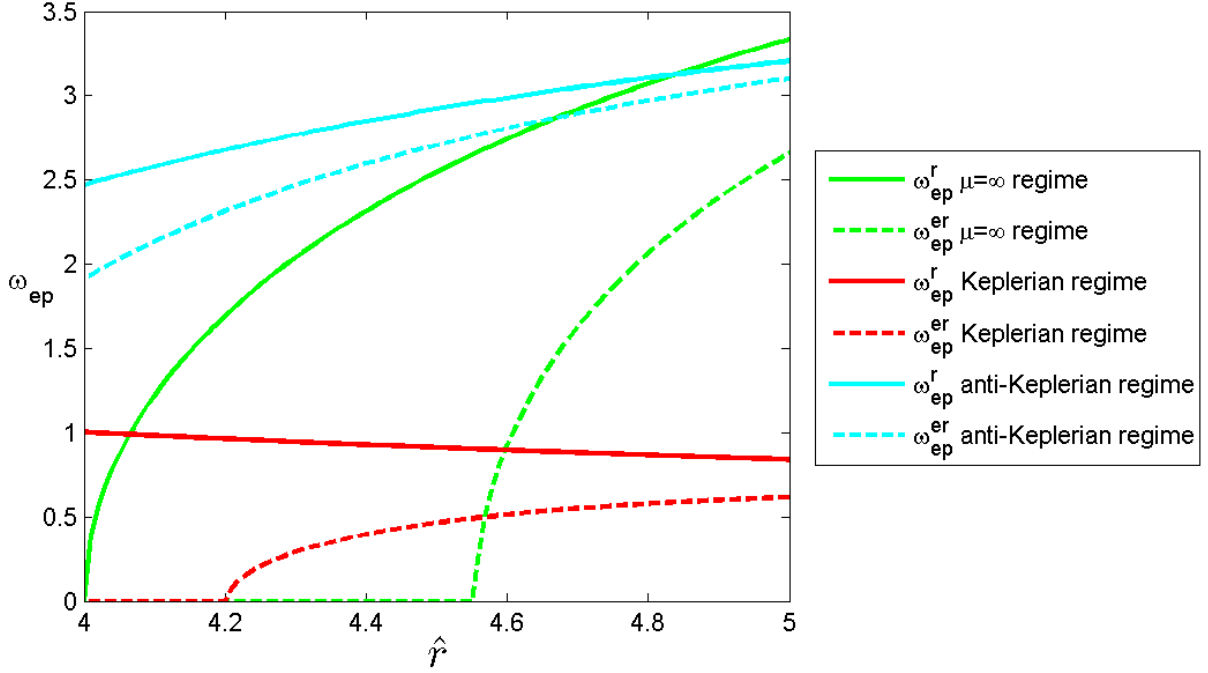


Figure 4.4: Rotational epicyclic frequency  $\omega_{ep}^r$  and elasto-rotational epicyclic frequency  $\omega_{ep}^{er}$  with  $ES = 1$  for five regimes.

The elastic force does not only enhance the centrifugal instability, but also it can induce an elastic instability when the outer cylinder rotates faster than the inner cylinder when the centrifugal force is no more destabilizing the Newtonian flow. This is the case for the Keplerian flow with a viscoelastic fluid with  $ES = 1$ . In figure 4.3, the elasto-rotational Rayleigh discriminant is negative near the inner cylinder, so that such a flow is potentially unstable to elasticity-driven perturbations.

### c. Potentially stable and unstable zone

The elasto-rotational Rayleigh discriminant  $\Psi_{er}(\hat{r})$  is a function of  $\hat{r}$  and it depends on three control parameters:  $\eta, \mu$  and  $ES$ . For each set of control parameters of  $(\mu, \eta, ES)$ , we calculate the

minimum  $\Psi_{er} = \min(\Psi_{er}(\hat{r}))$  among all possible values of  $\hat{r} \in [4, 5]$ . Then the flow is unstable if the smallest Rayleigh discriminant along  $\hat{r} \in [4, 5]$  is negative ( $\Psi_{er} < 0$ ). We plot in figure 4.5 the nodal surface  $\Psi_{er} = 0$  in the 3D parameter space of  $(\eta^2, \mu, ES)$ . The color on the surface represents the magnitude of  $\eta^2$ . The parameter space is separated into three zones: unstable zones for large and small  $\mu$  and stable zone for  $\mu \sim 1$ . For solutions with large values of  $ES$ , small rotation velocity difference ( $\mu$  approaches 1) is enough to destabilize the flow.

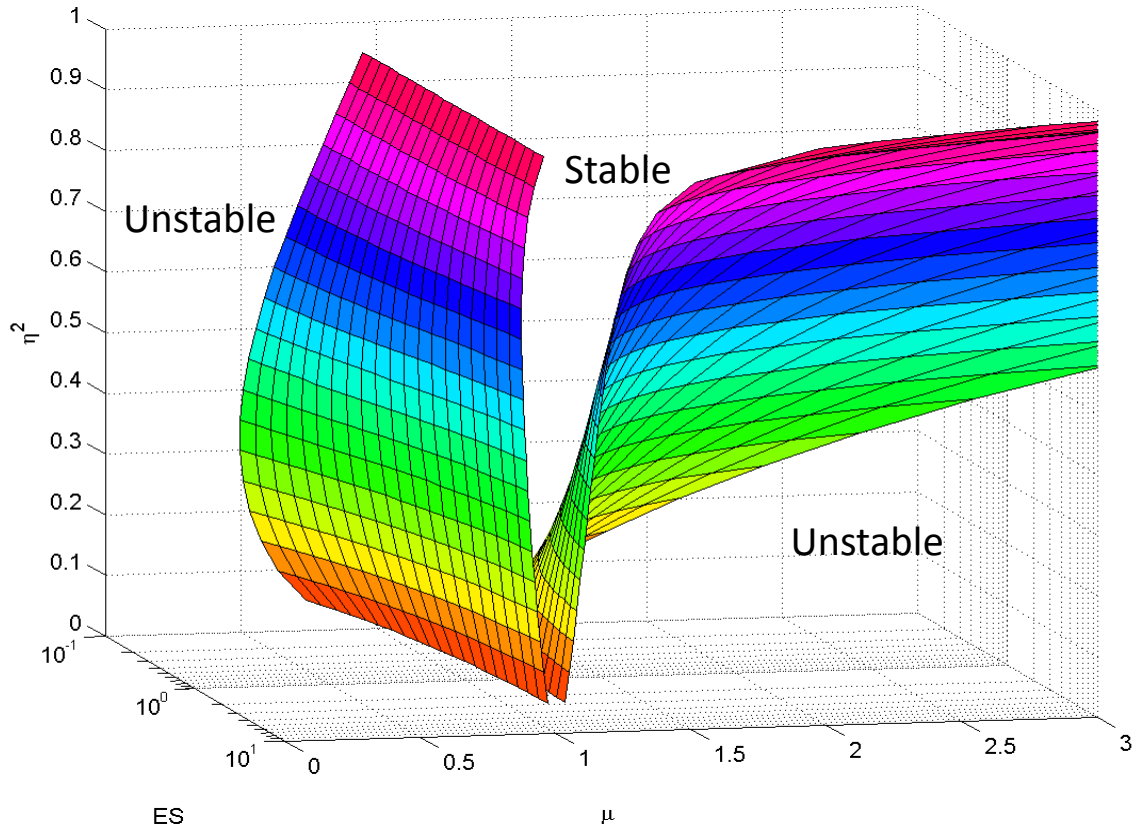


Figure 4.5: 3D plot of the nodal surface of the elastic Rayleigh discriminant.

To be more precise, we plot in figure 4.6 in the plane of  $(\mu, \eta^2)$  the Rayleigh lines  $\Psi_{er} = 0$  for different  $ES$  together with the Keplerian and anti-Keplerian lines. The rotational Rayleigh line corresponds to the value  $ES = 0$ . We observe that the Rayleigh lines (solid lines) with different polymer elasticity  $ES$  intersect the Keplerian and anti-Keplerian lines (dashed lines) at different values of the radius ratio  $\eta$ . For different values of  $\eta$ , there exist different values of polymer elasticity  $ES^*$  such that a flow in the Keplerian or anti-Keplerian regime can be destabilized. The values  $ES_k^*$  and  $ES_{ak}^*$  of the polymer elasticity in Keplerian and anti-Keplerian regime are plotted against  $\eta \in [0.1, 0.95]$  in figure 4.7; they increase with  $\eta$ . This means that to get elasticity-driven perturbations with less polymer elasticity, it is necessary to use cylindrical annulus with large gap i.e with small values of  $\eta$ . For the annular configuration with  $\eta = 0.8$ , we found  $ES_k^* = 0.672$  and  $ES_{ak}^* = 3.451$ .

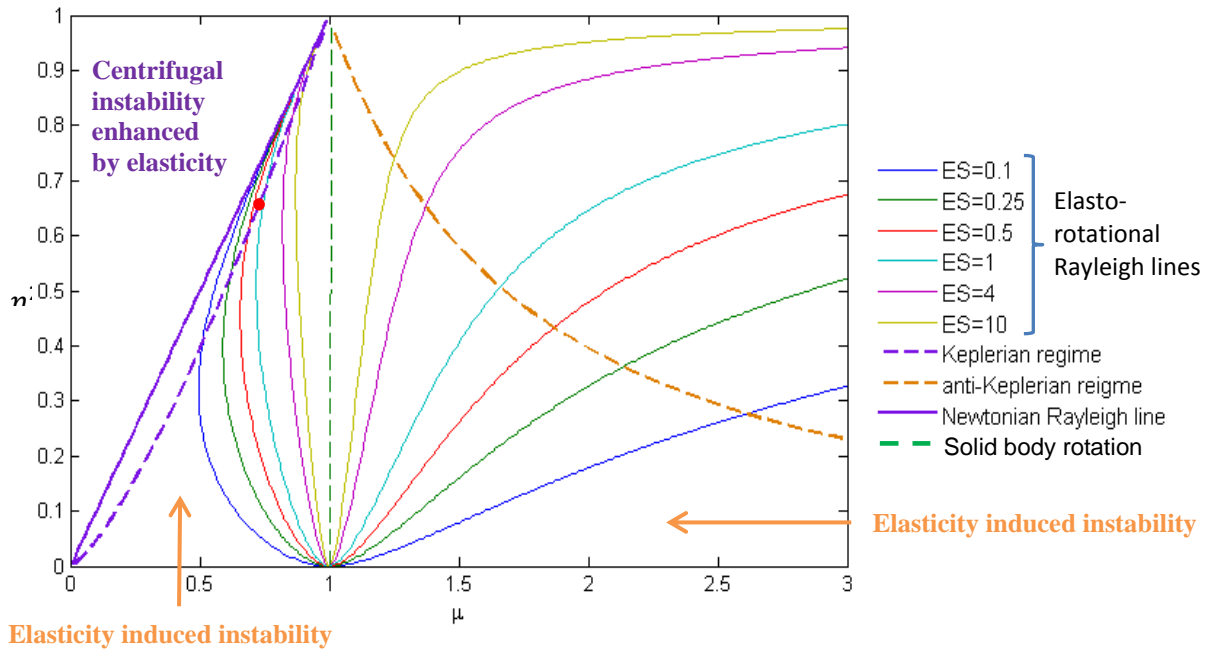


Figure 4.6: Rayleigh lines for different  $ES$  on  $(\mu, \eta^2)$  diagram.

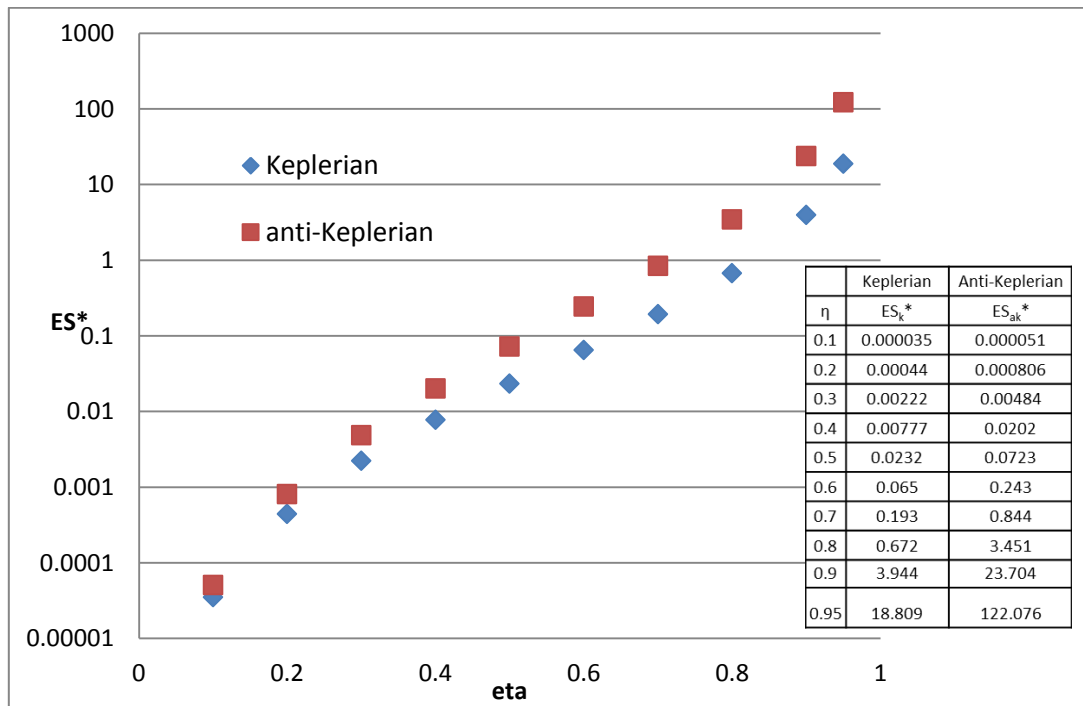


Figure 4.7: Critical polymer elasticity  $ES^*$  in respect to radius ratio  $\eta$  on Keplerian and anti-Keplerian regime.

To summarize, we plot a schematic diagram (figure 4.8) to present the two effects of the elastic contribution to the instability. In the diagram, the solid green line is the Rayleigh line on which the rotational Rayleigh discriminant vanishes. The solid orange lines are the Rayleigh lines on which the elasto-rotational Rayleigh discriminant vanishes. The position of the Rayleigh line moves with  $ES$ . For larger  $ES$ , the elastic Rayleigh lines approach the solid body rotation line.

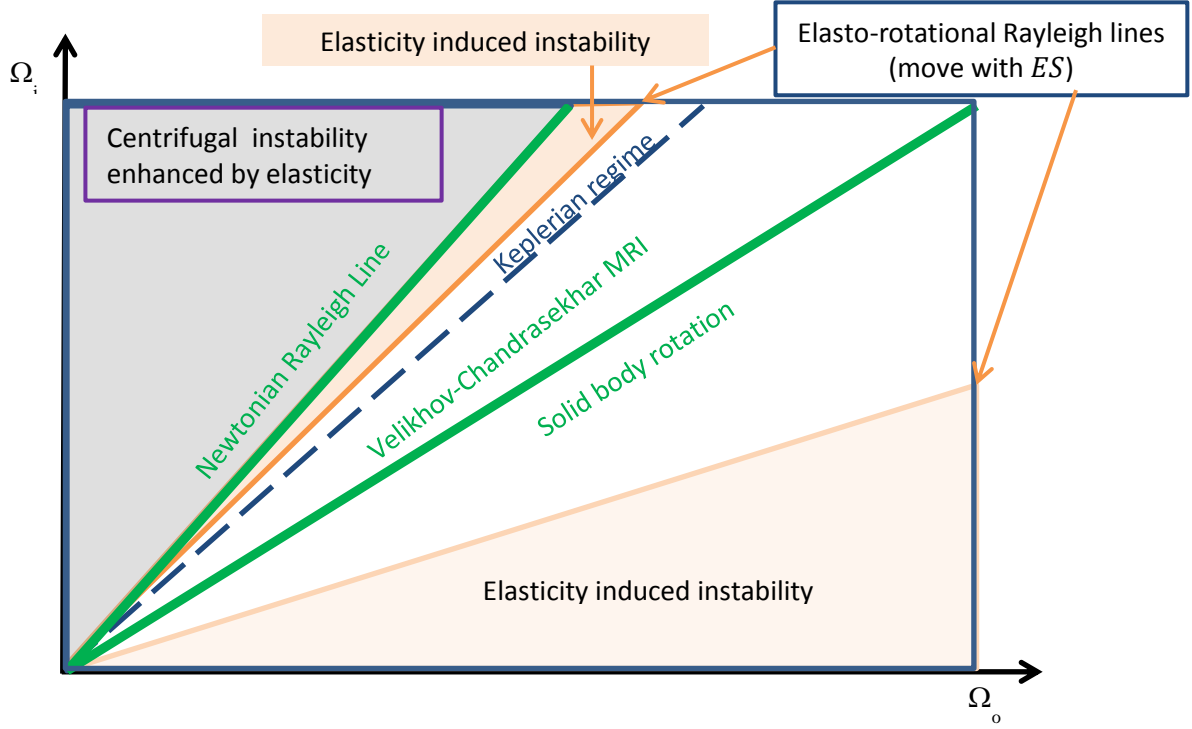


Figure 4.8: Schematic stability diagram according to elasto-rotational Rayleigh discriminant.

#### d. Analogy with the Michael criterion of MHD

The elasto-rotational Rayleigh discriminant has the same structure as the generalized Rayleigh discriminant in the rotating flow in the presence of an azimuthal magnetic field  $B_\theta$ . In this case, a rotating hydro-magnetic flow of ideal electrically conducting fluids is potentially unstable with respect to axisymmetric perturbations if [Davidson2013][Michael1954]:

$$\Phi_{mr} = \Phi_r - \frac{r}{\rho\mu_0} \frac{d}{dr} \left( \frac{B_\theta}{r} \right)^2 < 0 \quad 4.10$$

We define  $\Phi_{mr}$  as a magneto-rotational discriminant. If the magnetic field  $B_\theta$  varies with the radius as  $C/r^2$ ,  $\Phi_{mr}$  becomes:

$$\Phi_{mr} = \Phi_r + \Phi_m = \Phi_r + \frac{6C^2}{\rho\mu_0 r^6} \quad 4.11$$

In this case both the magnetic contribution  $\Phi_m$  and elastic contribution  $\Phi_e$  (expression 4.7) vary with the radius as  $1/r^6$ . Hence the elasto-rotational Rayleigh discriminant  $\Phi_{er}$  is analog to  $\Phi_{mr}$  and the elasto-rotational criterion is analog to the Michael criterion.

## 4.2. Linear stability analysis (LSA)

The elasto-rotational Rayleigh discriminant allows us to predict the potential instability in a Couette-Taylor system. However this criterion does not provide the sufficient condition because it assumes that the fluids are inviscid. Therefore, it is necessary to perform the linear stability analysis (LSA) of the flow to obtain precise predictions of the first instability of a viscoelastic laminar flow. As mentioned in chapter 1, many authors have performed the LSA of the viscoelastic fluid with Oldroyd-

B model, but these studies have treated only special cases: axisymmetric modes [Shaqfeh1996] [Kupferman1998], non-axisymmetric modes but without the variation of the viscosity ratio  $S$  [Avgoust1993]. The present study aims to address a thorough investigation of the stability of the viscoelastic flows for different values of  $S$ ,  $\eta$  and for different cases of the differential rotation of the cylinders: stationary outer cylinder, stationary inner cylinder, co-rotating cylinders in the Keplerian ratio or in the anti-Keplerian ratio.

Starting from this section, the dimensionless radius  $\hat{r}$  is replaced by  $r$  as only dimensionless equations are used from now on.

### a. Linear stability equations

The linear stability of viscoelastic fluid in Couette-Taylor system consists in addition of infinitesimally small perturbations to the dimensionless flow equations 2.23 and linearization about this base state (equation 3.6). As the base state depends only on the radial coordinate  $r$  and it is axisymmetric i.e. it is invariant along the cylinder axis and around the azimuthal direction, the small perturbations can be developed in normal modes of the form of  $[st + i(m\theta + qz)]$ . Here  $s = \sigma + i\omega$ , in which  $\sigma$  is the growth rate and  $\omega$  is the angular frequency;  $m$  and  $q$  are azimuthal and axial wavenumbers. So that the variables with perturbations are written as follows

$$\vec{U}(r) = \begin{pmatrix} 0 \\ V(r) \\ 0 \end{pmatrix} + \begin{pmatrix} u(r) \\ v(r) \\ w(r) \end{pmatrix} e^{(st+im\theta+iqz)}$$

$$\Pi(r) = \Pi(r) + p(r)e^{(st+im\theta+iqz)} \quad 4.12$$

$$\overline{\overline{T}}(r) = \begin{pmatrix} 0 & T_{r\theta}(r) & 0 \\ T_{r\theta}(r) & T_{\theta\theta}(r) & 0 \\ 0 & 0 & 0 \end{pmatrix} + \begin{pmatrix} t_{rr}(r) & t_{r\theta}(r) & t_{rz}(r) \\ t_{r\theta}(r) & t_{\theta\theta}(r) & t_{\theta z}(r) \\ t_{rz}(r) & t_{\theta z}(r) & t_{zz}(r) \end{pmatrix} e^{(st+im\theta+iqz)}$$

Then we substitute the expressions 4.12 to the dimensionless governing equations (2.23) and linearize the resulting equations by retaining only the terms of first order of the perturbations. We get the following dimensionless linearized perturbation equations:

$$\frac{u}{r} + Du + \frac{imv}{r} + iqw = 0$$

$$Re \left( \left( s + \frac{imV}{r} \right) u - \frac{2Vv}{r} \right) = -Dp + \left( \frac{t_{rr}}{r} + Dt_{rr} + \frac{imt_{r\theta}}{r} + iqt_{rz} - \frac{t_{\theta\theta}}{r} \right) + (1-S) \left( \frac{Du}{r} - \frac{u}{r^2} + D^2u - \frac{m^2u}{r^2} - q^2u - \frac{2imv}{r^2} \right)$$

$$Re \left( \left( s + \frac{imV}{r} \right) v + \frac{Vu}{r} + DVu \right) = -\frac{imp}{r} + \left( \frac{2t_{r\theta}}{r} + Dt_{r\theta} + \frac{imt_{\theta\theta}}{r} + iqt_{\theta z} \right) + (1-S) \left( \frac{Dv}{r} - \frac{v}{r^2} + D^2v - \frac{m^2v}{r^2} - q^2v + \frac{2imu}{r^2} \right) \quad 4.13$$

$$Re \left( s + \frac{imV}{r} \right) w = -ikp + \left( \frac{t_{rz}}{r} + Dt_{rz} + \frac{imt_{\theta z}}{r} + iqt_{zz} \right) + (1-S) \left( \frac{Dw}{r} + D^2w - \frac{m^2w}{r^2} - q^2w \right)$$

$$\left( 1 + ERes + ERe \frac{imV}{r} \right) t_{rr} - ERe \frac{2imT_{r\theta}u}{r} = 2SDu$$

$$\left( 1 + ERes + ERe \frac{imV}{r} \right) t_{r\theta} + ERe \left[ DT_{r\theta}u + \frac{Vt_{rr}}{r} - T_{r\theta}Du - \frac{imT_{\theta\theta}u}{r} - DVt_{rr} - \right.$$

$$\begin{aligned}
\frac{imT_{r\theta}v}{r} - \frac{uT_{r\theta}}{r} &= S \left[ Dv + \frac{imu}{r} - \frac{v}{r} \right] \\
\left( 1 + ERes + ERe \frac{imV}{r} \right) t_{rz} - ERe \frac{imT_{r\theta}w}{r} &= S [Dw + iqu] \\
\left( 1 + ERes + ERe \frac{imV}{r} \right) t_{\theta\theta} + ERe \left[ DT_{\theta\theta}u + \frac{2Vt_{r\theta}}{r} + \frac{2T_{r\theta}v}{r} - 2DVt_{r\theta} - 2T_{r\theta}Dv - \right. \\
\left. \frac{2imT_{\theta\theta}v}{r} - \frac{2T_{\theta\theta}u}{r} \right] &= S \left[ \frac{2imv}{r} + \frac{2u}{r} \right] \\
\left( 1 + ERes + ERe \frac{imV}{r} \right) t_{\theta z} + ERe \left[ \frac{Vt_{rz}}{r} - DVt_{rz} - T_{r\theta}Dw - \frac{imT_{\theta\theta}w}{r} \right] &= S \left[ \frac{imw}{r} + iqv \right] \\
\left( 1 + ERes + ERe \frac{imV}{r} \right) t_{zz} &= 2Siqw
\end{aligned}$$

The boundary conditions require that the perturbations vanish on the cylindrical surfaces  $r = a$  and  $r = b$ :

$$u = v = w = 0, \quad \frac{du}{dr} = 0 \quad 4.14$$

## b. Numerical methods

To solve the linear equations 4.13 together with the boundary conditions 4.14, we rewrite them as an eigenvalue problem in form:

$$\bar{A}\vec{X} = s\bar{B}\vec{X} \quad 4.15$$

where  $\vec{X} = (u \ v \ w \ p \ t_{rr} \ t_{r\theta} \ t_{rz} \ t_{\theta\theta} \ t_{\theta z} \ t_{zz})^T$  is the perturbation variables,  $\bar{A}$  and  $\bar{B}$  are second order matrices. This eigenvalue problem is solved by the Chebyshev collocation method with the Matlab solver "eigs".

The variable vector  $\vec{X}$  is projected on a discrete Chebyshev series  $S_c$  and then transformed to the mesh vector  $S_r$  which is concentrated on the boundaries of the domain:

$$S_r = \frac{S_c + 1}{2} + \frac{a}{d} \quad 4.16$$

The calculation of the eigenvalues depends also on the mesh grid number  $N$ , but the results converge as  $N$  gets larger. After several tests, we have chosen  $N = 100$  which is large enough to assure the right results and small enough to reduce the calculation time. When the mesh size is fixed, the eigenvalue  $s$  of the system is a function of the control parameters  $Re, E, \eta, \mu, S, m, q$ . Among all these control parameters,  $Re$  and  $\mu$  control the shear rate and rotation,  $E$  and  $S$  characterize the fluid properties, and  $m$  and  $q$  define the perturbations.

For a given set of parameters, there exist more than one eigenvalue that fit the eigenvalue problem. Taking for example  $Re = 500, E = 0.03, \eta = 0.8, S = 0.7, m = 0, q = 10$  on Keplerian regime  $\mu = \eta^{3/2}$ , we find that the eigenvalues are complex numbers presented by dots in figure 4.9. Among all the eigenvalues presented in figure 4.9, most of them converge along the mesh size. The converging eigenvalue which possesses the largest growth rate  $\sigma$  corresponds to the most unstable mode.

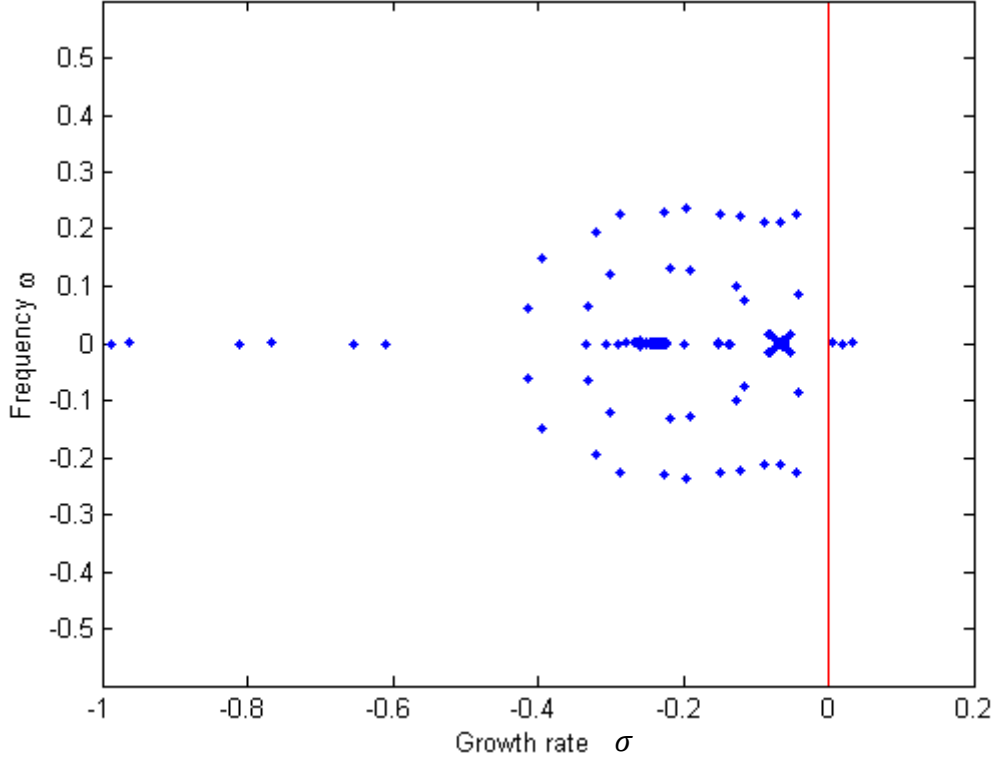


Figure 4.9: Eigenvalues of the linear equation with the parameters of  $Re = 500$ ,  $E = 0.03$ ,  $\eta = 0.8$ ,  $S = 0.7$ ,  $m = 0$ ,  $q = 10$ , on Keplerian regime  $\mu = \eta^{3/2}$ .

For fixed control parameters of  $Re$ ,  $E$ ,  $\eta$  and  $S$ , the eigenvalues with the largest growth rate vary for different wave numbers  $m \in \mathbb{Z}$  and  $q \in \mathbb{R}$ . So we change  $m$  and  $q$  to find the eigenvalue with the largest growth rate  $\sigma_{max}$  among all possible  $m$  and  $q$ .

For each fixed elasticity  $E$  and viscosity ratio  $S$  we calculated critical shear rate  $\dot{\gamma}_c$  which makes the largest growth rate  $\sigma_{max} = 0$  among a series of  $m$  and  $q$ . The  $m$  and  $q$  that minimize the  $\dot{\gamma}_c$  are called critical wave numbers  $m_c$  and  $q_c$  while the correspond frequency  $\omega_c$  is the critical angular frequency. The critical control parameters like  $Re_c$ ,  $Ta_c$ ,  $Wi_c$ ,  $K_c$  are deduced. To understand better the critical mode we investigate also the eigenfunctions of the variables  $\vec{X}$  corresponding to  $S_c$  and the azimuthal vorticity defined by:

$$\omega_\theta = \frac{\partial V}{\partial z} - \frac{\partial W}{\partial r} \quad 4.17$$

### c. Code validations

We have used our code to compute some cases found in literature in order to validate our code. Starting from the Newtonian fluids in the  $\mu = 0$  regime, we have got the same critical Taylor number  $Ta_c$  and critical wave number  $q_c$  for several  $\eta$  as previous researches [Swinney1981]. Then we have studied the purely elastic instability  $Re = 0$  of axisymmetric mode  $m = 0$  at small gap approximation  $\eta \sim 1$  and compared with the results provided by Larson & Shaqfeh [Larson1990]. In figure 4.10 we compare the results of Larson & Shaqfeh together with our calculations in terms of parameters used by Larson & Shaqfeh [Larson1990]. We have obtained similar critical curves with the same behavior. However our critical values are about 10% higher than the results of Larson & Shaqfeh.

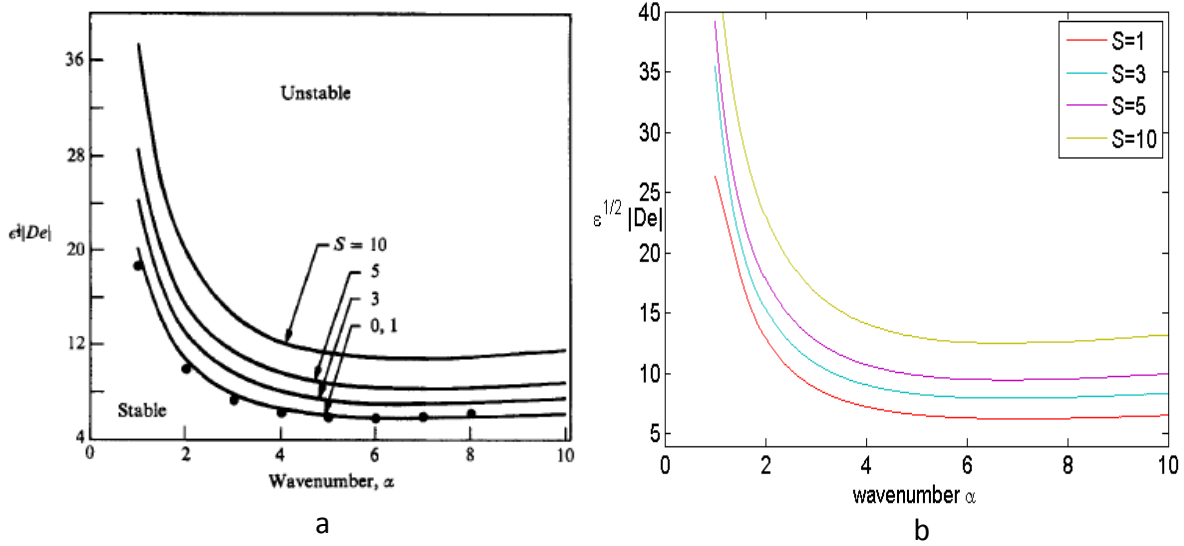


Figure 4.10: Critical curves of the most unstable axisymmetric mode of the purely elastic instability when  $Re = 0$  and  $m = 0$  at the small gap limitation  $\eta \sim 1$ . (a) Results of Larson & Shaqfeh. (b) Our results. All syntaxes in both figures are defined by the way of Larson & Shaqfeh [Larson1990].

Joo & Shaqfeh have provided LSA results of the inertia-elastic instability with  $Re \neq 0$  using the same simplified equations of small gap and axisymmetric mode [Joo1992]. They have found a competition between the purely elastic instability and the centrifugal instability which is represented by the crossed critical curves of two modes in figure 4.11 (a). Using the same control parameters of  $S = 0.8$ , we have obtained the similar critical curves of two modes: an inertia-elasticity mode at large  $Re$  and a purely elasticity mode at large  $Wi$ . Although our critical curves are still about 10% higher than the results of Joo & Shaqfeh the same instabilities and similar critical curves are reproduced.

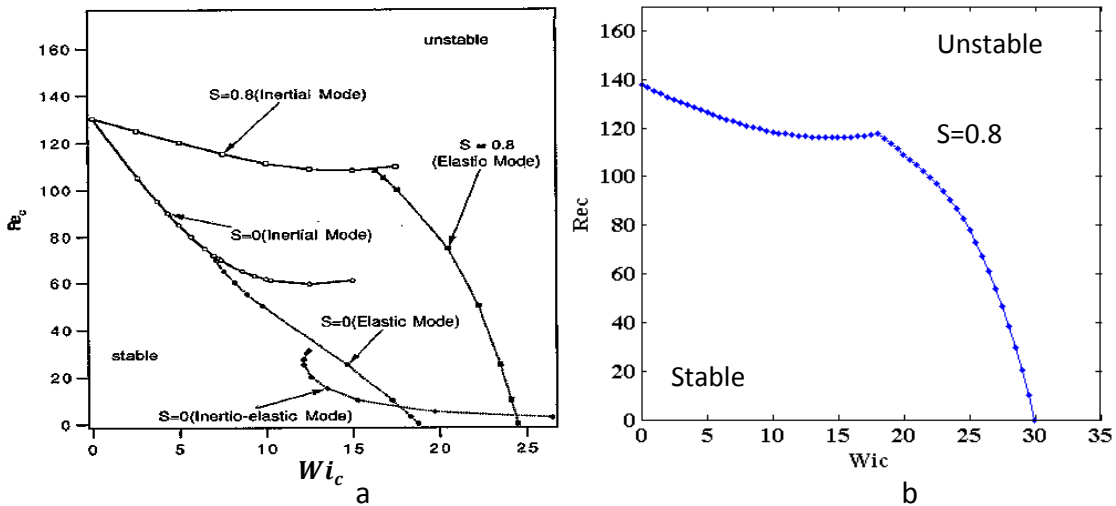


Figure 4.11: Critical curves  $Re_c - Wi_c$  represent two different unstable modes: purely elastic mode and inertia-elastic mode.  $S = 0.8$ ,  $m = 0$ ,  $\eta \sim 1$ . (a) Results of Joo et al. (b) Our results.

Larson & Shaqfeh [Larson1990] and Joo & Shaqfeh [Joo1992] have used simplified equations from the Oldroyd-B model, while we have used the exact equations. That is the reason why our

numerical results differ quantitatively from their results; and they are more precise than those of the previous studies.

The second test was done with control parameters of Avgousti who have used the same complete equations of Oldroyd-B model [Avgousti1993]. We plot in figure 4.12 (a) (b) the critical curves of Avgousti and ours, for a specific wavenumber  $q = 3.12$  for  $\nu_s/\nu_p = 3.76$ ,  $\eta = 0.95$ ,  $\mu = 0.5$  defined by Avgousti. The comparison between our results and those of Avgousti shows perfect agreement, so we confirm that our codes are reliable.

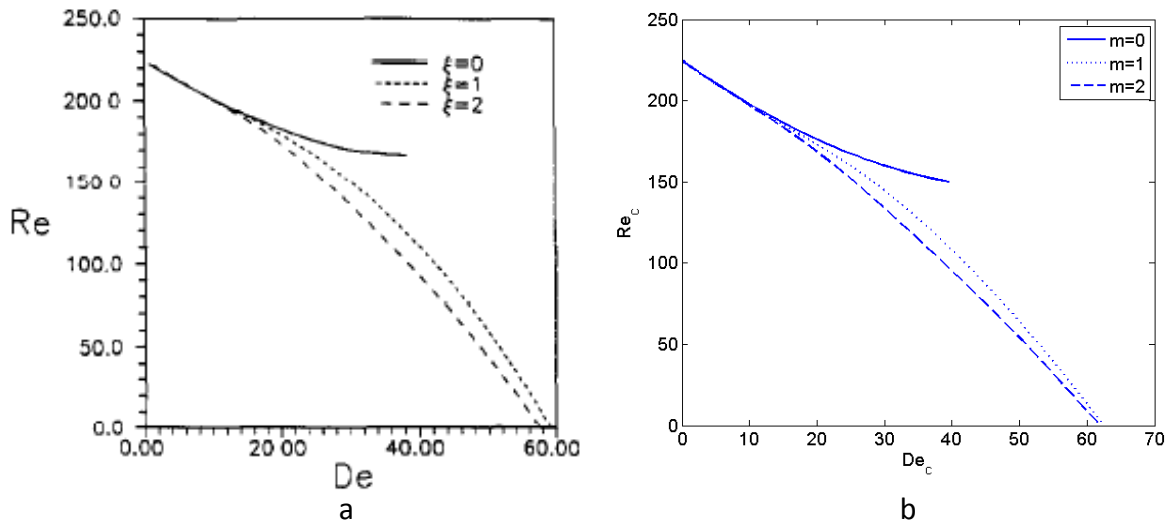


Figure 4.12: Critical curves for different azimuthal wavenumber (denoted by  $\xi$  for figure (a),  $m$  for figure (b)) for a specific wavenumber  $q = 3.12$  for  $\nu_s/\nu_p = 3.76$ ,  $\eta = 0.95$ ,  $\mu = 0.5$  defined by Avgousti. (a) Results of Avgousti. (b) Our results.

We have also studied the inertia-elasticity instability in the Keplerian regime with  $\eta = 0.95$ ,  $S = 0.5$ , which is the case studied by Ogilvie & Potter [Ogilvie2008]. Comparing our results to those of Ogilvie & Potter in figure 4.13, we can see similar critical curve with similar growth rate distribution and the same spiral mode. However our critical curve is about 10% higher than that of Ogilvie & Potter who have declared that they have only qualitative agreements with Avgousti et al [Avgousti 1993]. So we believe that our results are more reliable than those of Ogilvie & Potter.

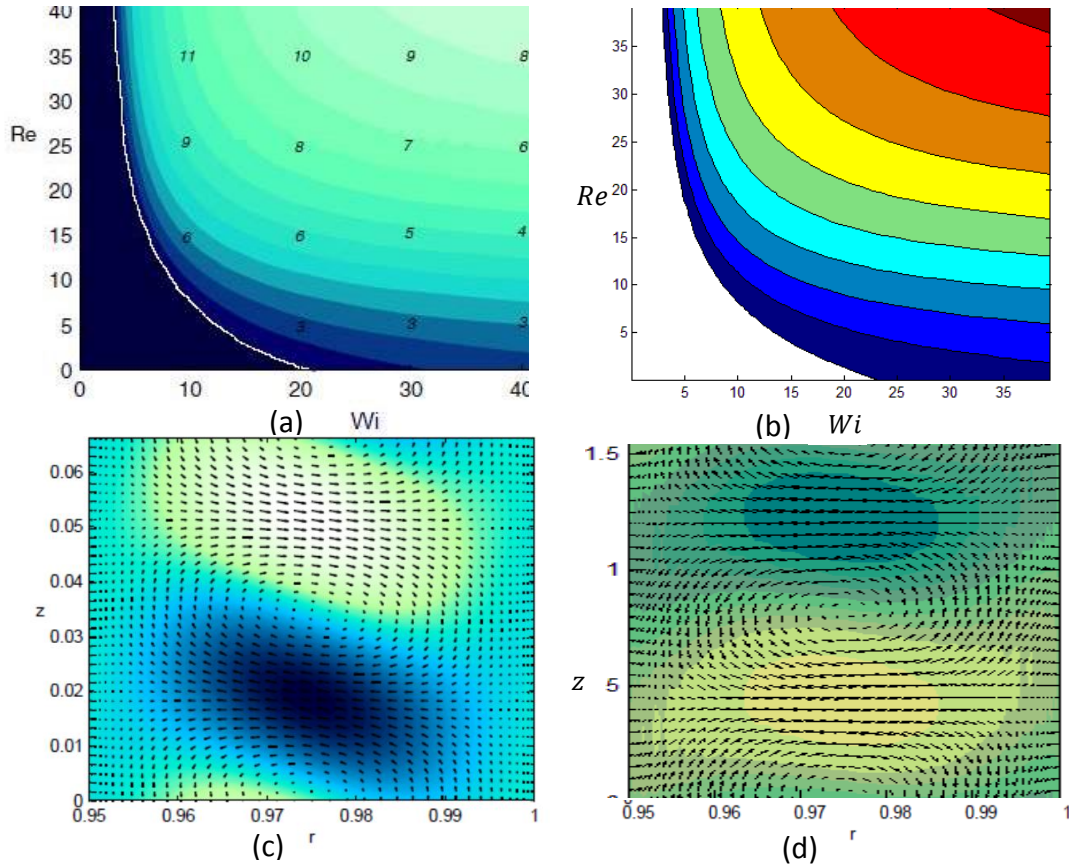


Figure 4.13: (a) (b): Contours of the growth rate  $s$  optimized with respect to  $m$  and  $q$  on map of  $(Re, Wi)$  for Keplerian case at  $\eta = 0.95, S = 0.5$ . (a) Results of Ogilvie & Potter where the white line represents the critical curve; (b) our results where the white zone represents negative growth rate. (c) (d): Eigenfunction of the preferred mode on a specific set of  $(Re, Wi)$  along the critical curve for  $Re = 40$ . The azimuthal velocity perturbation is indicated by color scale. (c) Results of Ogilvie & Potter (d) our results.

### 4.3 Conclusion

In this chapter we have introduced the theoretical methods to study the viscoelastic instability in a Couette-Taylor flow. We start by generalizing the rotational Rayleigh discriminant to include the elasticity. This has led us to the elasto-rotational Rayleigh discriminant. The analysis of these discriminants shows that the elasticity force enhances the centrifugal instability and can induce the purely elasticity-induced instability when the flow is centrifugally stable. The elasto-rotational Rayleigh discriminant is analog to the Michael's instability criterion for the circular Couette flow of conducting fluids in the presence of an azimuthal magnetic field

To get more precise predictions on the critical parameters, we have formulated the linear stability analysis of a viscoelastic flow with the complete Oldroyd-B model. The resulting eigenvalue problem was solved using our numerical code based on Matlab environment and using the Chebyshev collocation method. The code has been validated with comparison with some cases from the literature. The critical curves and critical modes that fit our experiments will be presented in the following chapters.



# Chapter 5:

## Experimental setup & Working fluids

---

This chapter describes the experimental setup and the working fluids. As the working fluids are viscoelastic, their rheology properties and the elastic properties are all well characterized before and after experiments.

### 5.1. Experimental setup

The experiments were conducted in a Couette Taylor system which consists of a flow in the gap between two vertical coaxial cylinders with the length  $l = 45\text{cm}$ . The inner cylinder is made by Plexiglas with the radius  $a = 4\text{cm}$  and the outer cylinder is made by Delrin with the radius  $b = 5\text{cm}$ . So the gap width of our Couette-Taylor system  $d = 1\text{cm}$ , the radius ratio  $\eta = 0.8$  and the aspect ratio  $\Gamma = 45$ .

Each cylinder is connected to a step motor so that the 2 cylinders can be controlled separately. The rotational velocity can reach 200 r/min, beyond this value the system will vibrate. The end plates of the top and the bottom rotate with the outer cylinder. As we have used cylinders of large aspect ratio  $\Gamma$ , the influence of the border effect on the central part of the cylinders can be ignored.

The Couette-Taylor system is immersed in a water tank of  $30\text{cm} \times 30\text{cm} \times 45\text{cm}$  connected by tubes to a thermostatic bath. We set the water circulation temperature to  $20^\circ\text{C}$ , however as the water tank is large, the water circulation is non-axisymmetric, and the rotation of viscous polymer solutions dissipates energy, we cannot control precisely the temperature in the Couette-Taylor system. Several temperature tests show that the temperature in the Couette-Taylor system is  $20^\circ\text{C} \pm 0.4^\circ\text{C}$ .

For visualization, we have added 2% Kalliroscope in our working fluids. Such a concentration does not modify the viscosity of the working fluid. The front view of the flow patterns can be observed using light spot while the cross section in the plane  $(r, z)$  is obtained. The flow patterns are recorded by a CCD camera supported by the Streampix software, and then the films are analyzed with the help of Matlab.

In each experiment, the gap between the two cylinders was filled with the prepared working fluids and the rotation velocities of the cylinders were increased step by step with a waiting period longer than 10 min on each step. As soon as the laminar base flow is entirely destabilized we recorded the critical velocity of the cylinders and the flow patterns with both gap view and front view. The transition from laminar flow to unstable flow is also recorded.

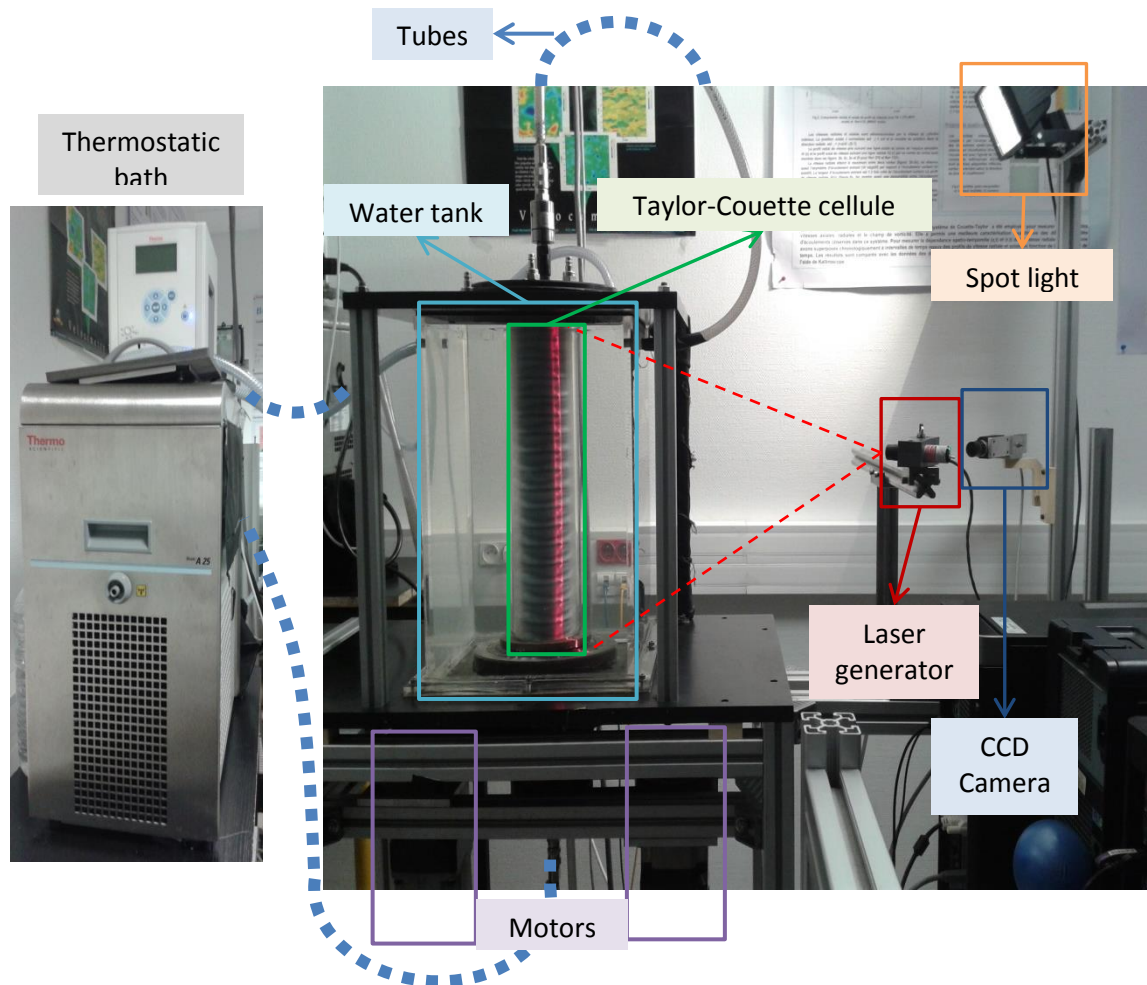
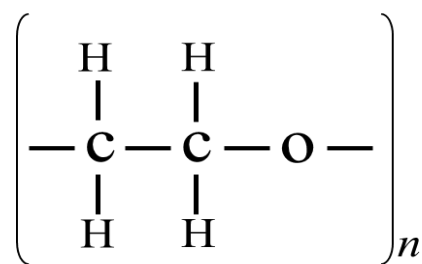


Figure 5.1: Experimental setup and its environment.

## 5.2. Preparation of working fluids



(a)



(b)

Figure 5.2: (a) Monomer of PEO and PEG (b) PEO sealed in a flacon.

The working fluid used in our experiments is the polymer solution of Polyoxyethylene (PEO) dissolved in mixture of Polyethylen glycol (PEG) and water. The PEO and the PEG are both neutral polymers with flexible linear chains of similar chemical properties. They are polymers of the same

monomer (presented in figure 5.2 (a)), while they differ from each other only by the degree of polymerization  $n$ . According to our supplier, the PEO we used has an average molar mass of  $8 \times 10^6$  so  $n_{PEO} \sim 1.8 \times 10^5$  while the PEG we used has an average molar mass of  $2 \times 10^4$  so  $n_{PEG} \sim 450$ . As the PEO has long chain and it is easily degradable, the PEO is sealed in small flacons of 2ml (presented in figure 5.2 b) and is stored in a freezer of  $-10^\circ\text{C}$ . The PEG is stored in plastic bottles in lab temperature.

In the final solutions, PEO works as the source of elasticity and viscosity while PEG contributes only to the viscosity. However the interaction between PEO and PEG affects also the final elasticity of the solution. The mixture of water and PEG is considered as the solvent to PEO as it has constant viscosity independent to the shear rate. In order to get large elasticity, we use 1000 ppm of PEO for all solutions, which is the maximum dissolvable quantity of PEO. The concentration of the PEG is changed from 2.5% to 25% by weight for different solutions. We have also added 2.5% of isopropyl alcohol to help the dissolution of PEO and its stabilization. We have added 2% of Kalliroscope for visualization.

### ***Solution preparation protocol***

The following protocol was followed to prepare the working solutions. Taking a solution of 1000 ppm PEO and 10% PEG as an example, first we prepared a solution of PEO (solution 1) and a solution of PEG (solution 2) separately, and then mixed them to get the final working solution.

Preparation of the solution 1

1. Weight 50g isopropyl alcohol in a beaker of 1L.
2. Weight 2000mg PEO and disperse it into the isopropyl alcohol.
3. Fill the beaker with demineralized and degassed water to total weight of 1kg.
4. Do not agitate.
5. Seal the beaker by a piece of cellophane and keep it in a fridge of  $8^\circ\text{C}$  for 3 to 5 days.

Preparation of the solution 2

1. Weight 200g PEG in a beaker.
2. Fill the beaker with demineralized and degassed water to a total weight of 1kg.
3. Stir the turbid liquid with a magnetic agitator until the solution becomes transparent.
4. Seal the beaker by a piece of cellophane and keep it in a fridge of  $8^\circ\text{C}$  for 3 to 5 days.

Mixing the solutions 1 and 2

1. Take out solution 1 and solution 2 from the fridge and leave them in laboratory until they returned to laboratory temperature.
2. Agitate each solution moderately for 30 minutes to 2 hours with a magnetic agitator.
3. Measure 0.95 kg liquid of each solution in a 2L beaker.
4. Agitate the mixture with a magnetic agitator for 1 to 4 hours.
5. Seal the beaker with a piece of cellophane and keep it in lab temperature for 3 to 5 days.
6. Add 2% of Kalliroscope into the solution and agitate it moderately for 10 minutes. Then the solution is good for rheology tests and experiments.

### 5.3. Viscosity measurements

The viscosity of a fluid measures the friction between fluid molecules in a shear flow. As our fluid is a mixture of two polymers, there are the solvent viscosity  $\rho\nu_s$  and the total viscosity  $\rho\nu$  to measure. These viscosities are measured by a shear stress rheometer (Anton Paar MC300) with a cone –plane measuring cell of radius  $R = 24.984 \text{ mm}$  and cone angle  $\alpha = 0.5^\circ$  (see figure 5.3).

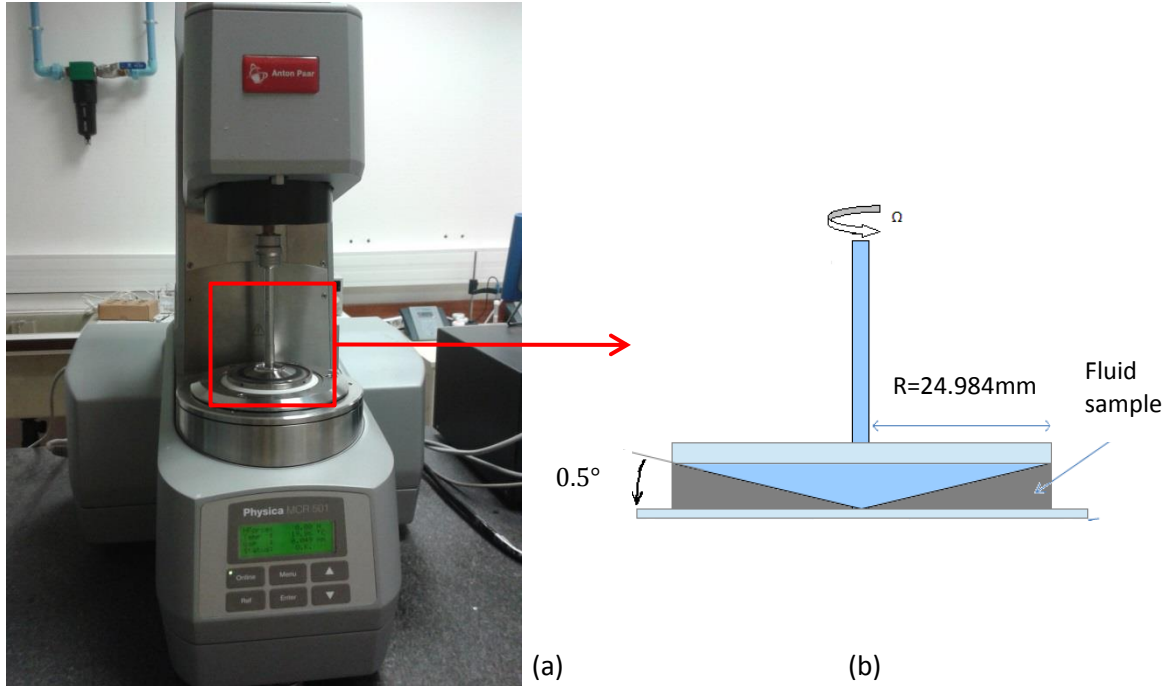


Figure 5.3: (a) The shear stress rheometer (Anton Paar MC300). (b) The cone-plane measuring cell.

To measure the viscosities, we fill the gap between the cone and the base plate with fluid sample and we rotate the cone in a constant rotational velocity  $\Omega$  so that the shear rate  $\dot{\gamma} \sim \Omega/\alpha$  is fixed. Then the rheometer measures the torque  $T$  that the cone receives and calculate the shear stress  $T_{r\theta}$ . As we increase the shear rate  $\dot{\gamma}$  step by step while waiting enough time for the cone to finish one complete tour at each step, the dynamic viscosity of the fluid sample  $\rho\nu$  is measured by the ratio between shear stress and the shear rate  $\rho\nu = T_{r\theta}/\dot{\gamma}$ .

The working temperature of the cone-plane cell is kept in  $20 \pm 0.01^\circ\text{C}$  which is the same temperature of our Couette-Taylor cell.

#### a. Solvent viscosity

We have prepared the PEG solvents separately for rheological tests following the preparation protocol of solution 2. The viscosities of the solvents are measured by swapping the shear rate from  $10^0$  (1/s) to  $10^2$ (1/s) by step of  $10^{0.1}$ (1/s) and the results are presented in figure 5.4. We verified that the solvent viscosities are constant within shear rates from 1 to 100 (1/s). The average viscosity of each solvent along tested shear rates is considered as the solvent viscosity  $\rho\nu_s$ . The solvent viscosity increases from 0.0025 (Pa · s) to 0.1418 (Pa · s) when the PEG concentration increases from 2.5% to 25%. This viscosity represents the friction between PEG molecules as the molecules of the water and isopropyl alcohol are too small to be negligible before the PEG molecules.

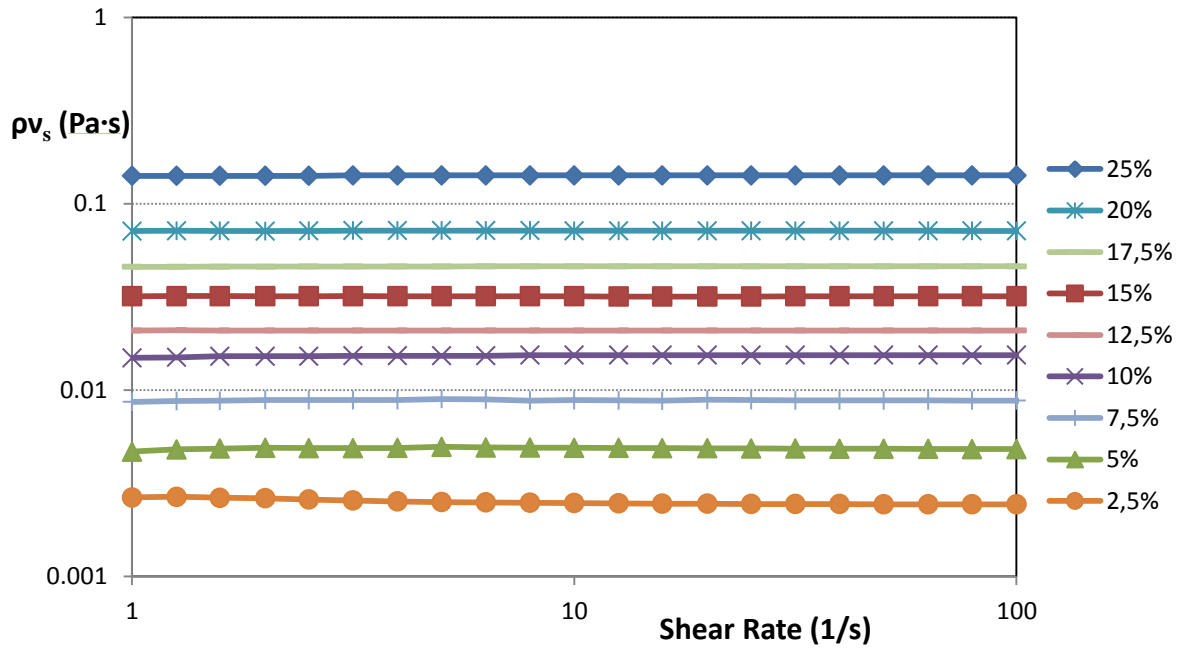


Figure 5.4: Solvent viscosity with respect to shear rates for PEG concentration from 2.5% to 25%.

### b. Fluid viscosity

The viscosities of our working fluids are measured by swapping the shear rate from  $10^{-0.5}$  (1/s) to  $10^3$  (1/s) by a step of  $10^{0.1}$  (1/s). Each solution is tested before and after the Couette-Taylor experiments and multiple solutions are prepared at each concentration of PEG. We recall that the PEO concentration is fixed to 1000ppm for all solutions. The results are presented in figure 5.5.

We observe that the fluid viscosity increases with the PEG concentration. As we have fixed the PEO concentration to 1000 ppm for all solutions, more PEG a solution contains, larger viscosity it has. The viscosities decrease slowly with the shear rate so that the shear thinning effect is weak. The more PEG a solution contains, the weaker is the shear thinning. Even for the most shear-thinning solution (the one containing 2.5% PEG) the viscosity decreases by 60% in a shear rate range of 3.5 decades. As our experiments cover only 1 decade ( $1$  to  $10$   $s^{-1}$ ), the shear-thinning effect is negligible. So our working fluids almost fit the Oldroyd-B model.

When the shear rate becomes larger than a certain critical value the viscosity raises again because the flow is no longer laminar and instability appears. The instability appears at smaller shear rate for a solution which contains more PEG and has higher viscosity.

It is known that the polymer solutions are sensible to the condition of preparation (waiting time, agitation time, agitation magnitude...) as the PEO molecules are long and fragile, the solutions of the same PEG concentration may have different viscosities. The viscosity was measured before and after each experiment and it decreases because the rotation breaks polymer chains.

The total solution viscosity  $\rho v$  is determined at the plateau of the measured viscosity curve (i.e. in the limit of vanishing shear rate) for each solution. With total fluid viscosity  $v$  and the solvent viscosity  $v_s$ , the polymer viscosity is then calculated by  $v_p = v - v_s$ .

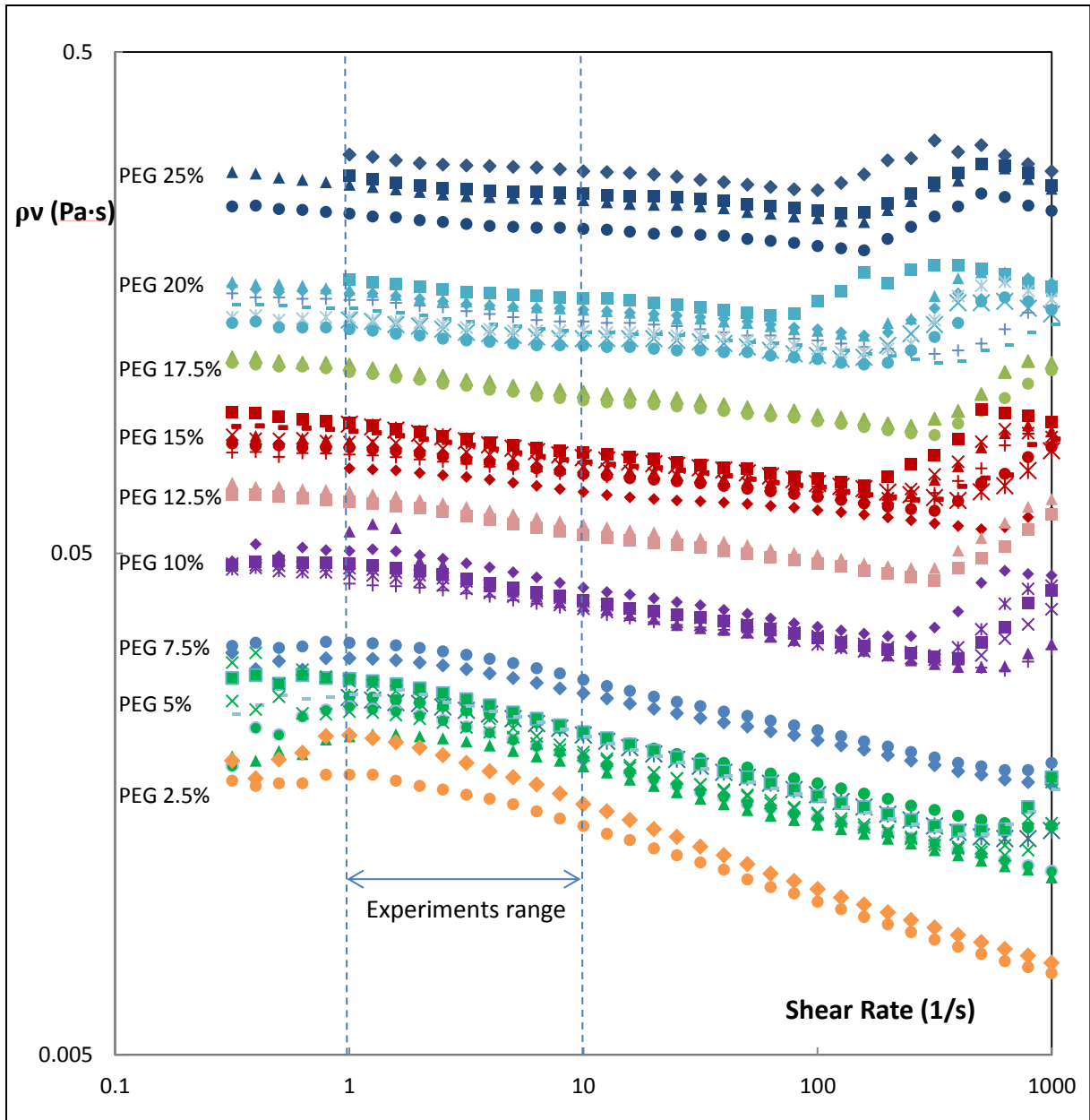


Figure 5.5: Dynamic viscosity of working fluids of different PEG concentrations in respect to shear rate. Each PEG concentration is represented by one color in the diagram. Dashed lines – working range of experiments.

### c. Variation of the viscosity with PEG concentration

To get a clear view of the dependence of the viscosities to the PEG concentration ( $C_{PEG}$ ) we plotted the three viscosities ( $\rho v_s, \rho v, \rho v_p$ ) in respect to the  $C_{PEG}$  in figure 5.6. We found that the  $C_{PEG}$  functions of all the three viscosities follow exponential laws. However the polymer viscosity includes not only the friction between POE molecules and also the friction between POE and PEG molecules. So the polymer viscosity  $\rho v_p$  increases with  $C_{PEG}$ . In figure 5.6 the viscosity error is smaller than the mark.

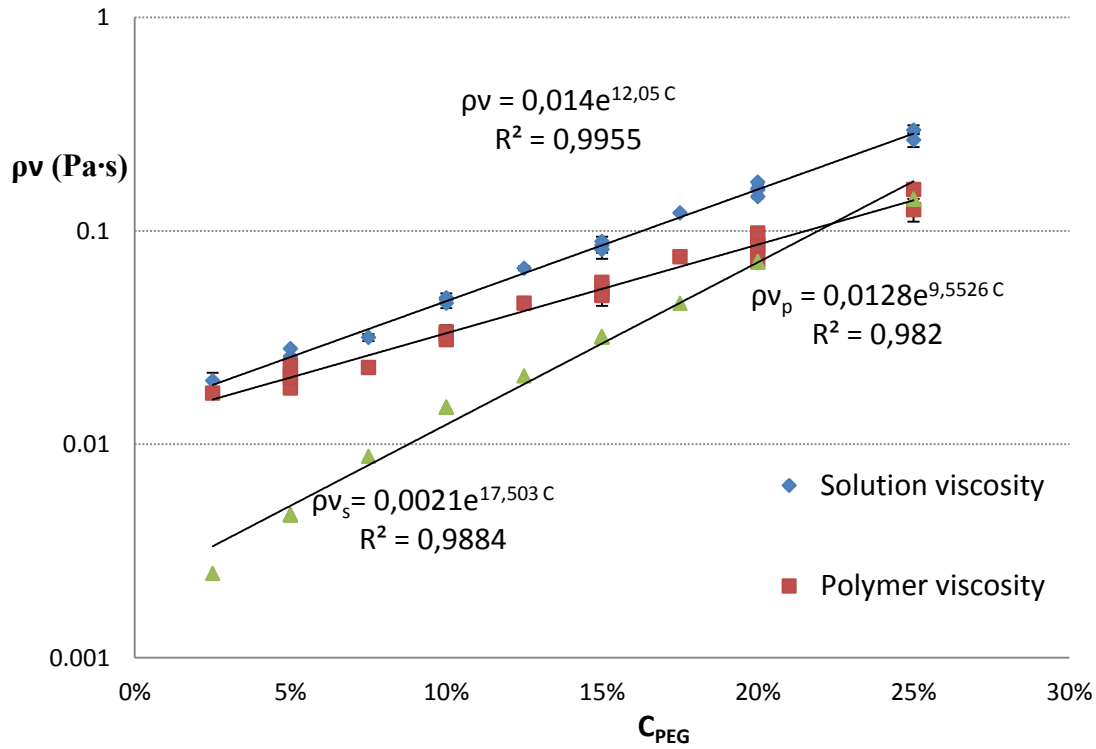


Figure 5.6: Total solution viscosity  $\rho v$ , polymer viscosity  $\rho v_p$  and solvent viscosity  $\rho v_s$  with respect to the PEG concentrations and their fitting curves for  $C_{PEO} = 1000 \text{ ppm}$ .

As presented in figure 5.6 the polymer viscosity  $\rho v_p$  increases slower than the total viscosity  $\rho v$  so the viscosity ratio  $S = v_p/v$  decreases with  $C_{PEG}$ . We present  $S$  with respect to  $C_{PEG}$  in figure 5.7 and we can see that  $S$  decreases linearly with  $C_{PEG}$ .

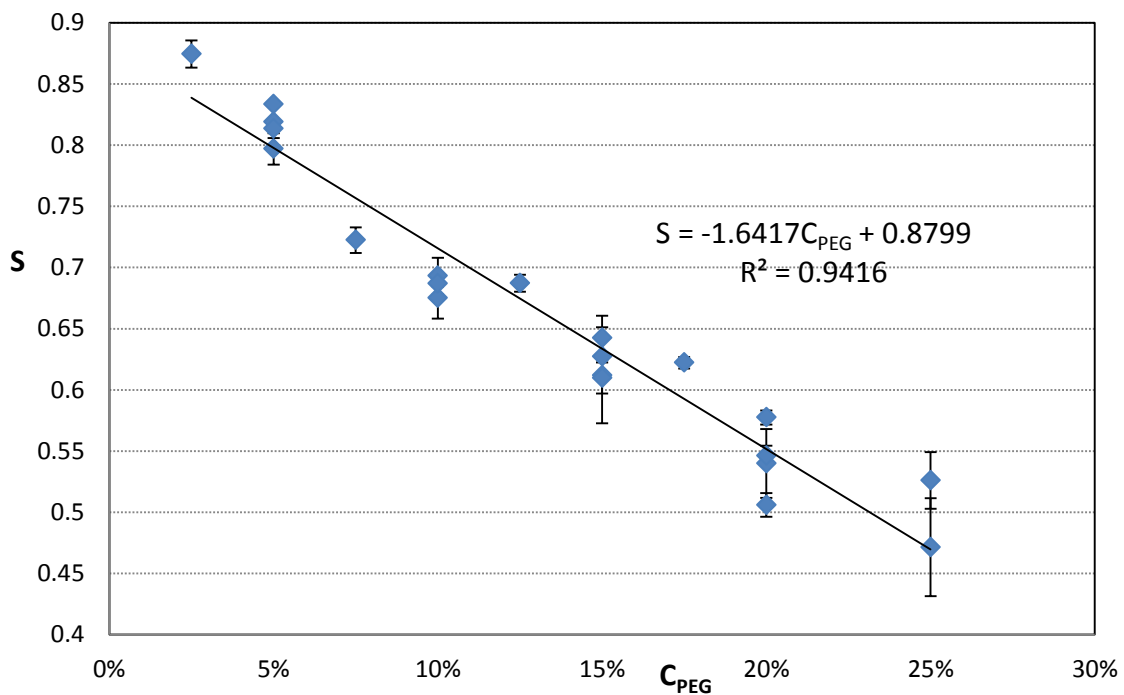


Figure 5.7: Viscosity ratio  $S$  with respect to PEG concentration.

### 5.4. Relaxation time of the solutions

The measurement of the relaxation time of a viscoelastic fluid is an unresolved problem, where different methods provide different results. In this thesis three different methods were applied to estimate the relaxation time, these relaxation times are denoted by  $\tau_e$  for the extensional relaxation time,  $\tau_m$  for the molar mass relaxation time and  $\tau_{N1}$  for the first normal stress difference relaxation time.

#### a. Three relaxation times

The extensional relaxation time is measured by an extensional rheometer (CaBER), presented in figure 5.8, which consists of 2 steel plates and a laser system. To measure the relaxation time, we first fill the gap between the two plates of radius  $r = 3mm$  and the initial gap  $d_i = 3.0mm$  with a sample of working fluid. Then we stretch the upper plate quickly to its final position of the final gap  $d_f \sim 8.7mm$  while the bottom plate is fixing. Hence the fluid between the two plates is stretched and broken into 2 smaller drops. In the meantime, the filament connecting the drops gets thinner and thinner until finally it breaks up. The laser system which lies in the middle of the 2 plates measures the filament diameter  $D$  as a function of time. The temperature of the measuring cell is stabilized by a thermostatic bath to  $20 \pm 0.1^\circ C$ .

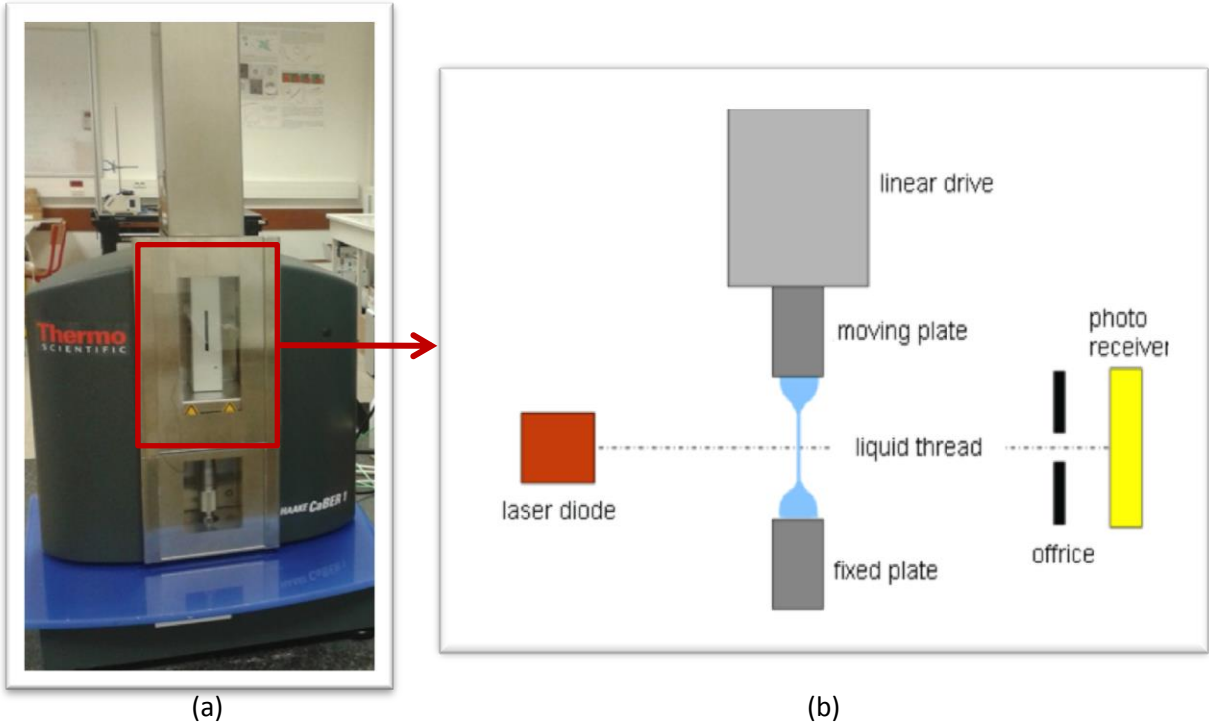


Figure 5.8: The photo of extensional relaxation time and the principle of the measurement.

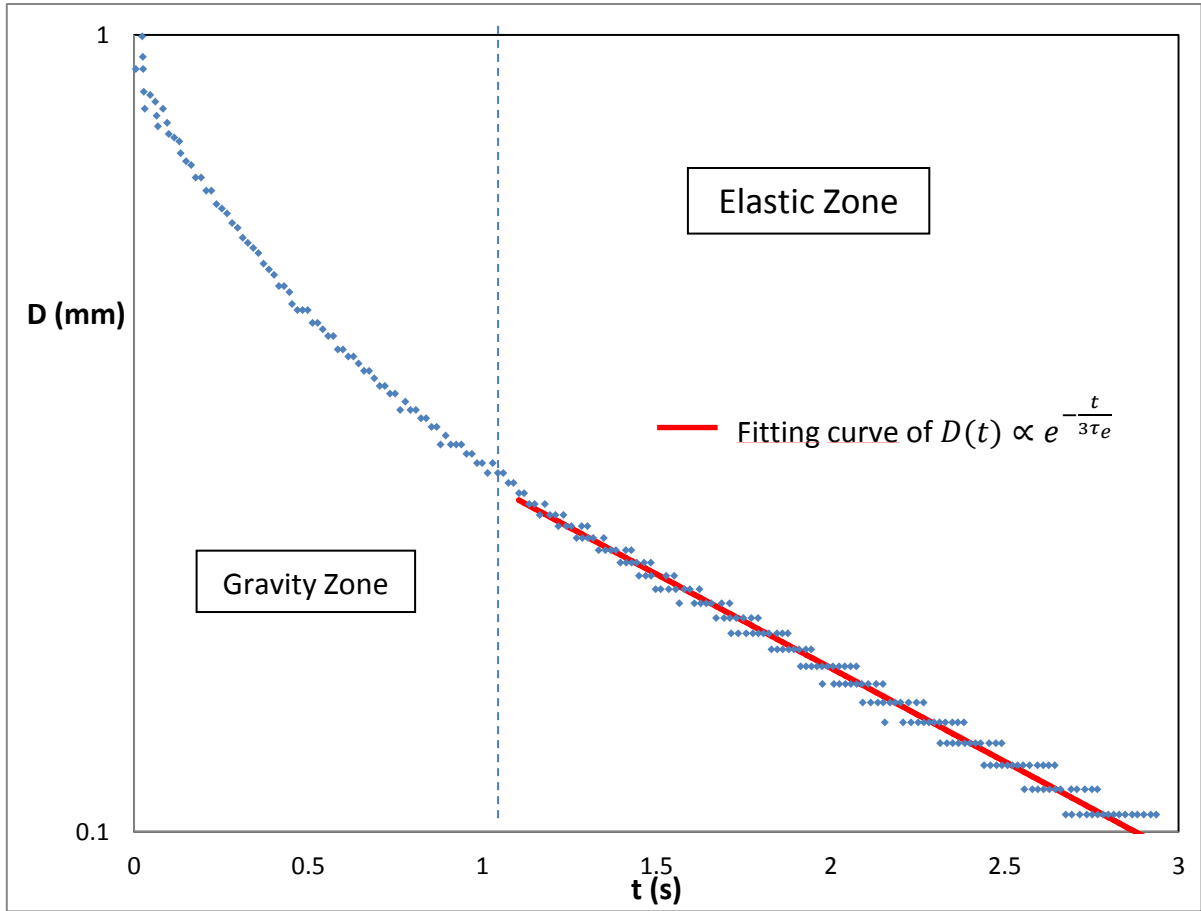


Figure 5.9: Variation of the filament diameter with the time, experimental data for a solution of 10% PEG and 1000 ppm PEO measured by CaBER.

Taking a fluid of 10% PEG and 1000 ppm PEO as an example, the filament diameter data in respect to time is presented in figure 5.9. The data are separated into two processes, where the first process is largely affected by the gravity while in the second process the elastic force of the fluid dominates the evolution of the filament. In the second process, the filament diameter  $D$  is proportional to an exponential function of time:

$$D(t) \propto e^{-t/3\tau_e} \quad 5.1$$

where the extensional relaxation time  $\tau_e$  appears as a parameter (see CaBER manual). So the extensional relaxation time  $\tau_e$  is obtained by fitting the experimental data to the equation 5.1. For each measurement five tests are taken to get  $\tau_e$ .

The molar mass relaxation time  $\tau_m$  is determined by the molecular model of viscoelastic fluids [Bird1977] where the  $\tau_m$  is defined by equation 5.2. In this equation  $C_i$  is the mole number of the PEO in the solution,  $R$  is the perfect gas constant and  $T$  is the temperature.

$$\tau_m \equiv \frac{\rho v_p}{C_i R T} \quad 5.2$$

The first normal stress difference relaxation time  $\tau_{N1}$  is defined by:

$$\tau_{N1} \equiv \frac{N_1}{2v_p \dot{\gamma}^2} \quad 5.3$$

where  $N_1$  is measured by the shear stress rheometer (Anton Par MC300) and then adjusted by the centrifugal force of the cone. Taking a solution of 15%PEG and 1000 ppm PEO as an example, the experimental data of a shear stress in figure 5.10 show that the adjusted  $N_1$  is proportional to  $\dot{\gamma}^2$  at large  $\dot{\gamma}^2$  so that the equation 5.3 is validated.

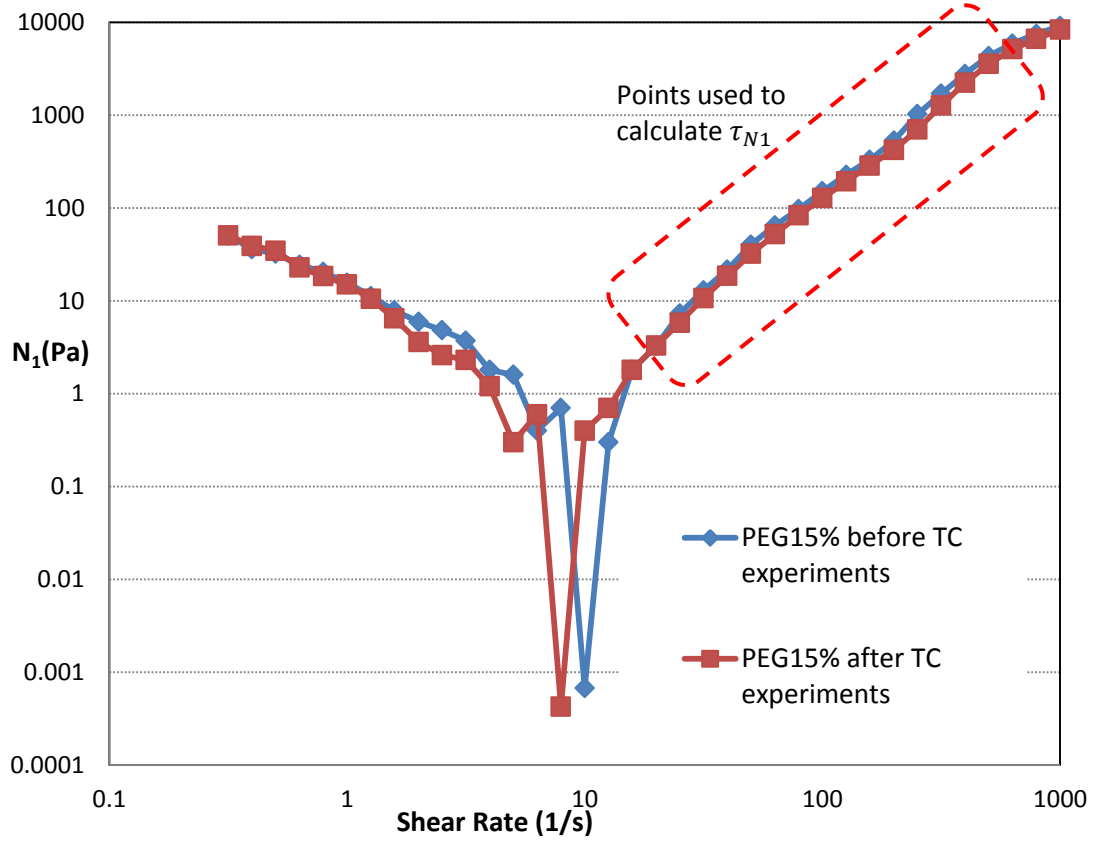


Figure 5.10: Adjusted first normal stress difference  $N_1$  in respect to the shear rate  $\dot{\gamma}$ . The points in the red dashed rectangular are used to estimate  $\tau_{N1}$ .

### b. Variation of the relaxation with the PEG concentration

Because of the degradation of the polymer solutions during Couette-Taylor experiments, the 3 relaxation times are measured or estimated before and after the Couette-Taylor experiments. We plot the three relaxation times of all tested solutions as function of the PEG concentration  $C_{PEG}$  in figure 5.11. In general, the relaxation times increase with  $C_{PEG}$ . The molar mass relaxation time  $\tau_m$  follows an exponential law while the other relaxation times are respectively disordered, as their coefficient of determination ( $R^2$ ) is small.

Except for one solution of 15% PEG, for which  $\tau_{N1} > \tau_m$ , the relaxation times of all solutions follow the inequality

$$\tau_e > \tau_m > \tau_{N1} \quad 5.4$$

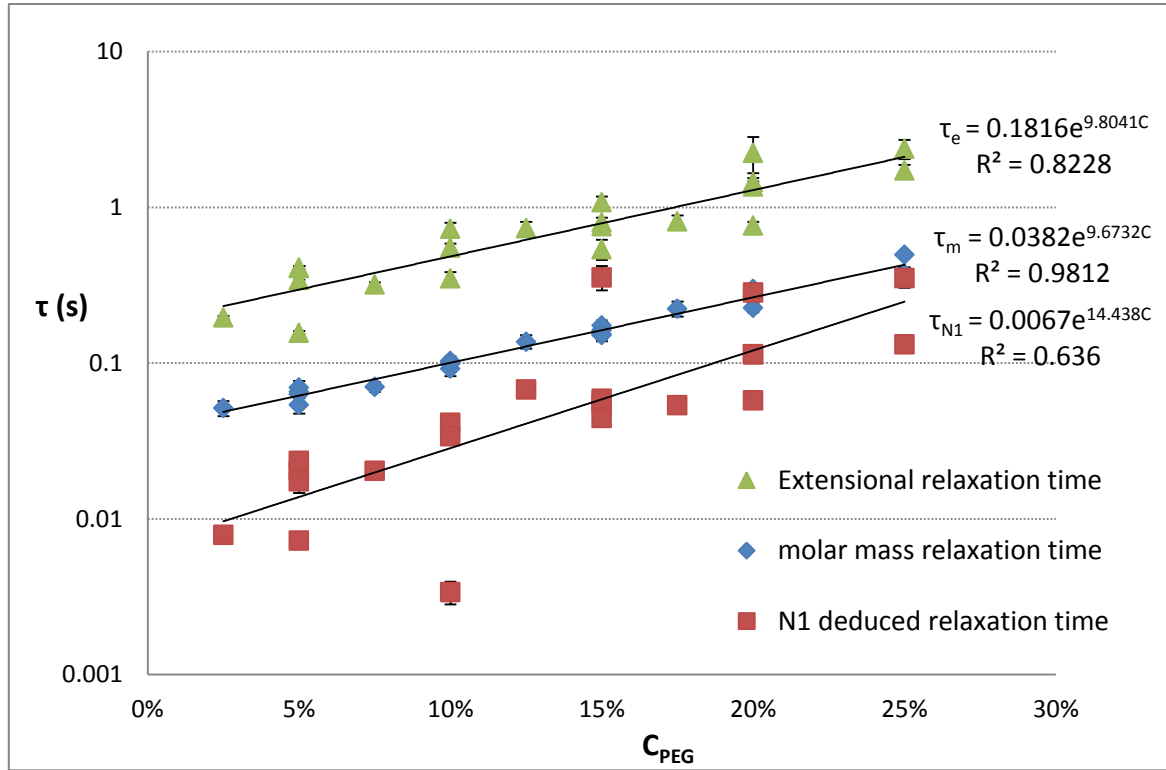


Figure 5.11: Variation of the relaxation times  $\tau$  with PEG concentration.

With these relaxation times, we defined three elasticities by  $E_e = \tau_e/\tau_v$ ,  $E_m = \tau_m/\tau_v$  and  $E_{N1} = \tau_{N1}/\tau_v$ , where  $\tau_v = d^2/\nu$  is the viscous diffusion time. We plotted in figure 5.12 the elasticities with respect to  $C_{PEG}$ . With no surprise, like the relaxation times, the elasticities increase with  $C_{PEG}$  and we have  $E_e > E_m > E_{N1}$  except for one solution of 15% PEG. However the  $E_e$  and  $E_{N1}$  are less disordered comparing to the  $\tau_e$  and  $\tau_{N1}$  and they correspond better to an exponential law.

At last we plotted in figure 5.13 the elasticities  $E$  in respect to the viscosity ratio  $S$  as they are the most important dimensionless parameters to characterize a viscoelastic fluid. Generally speaking,  $E$  decreases with  $S$ .

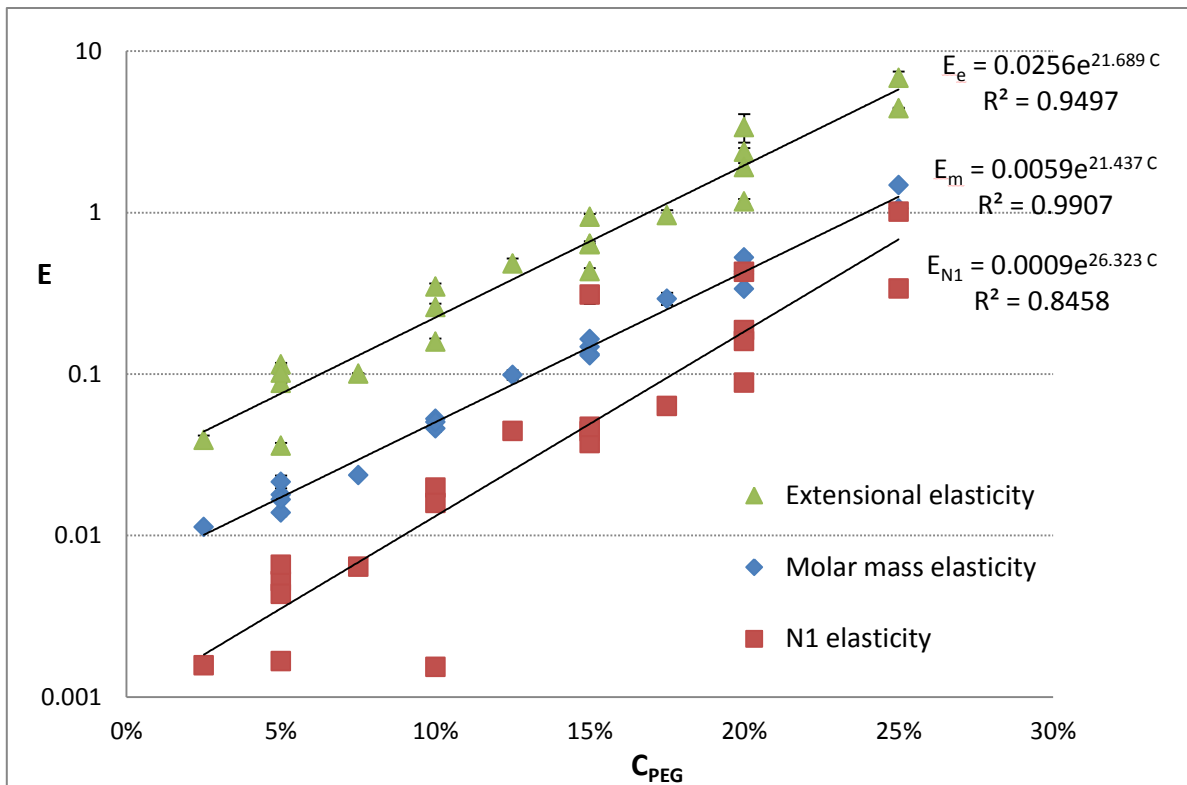


Figure 5.12: Variation of the Elasticities  $E$  with the PEG concentration.

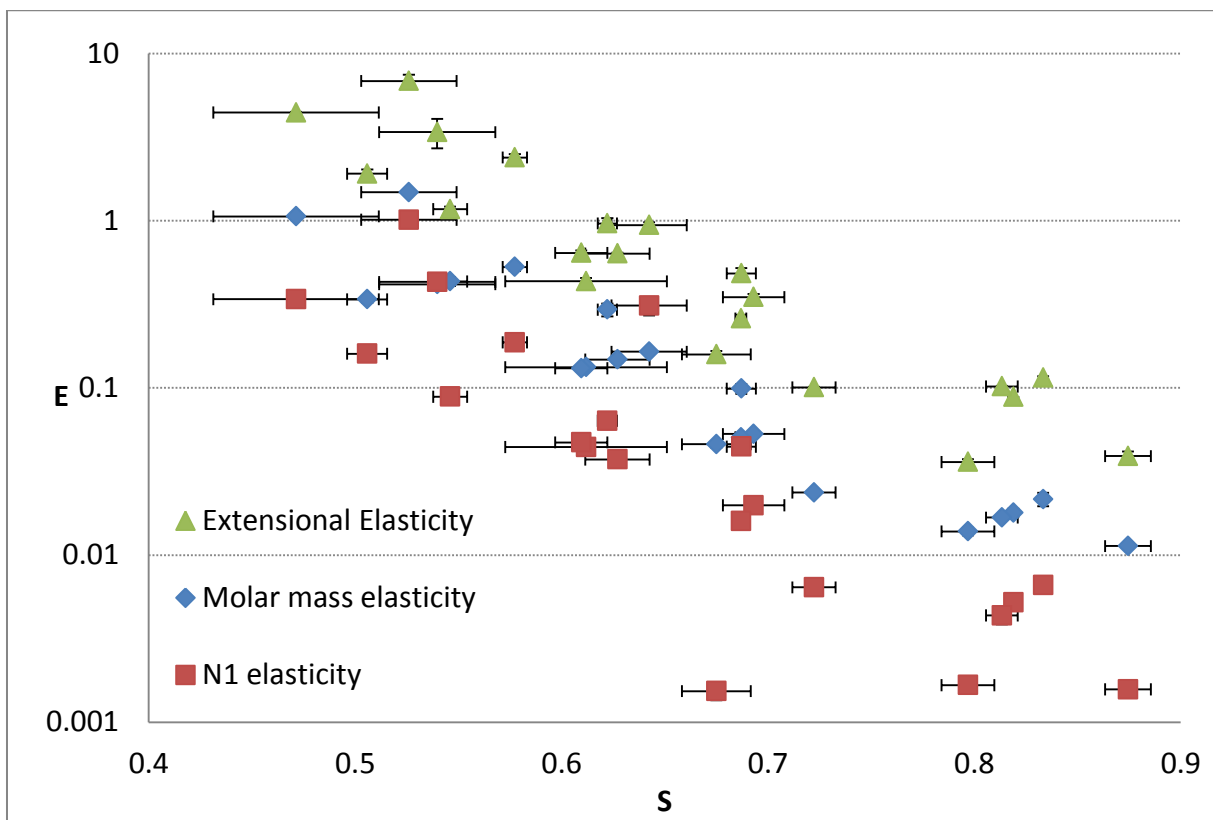


Figure 5.13: Variation of the Elasticities  $E$  with the viscosity ratio  $S$ .

## 5.5. Conclusion

In this chapter we have presented the experimental setup, the basic experimental procedures and the working fluids which consist of POE, PEG water and isopropyl alcohol and their preparation protocols. The solvent viscosity  $\rho\nu_s$  and the total solution viscosity  $\rho\nu$  were measured by a shear rheometer (Anton Paar MC300). The viscosity of our working fluids show weak shear thinning effect, so that they are considered as fluids which fit approximately the Oldroyd-B model.

As we have fixed the POE concentration to 1000ppm and varied the PEG concentration  $C_{PEG}$ , for all solutions the viscosities  $\rho\nu, \rho\nu_s, \rho\nu_p$  increase with  $C_{PEG}$  while the viscosity ratio  $S$  decreases with  $C_{PEG}$ . The relaxation time of the working fluids is estimated with three different ways. Denoted by  $\tau_e, \tau_m, \tau_{N1}$  these relaxation times could differ from each other by more than 20 times for the same fluid. For most solutions the relaxation times  $\tau_e, \tau_m, \tau_{N1}$  and the elasticities  $E_e, E_m, E_{N1}$  increase with  $C_{PEG}$ .



# Chapter 6: Viscoelastic instability in the annulus with one rotating cylinder

---

In the present chapter, we will present the theoretical and experimental results obtained in the case when either the inner cylinder or the outer is rotating the other being fixed ( $\mu = 0$  and  $\mu = \infty$ ).

## 6.1. Annular flow for $\mu = 0$

The stability of viscoelastic flow in the Couette flow when only the inner cylinder is rotating has been widely investigated by many authors. The present study has revisited the analysis of this flow and it sheds new light on the aspects that were ignored so far in the experimental and theoretical studies. A particular attention is drawn on the role of the polymer elasticity parameter  $ES$ .

### 6.1.1. LSA results

The stability analysis of the circular Couette flow with  $\mu = 0$  described in the chapter 3 is performed using the LSA codes described in section 4.2.

#### a. Marginal stability curves

The growth rate of the eigenvalue problem in the Keplerian regime for  $\eta = 0.8$  is a function of parameters as  $\sigma = f(Ta, E, S, q, m)$ . The marginal stability is given by the largest growth rate that leads to instability i.e.  $\sigma = 0$  or  $f(Ta, E, S, q, m) = 0$ . For a fixed value of  $E$  and  $S$ , the hypersurface reduces to a marginal surface  $f(Ta, q, m) = 0$ . In practice, we fix  $m$  and look for the marginal curve of  $Ta(q)$  for different  $m$ , the value of  $\omega$  is determined simultaneously. We plot in figure 6.1 the marginal stability curves  $Ta(q)$  for different values of the azimuthal wavenumber  $m$  and for  $E = 0.01, 0.1, 1$ . The shape of these curves is very sensitive to the elasticity number  $E$ . For small  $E$  (Figure 6.1 (a, b)), the marginal curve of  $m = 0$  has a clear minimum which determines the critical point  $(q_c, Ta_c)$  of the critical mode. For  $E = 0.01$ , the critical mode is axisymmetric and stationary while for  $E = 0.1$ , critical mode is non-axisymmetric and oscillatory. But for larger  $E$  (Figure 6.1 ©) the bottom of the marginal curve of  $m = 1$  is so flat that it is difficult to define the critical mode. In this case, several perturbation modes of different  $q$  may interact with each other. So, for large values of the elasticity number, within linear stability analysis, the critical mode is a linear superposition of non-axisymmetric modes in the neighborhood of the apparent “ $q_c$ ”.

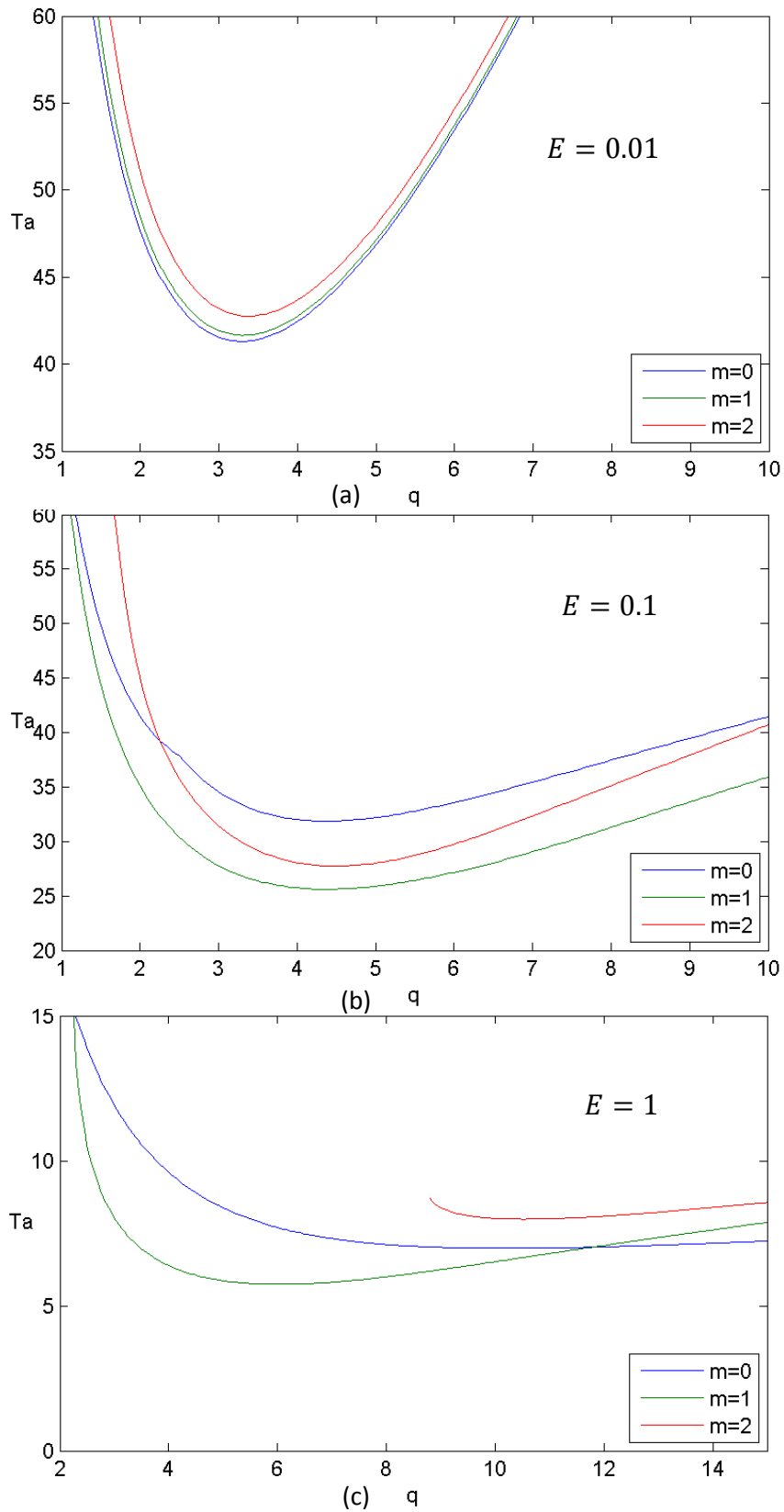


Figure 6.1: Marginal curves  $Ta(q)$  for different  $m$  at chosen  $E$  for  $S = 0.6$ . (a)  $E = 0.01, Ta_c = 41.31, q_c = 3.3, m_c = 0, \omega_c = 0$  (b)  $E = 0.1, Ta_c = 25.62, q_c = 4.35, m_c = 1, \omega_c = -0.034 < 0$  (c)  $E = 1, Ta_c = 5.74, q_c = 5.95, m_c = 1, \omega_c = 0.014 > 0$ .

### b. Variation of the critical parameters with $E$

The critical values  $(Ta_c, q_c, m_c, \omega_c)$  depend on the solution parameters  $E, S$ . We have fixed the viscosity ratio  $S$  and have computed the critical parameters  $Ta_c$  and  $q_c$  for a chosen value of the azimuthal wavenumber  $m$ . In Figure 6.2, the curve of the  $Ta_c(E)$  is plotted for different  $m$  for  $S = 0.6$ . We observe that for  $m = 0, 1, 2$  the  $Ta_c$  decreases slowly with increasing  $E$  for  $E \leq 0.1$ , and then rises suddenly forming a sharp peak, and again it decreases. The sharp peak corresponds to a change of mode, where 2 critical modes of different  $\omega_c$  and  $q_c$  compete with each other. Taking the mode  $m = 0$  as an example, the critical mode is stationary ( $\omega_c = 0$ ) before the peak ( $E < 0.08$ ), and it is oscillatory ( $\omega_c \neq 0$ ) after the peak ( $E > 0.08$ ). The mode  $m = 1$  does not show any peaks when  $Ta_c$  decreases with  $E$ .

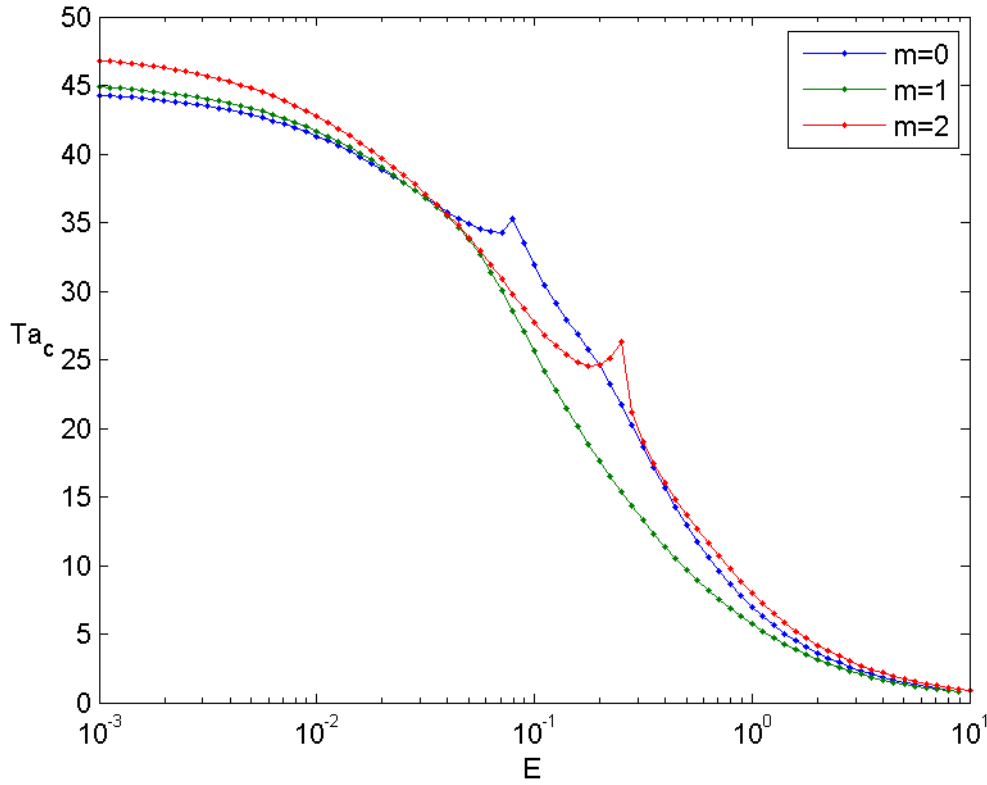


Figure 6.2: Variation of the critical values of  $Ta_c$  with  $E$  for different  $m$  at fixed  $S = 0.6$ .

Comparing these modes, we can see that the most unstable mode is  $m = 0$  at  $E < 0.03$  and  $m = 1$  at large  $E > 0.03$ . However the mode  $m = 1$  can also be separated into 2 parts by the sign of critical frequency,  $\omega_c < 0$  at  $0.03 < E < 0.38$  and  $\omega_c > 0$  at  $E > 0.38$ . In Figures 6.3, the variation of the critical parameters with the elasticity number are plotted for  $S = 0.6$ . For small values of  $E < 0.03$ , critical modes are stationary and axisymmetric, they are Taylor vortices (TVF) as in the case of Newtonian liquid. For  $E > 0.03$  the critical modes are oscillatory non axisymmetric modes with  $\omega_c < 0$  or  $\omega_c > 0$ . The axial wavenumber of the Taylor Vortex Flow is almost constant while that of oscillatory non-axisymmetric modes increases with  $E$  up to 2.6 times  $q_c(E = 0)$  corresponding to vortices of size  $d/2.6$ , i.e. almost three vortices in the gap. The frequency  $|\omega_c|$  of the non-axisymmetric modes decreases with  $E$  for  $E \in [0.03, 0.38]$  and then weakly increases with  $E$  up to  $\omega_c = 0.02$  for  $E = 1$ .

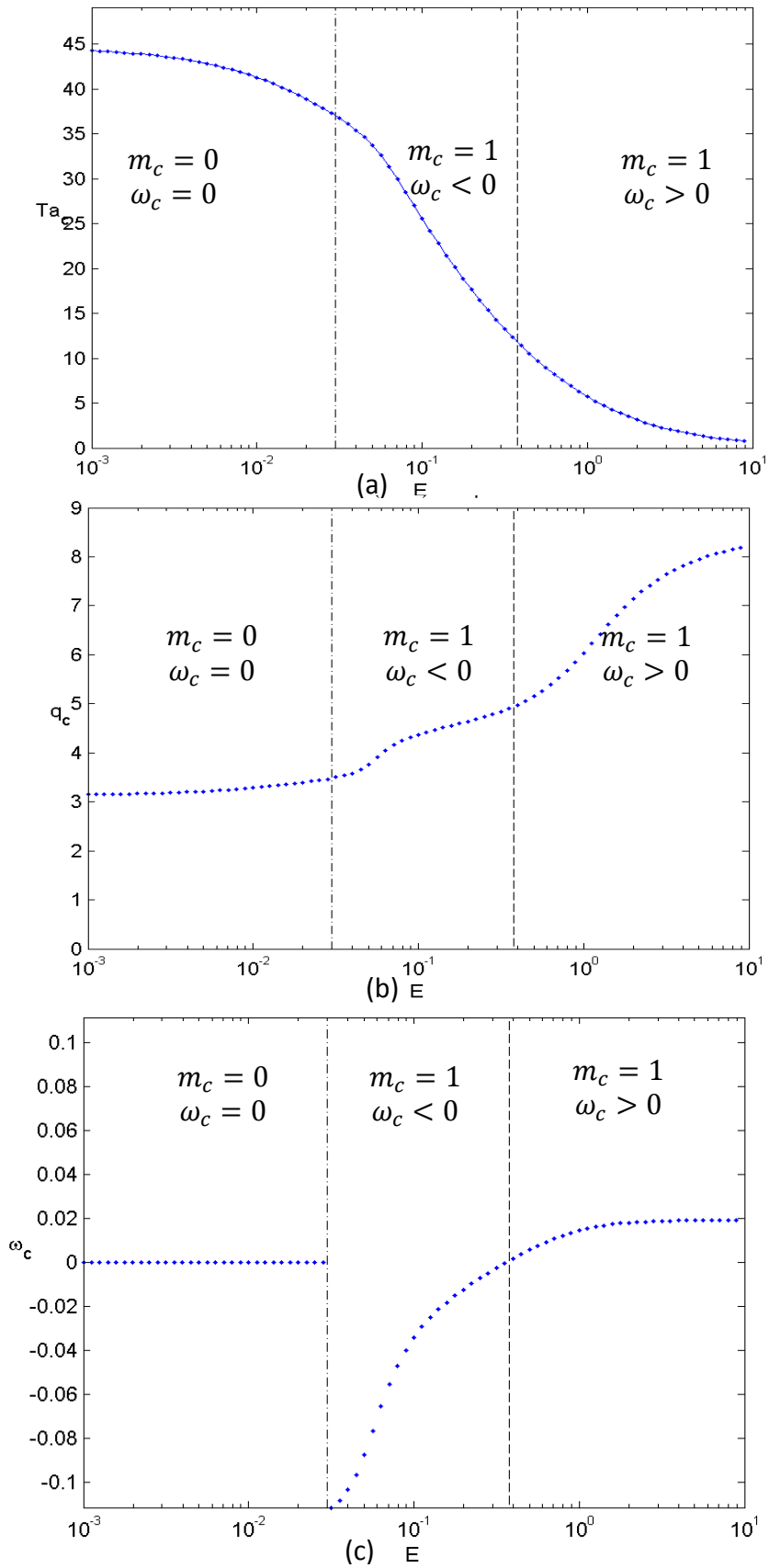


Figure 6.3: Variation of the critical parameters with the elasticity number  $E$  for  $S = 0.6$  in  $\mu = 0$  regime: a)  $a_c(E)$ ; b)  $q_c(E)$ ; c)  $\omega_c(E)$ . Loose dashed vertical line separates critical azimuthal wave numbers  $m_c$ . Dense vertical line separates the positive and negative angular frequency.

For each polymer solution (i.e. for a given value of  $S$ ), there exist a point in the plane  $(E, Ta_c)$  where two modes with different spatio-temporal properties can coexist. This point is called *codimension-two point*. For  $S = 0.6$ , the properties of this codimension-two point is given in the Table :

$E$	$Ta_c$	$q_c$	$m_c$	$\omega_c$
0.03	37	3.47	0	0
		3.51	1	-0.11

Table 6.1: Codimension-two point for  $S = 0.6$  in  $\mu = 0$  regime.

The color maps in figure 6.4 show flow patterns of different critical modes, from which we observe that for  $m = 1$  the flow pattern inclines to the inner cylinder when  $\omega_c < 0$  while it inclines to the outer cylinder when  $\omega_c > 0$ . To provide more details about the non-axisymmetric critical mode, we present in figures 6.5 – 6.7 the velocity field, the azimuthal vorticity and the variations of pressure and normal stress differences ( $N_1$  and  $N_2$ ) in the gap for the cases of  $E = 0.01$ ,  $E = 0.1$ , and  $E = 1$ . The inner cylinder is on the left and the outer cylinder is on the right. The ratio  $N_2/N_1$  decreases with  $E$  from 100 (for  $E = 0.01$ ) to 1 (for  $E = 1$ ), suggesting that the perturbations of the first normal stress difference dominate the second normal stress difference in the purely elastic regime where  $E \rightarrow \infty$ .

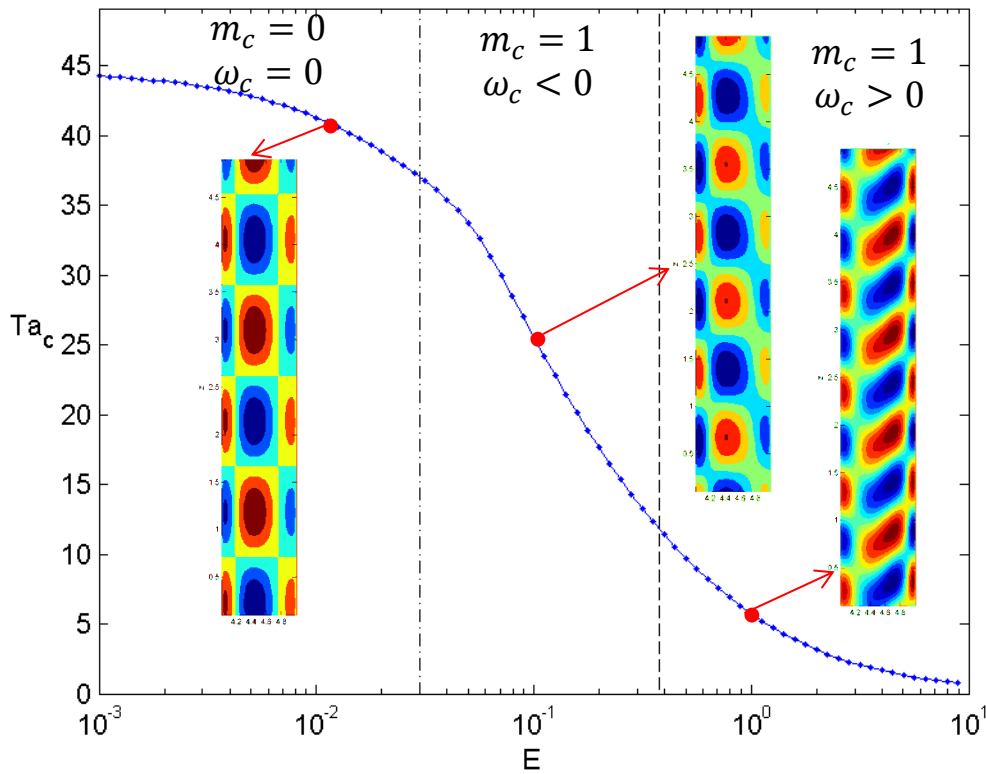


Figure 6.4: Color: Vorticity  $\omega_\theta$  of the critical modes in the gap for different values of the elasticity number  $E$  and for  $S = 0.6$  in  $\mu = 0$  regime. Solid line: critical curve  $Ta_c(E)$ .

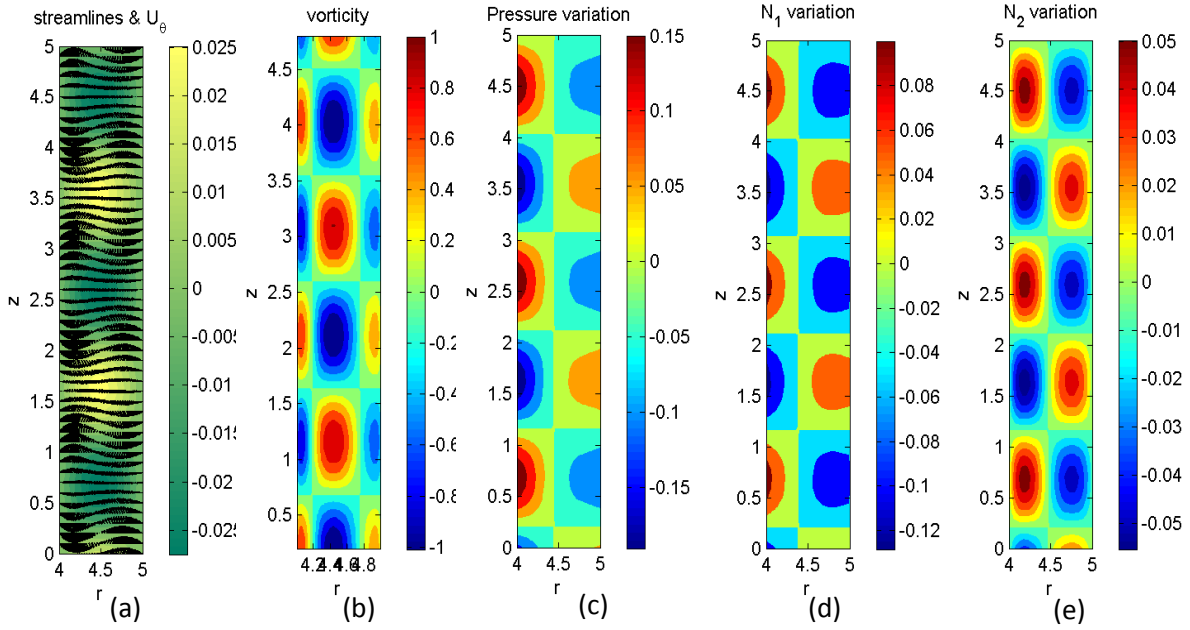


Figure 6.5: Critical mode for  $S = 0.6, E = 0.01, Ta_c = 41.3$  on  $\mu = 0$ , with  $m = 0, q_c = 3.28, \omega_c = 0$ . (a) Black arrows represent the velocity field in  $(r, z)$  direction while the colors represent the azimuthal velocity  $V$  (b) the vorticity  $\omega_\theta$  (c) the pressure variation (d) the  $N_1$  variation © the  $N_2$  variation. Color maps of (b, c, d, e) represent the relative amplitude.

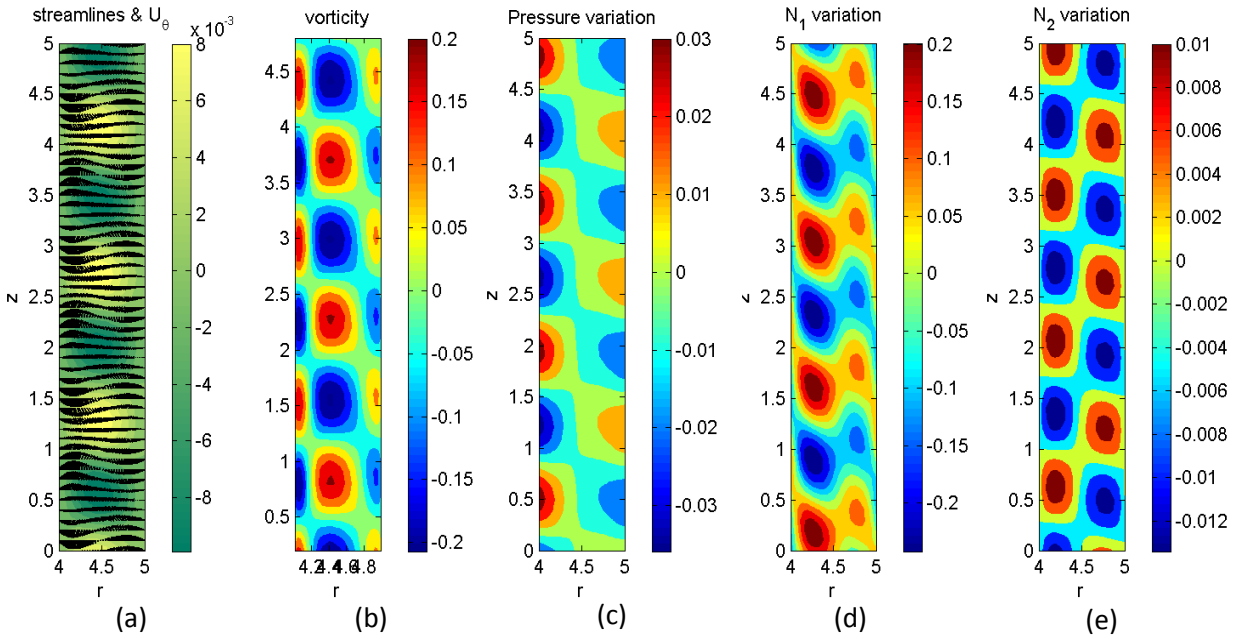


Figure 6.6: Critical mode for  $S = 0.6, E = 0.1, Ta_c = 27.2$  in  $\mu = 0$  regime, with  $m = 1, q_c = 4.37, \omega_c = -0.034$ . (a) Black arrows represent the velocity field in  $(r, z)$  direction while the colors represent the azimuthal velocity  $V$  (b) the vorticity  $\omega_\theta$  (c) the pressure variation (d) the  $N_1$  variation © the  $N_2$  variation. Color maps of (b, c, d, e) represent the relative amplitude.

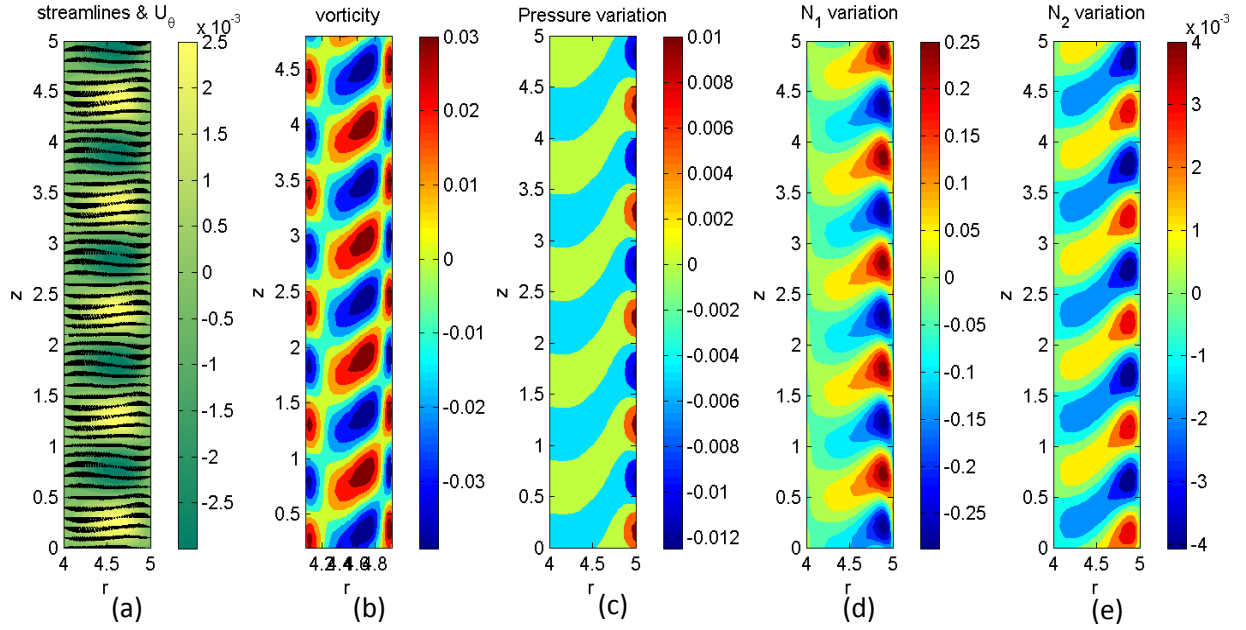


Figure 6.7: Critical mode for  $S = 0.6$ :  $E = 1$ ,  $Ta_c = 5.74$  in  $\mu = 0$  regime, with  $m = 1$ ,  $q_c = 6.03$ ,  $\omega_c = 0.014$ . (a) Black arrows represent the velocity field in  $(r, z)$  direction while the colors represent the azimuthal velocity  $V$  (b) the vorticity  $\omega_\theta$  (c) the pressure variation (d) the  $N_1$  variation © the  $N_2$  variation. Color maps of (b, c, d, e) represent the relative amplitude.

### c. Effect of the viscosity ratio on the critical states

The second step was to determine the role of the viscosity ratio  $S$  in the viscoelastic instability. We have computed the critical curves for different values of  $S$  from 0.05 to 0.9 and super-imposed the critical curves corresponding to different  $S$  in one figure. We plot in figure 6.8 the critical curves  $Ta_c(E)$  for different  $S$ . At small  $E$  all curves approach the same critical Taylor number of  $Ta_c = 44.7$  which is the critical Taylor number at the Newtonian limit of  $E = 0$ . At larger  $E$ ,  $Ta_c$  decreases rapidly with  $E$  but for large  $E$ , the decrease of  $Ta_c$  slows down when  $Ta_c < 1$  corresponding to the onset of the purely elastic instability. Theoretically the critical curves cross the horizontal axis only on the purely elastic limitation of  $E = \infty$ . The curves with  $S = \{0.6, 0.7, 0.8, 0.9\}$  intersect each other in a small area around the point  $(E^* = 0.3, Ta_c^* = 13.5)$  such that the polymer viscosity is stabilizing on the left of the intersection and destabilizing on the right. The solutions with very small  $S < 0.1$  have critical curves which do not intersect each other at least for  $E < 10$ .

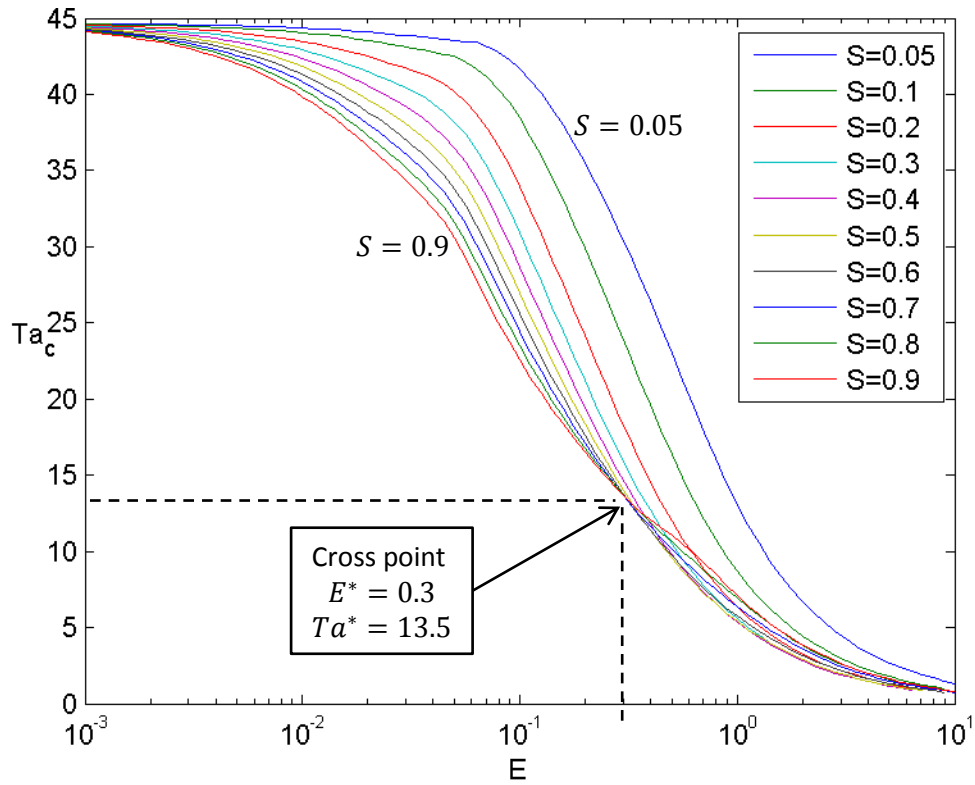


Figure 6.8: Critical curves  $Ta_c(E)$  for different  $S$  in  $\mu = 0$  regime.

Beside the solution elasticity  $E$ , it is possible to introduce the parameter  $\{E\} = ES$  which represents the polymer elasticity. In figure 6.9 we present the critical Taylor number  $Ta_c$  in respect to  $ES$ . For small values of  $ES$  ( $< 2 \cdot 10^{-3}$ ), all curves tend to form a unique limiting curve insensitive to  $S$  with  $S$  destabilizing the flow. The effect of the elasticity on the threshold becomes sensitive as soon as  $ES > 10^{-3}$ . For large values of  $ES$ , the curves are distinct and  $Ta_c$  increases with it, which means that the polymer viscosity has a stabilizing effect on the flow.

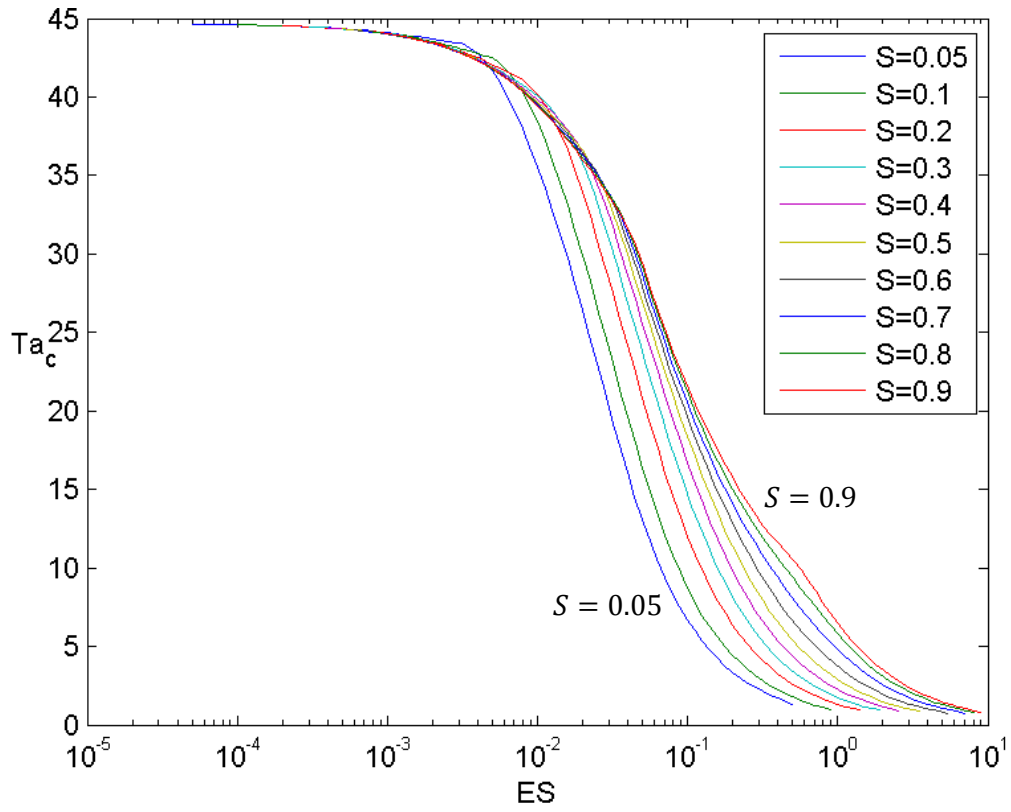


Figure 6.9: Critical curves  $Ta_c(ES)$  for different  $S$  in  $\mu = 0$  regime.

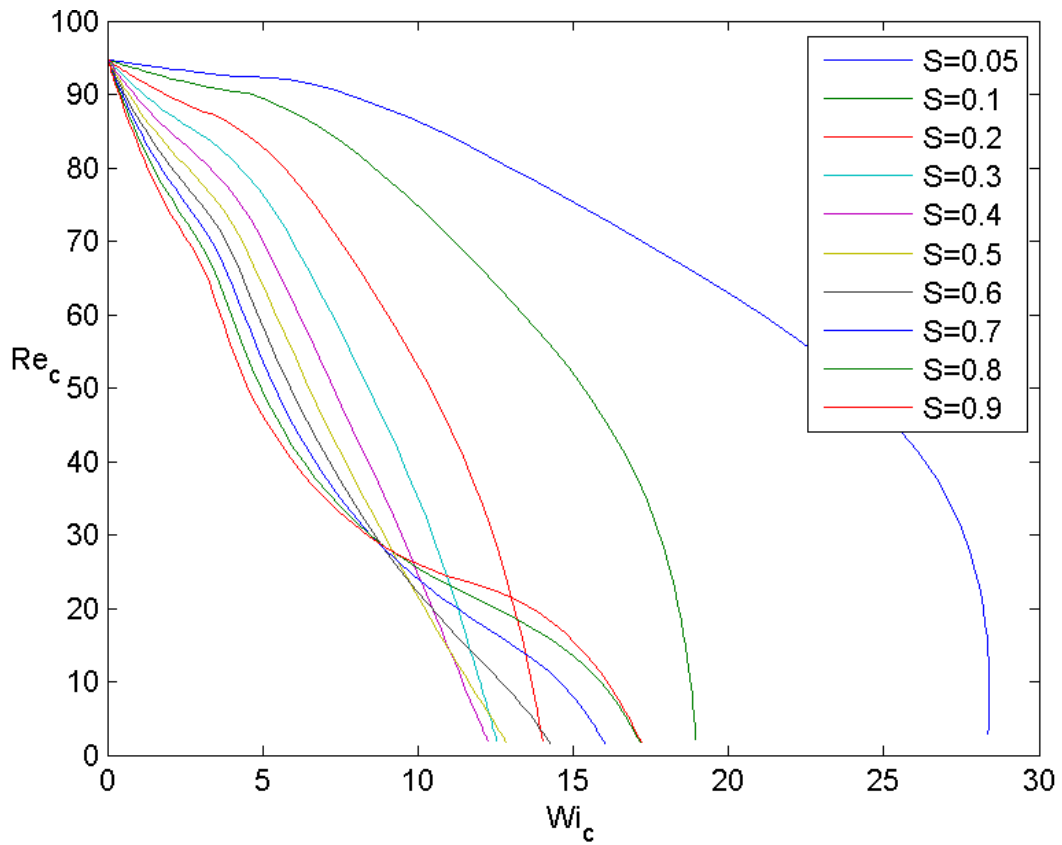


Figure 6.10: Critical curves  $Re_c(Wi_c)$  at critical wave numbers for different  $S$  in  $\mu = 0$  regime.

As  $Re$  and  $Wi$  are the most studied control parameter of the viscoelastic instability, we have plotted in figure 6.10 the critical curves of  $Re_c(Wi_c)$  for different  $S$ . We can see that all curves cross the vertical axis of  $Wi = 0$  at the same point of  $Re_c = 94.7$  corresponding to the Newtonian case; then  $Re_c$  decreases with  $Wi_c$ . Although the values of  $Wi$  are not presented for small  $Re$ , we know that the critical curves of  $Re_c(Wi_c)$  cross the horizontal axis of  $Re = 0$  at certain  $Wi_0$  that corresponds to the onset of the purely elastic instability. The case of the purely elastic instability will be discussed in chapter 9.

Another control parameter related to the  $Wi$  is the modified Weissenberg number  $K_c = \sqrt{2Sd/(a+b)} Wi_c$ , defined by Groisman & Steinberg [groisman1998] which includes the viscosity ratio and the curvature. Figure 6.11 presents the critical curves of  $Ta_c(K_c)$ , we can see that except for the curves of the two very low values of  $S$  ( $S = 0.05, S = 0.1$ ), all critical curves cross each other around  $K_c^* = 2.4 \pm 0.1, Ta_c^* = 21 \pm 1$ . The line  $K_c = K_c^*$  separates the plane  $(K_c, Ta_c)$  into two zones where the polymer viscosity plays opposite roles: for  $K_c < K_c^*$ , the polymer viscosity destabilizes the flow but for  $K_c > K_c^*$ , it stabilizes the flow.

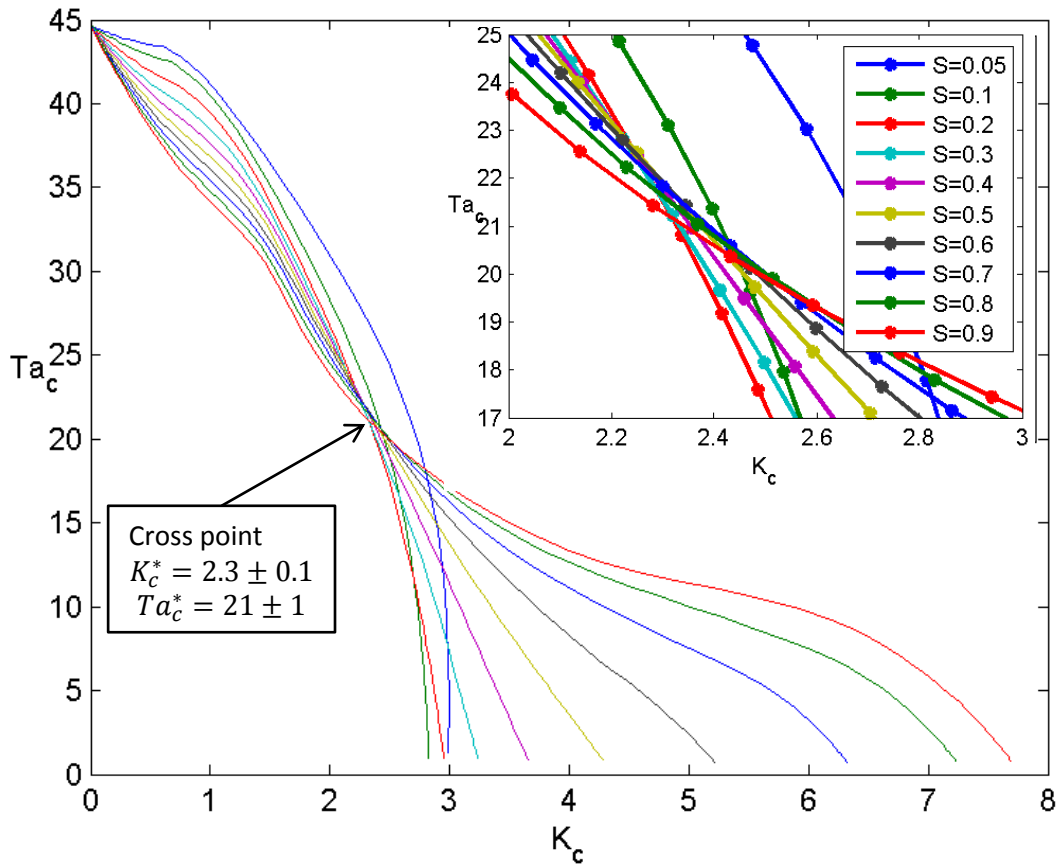


Figure 6.11: Critical curves  $Ta_c(K_c)$  for different values of  $S$  in  $\mu = 0$  regime. The insert figure on the right top corner is a zoom in around the “intersection point”.

The variations of the frequency and axial wavenumber of the critical modes for different  $S$  with ES are plotted in figure 6.12 and 6.13 respectively. In figure 6.12 we can see that the sign change of  $\omega_c$  in the mode  $m = 1$  exists only for large  $S$ . For small viscosity ratio  $S \in \{0.05, 0.1, 0.2, 0.3\}$  the angular frequency  $\omega$  is always negative in the calculated range of elasticity  $E \in \{10^{-3}, 10^1\}$ . The critical frequency curves in the plane  $(ES, \omega_c)$  intersect each other at one common point ( $ES^* \sim$

0.055,  $\omega_c^* \sim -0.04$ ). The effect of the polymer elasticity on the critical wavenumber becomes significant for  $ES > 2 \cdot 10^{-3}$  when  $q_c$  starts to increase with  $ES$  (figure 6.13). The critical curves for large  $S \in \{0.5, 0.9\}$ , which possess positive frequencies  $\omega_c > 0$  with  $m = 1$ , show a sudden increase at large  $ES$ , while the critical curves with small  $S \in \{0.05, 0.3\}$  tend asymptotically to constant values at large  $ES$ .

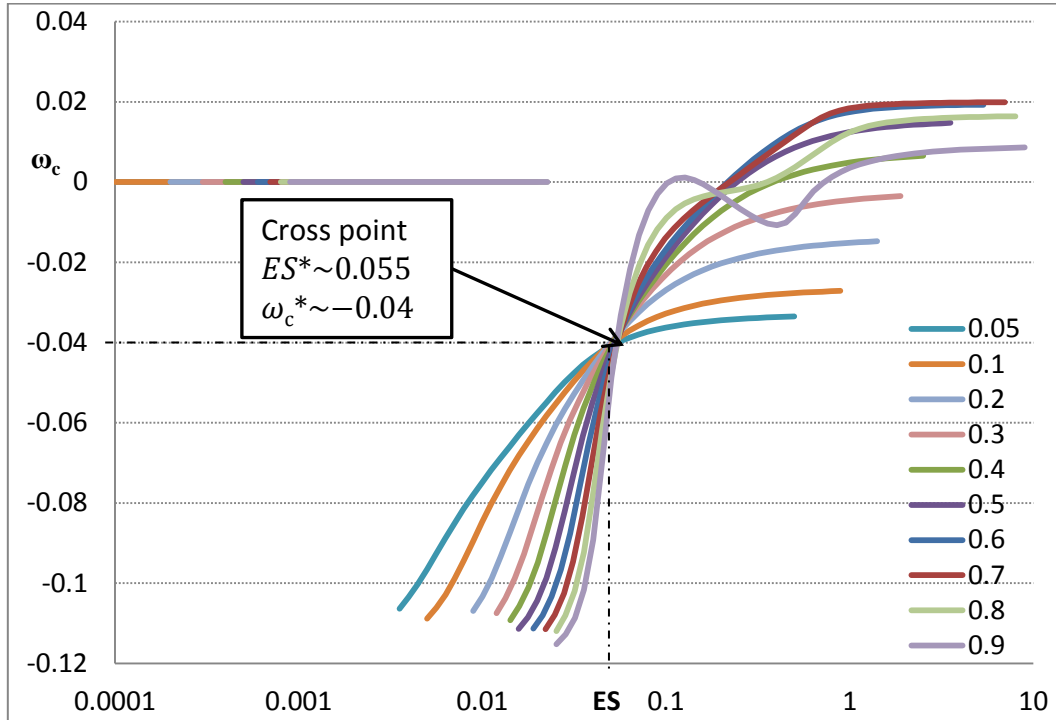


Figure 6.12: Variation of the critical angular frequency  $\omega_c$  with  $ES$  for different  $S$  in  $\mu = 0$  regime.

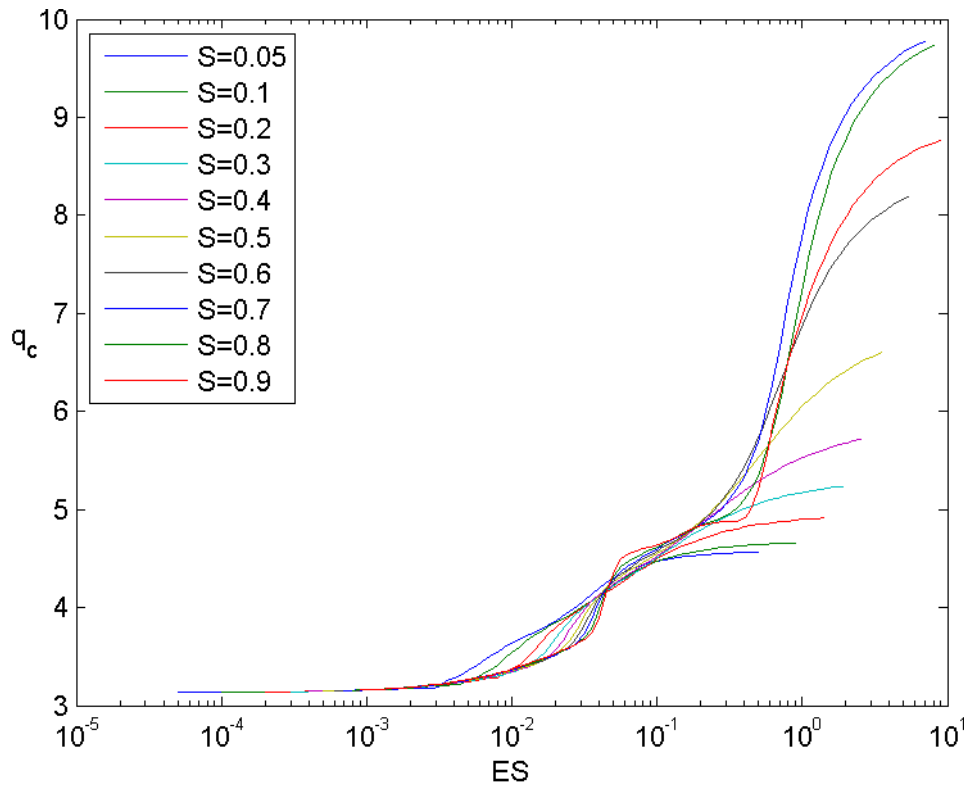


Figure 6.13: Variation of the critical wave number  $q_c$  with  $E$  for different  $S$  in  $\mu = 0$  regime.

### 6.1.2. Experimental results

We have followed the experimental procedures described in chapter 5. The inner cylinder was rotating and the outer cylinder was fixed. The experimental results are presented and compared with some of the LSA predictions.

To present the experimental results, both dimensional and dimensionless frequencies ( $f$  and  $\omega$ ) and wavenumbers ( $k$  and  $q$ ) are used. The elasticity defined by the molar mass relaxation time  $E_m$  (see section 5.4) is used to introduce the flow patterns as it is the most widely used elasticity in the literature.

#### a. Flow patterns

In figure 6.14, 6.15, 6.17 we present one by one the gap view, the front view and the space-time diagram of the three critical modes: stationary axisymmetric vortices or Taylor vortices for small elasticity  $E$ , standing waves also called ribbons for intermediate values of  $E$  and disordered vortices for large values of  $E$ . In the figures are shown only the central parts of the flow patterns away from the endplates. The vertical shadows in the front view are nothing but a reflection of a support pillar of the setup, and this reflection shadow will appear at all the following front view photos. The gap view is captured by the reflection of a laser sheet which sweeps the  $(r, z)$  plane. The space-time diagram is created by superposition of recorded vertical lines at regular time intervals.

The Taylor vortex mode have the same structure as in the Newtonian case (figure 6.14) with  $m_c = 0$   $\omega_c = 0$ . This agrees with the LSA which predicted axisymmetric and stationary mode for small values of  $ES$  (see figure 6.2).

The Ribbons mode is composed of counter propagating waves (figure 6.15), they are non-axisymmetric and oscillatory ( $m_c \neq 0, \omega_c \neq 0$ ). The Ribbons mode is composed of counter propagating waves which can be obtained by complex demodulation. Figure 6.16 represents the resulting left and right propagating waves from demodulation of the Ribbons mode. The LSA has predicted critical mode of ( $m_c = 1, \omega_c < 0$ ) for intermediate  $ES$ . However as it is difficult to determine the azimuthal wave number  $m_c$  and the sign of  $\omega_c$  experimentally, we may say the non-axisymmetric and oscillatory mode agrees with the LSA prediction for intermediate  $ES$ .

Like the Ribbons mode, the disordered vortices mode is composed of non-regular and non-stationary waves (figure 6.17) ( $m_c \neq 0, \omega_c \neq 0$ ). The horizontal fine black lines in front view of the cylinder (figure 6.17 b) are the central of counter rotating pairs of vortices These central lines of the counter rotating vortices are inclined which means that this mode is not axisymmetric. The space-time diagram (figure 6.17 c) exhibits the chaotic behavior of the pattern.

We compare the long-time acquisition of space-time diagrams of these modes in figure 6.17 to provide a general impression of these three modes. The central lines of the counter rotating vortices pairs tend to approach each other and merge into new vortices, while new vortices appear randomly from the left area. Thus, the disordered waves mode is composed of non-axisymmetric and unsteady vortices which are created and vanish randomly.

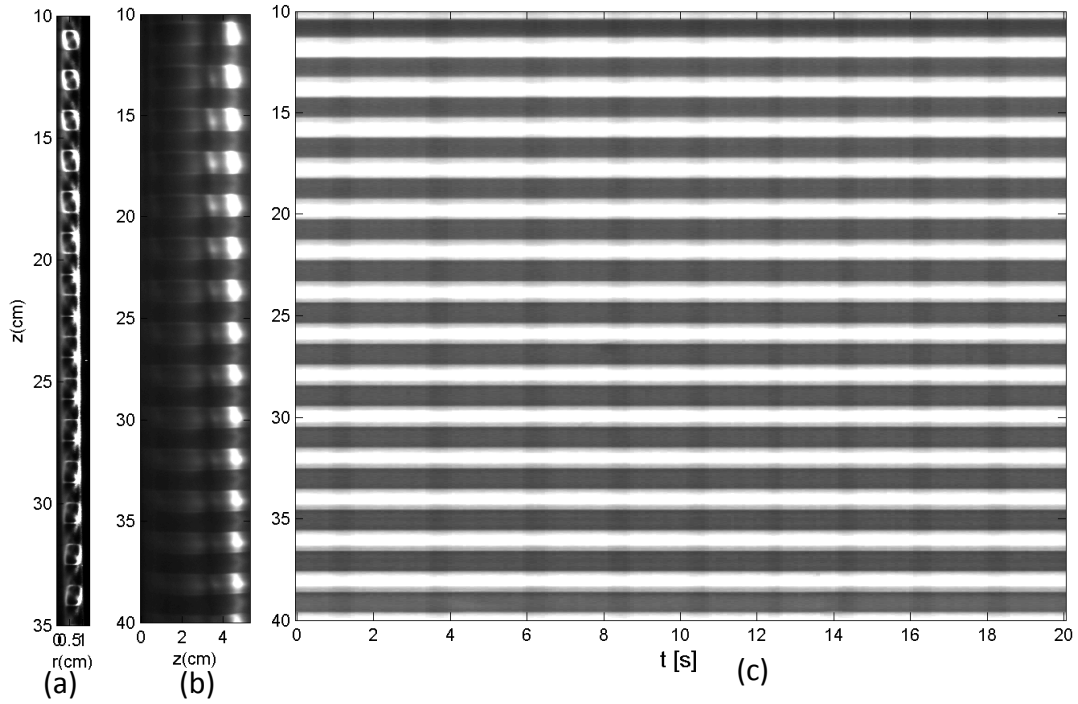


Figure 6.14: Taylor vortex mode observed in a solution of 1000ppm PEO and 2.5% PEG ( $Ta_c = 28.8, E_m = 0.011, S = 0.87$ ) in  $\mu = 0$  regime: (a) gap view, (b) front view, (c) space-time diagram of the front view.

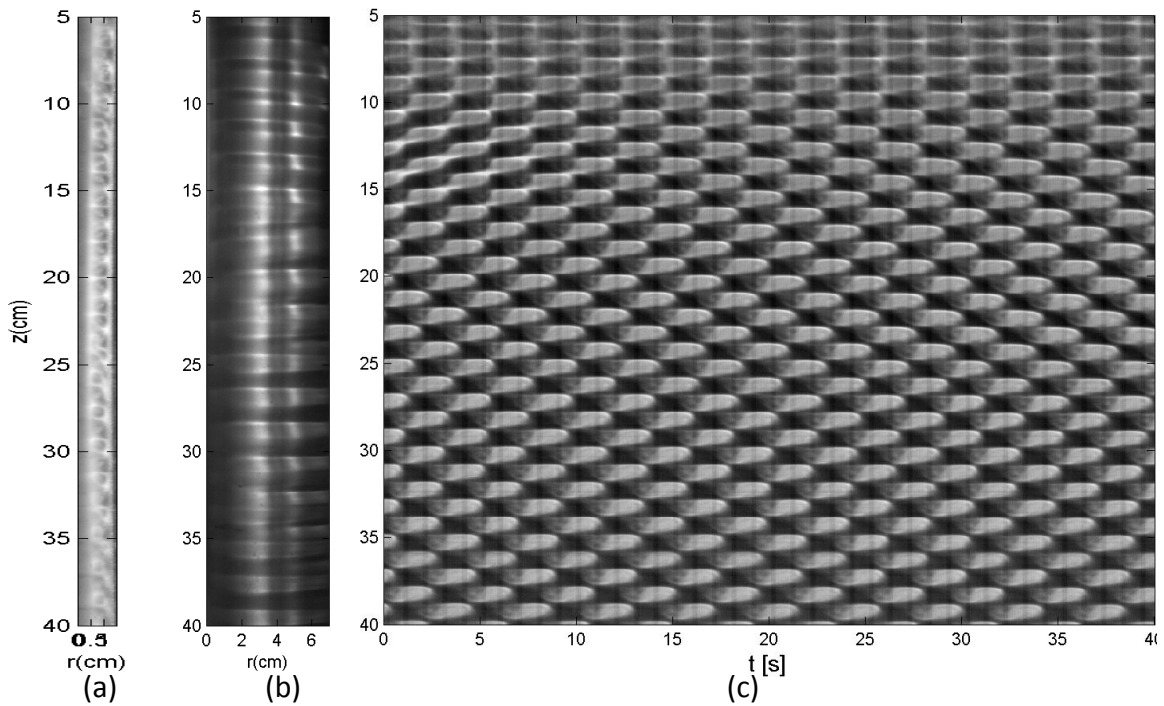


Figure 6.15: Critical mode of Ribbons at  $Ta_c = 28.4, E_m = 0.0168, S = 0.81$  in  $\mu = 0$  regime for a solution of 1000ppm PEO and 5% PEG. (a) gap view (b) front view (c) space-time diagram of the front view.

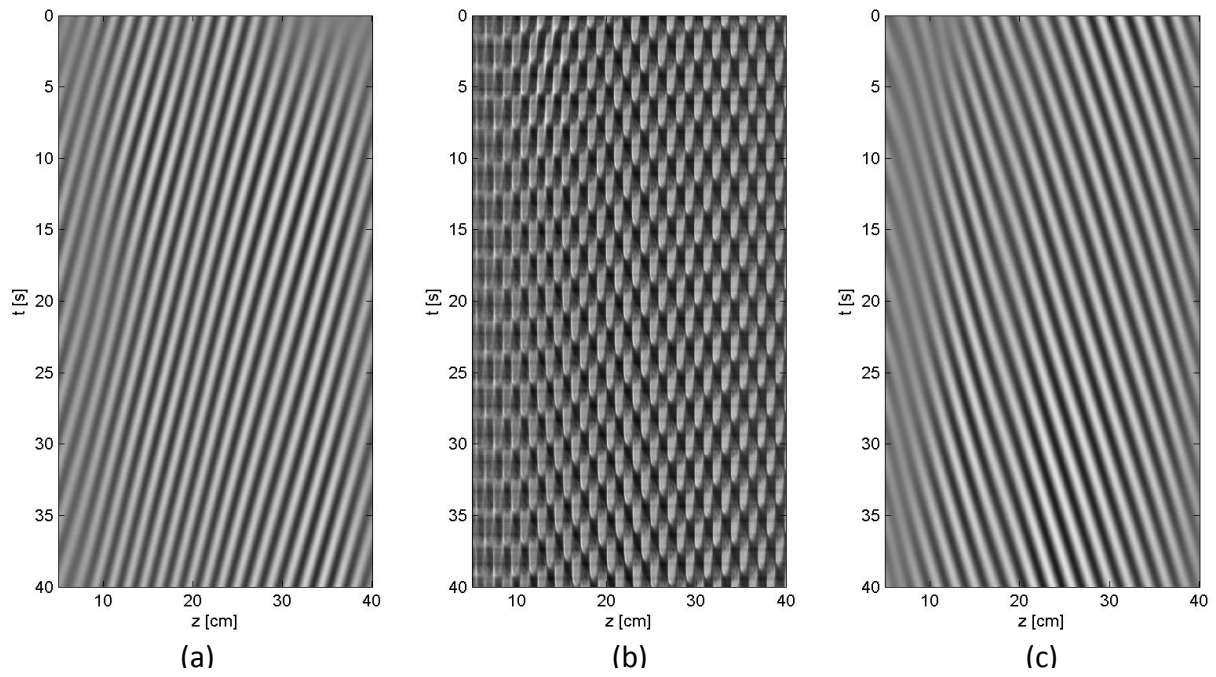


Figure 6.16: Demodulation of the space-time diagram of the Ribbons mode. (a) demodulated left wave (b) space-time diagram (c) demodulated right wave.

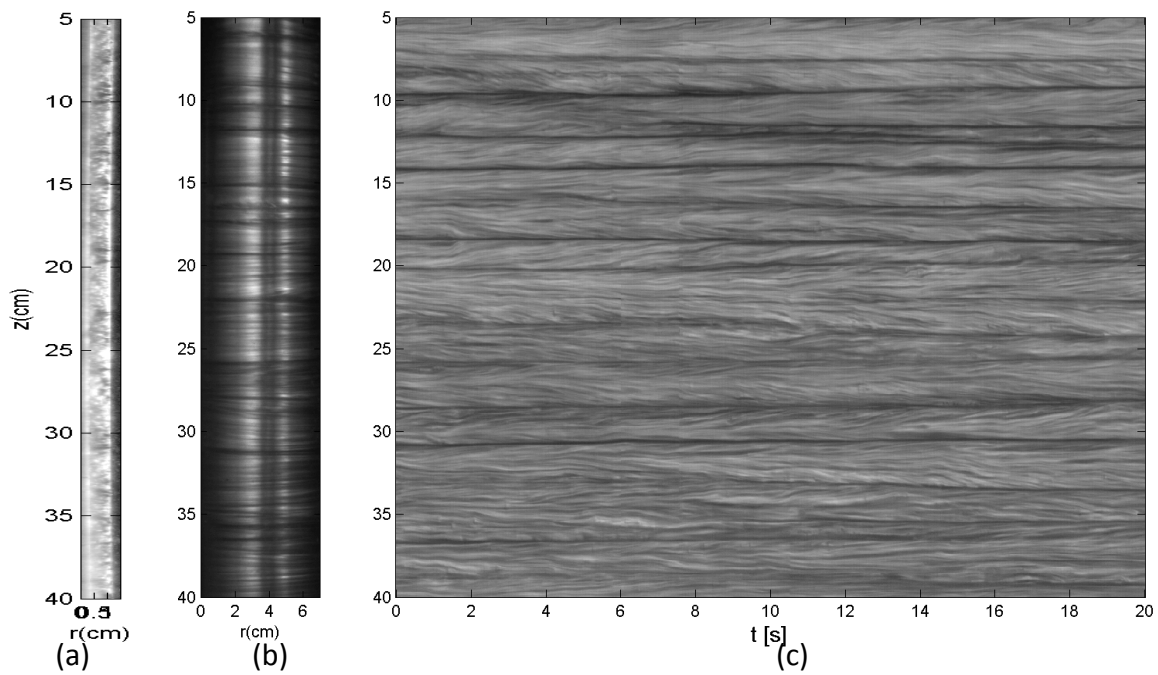


Figure 6.17: Critical mode of Disordered Vortices at  $Ta_c = 12.1, E_m = 0.131, S = 0.61$  in  $\mu = 0$  regime for a solution of 1000ppm PEO and 15% PEG. (a) gap view (b) front view (c) space-time diagram of 20s of the front view.

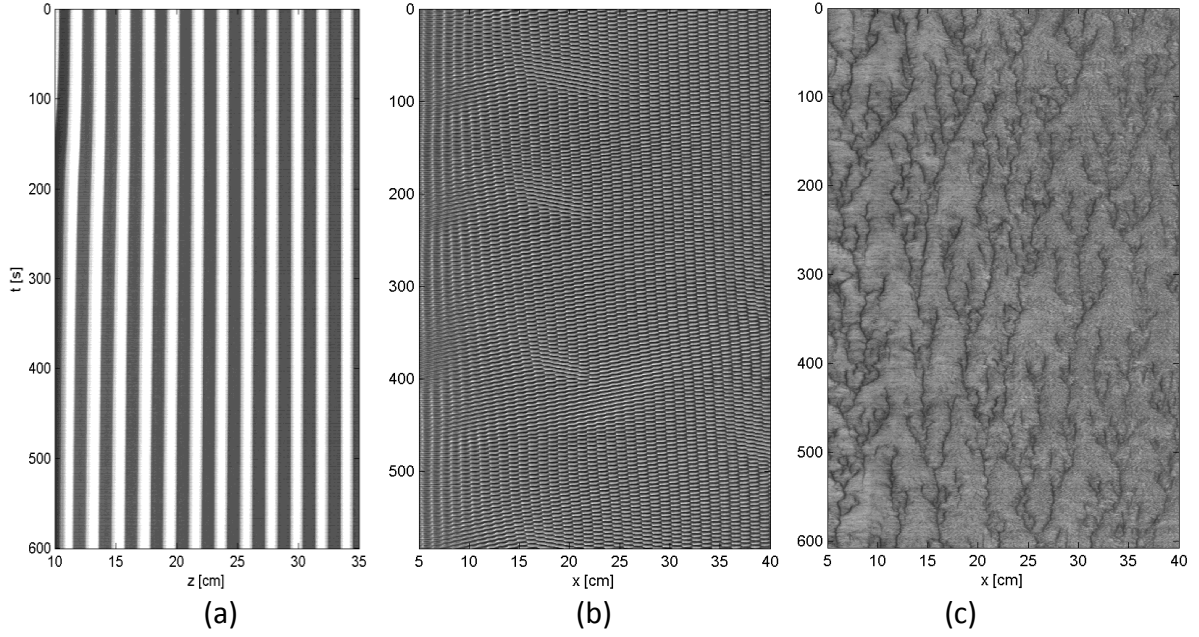


Figure 6.18: Space-time diagram of 600s for 3 different modes: (a) Taylor Vortex (b) Ribbons (c) Disordered vortices.

To study more precisely the critical axial wave number  $q_c$  and the critical frequency  $\omega_c$  we have applied the 2D Fourier transformation on the long-time space-time diagram (figure 6.18) of each working fluid. Then we non-dimensionlize  $k_c$  to the critical wave number by  $q_c = 2\pi dk_c$  and the critical angular velocity  $f_c$  by  $\omega_c = 2\pi f_c/\dot{\gamma}$ . These critical values are then compared with the previous LSA results.

The Taylor vortex mode and the Ribbons mode have a well-defined wave number and frequency in the spectra. The disordered vortices modes have smooth spectra (figure 6.19), so that no evident critical wavenumber  $k_c$  nor critical frequency  $f_c$  can be identified from them, except the flicker frequency of the spotlight (black dashed line).

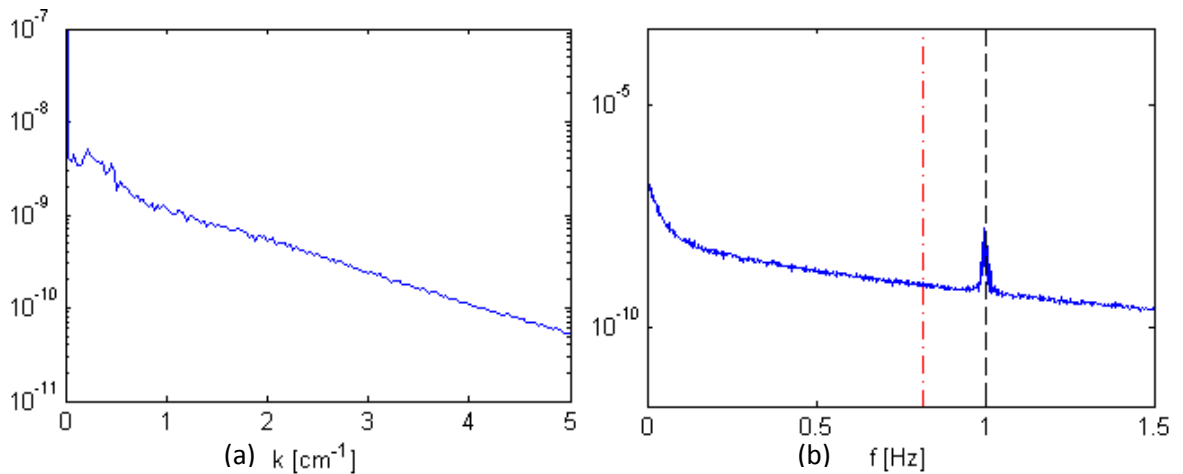


Figure 6.19: Fourier spectra of the Disordered Vortices for a solution of 1000ppm PEO and 15% PEG ( $Ta_c = 12.1, E_m = 0.131, S = 0.61$ ) in  $\mu = 0$  regime: (a) space spectrum (b) time spectrum. Red dashed line – the frequency of the inner cylinder. Black dashed line – the flicker frequency of the spot light.

While the Taylor Vortex and the ribbons appear suddenly and everywhere along all the length of the cylinders, the Disordered Vortices appear first at the top or bottom endplate and then propagate slowly to the other endplate (figure 6.20-a). The fast Fourier transform of the space-time diagram of the transient state returns smooth spectra of  $f$  and  $k$  (figure 6.20 (b) (c)).

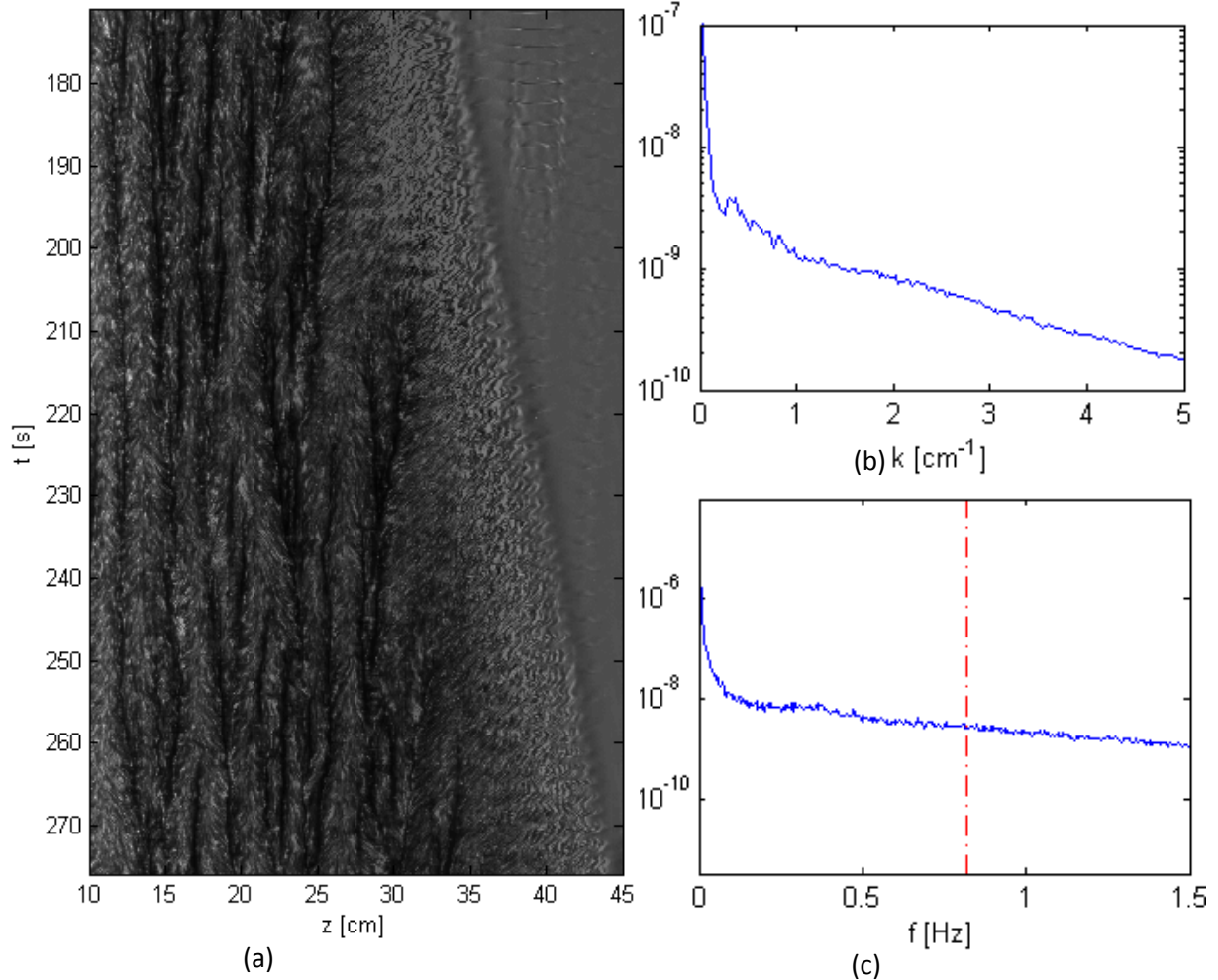


Figure 6.20: Transition to Disordered Vortices for a solution of 1000ppm PEO and 15% PEG ( $Ta_c = 12.1, E_m = 0.131, S = 0.61$ ) in  $\mu = 0$  regime. (a) Space-time diagram of the transient state, (b) space spectrum, (c) time spectrum. The y axis of the spectrums is the magnitude of the Fourier transformation.

### b. Comparison with LSA results

Three different relaxation times ( $\tau_e, \tau_m, \tau_{N1}$ ) are used to define the experimental values of the solution elasticity  $E$  and the polymer elasticity  $ES$ . We plotted in figure 6.21 the experimental critical Taylor number  $Ta_c$  versus the parameter  $ES$ , against three values of  $ES$  corresponding to different relaxation times (figure 6.21). The critical curves predicted by LSA corresponding to the working solutions are plotted for values of  $S$  between 0.5 and 0.9. The experimental values of  $Ta_c$  decrease with  $ES$  in the same way as the theoretical values of  $Ta_c$  from LSA: they decrease slightly at small  $ES$  then decrease quickly at large  $ES$ . The threshold of stationary vortices is almost independent of  $ES$ . The decrease of  $Ta_c$  corresponds to the ribbon state and to disordered waves. The critical curves  $Ta_c(ES)$  from LSA lie between those corresponding to elasticity defined by molar mass relaxation

time and the extensional relaxation time. At larger  $ES$ , the LSA critical curves are closer to those with elasticity defined with the extensional time.

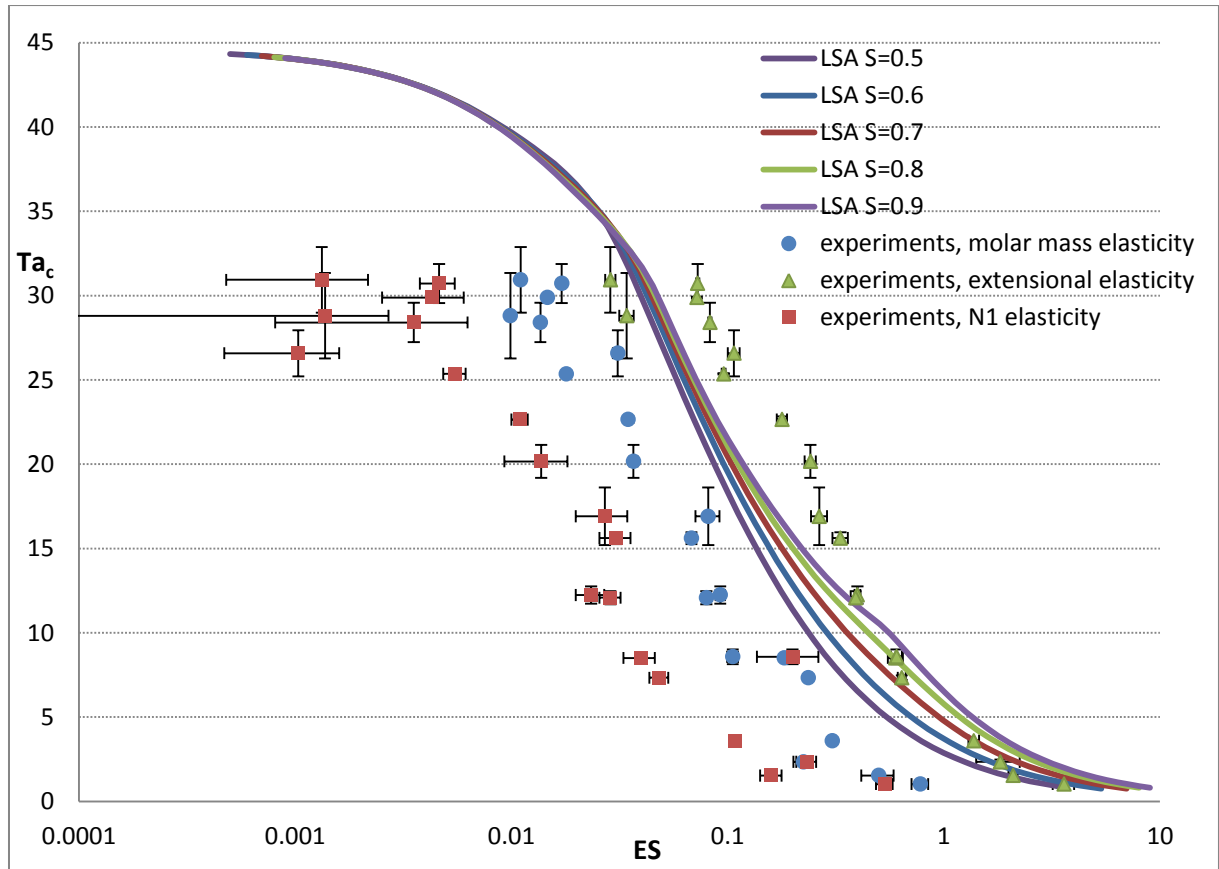


Figure 6.21: Variation of the critical values of  $Ta$  with the polymer elasticity  $ES$  in  $\mu = 0$  regime. Solid points represent experimental critical values, 3 colors correspond to 3 different definitions of elasticity. Within each definition of elasticity (see section 5.4), each point represents one tested solution. Continuous lines are the LSA critical curves for different  $S$ .

In figure 6.22, we keep only the elasticity defined by the molar mass. The critical modes occur in form of different types depending on the polymer elasticity  $ES$ . So, the critical points can be gathered into three different groups: for small values of  $ES$ , the critical modes are the Taylor Vortex, for intermediate values of  $ES$ , the critical modes are the ribbons and for large  $ES$ , the critical modes are Disordered Vortices. The separation lines of the axisymmetric stationary mode and the non-axisymmetric oscillatory mode from LSA are situated near the edge of the Taylor vortex mode and the ribbons mode. Considering the difficulty to estimate the elasticity, the experimental critical modes correspond to the LSA predictions.

Then we sum up the  $\omega_c$  of all the experimental critical modes and the LSA predictions in figure 6.23. The experimental angular frequencies follow qualitatively the behavior of the theoretical values: at small elasticity, the Taylor Vortex mode has null frequency; for intermediate values of  $ES$ , the ribbons mode has a finite frequency which decreases with  $ES$ ; for disordered vortices, there is no well-defined frequency because of their chaotic behavior.

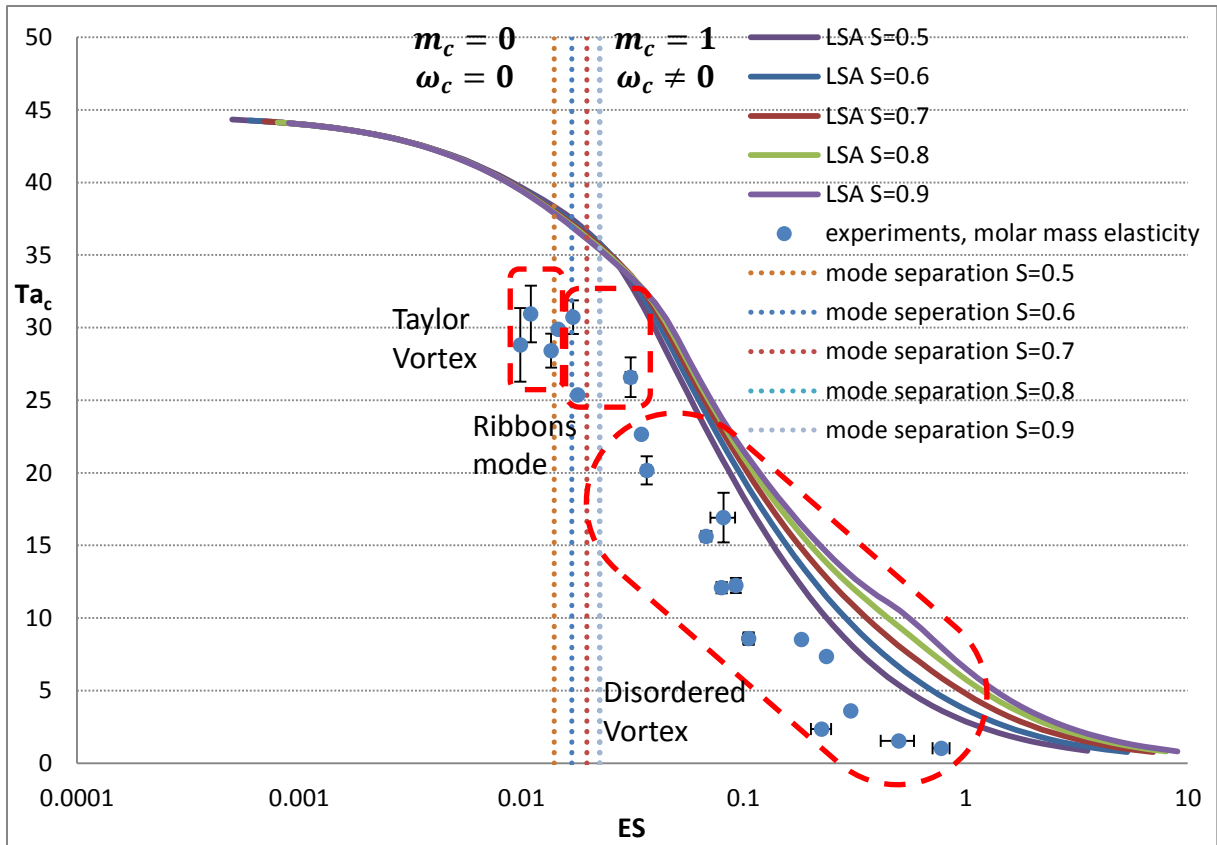


Figure 6.22: Variation of the critical values of  $Ta_c$  with the polymer elasticity  $ES$  defined by the mass molar relaxation time in  $\mu = 0$  regime. Solid points represent experimental critical values. Dashed rectangles are groups of different critical modes. Continuous lines are LSA critical curves for different values of  $S$ . Dashed lines separate the stationary axisymmetric mode and the non-axisymmetric oscillatory mode from LSA.

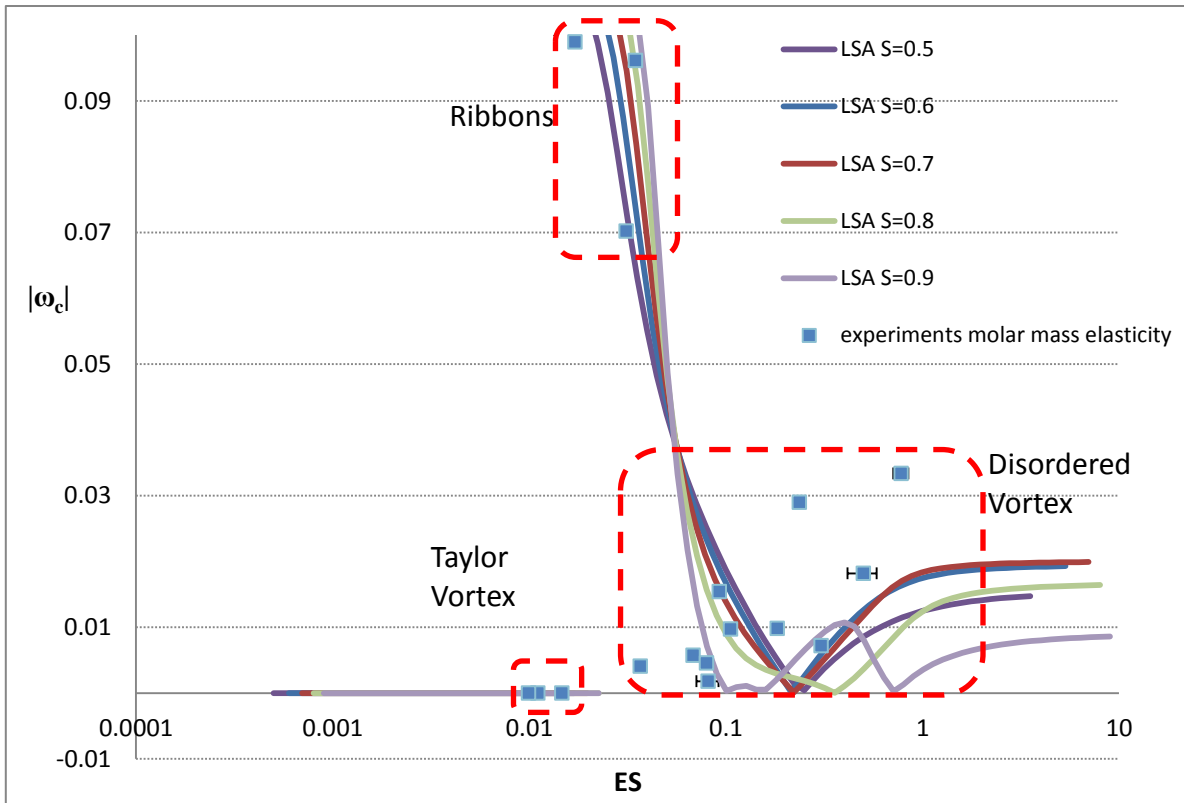


Figure 6.23: Variation of the critical angular frequency  $|\omega_c|$  with  $ES$  defined with molecular relaxation time in  $\mu = 0$  regime. Solid points – experimental critical values. Dashed rectangles – groups of different critical modes. Continuous lines – theoretical critical angular frequencies for different  $S$ .

In figure 6.24 we present the dimensionless wave number  $q_c$  with the LSA predictions. The critical wavenumbers  $q_c$  of the Taylor Vortex mode and the Ribbons follow qualitatively the predictions of the LSA, however the  $q_c$  of the Disordered Vortices stays away from the LSA predictions. As shown in figure 6.1 ©, the marginal curves of large  $E$  have flat bottom. This makes it hard to distinguish a dominant wave number, which means waves of several wave numbers coexist. Our experimental space-time diagram and the spectra confirm the existence of many waves yielding the chaotic vortices via the superposition of these waves.

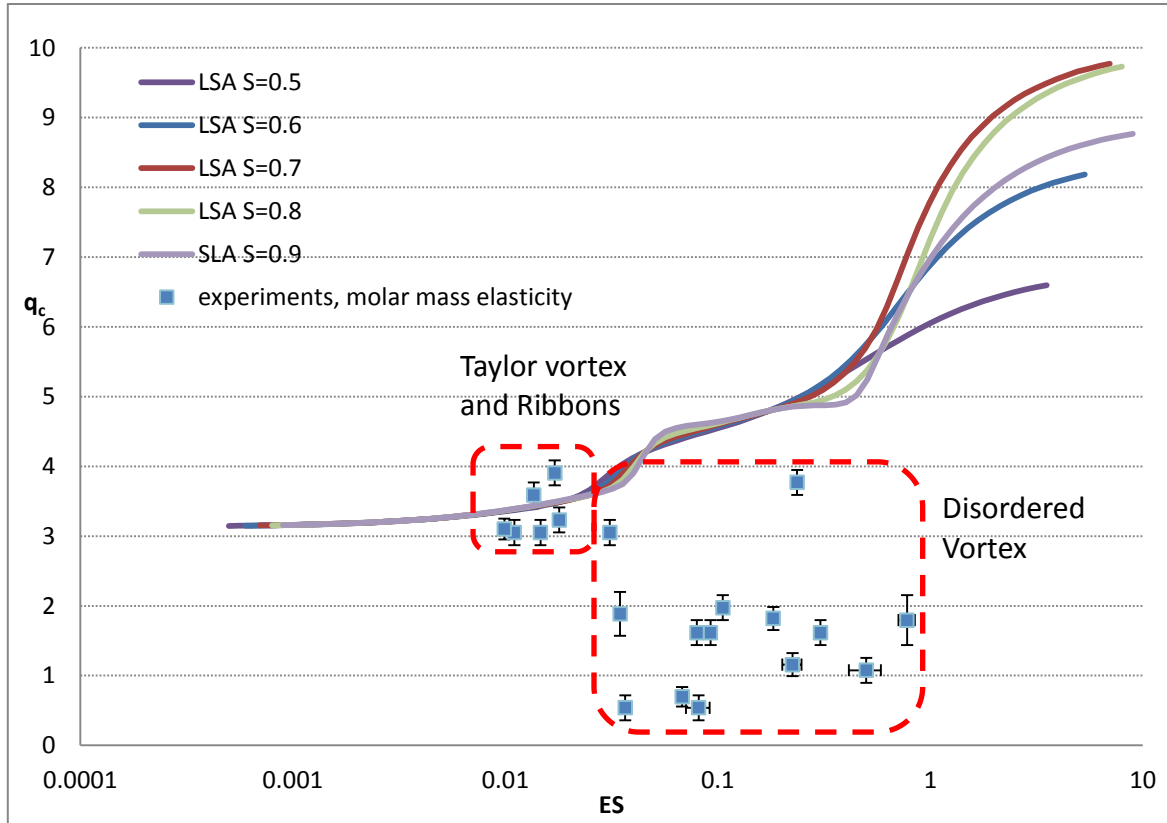


Figure 6.24: Dimensionless critical axial wave number  $q_c$  in  $\mu = 0$  regime. Solid lines – LSA critical wave numbers for different  $S$ . Solid points – experimental critical values. Dashed circle – group of different critical modes

### c. Comparison with previous results

We have observed the disordered vortices mode for fluid with  $ES > 0.035$ . Compared to the purely elastic mode first observed by Larson et al. [Larson1990], the disordered vortices (DV) mode has the same flow pattern as the purely elastic mode. However, the purely elastic mode is observed for fluids of very large  $E$  and at negligible  $Ta_c$ .

The same flow pattern corresponding to the purely elastic mode were also observed for fluid of  $E = 15, S = 0.13$  at  $Ta_c = 0.056$  by Baumert & Muller [Baumert1999] in a Couette-Taylor system of  $\eta = 0.827$ .

In the same system of  $\eta = 0.827$ , Baumert & Muller have observed also stationary counter-rotating vortices for less elastic fluid ( $E = 0.0562, S = 0.13$ ) at  $Ta_c = 14.5$ . For fluids of similar elasticity ( $0.017 < E < 0.031$ ) we have observed the Ribbons mode. The Taylor vortex (TV) mode is only observed for less elastic fluids.

In a system of  $\eta = 0.829$ , Groisman & Steinberg [Groisman1998] have observed the Taylor vortex mode for solutions with  $E < 0.08$  and disordered oscillations mode for  $0.08 < E < 30$  when increasing the rotation velocity. The critical Weissenberg number for the first transition is comparable to our experimental results.

Previously in LOMC, Façal Kelai has done similar experiments with the same setup  $\eta = 0.8$  and the similar working solutions in the  $\mu = 0$  regime [Kelai2011]. He has used solutions of small viscosity ratio  $S \in (0.05, 0.3)$ , except for the Taylor vortex mode which was obtained in shear-thinning solutions. His points lie on the left side of ours because our solutions have larger  $S$ . He has also observed three different modes and recorded the corresponding critical values.

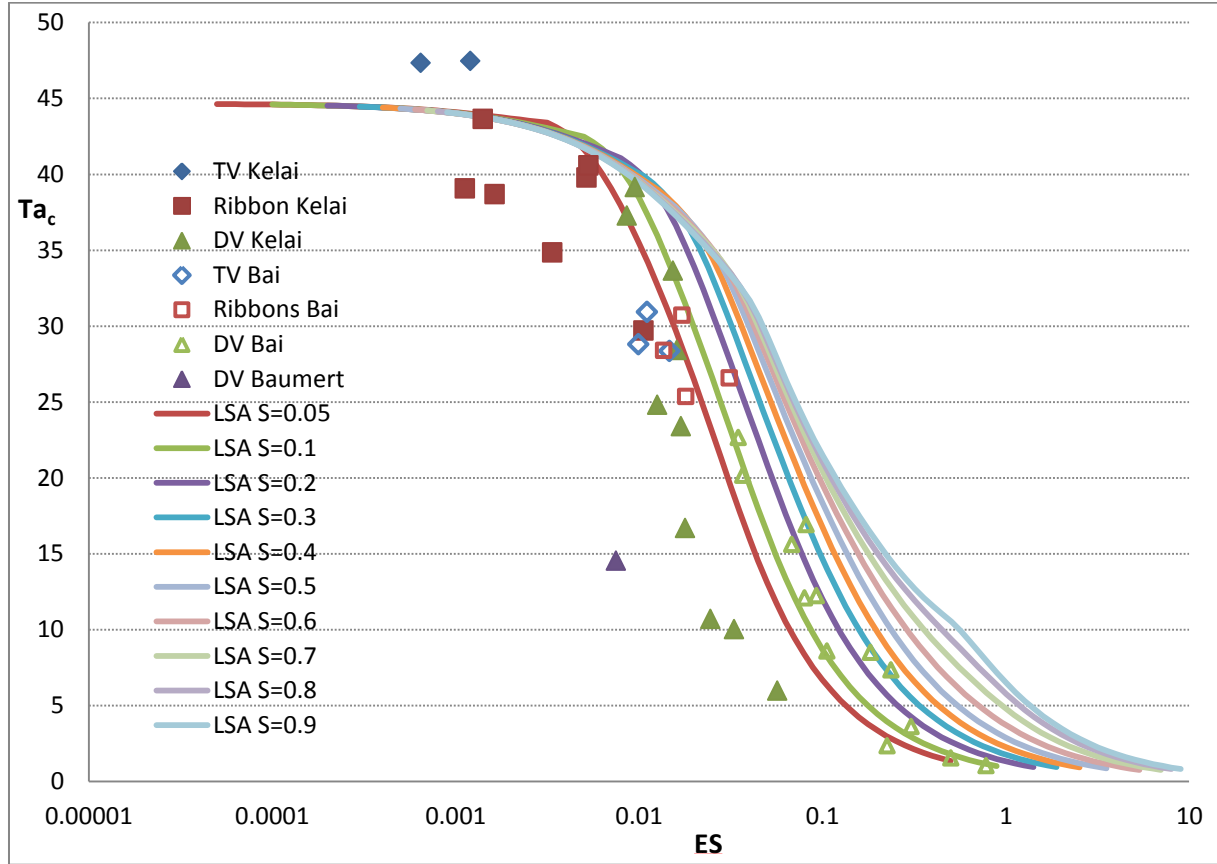


Figure 6.25: Critical values on regime of  $\mu = 0$ . Continuous lines – LSA critical curves. Solid points – Kelai’s experiments. Open points – our experiments. Violet triangle – Baumert’s experiment.

In figure 6.25, we compare our experimental values with those of Kelai and of Baumert together with LSA data, we observe that the experimental results of Kelai have larger  $Ta_c$  than ours and they fit better the LSA critical curves. The  $Ta_c$  of the less elastic fluid of Baumert is found smaller than our results and far away from the LSA critical curves. Note that the radius ratio  $\eta$  of the cylinders used by Baumert is different from ours, and the waiting time of Baumert is much longer than ours.

#### d. Supercriticality or subcriticality

We recall that all the previous results are obtained by increasing step by step the rotation velocity of the inner cylinder. We have also decreased the rotation velocity of the inner cylinder step by step to see if the instability disappears at the same critical values. We found out that the Taylor Vortex mode and the Ribbons mode disappear as long as the cylinder rotates slower than the critical velocity observed when increasing it, while the Disordered Vortices mode stays unstable at velocities smaller than the critical velocity when increasing it. So the Taylor Vortex mode and the Ribbons

mode are supercritical instability modes while the Disordered Vortices mode is a subcritical instability mode.

## 6.2. Annular flow with $\mu = \infty$

When we rotate the outer cylinder while fixing the inner cylinder, the fluid in the outer part rotates faster than inner part and the centrifugal force is no longer destabilizing, only the elastic force may destabilize the flow.

### 6.2.1. LSA results

Analyzing by the same LSA code with the base flow of  $\mu = \infty$  regime, we have found out that the most unstable mode is always axisymmetric with  $m_c = 0$ . Taking  $S = 0.7$  as an example, we plot in figure 6.26 the marginal stability curves  $Ta(q)$  for different values of  $m$  at  $E = 1$ . The lowest marginal curve of  $m = 0$  possesses very flat bottom that makes it difficult to determine the critical wavenumber  $q_c$ . So several perturbation modes of different  $q$  may coexist .

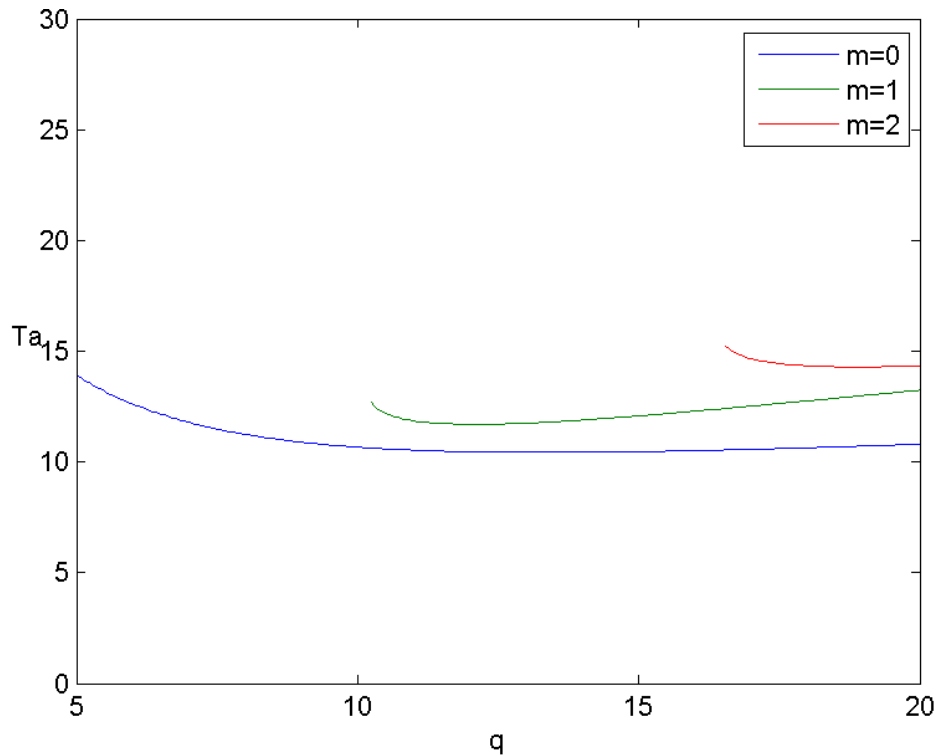


Figure 6.26: Marginal curves  $Ta(q)$  for different  $m$  at  $S = 0.7$  and  $E = 1$ .

Figure 6.27 presents the variation of the critical Taylor number  $Ta_c$  with the solution elasticity  $E$  for different azimuthal wave number  $m$ . For all  $m$  calculated,  $Ta_c$  decreases with  $E$ . The  $Ta_c$  of the axisymmetric mode  $m = 0$  is much smaller than the other modes ( $m = 1$  and  $m = 2$ ) so that the axisymmetric mode  $m = 0$  is the most unstable mode for all calculated values of  $E$ .

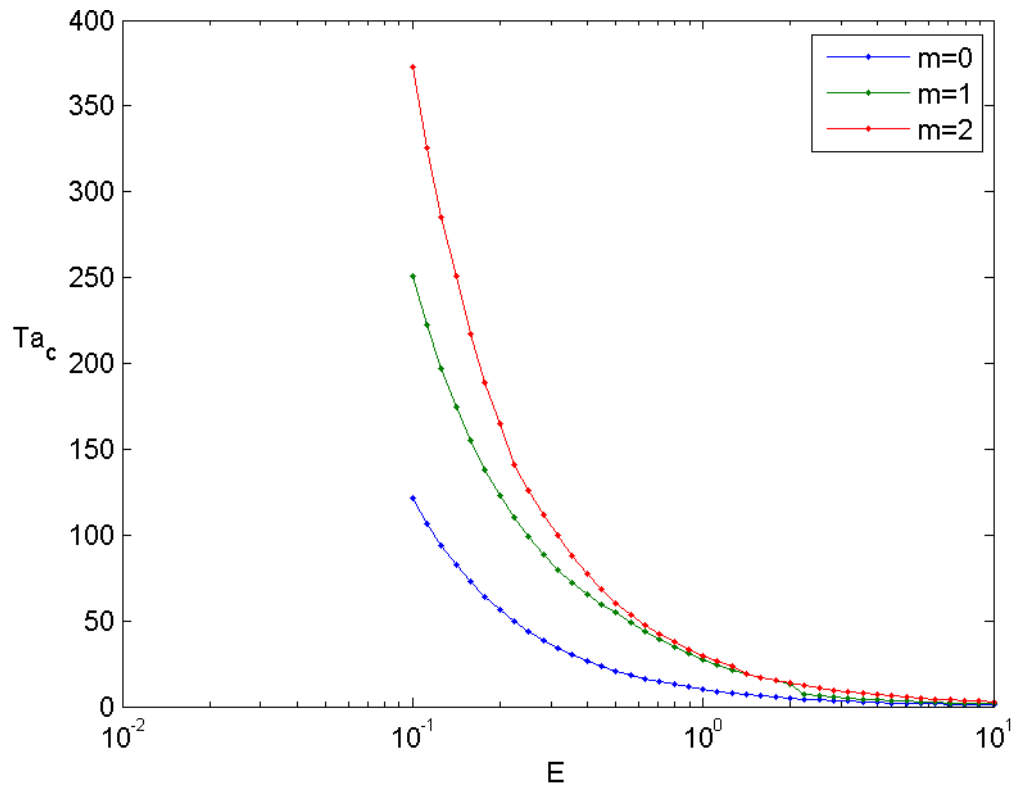


Figure 6.27: Critical curves  $Ta_c(E)$  for different  $m$  at fixed  $S = 0.7$  in  $\mu = \infty$  regime.

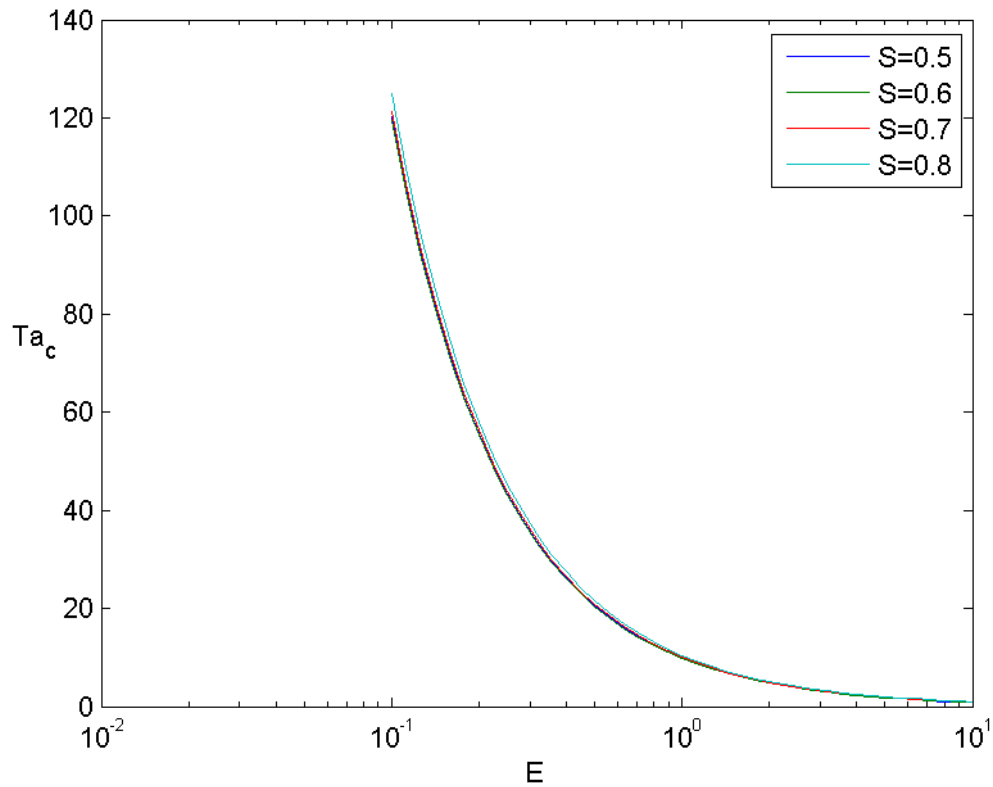


Figure 6.28: Critical curves,  $Ta_c(E)$  for different  $S$  in  $\mu = \infty$  regime.

Then we super-impose in figure 6.28 the critical curves  $Ta_c(E)$  for different  $S \in [0.5, 0.8]$ . We observe that the critical curves of  $Ta_c(E)$  for different  $S$  are very close to each other, which means that for the  $\mu = \infty$  regime the viscosity ratio  $S$  has weak effects on the viscoelastic instability. As the centrifugal force is no longer destabilizing in the  $\mu = \infty$  regime, the only destabilizing force is the elastic force which is independent to the polymer viscosity ratio  $S$ . The critical curve can be fitted by a power law  $Ta_c(E) = AE^{-\alpha}$  with  $\alpha = 1.048, A = 10.295$ , and the coefficient of determination  $R^2 = 0.9996$ .

We present in Figure 6.29 the critical curves in the plane  $(Wi_c, Re_c)$  for different  $S$ . Unlike in the  $\mu = 0$  regime,  $Re_c$  increases with  $Wi_c$  and the critical curves for different  $S$  do not cross each other. For all calculated values of  $Wi_c$ , larger  $S$  reduces  $Re_c$  showing that polymer viscosity destabilizes the flow. The intersection points between the critical curves and the horizontal axis determine the onsets  $Wi_c$  to the purely elastic instability. This will be discussed in chapter 9.

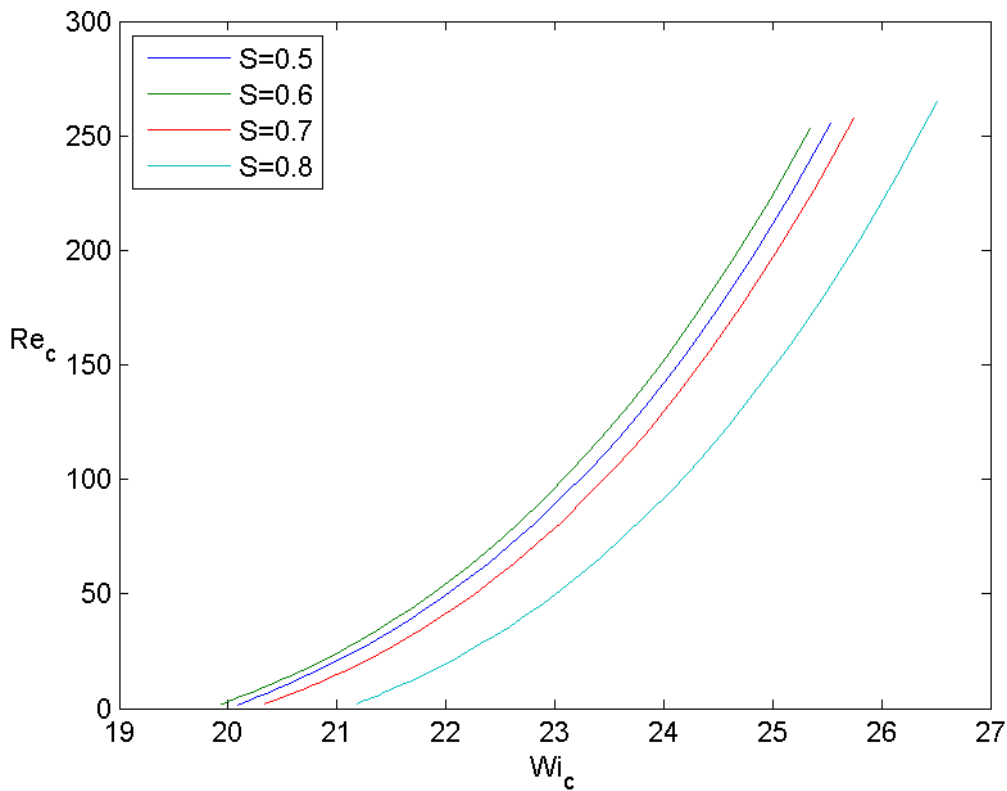


Figure 6.29: Critical curves  $Re_c(Wi_c)$  for different  $S$  in  $\mu = \infty$  regime.

Then we look into the axisymmetric critical mode. We plot in figure 6.30 the critical angular frequency  $\omega_c$  and the critical axial wave number  $q_c$  in respect to  $E$  for different  $S$ . We observe that the critical modes are not stationary as the critical frequency is not zero ( $\omega_c \neq 0$ ) and the angular frequency increases with  $E$ . The axial wave number  $q_c$  decreases with  $E$ . In the calculated range of  $E \in \{0.1, 10\}$ ,  $q_c > 10$ , or the corresponding wavelength  $\lambda_c/2 < d$ , so that the critical mode occurs in the form of flattened vortices. Similar to figure 6.29, the critical curves of  $\omega_c$  and  $q_c$  for different  $S$  are almost parallel to each other, the larger  $S$  makes larger critical values of  $\omega_c$  and  $q_c$ .

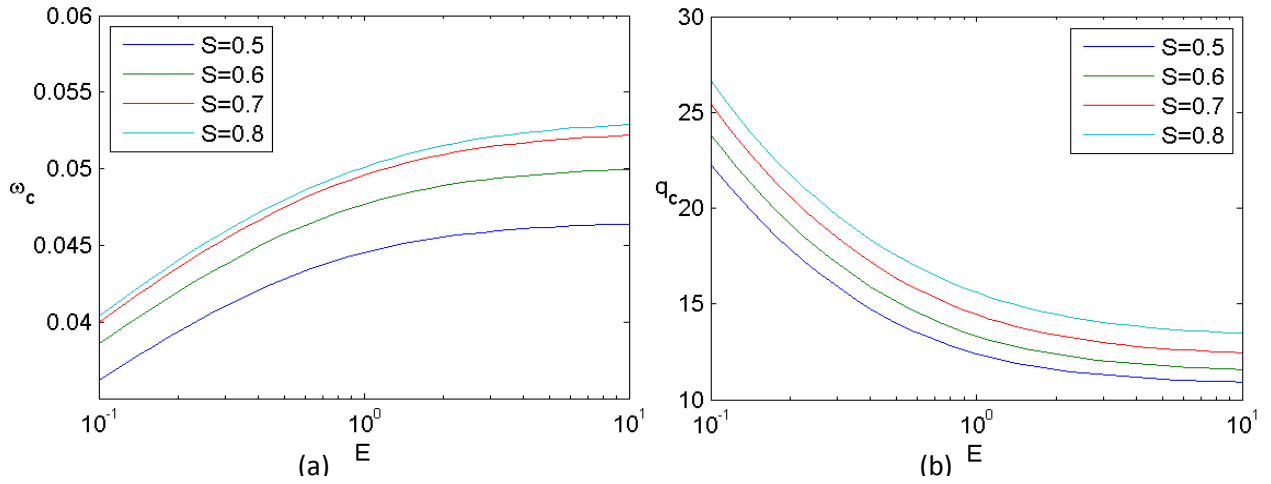


Figure 6.30: Variation of the critical parameters with  $E$  for different values of  $S$  in  $\mu = \infty$  regime: (a) angular frequency  $\omega_c$  (b) axial wave number  $q_c$ .

To provide a general view of the critical modes in  $\mu = \infty$  regime, we plot in figure 6.31 the flow patterns for solution of  $S = 0.7, E = 1, Ta_c = 4.73$  with  $m_c = 0, q_c = 14.4, \omega_c = 0.050$ . The flow properties including velocity field, the vorticity, the pressure variation and the  $N_1$  variation are plotted in the section of  $(r, z)$ . The pressure variation and the  $N_2$  variation presented by figure 6.30 © © are negligible compared to the  $N_1$  variation and the vortices are flattened and instability lies near the inner cylinder (left wall).

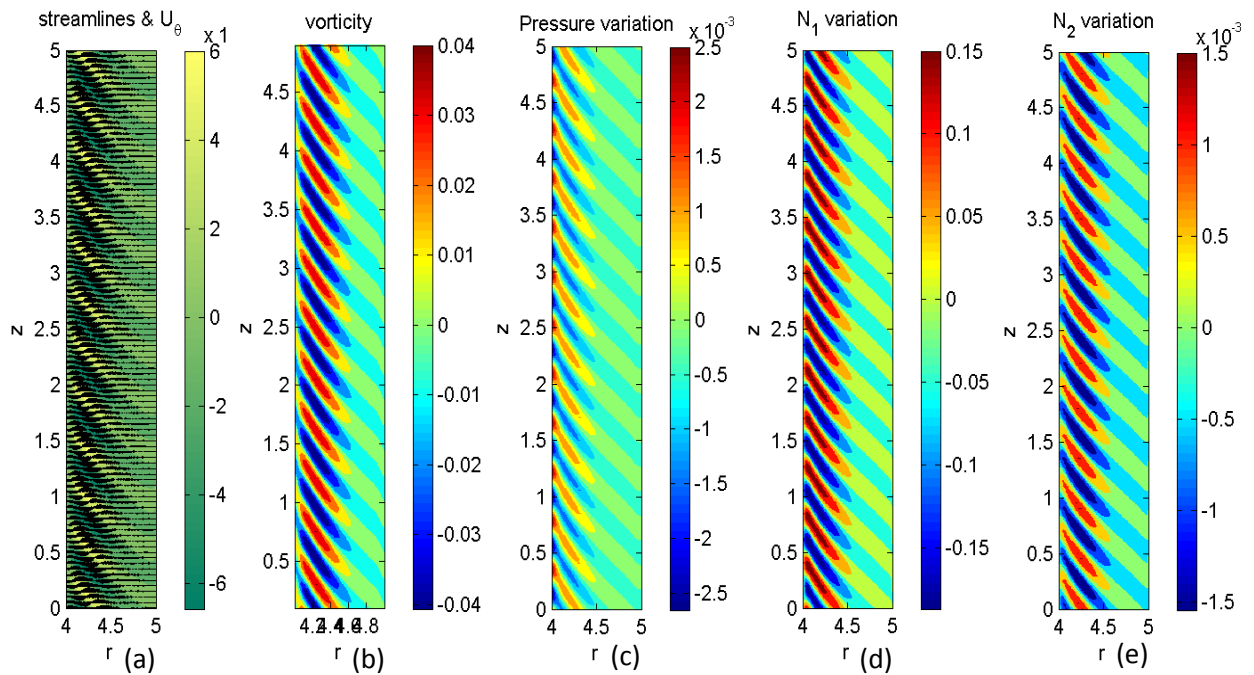


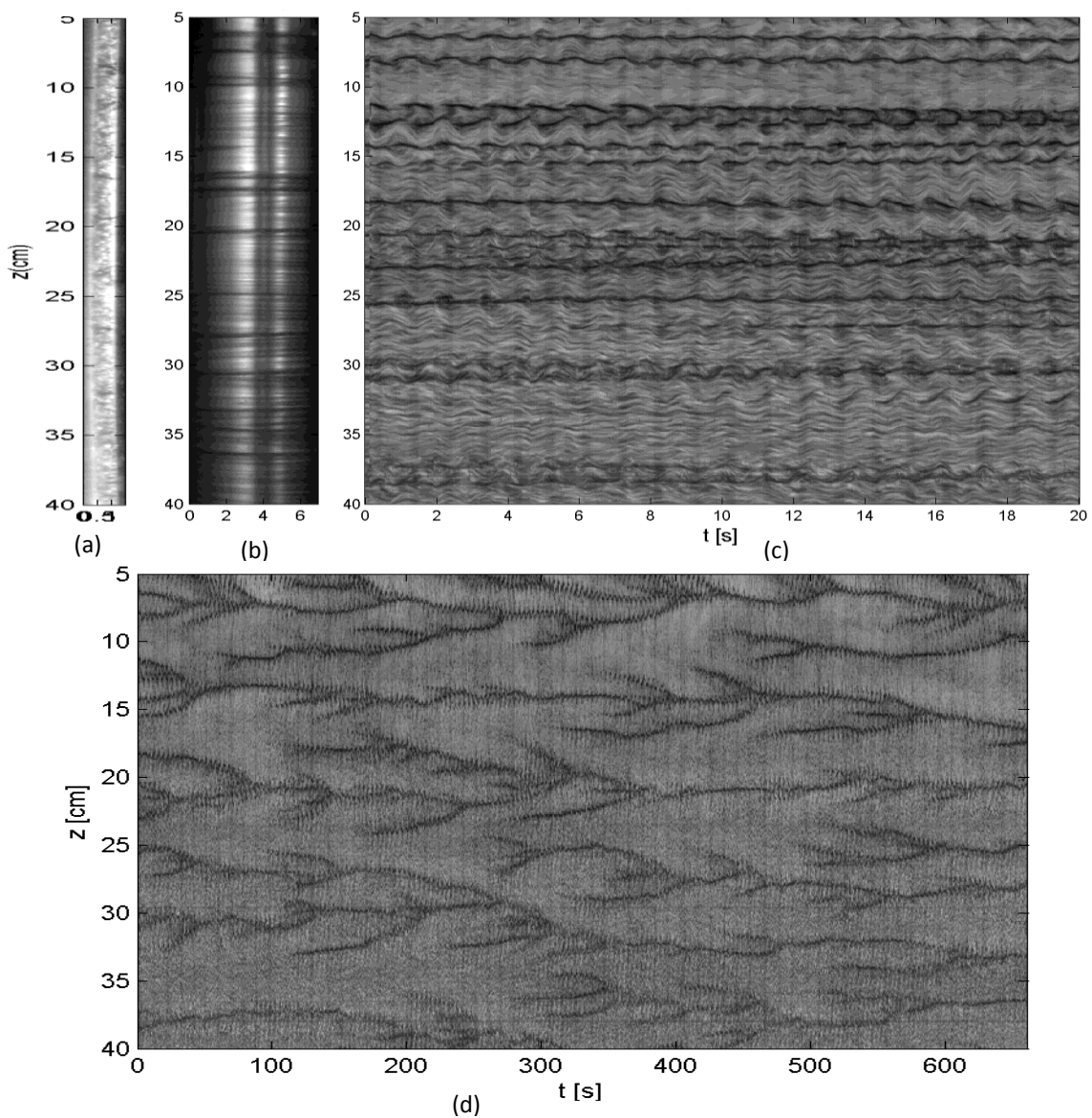
Figure 6.31: Critical mode for  $S = 0.7, E = 1, Ta_c = 4.73$  on  $\mu = \infty$ , with  $m = 0, q_c = 14.4, \omega_c = 0.050$ . (a) Black arrows represent the velocity field in  $(r, z)$  direction while the colors represent the azimuthal velocity  $V$  (b) the vorticity  $\omega_\theta$  (c) the pressure variation (d) the  $N_1$  variation © the  $N_2$  variation. Color maps of (b, c, d, e) represent the relative amplitude.

## 6.2.2. Experimental results

In the regime of  $\mu = \infty$ , we repeat the same procedure on the all solutions used in  $\mu = 0$  regime, but only the solutions of large elasticity could be destabilized. As predicted by the LSA we have observed only one critical mode in form of the Disordered Vortices as described in  $\mu = 0$  regime.

### a. Flow patterns

To show the experimental critical mode, we present in figure 6.32 the gap view, the front view, the space-time diagrams and the Fourier spectrums of the critical Disorder Vortices mode. Although we may observe temporal oscillations of certain flow patterns in figure 6.32 © which do not exist in  $\mu = 0$  regime, this mode is the same Disordered Vortices mode as in the  $\mu = 0$  regime. Because this oscillation is not related to any propagating waves, it reflects the rotation of the outer cylinder.



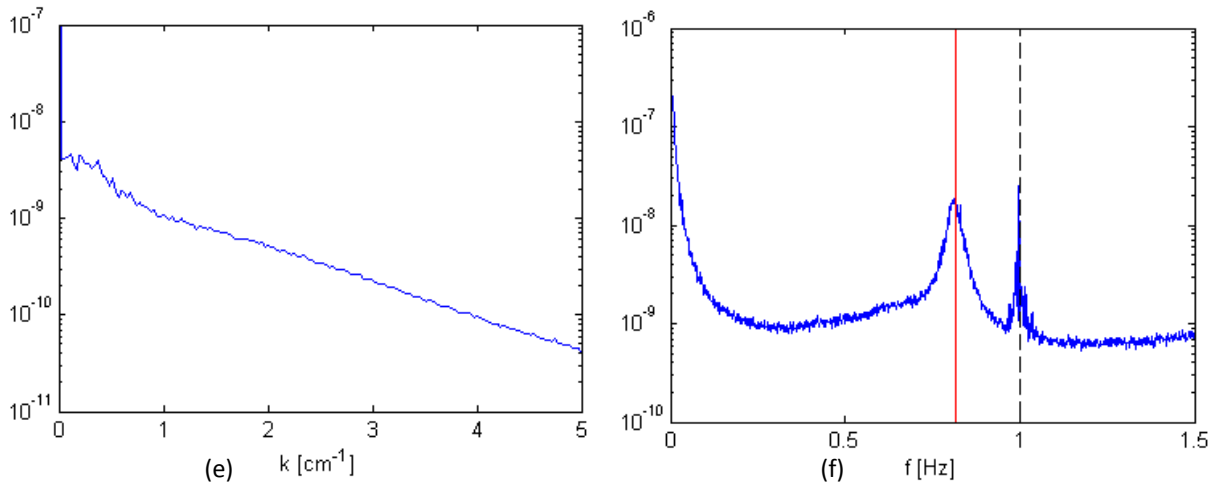


Figure 6.32: Critical mode of Disordered Vortices at  $Ta_c = 15.4$ ,  $E_m = 0.131$ ,  $S = 0.61$ ,  $\mu = \infty$  for a solution of 1000ppm PEO and 15% PEG. (a) gap view (b) front view (c) space-time diagram of 20s of the front view (d) long-time space-time diagram © space spectrum (f) time spectrum. Red dashed line – the frequency of the inner cylinder. Black dashed line – the flicker frequency of the spot light.

**b. Comparison with LSA results**

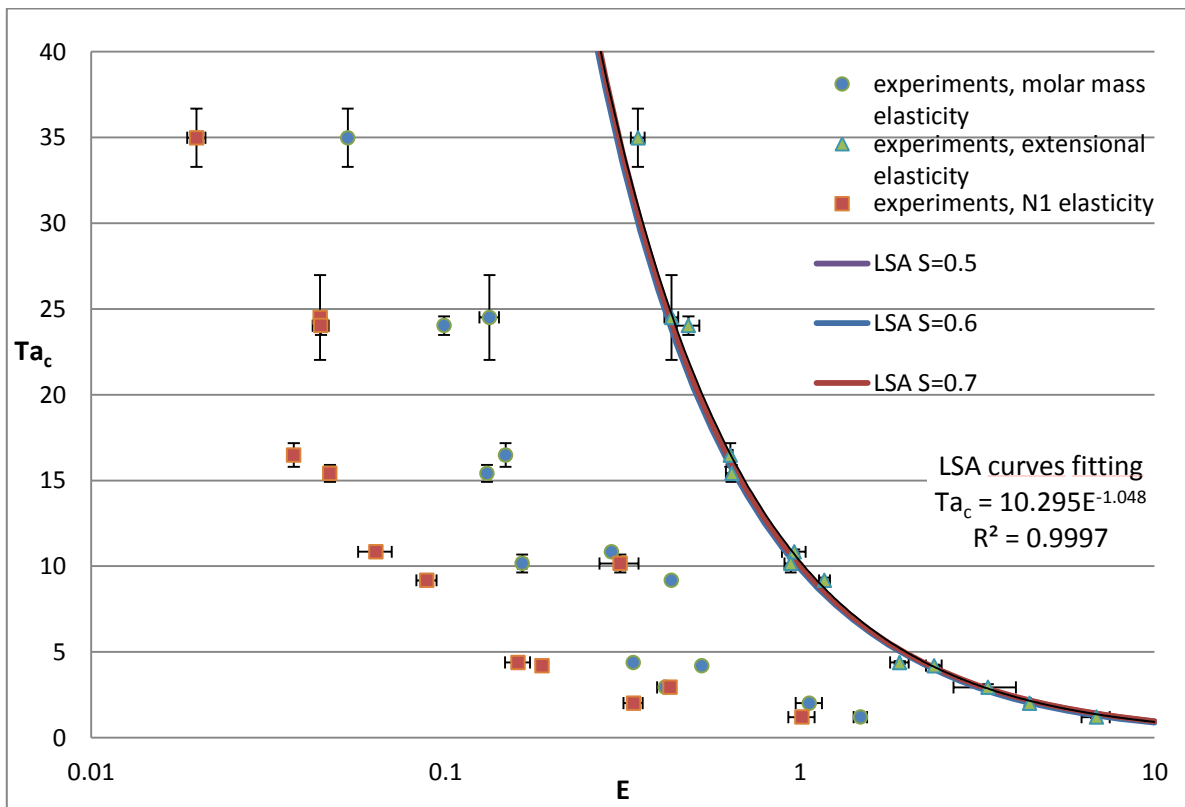


Figure 6.33: Critical values of the transition from laminar flow to unstable flow on regime of  $\mu = \infty$ . Solid lines – LSA critical curves for different  $S$ . Solid points – experimental transient values, 3 colors represent 3 different definitions of elasticity. Within each definition of elasticity, each point represents one solution tested.

To compare the experimental results to the LSA predictions, we resume the critical values of  $Ta_c(E)$  measured experimentally by three different relaxation times together with the LSA critical curves in figure 6.33. We use  $E$  instead of  $ES$  as the control parameter because the LSA critical curves of different  $S$  are close to each other on  $Ta_c(E)$  (figure 6.27). We remove the LSA critical curves of  $S = 0.8$  because the viscosity ratio  $S$  of the solutions that can be experimentally destabilized in the  $\mu = \infty$  regime lies in the range of  $S \in (0.5, 0.7)$ . We observe that the experimental critical values  $Ta_c$  decrease with  $E$  defined by three relaxation times. This follows the trend of the LSA critical curves. The points corresponding to the elasticity  $E_e$  defined by the extensional relaxation time fit perfectly with the LSA critical curves.

As explained in the previous section, it is very difficult to determine experimentally the critical values of the Disorder vortices mode, so it is not surprising that the experimental  $\omega_c$  and  $k_c$  show only weak agreements to the LSA predictions (see figure 6.34 and 6.35).

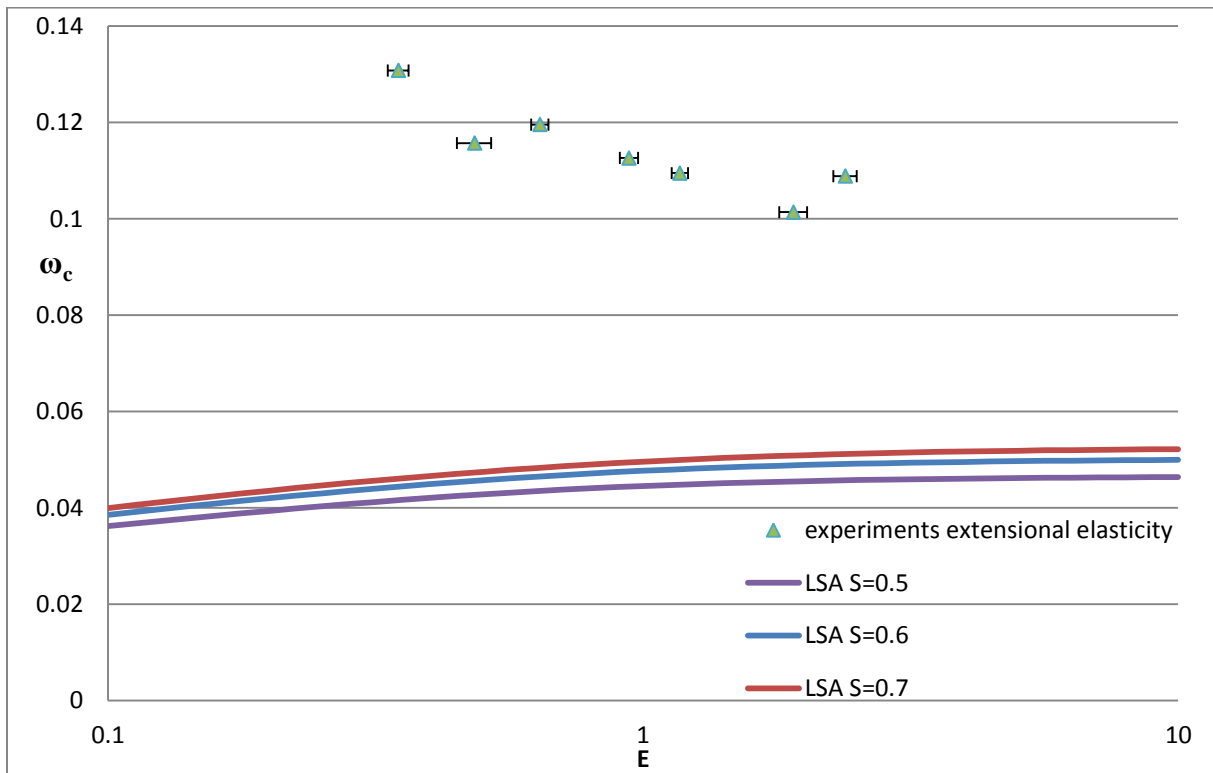


Figure 6.34: Variation of the critical angular velocity  $\omega_c$  in  $\mu = \infty$  regime with solid points – experimental critical values for  $E$  defined by extensional relaxation time. Continuous lines – the LSA critical curves for different  $S$ .

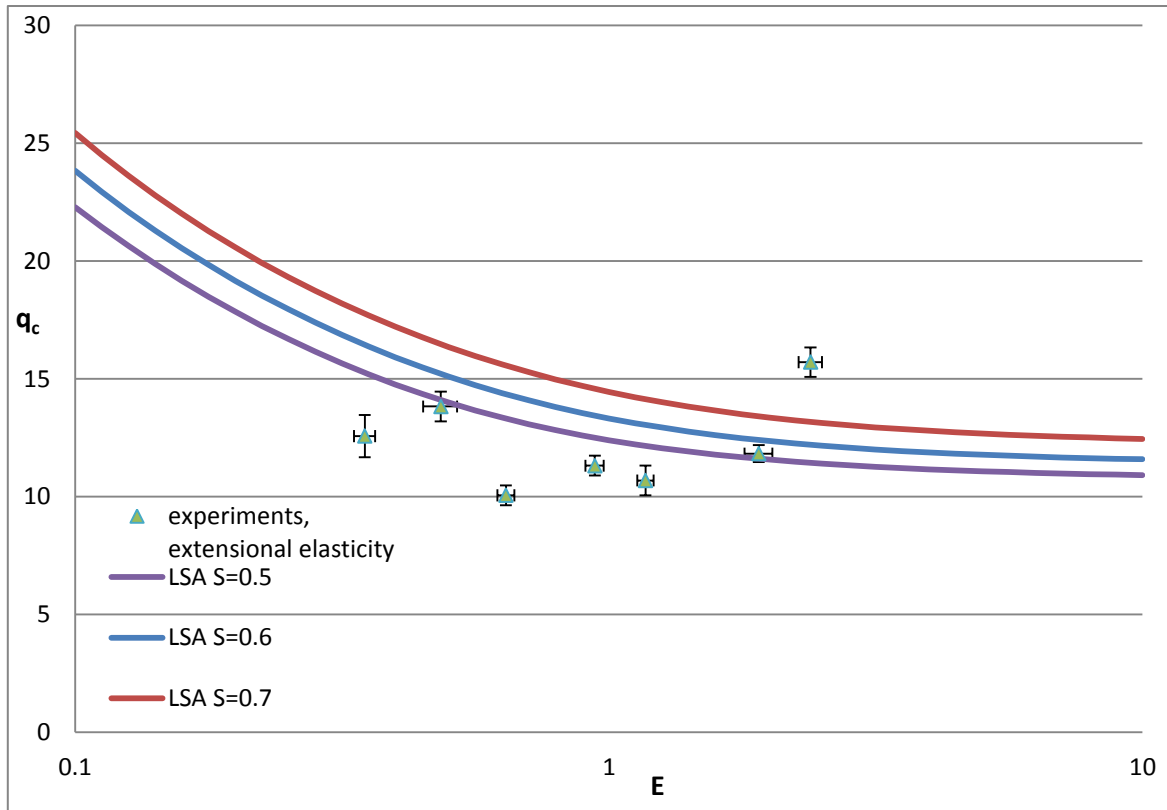


Figure 6.35: Variation of the critical axial wave number  $q_c$  with  $E$  in  $\mu = \infty$  regime. Solid points – experimental critical values for  $E$  defined by extensional relaxation time. Continuous lines – LSA critical curves for different  $S$ .

### c. Comparison to the previous results

In rotating the outer cylinder while fixing the inner cylinder, both Baumert and Kelai have observed the purely elastic mode [Baumert1997] [Kelai2011]. We super-impose in figure 6.36 the critical values of the experiments of Baumert, Kelai and ours together with the LSA critical curves. The experimental elasticity for all the authors is estimated by the molar mass. We can see that the critical values of all these experiments show good coherence between each other and parallel to the LSA critical curves.

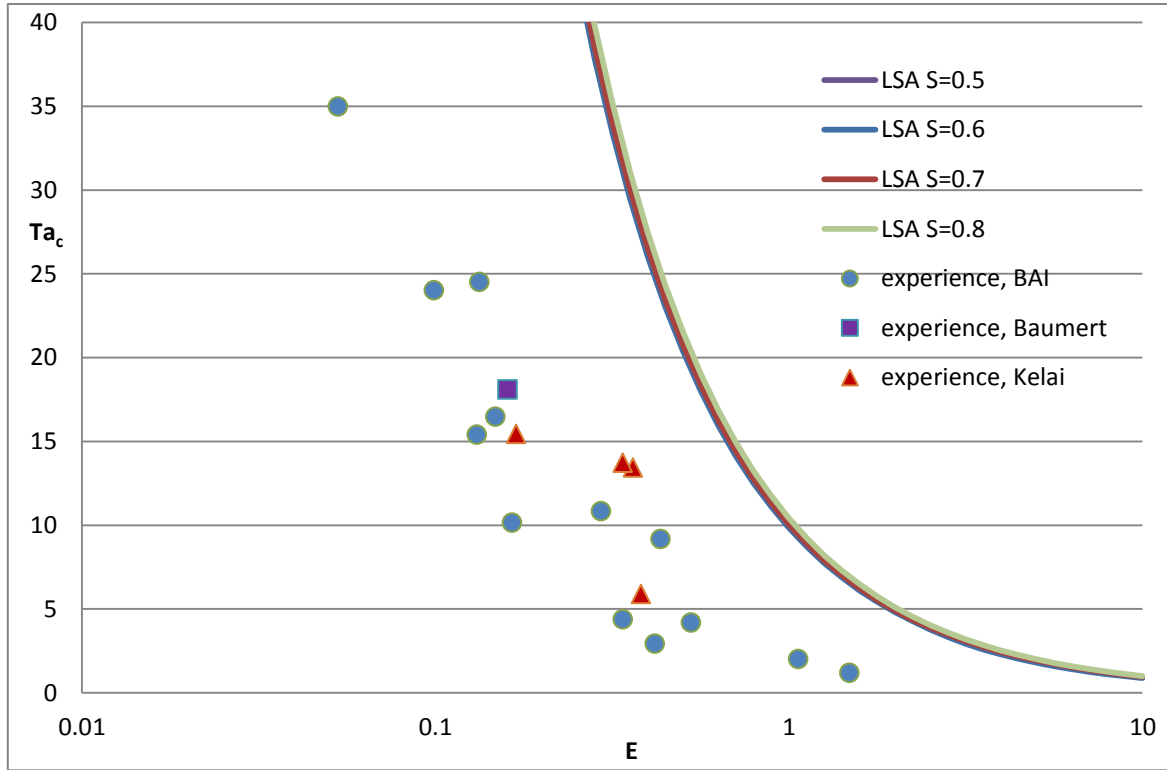


Figure 6.36: Critical values on regime of  $\mu = \infty$ . Continuous lines – LSA critical curves. Blue circle –our experiments. Red triangle – experiments of Kelai. Violet squire – experiment of Baumert.

### 6.3. Conclusion

In this chapter we have compared our LSA results and experimental results in the rotation regimes of  $\mu = 0$  and  $\mu = \infty$ . We found that they agree with each other qualitatively in almost all the cases and agree with each other quantitatively in some cases. In both regimes,  $Ta_c$  decreases with  $E$ , but we have observed theoretically and experimentally three different critical modes from small  $E$  to large  $E$ : Taylor vortex mode, Ribbons mode and Disordered vortices mode for  $\mu = 0$  regime, while for  $\mu = \infty$  regime, only one axisymmetric oscillatory mode was critical. The LSA critical curves of  $Ta_c(E)$  lie between the experimental points elasticity of which is defined by the molar mass relaxation time ( $E_m$ ) and the extensional relaxation time ( $E_e$ ) for  $\mu = 0$  regime while they lie exactly on the  $E_e$  defined experimental points for  $\mu = \infty$  regime. For the  $\mu = 0$  regime, the LSA critical curves are much closer to the  $E_e$  defined points than the others when the critical mode is disordered vortices mode. As the elasticity  $E$  indicates the elastic force of the fluid, we may conclude that the disordered vortices mode appears when the elastic force dominates the flow which corresponds to the cases of large  $E$  in  $\mu = 0$  regime and the  $\mu = \infty$  regime where the centrifugal force stabilizes the flow. The extensional relaxation time defined elasticity  $E_e$  is the best parameter that characterizes the elastic force. In the  $\mu = 0$  regime, the change of critical modes indicates that the dominant destabilizing force switches from centrifugal force to elastic force as the fluid elasticity  $E$  increases. We observe the Taylor vortices mode as in the Newtonian fluid at small  $E$  and disordered vortices mode which is the same as  $\mu = \infty$  regimes. So that the Ribbons mode can be considered as the critical mode in which the centrifugal force is comparable to the elastic force. Besides, we have found theoretically that in the  $\mu = 0$  regime the viscosity ratio  $S$  destabilizes the flow at small modified Weissenberg number  $K$  while it stabilizes the flow at large  $K$ .

# Chapter 7: Viscoelastic instability in Keplerian regime and the MRI analogy

The present chapter is devoted to the analogy between the viscoelastic instability (VEI) in the Couette-Taylor system and the magnetorotational instability (MRI) responsible of angular momentum transportation in accretion disks in Astrophysics. After the LSA and experimental results in the Keplerian regime, we study the anti-Keplerian regime in order to discriminate the modes that are not MRI-analogs.

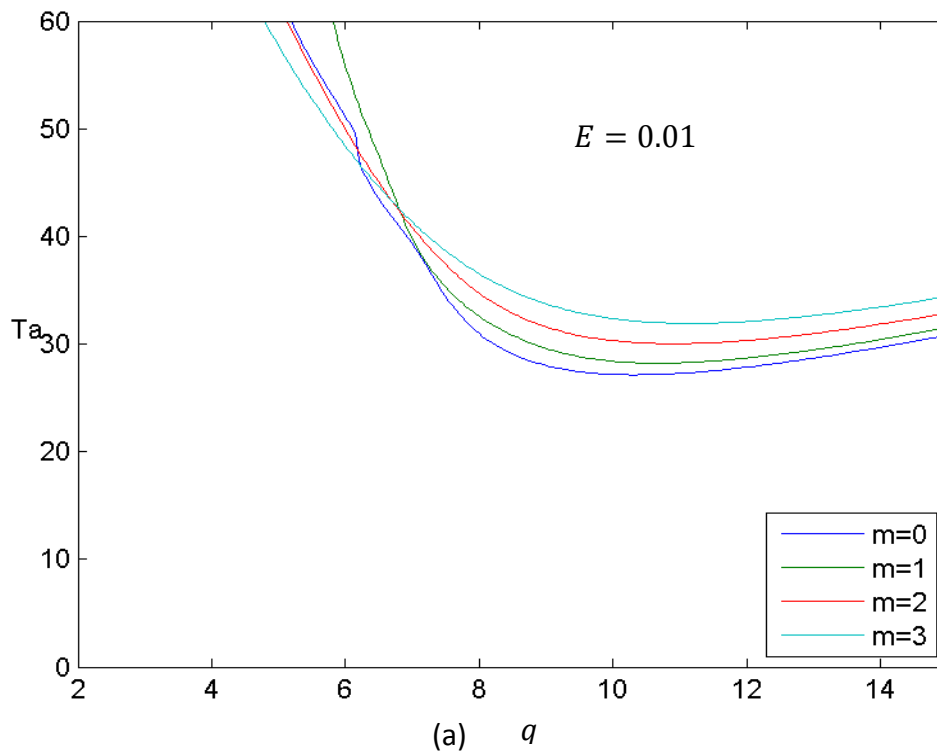
## 7.1. The Keplerian regime

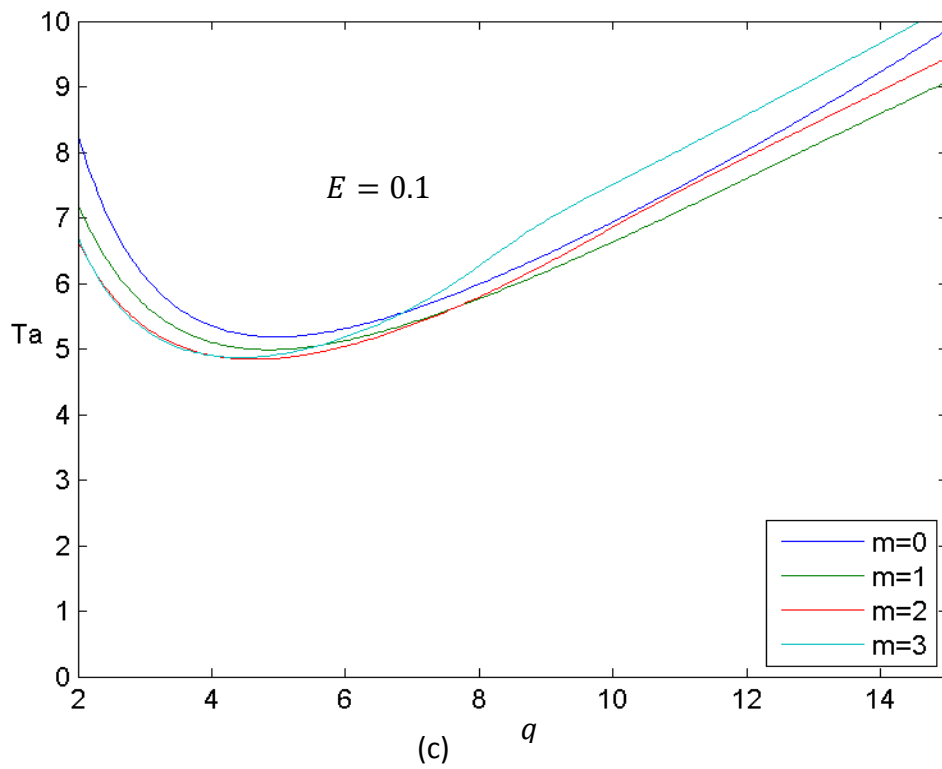
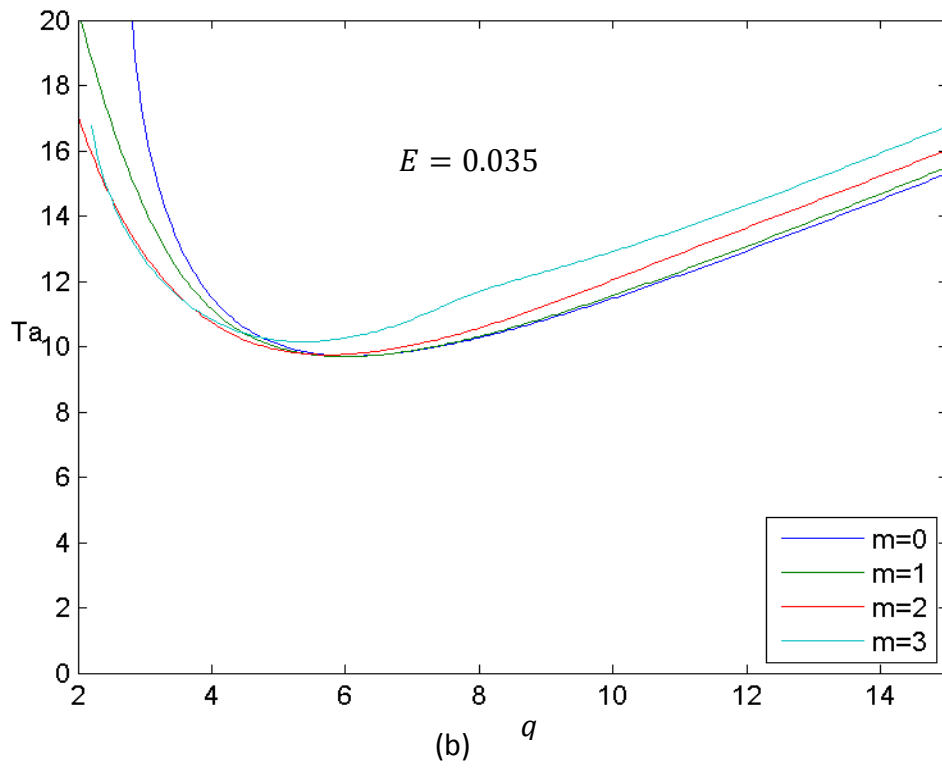
According to Rayleigh stability criterion discussed in chapter 4, the Newtonian Couette flow in the Keplerian rotation regime ( $\mu = \eta^{3/2}$ ) is stable, while the viscoelastic Couette flow can be destabilized, which yields to elasto-rotational instability modes. Our study will focus on the Keplerian regime in annular geometry with radius ratio  $\eta = 0.8$  corresponding to the experimental configuration i.e.  $\mu = 0.716$ .

### 7.1.1. LSA results

#### a. Marginal stability curves

In figure 7.1, we have plotted the marginal stability curves  $Ta(q)$  for  $S = 0.6$  and four different values of  $E = \{0.01, 0.028, 0.1, 1.0\}$ .





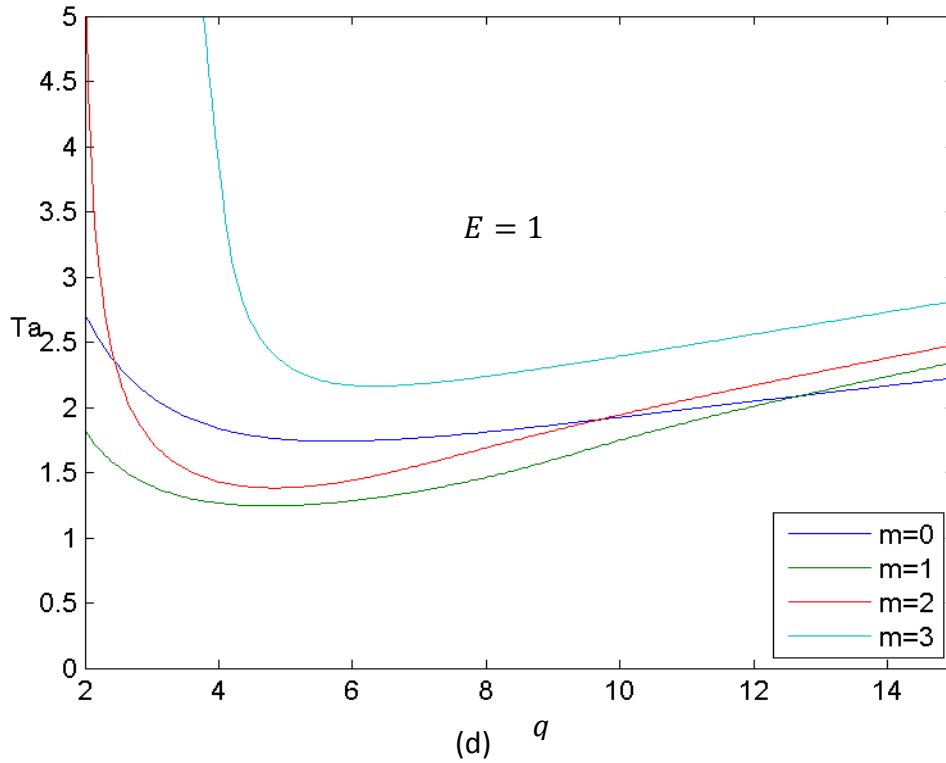


Figure 7.1: Marginal curves  $Ta(q)$  for different  $m$  at chosen  $E$ . (a)  $E = 0.01$  (b)  $E = 0.036$ , (c)  $E = 0.1$ , (d)  $E = 1$ .

We can see from figure 7.1 (a) that for small  $E$  the  $Ta_c$  of  $m = 0$  is clearly separated from the other  $m$ , so that the axisymmetric mode  $m = 0$  dominates. But for larger  $E$  figure 7.1 (b) (c) the  $Ta_c$  of several  $m$  are close to each other, so that several modes may become critical and interact with each other. For large  $E$  (figure 7.1 (d)), the bottom of the marginal curve is so flat that several modes of different  $q$  are critical and may interact with each other.

### **b. Variation of the critical parameters with $E$**

Figure 7.2 illustrates the variation of the critical Taylor number  $Ta_c$  with  $E$  for  $S = 0.6$  with different azimuthal wave number  $m \in \{0, 1, 2, 3\}$ . The critical values  $Ta_c$  decrease with  $E$  and the curves for different  $m$  are close to each other. In the vanishing elasticity solution, the threshold tends to infinity in agreement with the stability of the Newtonian flow in the Keplerian rotation regime. The decrease of the critical value  $Ta_c$  with the elasticity of the polymer solution means that the elasticity plays a destabilizing role in the Keplerian regime.

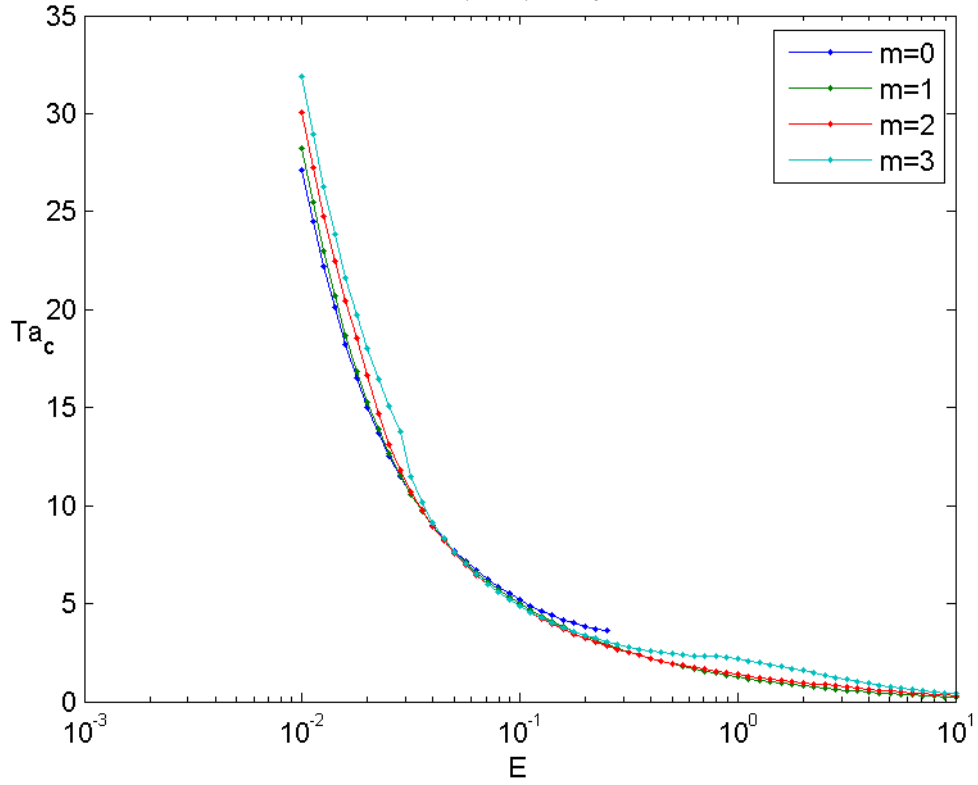


Figure 7.2: Critical curves,  $Ta_c(E)$  for different  $m$ ,  $S = 0.6$  on Keplerian regime.

For each value of the elasticity  $E$ , we plot the lowest value of  $Ta_c$  among  $m \in (0, 1, 2, 3)$ . The resulting critical curve  $Ta_c(E)$  determines the instability threshold and it is plotted in figure 7.3 together with critical  $m_c$ , and the color map of vorticity of the critical modes. The variations of the critical angular frequency  $\omega_c$  and axial wave number  $q_c$  with  $E$  are plotted in figure 7.4 and figure 7.5. The axisymmetric mode is stationary as  $\omega = 0$  and the corresponding vortices are flattened as  $q_c > 2\pi$  i.e. the corresponding wavelength  $\lambda_c < d$  while the non-axisymmetric modes are non-stationary as  $\omega_c \neq 0$ .

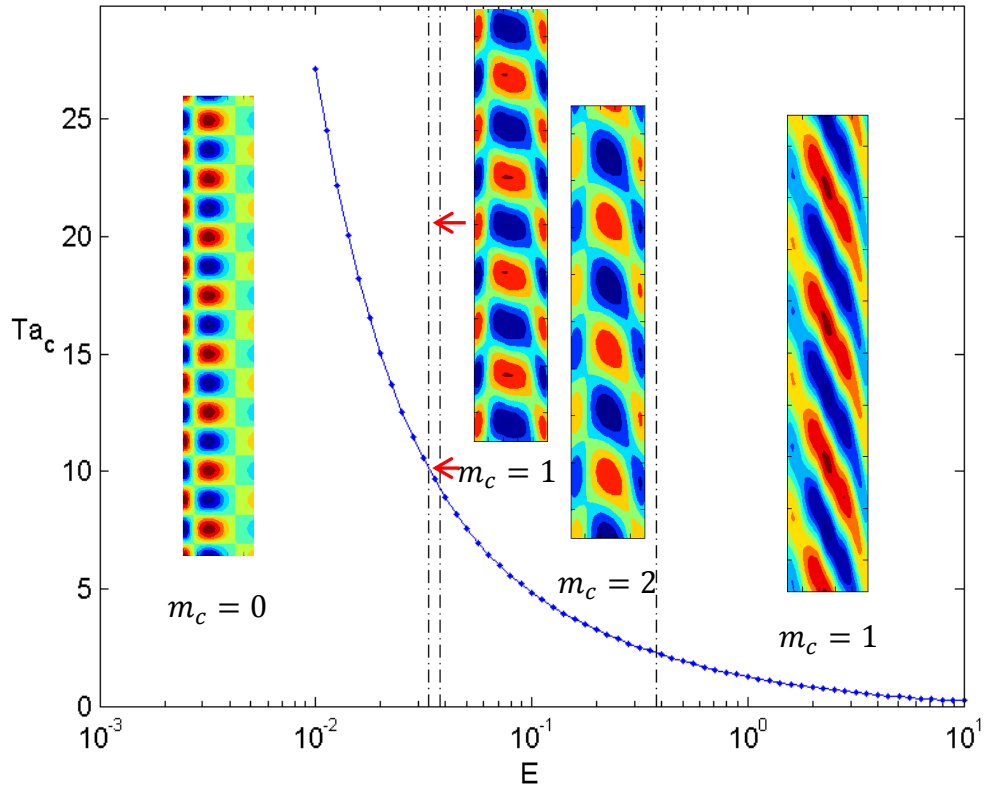


Figure 7.3: Variation of the critical curve  $Ta_c(E)$  for  $S = 0.6$  on Keplerian regime. Black dashed lines separate critical azimuthal wave number  $m_c$ . Color maps – vorticity  $\omega_\theta$  in the gap plane  $(r, z)$ , where red represents positive values and blue represents negative values .

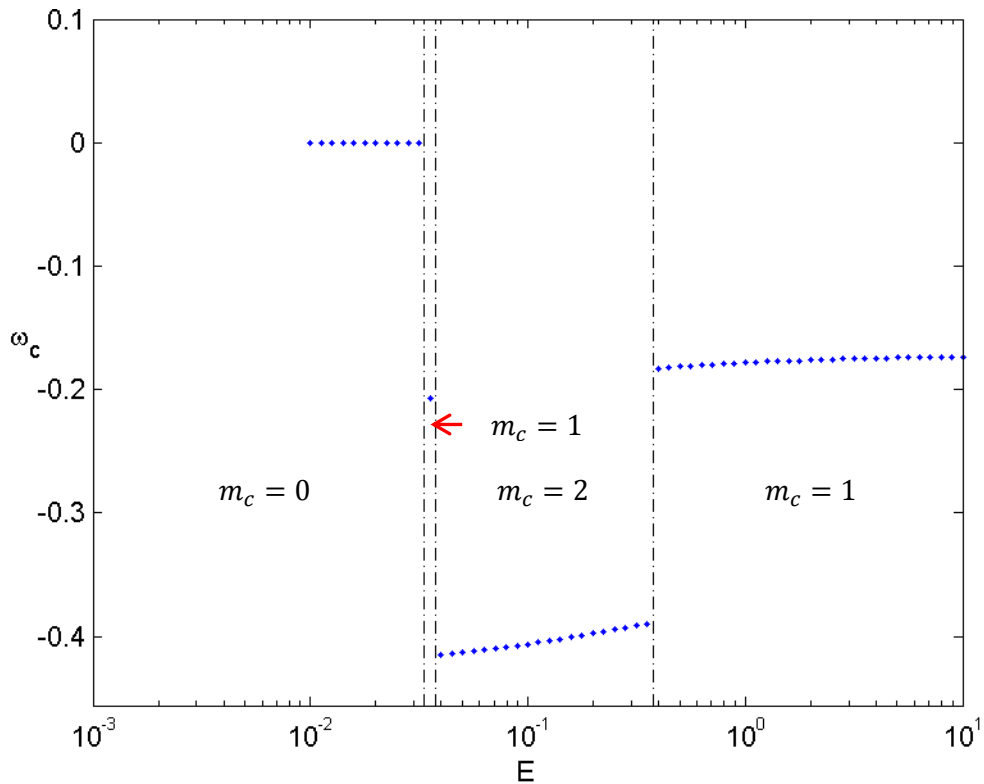


Figure 7.4: Variation of the critical frequency of the critical modes with  $E$  and  $S = 0.6$  in Keplerian regime. Dashed vertical lines separate different  $m_c$ .

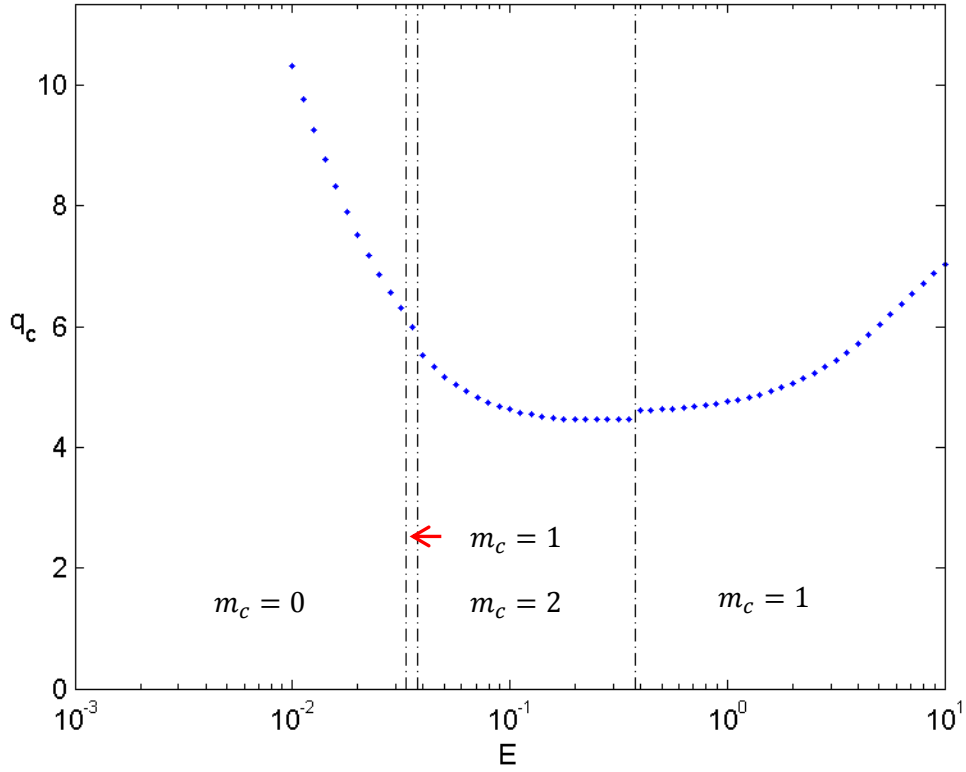


Figure 7.5: Variation of the critical axial wavenumber  $q_c$  of the critical modes with  $E$  for  $S = 0.6$  on Keplerian regime. Dashed vertical lines separate different  $m_c$ .

For each polymer solution (i.e. for a given value of  $S$ ), there exist codimension-two points in the plane  $(E, Ta_c)$  where two modes with different spatio-temporal properties can coexist. For  $S = 0.6$ , we have 3 codimension-two points whose properties are given in the Table :

$E$	$Ta_c$	$q_c$	$m_c$	$\omega_c$
0.034	10.1	6.31	0	0
		5.99	1	-0.21
0.038	9.3	5.99	1	-0.21
		5.52	2	-0.41
0.377	2.28	4.47	2	-0.39
		4.62	1	-0.18

Table 7.1: Codimension-two points for  $S = 0.6$  in Keplerian regime

Thus, for a rotating flow in the Keplerian regime of a solution with  $S = 0.6$ , the critical mode depends on the solution elasticity: it is axisymmetric and stationary at small  $E$ , while the critical mode is composed by the interaction of several non-axisymmetric modes at large  $E$ . This property is also validated for other  $S$ . To provide more details about different critical modes, we present from figure 7.6 to 7.9 the gap view of the features of the critical modes including the velocity fields, the vorticity, the variation of pressure  $N_1$  and  $N_2$ . The perturbations of the  $N_1$  and  $N_2$  are comparable for the stationary axisymmetric modes and the disordered wave modes; while for the purely elastic mode, the  $N_2$  is negligible compared to the perturbation of the  $N_1$ .

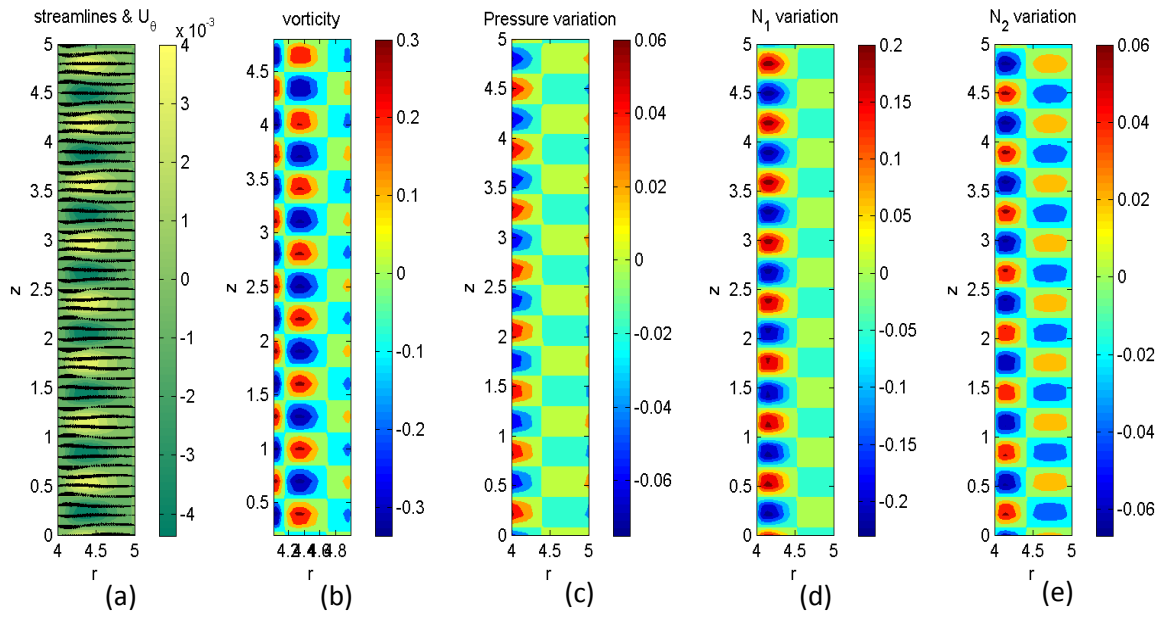


Figure 7.6: Critical mode for  $S = 0.6$ ,  $E = 0.01$ ,  $Ta_c = 273$  in Keplerian regime, with  $m = 0$ ,  $q_c = 10.3$ ,  $\omega_c = 0$ . (a) Black arrows represent the velocity field in  $(r, z)$  direction while the colors represent the azimuthal velocity  $V$  (b) the vorticity  $\omega_\theta$  (c) the pressure variation (d) the  $N_1$  variation © the  $N_2$  variation. Color maps of (b, c, d, e) represent the relative amplitude.

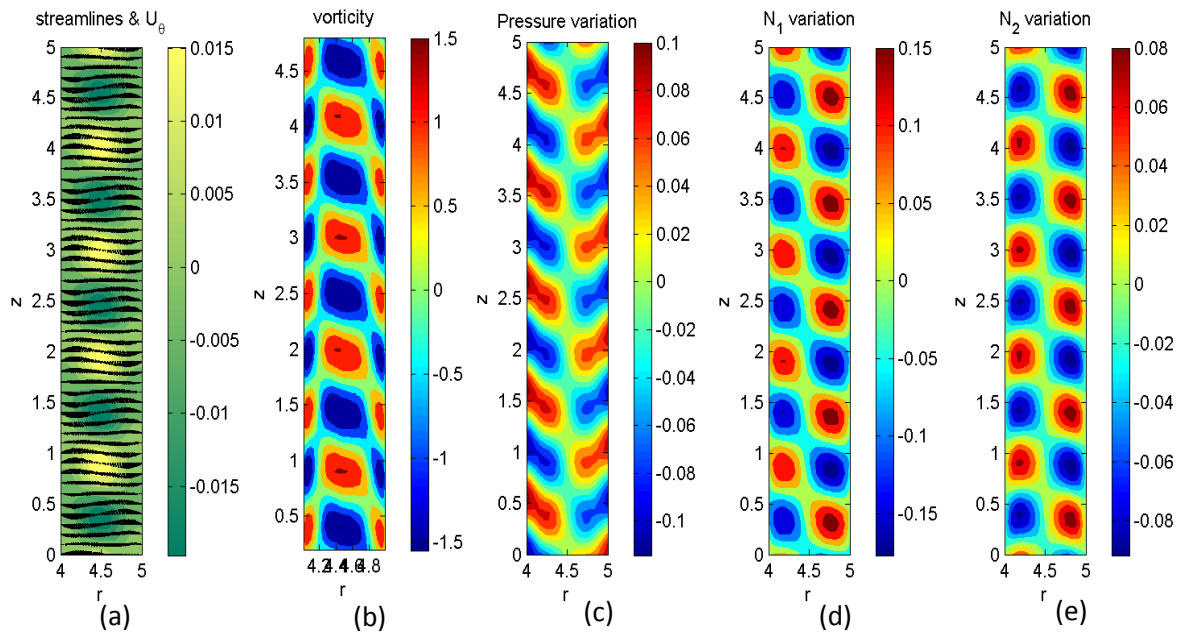


Figure 7.7: Critical mode for  $S = 0.6$ ,  $E = 0.035$ ,  $Ta_c = 97.4$  in Keplerian regime, with  $m = 1$ ,  $q_c = 5.98$ ,  $\omega_c = -0.207$ . (a) Black arrows represent the velocity field in  $(r, z)$  direction while the colors represent the azimuthal velocity  $V$  (b) the vorticity  $\omega_\theta$  (c) the pressure variation (d) the  $N_1$  variation © the  $N_2$  variation. Color maps of (b, c, d, e) represent the relative amplitude.

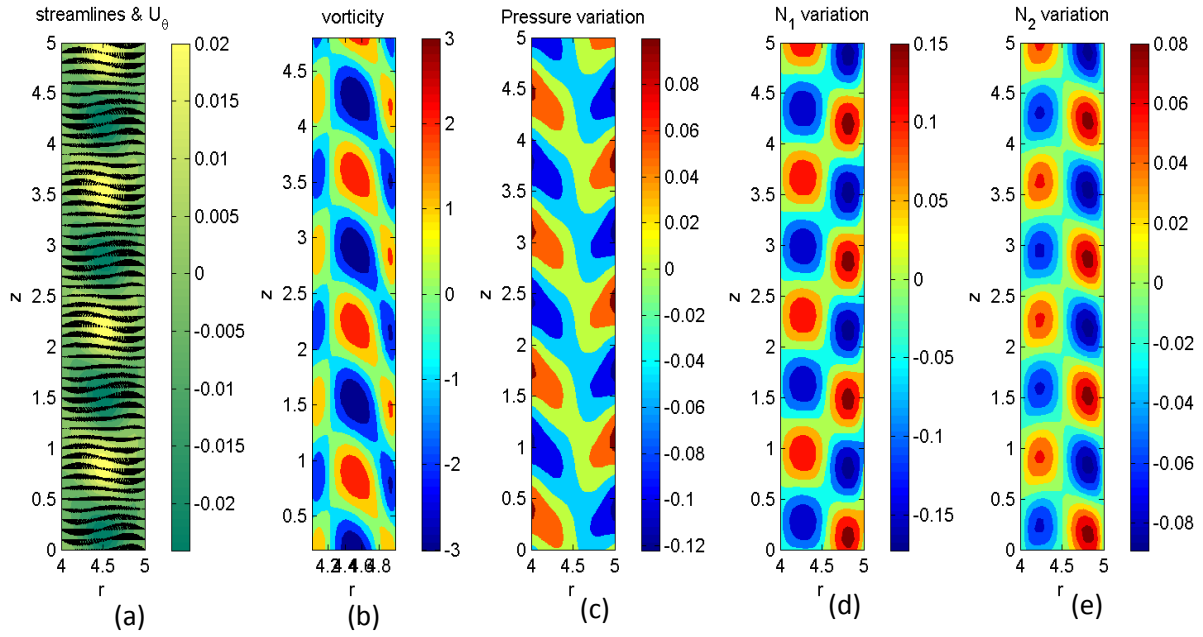


Figure 7.8: Critical mode for  $S = 0.6$ ,  $E = 0.1$ ,  $Ta_c = 48.6$  in Keplerian regime, with  $m = 2$ ,  $q_c = 4.62$ ,  $\omega_c = -0.406$ . (a) Black arrows represent the velocity field in  $(r, z)$  direction while the colors represent the azimuthal velocity  $V$  (b) the vorticity  $\omega_\theta$  (c) the pressure variation (d) the  $N_1$  variation © the  $N_2$  variation. Color maps of (b, c, d, e) represent the relative amplitude.

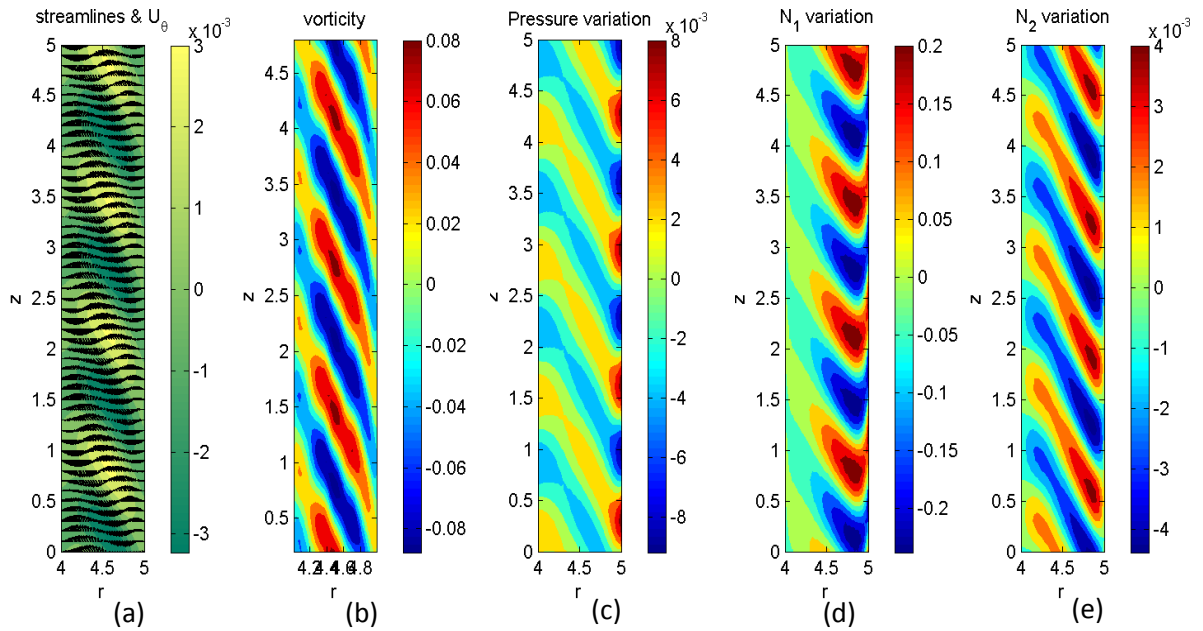


Figure 7.9: Critical mode for  $S = 0.6$ ,  $E = 1$ ,  $Ta_c = 12.5$  in Keplerian regime, with  $m = 1$ ,  $q_c = 4.75$ ,  $\omega_c = -0.178$ . (a) Black arrows represent the velocity field in  $(r, z)$  direction while the colors represent the azimuthal velocity  $V$  (b) the vorticity  $\omega_\theta$  (c) the pressure variation (d) the  $N_1$  variation © the  $N_2$  variation. Color maps of (b, c, d, e) represent the relative amplitude.

### c. Effect of the viscosity ratio on the critical states

The variation of the threshold  $Ta_c(E)$  with  $S$  is plotted in figure 7.10. For  $E < 1$ , the curves are distinct and for each value of  $E$ , solution with large  $S$  are more unstable. For  $E > 1$ , all curves converge into one curve, the threshold becomes independent of  $S$  and tends to a small value of  $Ta_c = 0$ . This suggests that the instability mode has changed: for  $E < 1$ , both the rotation and the elasticity intervene to generate the elasto-rotational instability (ERI) while for  $E > 1$ , the instability is induced by the elasticity as predicted by the generalized Rayleigh criterion. The latter is called purely elastic instability (PEI).

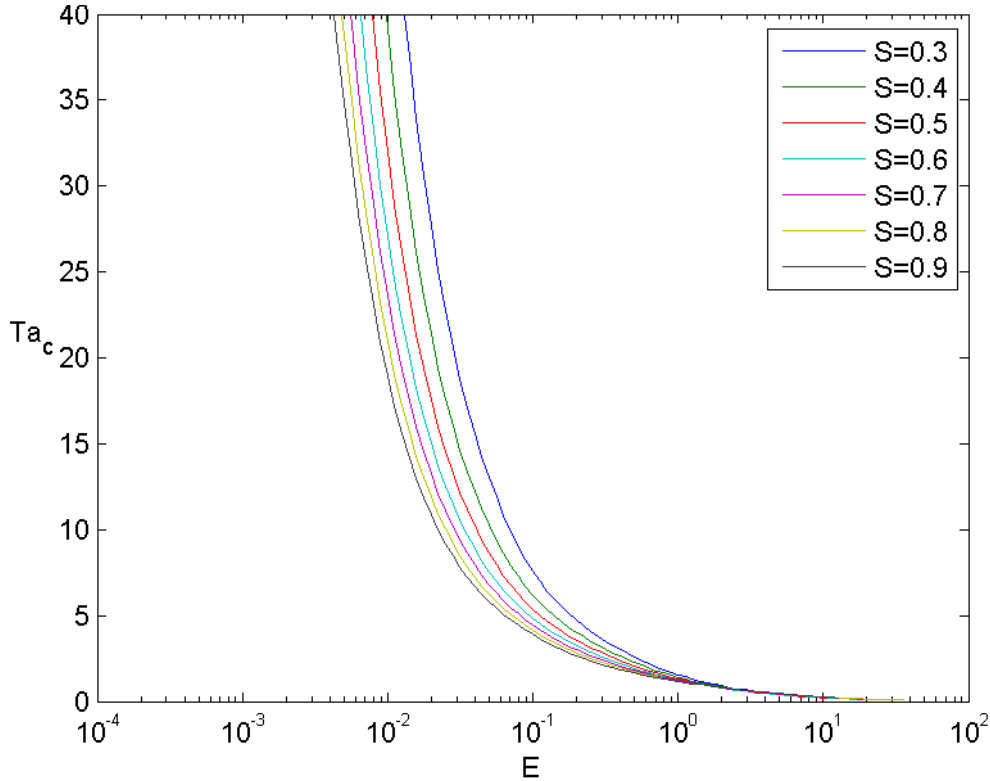


Figure 7.10: Critical curves  $Ta_c(E)$  for different  $S$  in Keplerian regime.

The variation of the critical modified Weissenberg number  $K_c = \sqrt{2Sd/(a+b)} Wi_c$  (see [Groisman1998]) with the solution elasticity  $E$  is plotted in figure 7.11 and yields a cross point of all curves with different values of  $S$  at  $E^* = 0.27, K^* = 0.45$ . For  $E < E^*$ , the viscosity ratio is destabilizing while for  $E > E^*$ , it is stabilizing.

When we plot the critical Taylor number  $Ta_c$  versus  $ES$  instead of  $E$ , all curves of different  $S$  converge into one curve (figure 7.12). It means that for the Keplerian regime, the polymer viscosity  $ES$  is a better control parameter than the solution elasticity  $E$ . The elasto-rotational Rayleigh line separates the unstable area into the elasto-rotational unstable zone (on the left) and purely elastic unstable zone (on the right). The elasto-rotational unstable zone is then separated by different critical modes: stationary axisymmetric mode for small  $ES$  and oscillatory non-axisymmetric mode for large  $ES$ .

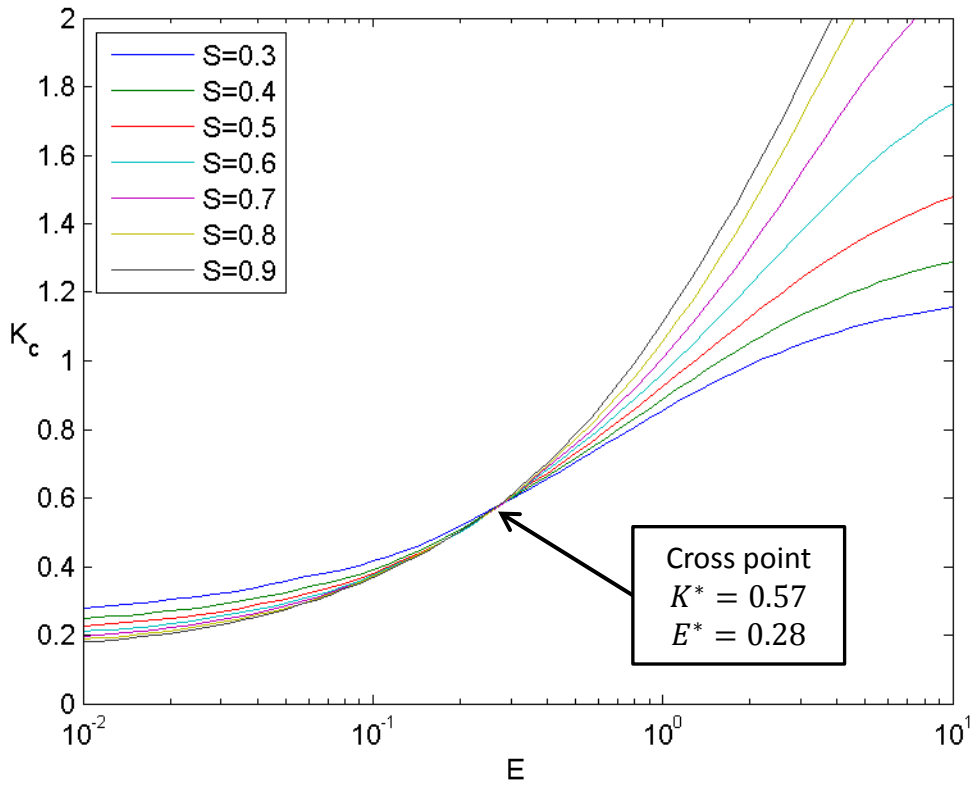


Figure 7.11: Critical curves  $K_c(E)$  for different  $S$  in Keplerian regime.

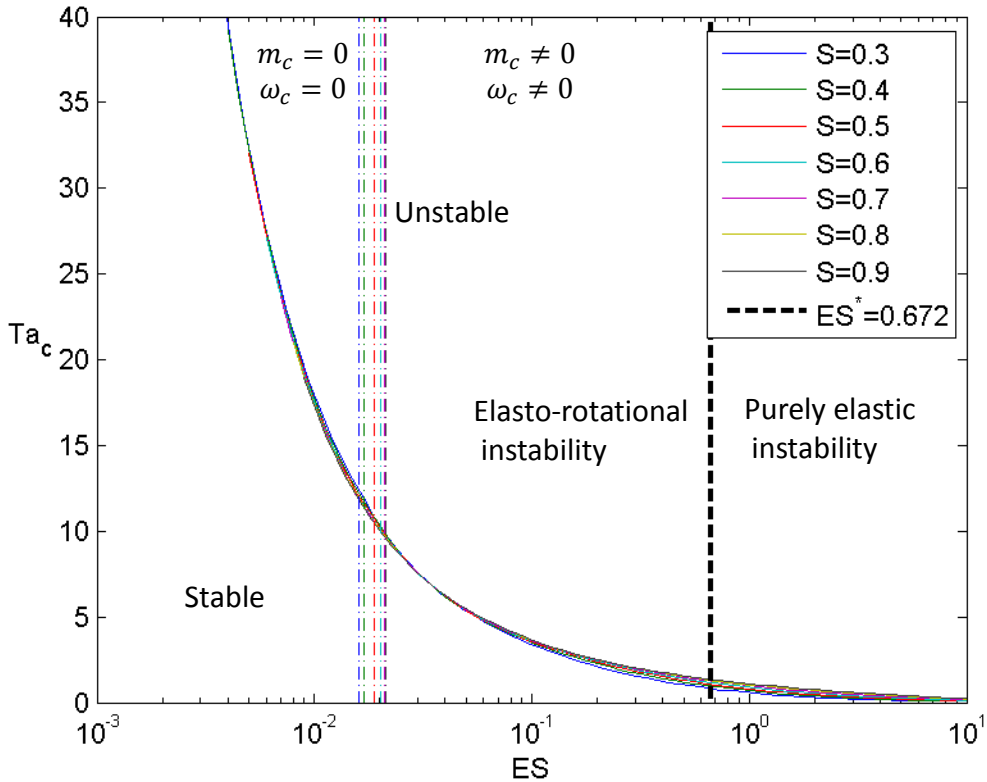


Figure 7.12: Critical curves,  $Ta_c(ES)$  for different  $S$ : the black dashed line is the elasto-rotational Rayleigh line  $ES^* = 0.672$  that separates the potential stable from the potentially unstable zone to the elasticity-induced perturbations. The colored dashed lines separate the stationary axisymmetric mode and oscillatory non-axisymmetric mode.

Figure 7.13 presents the critical curves of  $Ta_c(K_c)$  which shows that all curves cross at one point of  $K_c^* = 0.86$ ,  $Ta_c^* = 1.5$ . This figure shows in a clear manner that the polymer viscosity plays two opposite roles: the polymer viscosity destabilizes the flow together with the elasticity when  $K_c < K_c^*$  while when  $K_c > K_c^*$  it stabilizes the flow and the elasticity remains the sole destabilizing factor. In particular, purely elastic instability mode is suppressed by the increase of the viscosity ratio  $S$ . From practical point of view, the best solvents to realize purely elastic instability are those with large viscosity while those appropriate to realize elasto-rotational instability are those with large values of  $S$ .

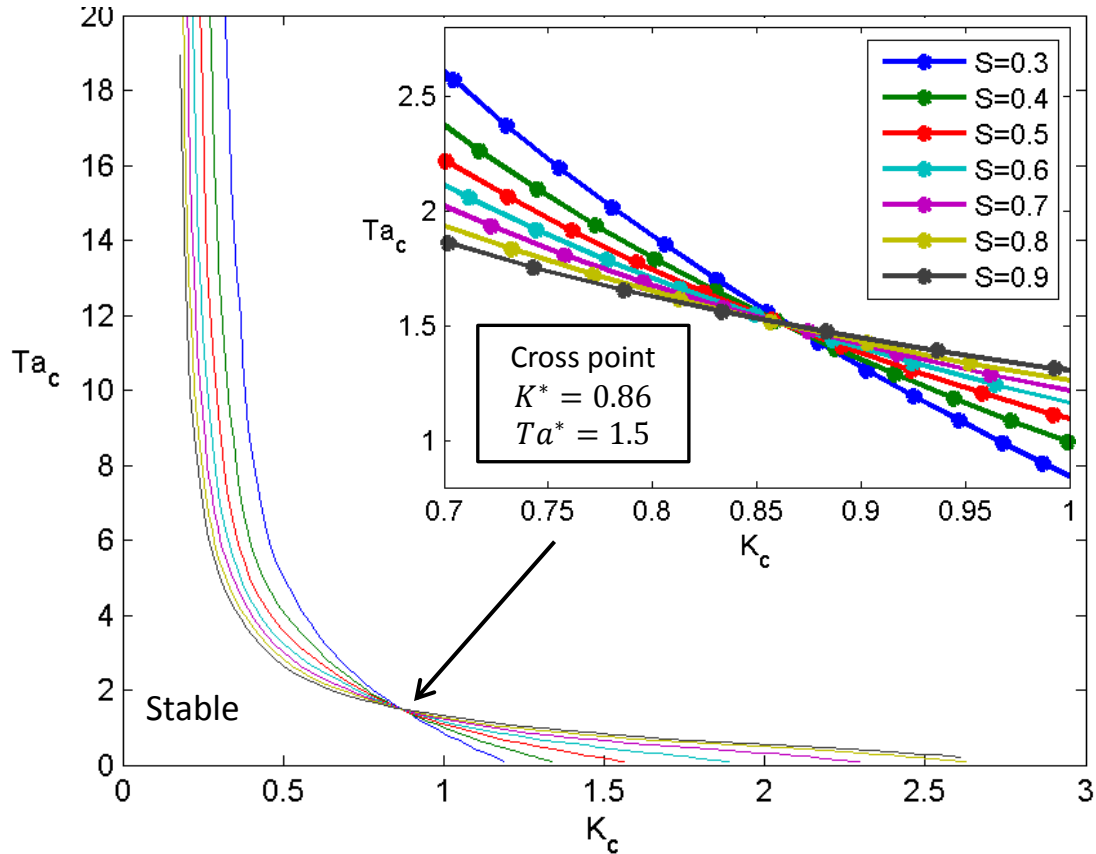


Figure 7.13: Critical curves  $Ta_c(K_c)$  for different  $S$  in Keplerian regime.

In the intersection point, the viscosity ratio  $S$  has no influence on the critical parameter  $Ta_c$ . The intersection occurs between curves corresponding to oscillatory states (waves). The point  $(K^*, Ta^*)$  corresponds to values of  $ES \in [0.32, 0.48]$  for  $S \in [0.3, 0.8]$  well below the value  $ES^* = 0.672$ . According to elasto-rotational Rayleigh criterion, the modes observed before the intersection point are due to the combined destabilizing effect from the rotation and the elasticity and are called elasto-rotational instability. The modes observed after the intersection point are destabilized only by the elasticity and can be attributed to purely elastic instability.

Figure 7.13 indicates that the modified Weissenberg number  $K$  contains some meaningful information for the viscoelastic instability in the Keplerian regime. This suggests to link it to the elastic number  $E$ .

As the  $Re$  and  $Wi$  are widely used as the control parameters of the viscoelastic instability in the Couette-Taylor system, we plot in figure 7.14 the critical curves in the plane  $(Wi, Re)$  for different  $S$ . Note that in the LSA calculation the elasticity is varied so that  $Wi$  is denoted as  $Wi_c$  as it

is deduced by  $Wi_c = E \cdot Re_c$ . We observe that when  $Wi_c$  decrease the  $Re_c$  increase and the critical curves  $Re_c(Wi_c)$  will never cross the vertical axis. The threshold  $Re_c$  decreases with  $Wi_c$ , and the critical curves cross the horizontal axis of  $Re_c = 0$  at certain  $Wi_0$ , corresponding to the onset of the purely elastic instability which will be discussed later. The role of polymer viscosity is inverted (from destabilization to stabilization) for small and large values of  $Wi_c$  as the critical curves intersect each other as  $Wi_c$  increases.

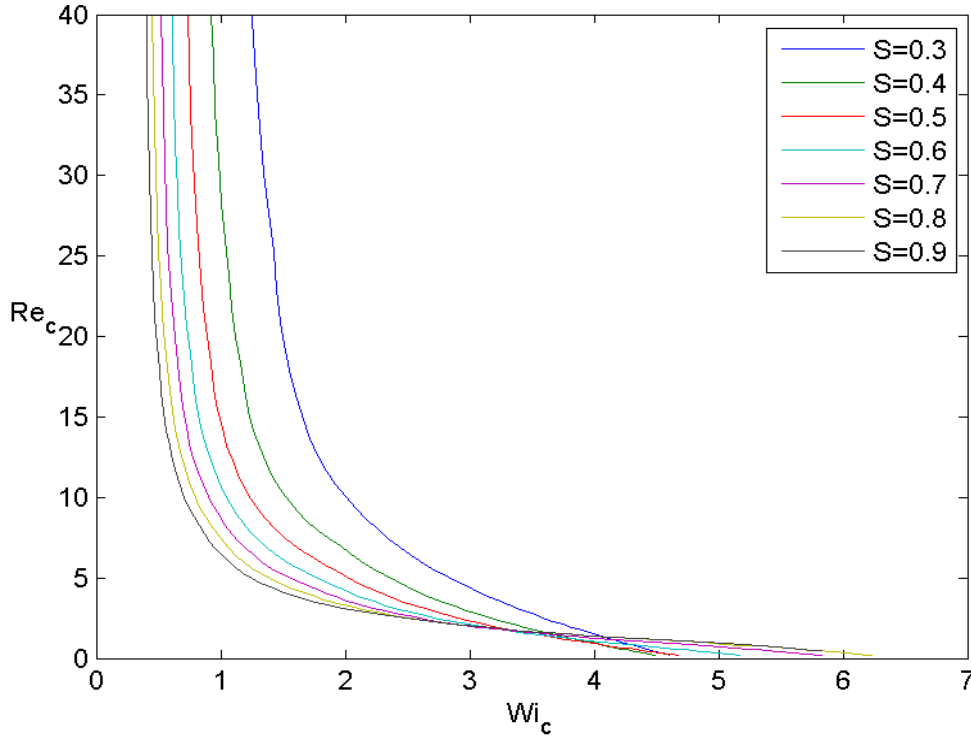


Figure 7.14: Critical curves,  $Re_c(Wi_c)$  for different  $S$  in Keplerian regime.

### 7.1.2. Experimental results

The experiments were conducted by increasing the rotation velocity of the cylinders in the Keplerian ratio  $\mu = \eta^{3/2} = 0.716$  step by step and then waiting at least 20 min on each step. The inner cylinder and the outer cylinder share the same acceleration rate to avoid spurious instabilities. The increase of the rotation velocity was done until the pattern was formed in the flow. We waited about 20 min before recording the flow. The higher instability modes were not investigated in this experiment because we were interested in the detection of the onset and the nature of the flow patterns. A ramping up and down was also done to check the critical nature of the transition (supercritical or subcritical).

#### a. Flow patterns

Different types of flow patterns were observed in the Keplerian rotation regime when the rotation velocity of the cylinders exceeded a critical value, which depends on the elasticity and viscosity ratio of the flow solution. As the Newtonian flow is stable in the Keplerian regime, we were guided by the results of the linear stability analysis. For, we choose a solution with a given elasticity  $E$  and viscosity ratio  $S$ , this allowed to minimize the search of the critical states. The observed flow patterns show three different types: axisymmetric stationary vortices, disordered waves, disordered waves with solitary vortices and purely elastic mode.

### Axisymmetric stationary vortices

For small values of the elasticity number, the critical mode appears in form of stationary axisymmetric vortices. Their size is smaller than the gap width; in fact their dimensionless wavenumber  $q_c$  varies between 6 and 10 for the solutions we have worked with. Figure 7.15 is an illustration of this mode for a solution with  $E_m = 0.017$ ,  $S = 0.81$ . The spectra of the space-time diagram (figure 7.15-c) are given in figure 7.16. The peak of the dominant wavenumber is evidenced in the space spectrum (figure 7.16-a), it yields  $\lambda_c = 0.96 \text{ cm} < 2d = 2 \text{ cm}$ . The frequency peaks in the temporal spectrum (figure 7.16-b) correspond to either the cylinder rotation frequencies or their combinations.

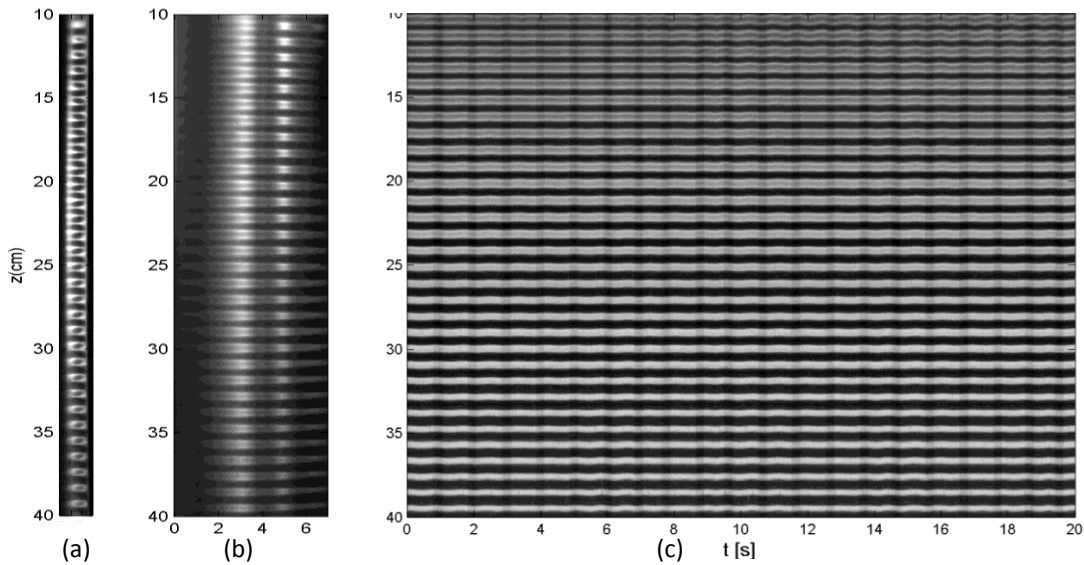


Figure 7.15: Flow patterns and space-time diagram on Keplerian regime at  $Ta_c = 8.50$ ,  $E_m = 0.017$ ,  $S = 0.81$ . (a) Gap view by laser sheet, (b) Front view, (c) Space-time diagram. The space-time diagram seems wavy, however all the wavy frequencies are related to the rotational cylinders.

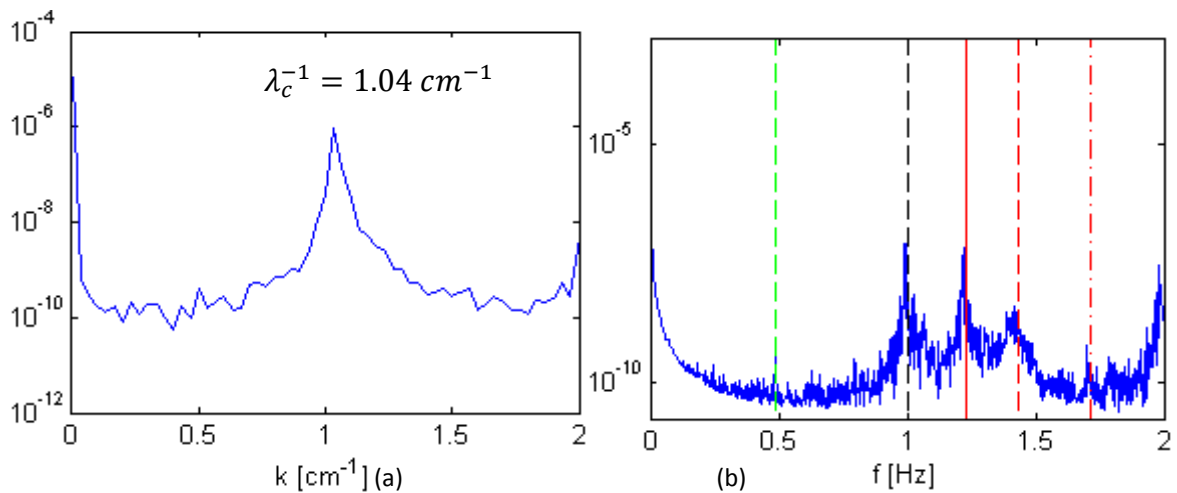


Figure 7.16: Fourier spectra of the space-time diagram on Keplerian regime at  $Ta_c = 8.50$ ,  $E_m = 0.017$ ,  $S = 0.81$ . (a) space spectrum, (b) time spectrum. Red lines – rotation frequencies of the inner and outer cylinder and the mean rotation of them. Green dashed line – a combination of frequencies of the cylinders ( $2\Omega_o - \Omega_i$ ). Black dashed line – flicker frequency of the spot light.

The stationary axisymmetric vortices observed in the Keplerian rotation regime are distinct from the Taylor vortices that were observed in the case of  $\mu = 0$  for small values of the elasticity. In fact, these new vortices are flatten (their size  $\lambda_c/2 < d$ ) while the Taylor vortices in  $\mu = 0$  regime have a circular shape ( $\lambda_c/2 \approx d$ ). The flattening of these vortices ( $f = (d - \lambda_c/2)/d$ ) increases as  $ES$  decreases. A comparison of the stationary axisymmetric vortices observed in the Keplerian rotation regime and Taylor vortices observed in the case of  $\mu = 0$  is given in the figure 7.17, where the front view and the longtime space-time diagram are compared.

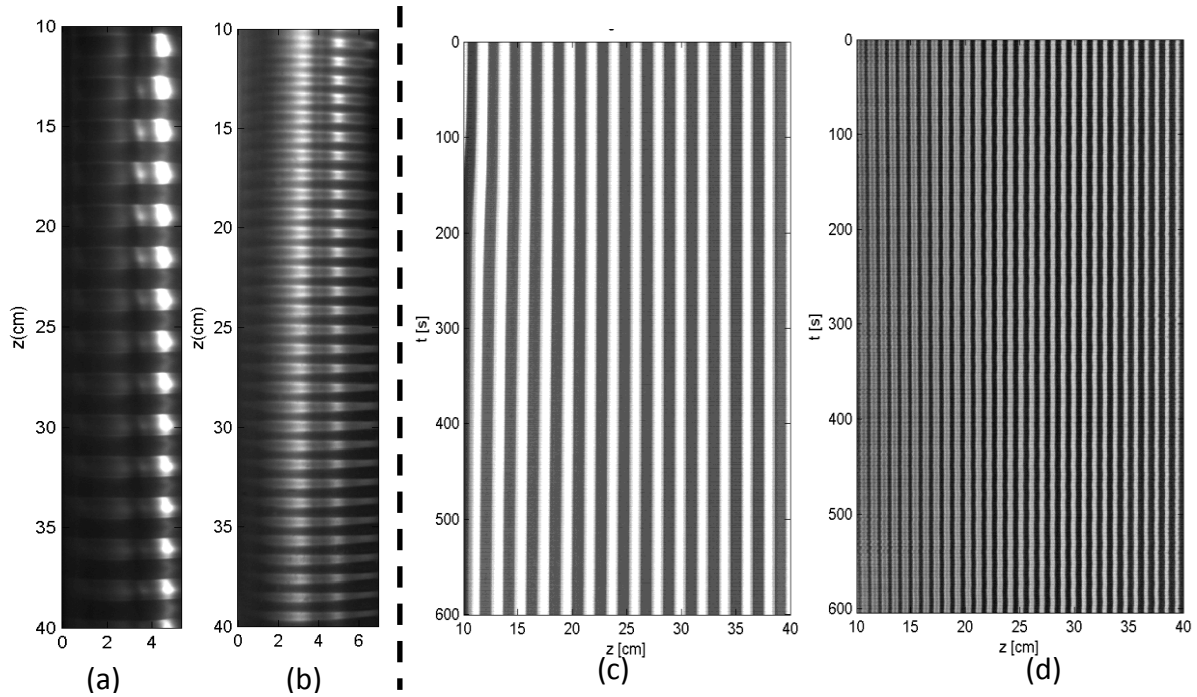


Figure 7.17: Comparison between the critical modes: (a) (b) Front view of the Taylor Vortex mode (a) and the Stationary and Axisymmetric mode (b); (c) (d) space-time diagram of 10 mins of the Taylor Vortex mode (c) and the Stationary and Axisymmetric mode (d).

#### Disordered waves mode

For intermediate values of  $ES$  i.e.  $0.03 < ES < 0.1$ , the critical mode appears in form of the disordered waves (figure 7.18). These waves are formed by counter propagating waves. In fact, they are generated from the endplates and they propagate until they reach each other in the central part of the flow system. As long as the waves have not met in the central part, they have a single frequency and wavenumber. But as soon as they meet, they interact strongly and the nonlinear effects dominate and generate the Disordered Waves.

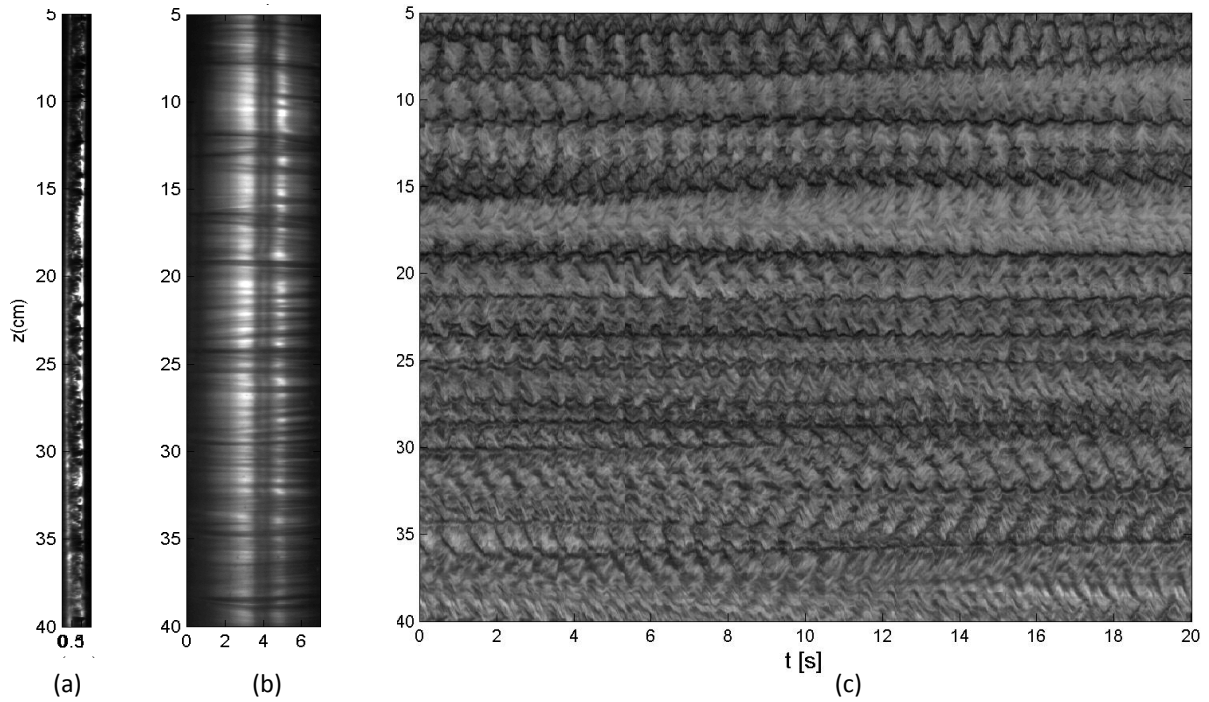


Figure 7.18: Flow patterns and space-time diagram of the Disordered Waves mode on Keplerian regime at  $Ta_c = 2.86$ ,  $E_m = 0.13$ ,  $S = 0.61$ . (a) Gap view by laser sheet (b) Front view (c) Space-time diagram.

The Fourier spectrum presented in figure 7.19 (b) indicates that the repeat of certain flow pattern in figure 7.18 (c) has the same frequency of the rotation of the outer cylinder because it is the only peak beside the spot light flicker. The small hill in figure 7.19 (b) at small frequency is related to the difference between the mean frequency and the outer cylinder rotation ( $\Omega_o - \langle \omega \rangle$ ). In the other cases, the main peak may also be the mean frequency  $\langle \omega \rangle$  of the two cylinders. These kinds of peaks that are related to the rotation of the cylinders are not related to the flow patterns.

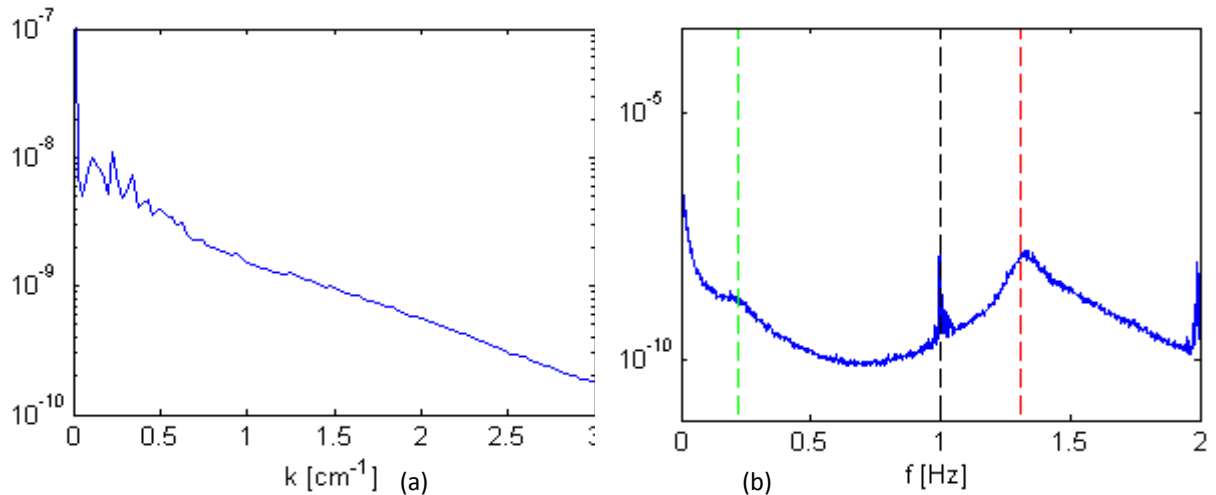


Figure 7.19: Fourier spectrums of the space-time diagram on Keplerian regime at  $Ta_c = 2.86$ ,  $E_m = 0.13$ ,  $S = 0.61$  (a) space spectrum (b) time spectrum. Red dashed line – the frequency of the inner cylinder. Black dashed line – the flicker frequency of the spot light. Green dashed line – the frequency difference of  $\Omega_o - \langle \omega \rangle$ .

Then we look into the space-time diagram and its spectra at the transition. The instability appears at the bottom of the cell and propagates very slowly to the top end. We present in figure 7.20 (a) the space-time diagram of the bottom part ( $z \in [30, 45](cm)$ ), from which we can see waves on the border of the stable and unstable zone. The corresponding space and time Fourier spectra (figure 7.20 (b)(c)) exhibit clear pics of the critical wave number  $k_c$  and the critical frequency  $f_c$ .

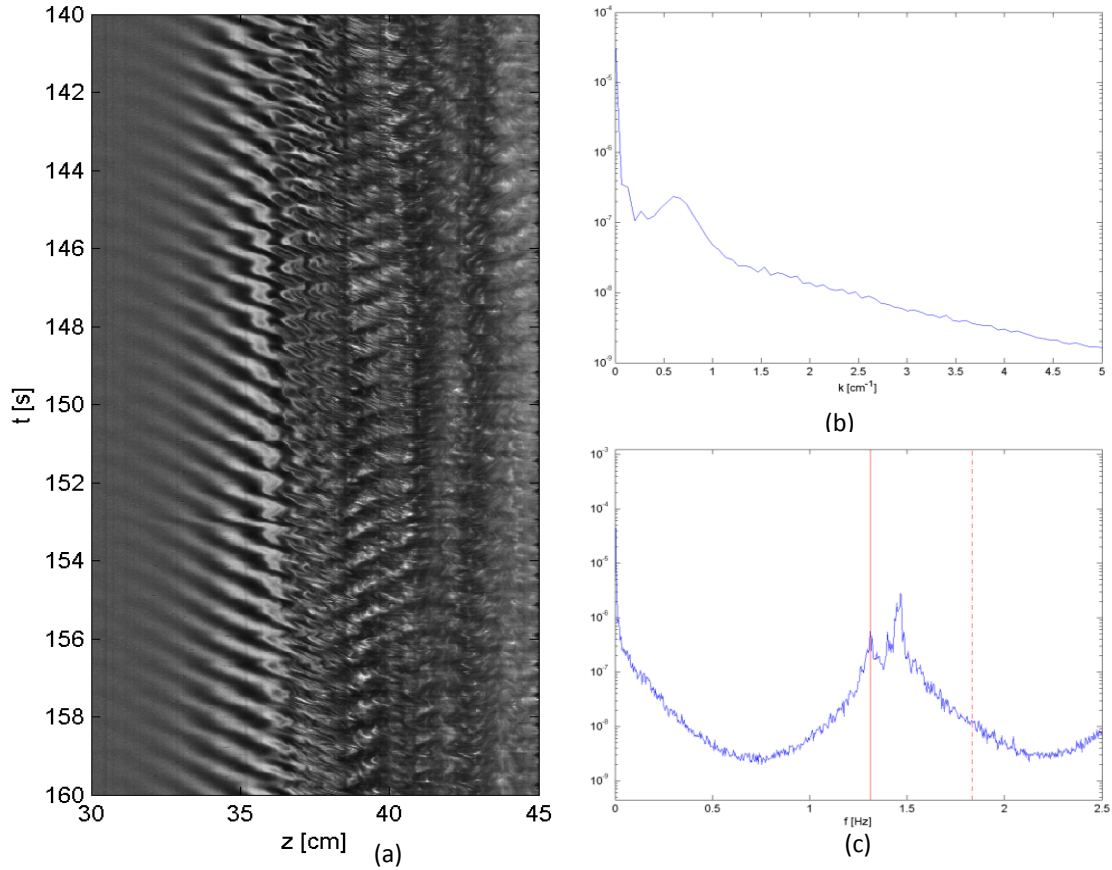


Figure 7.20: Space-time diagram and Fourier spectra of the Disordered Waves mode on Keplerian regime at  $Ta_c = 2.86$ ,  $E_m = 0.13$ ,  $S = 0.61$  for a wave generated near the bottom endplate. (a) Space-time diagram (b) space spectrum (c) time spectrum. Red solid line – outer cylinder rotation frequency. Red dashed line – inner cylinder rotation frequency.

We have demodulated the space-time diagram at the transition. A zoom in space-time diagram of 20s and the demodulated waves, show that the  $k_c$  and  $f_c$  correspond to the waves on the edge of the unstable zone. The zoom in space-time diagram and the demodulated waves are presented in figure 7.21.

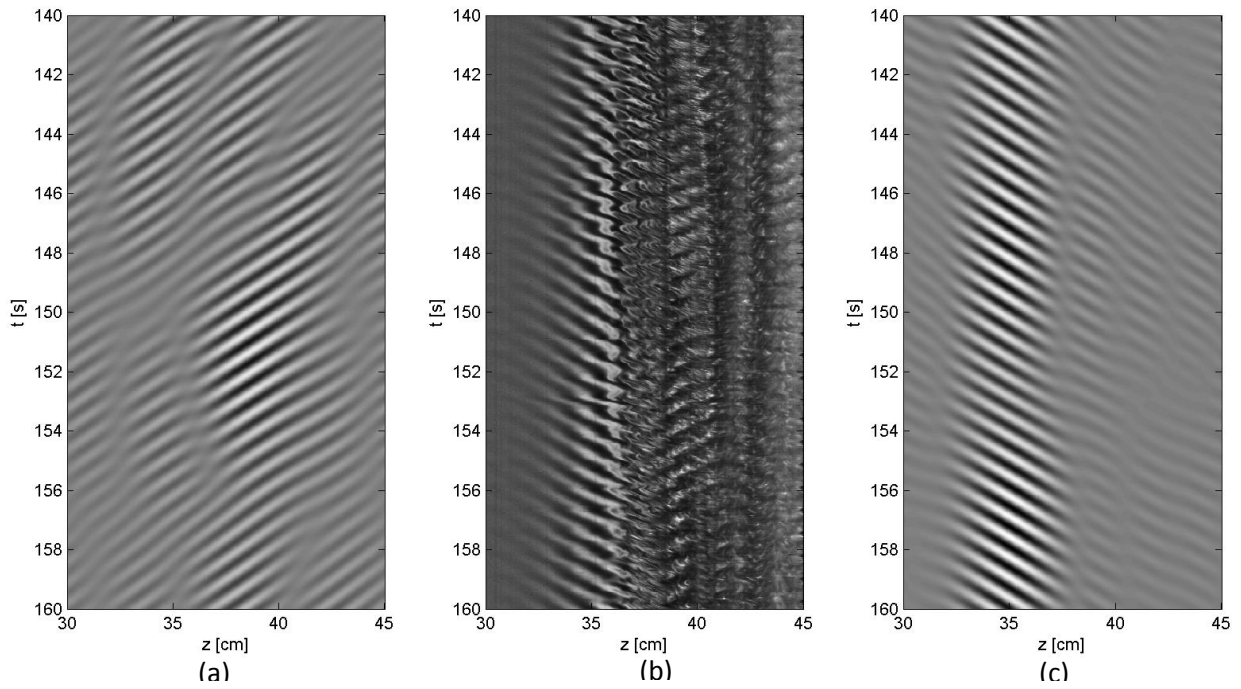


Figure 7.21: Demodulation of the zoom in space-time diagram of the transition.  $Ta_c = 2.86$ ,  $E_m = 0.13$ ,  $S = 0.61$ . (b) Space-time diagram of the transition (a) (c) Demodulated wave.

The demodulation of the space-time diagram of the saturated wave yields two counter propagating waves (Figure 7.22).

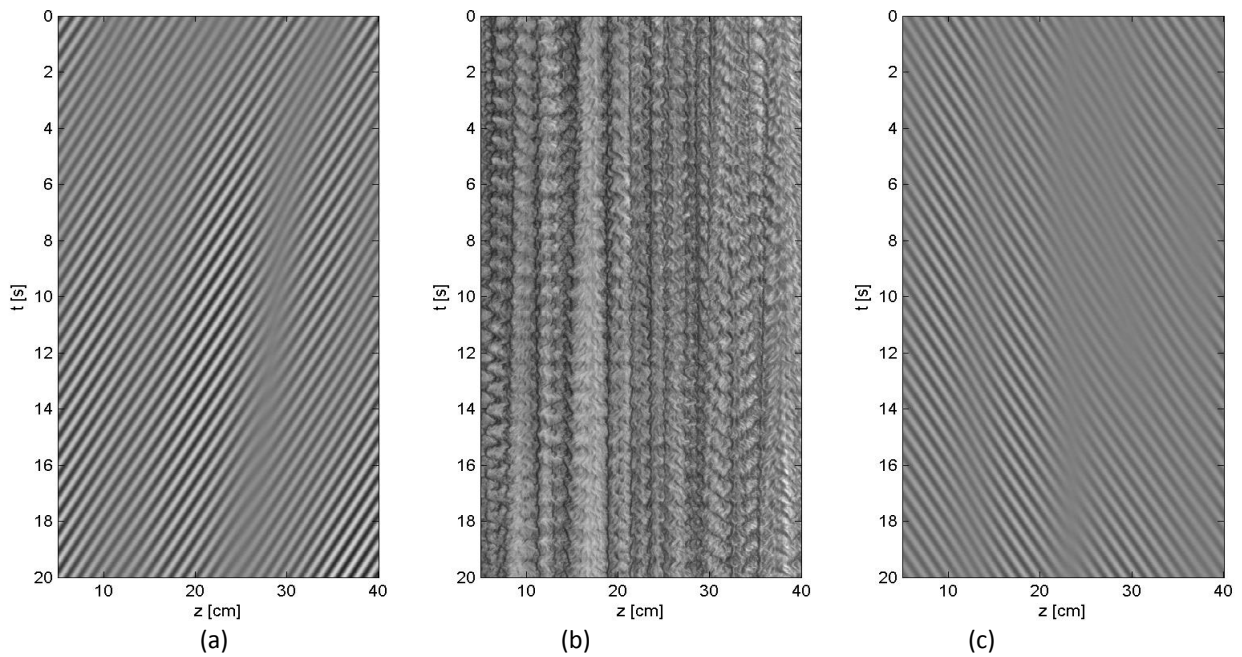


Figure 7.22: Demodulation of the space-time diagram of the Disordered Waves mode.  $Ta_c = 2.86$ ,  $E_m = 0.13$ ,  $S = 0.61$ . (a) Demodulated left wave (b) Space-time diagram of the saturated flow (c) Demodulated right wave.

We compare these two modes by presenting in figure 7.23 (a) (b) the longtime space-time diagram of the Disordered Vortices mode and the Disordered Waves mode. These modes are similar to each other as in both of them the counter rotating vortices pairs (represent by dark lines) tend to approach each other and immerge while new vortices pairs are created randomly. However when the transient space-time diagrams are compared (figure 7.23 (c)(d)) we can see that there exists no waves in the disordered vortices mode.

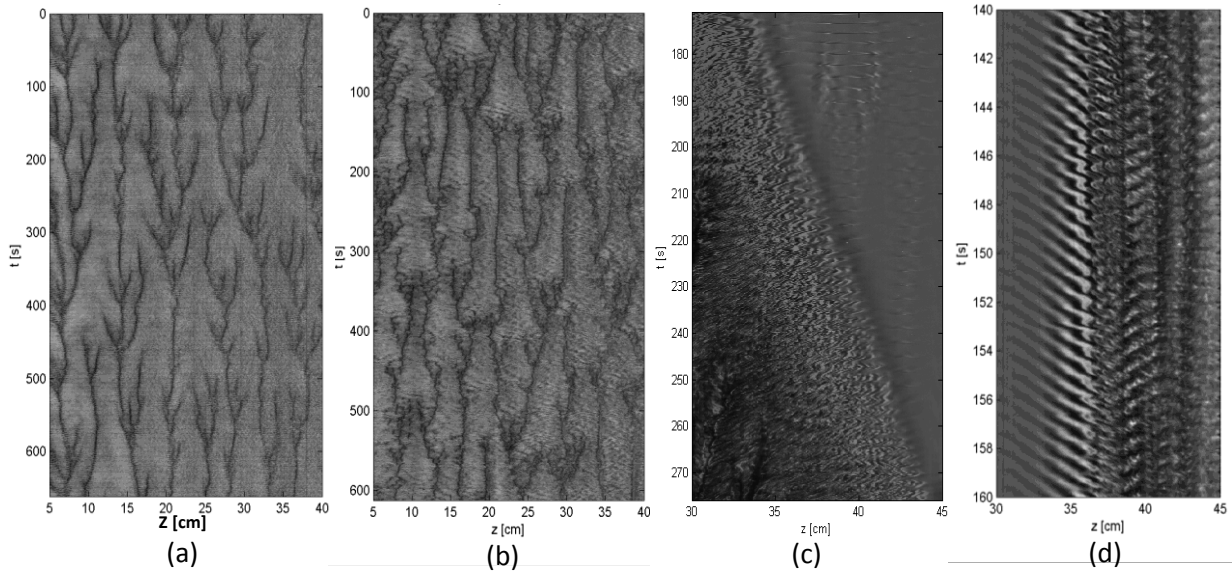


Figure 7.23: Comparison between the critical modes: (a) (b) longtime space-time diagram of Disordered Vortices mode (a) and Disordered Waves mode (b); (c) (d) transient space-time diagram of Disordered Vortices mode(c) and Disordered Waves mode (d).

#### Disordered waves with solitary vortices

For fluids of  $E = 0.29, S = 0.62$  and  $E = 0.43, S = 0.55$  quasi-stationary stable vortices are formed in the disordered wave patterns (figure 7.24). These vortices are called solitary vortices. They result from strong nonlinear interactions of the disordered waves and they are sustained by these waves. The Fourier spectra show also the coexistence of the steady vortices (peaks with small space wave number  $k$  in figure 7.24 e) and the disordered waves (pic distinct to the rotational frequencies in figure 7.24 f).

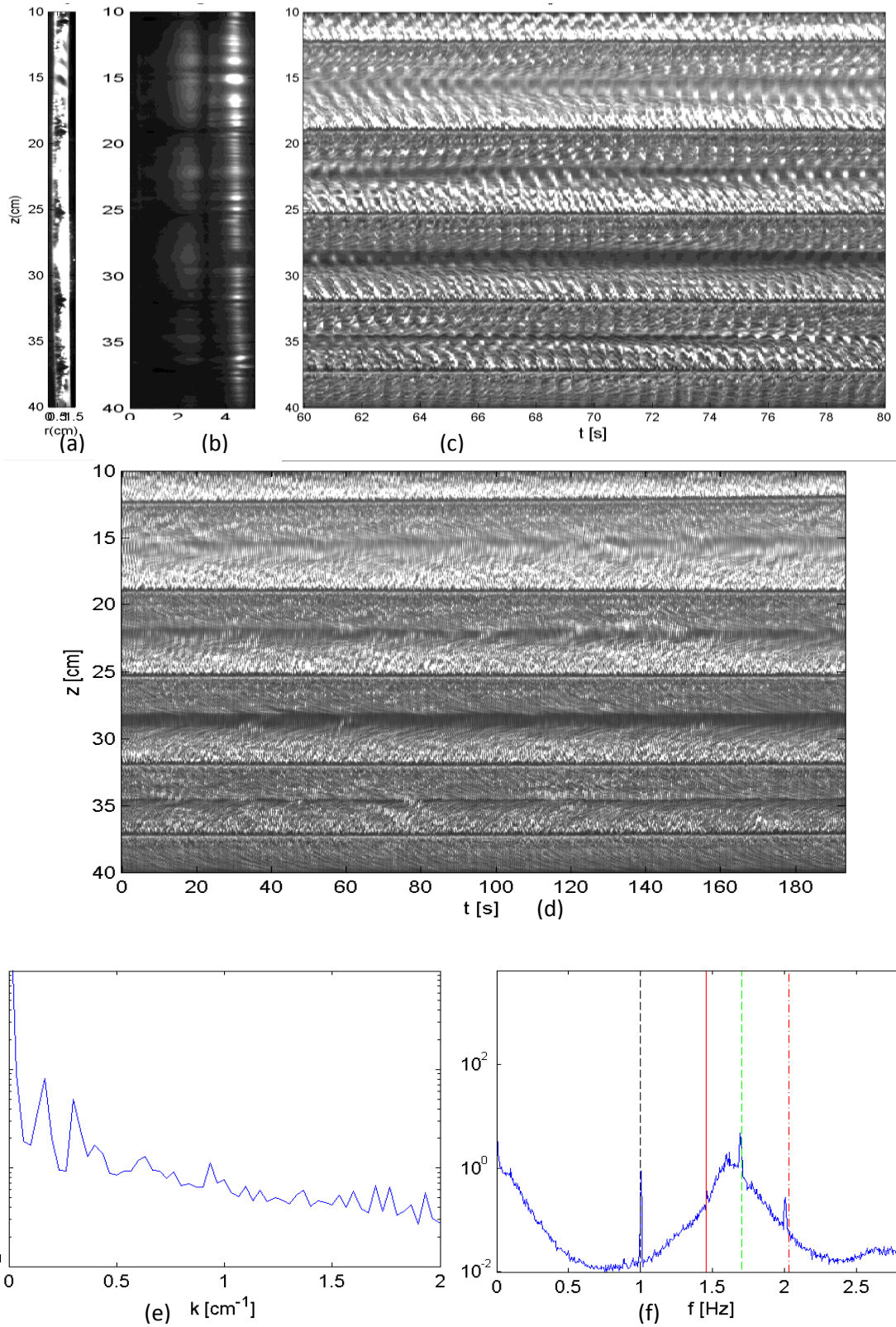


Figure 7.24: Flow patterns and space-time diagram of the Solitary Vortices mode on Keplerian regime at  $Ta_c = 2.15$ ,  $E_m = 0.29$ ,  $S = 0.62$ . (a) Gap view by laser sheet (b) Front view (c) Space-time diagram. (d) long time space-time diagram. © space spectrum (f) time spectrum. Red line and dashed line – the frequency of the inner and outer cylinder. Black dashed line – the flicker frequency of the spot light. Green dashed line – the mean frequency  $\langle \omega \rangle$ .

The Solitary Vortices mode can be demodulated into counter propagating waves. As the propagating waves are separate to the solitary vortices, it is easier to distinguish its critical wavenumber and critical angular velocity. The space-time diagram and its demodulated waves are presented in figure 7.25.

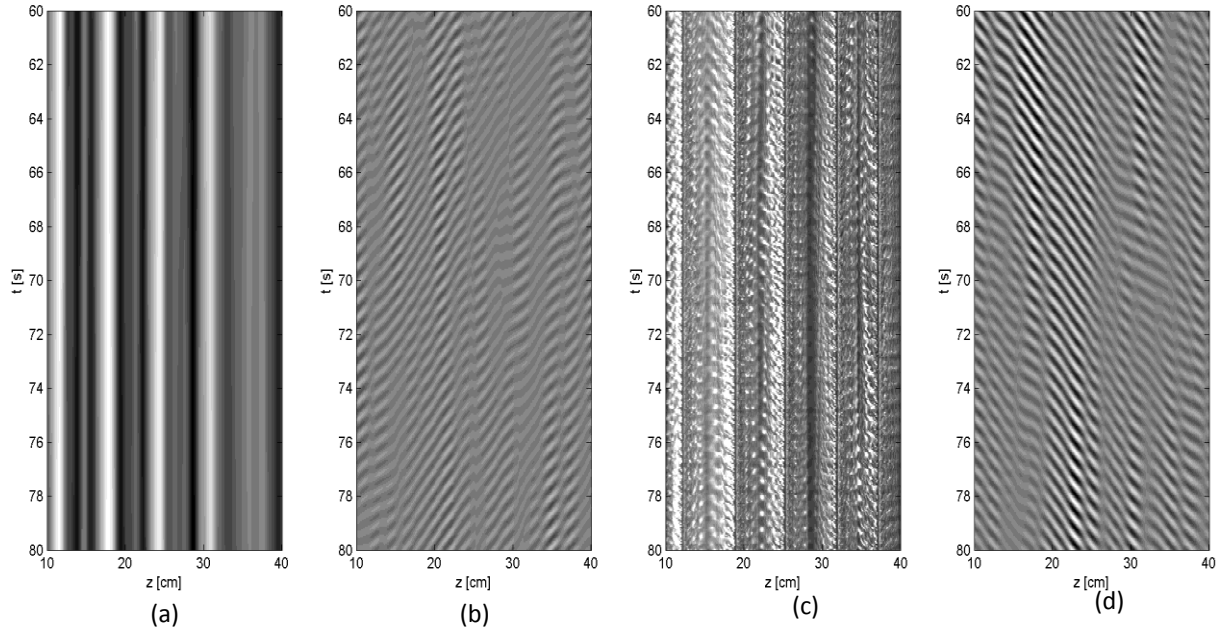


Figure 7.25: Demodulation of the space-time diagram of the Solitary Vortices mode at  $Ta_c = 2.15$ ,  $E_m = 0.29$ ,  $S = 0.62$ . (a) Demodulated stationary mode (b) Demodulated left wave (c) Space-time diagram (d) Demodulated right wave.

### Purely elastic modes

For large values of the elasticity, the instability is driven by the elastic force and its threshold should be very small. This is the situation encountered in the experiment when  $ES > 1$ . To reach this mode, more elastic fluids are needed.

### Supercritical vs subcriticality of the instability

To test the subcritical or supercritical nature of the transition to the different modes observed in the Keplerian case, we have tested the existence of the hysteresis between the ramping up and the ramping down the rotation of the cylinders. No significant hysteresis was found for the stationary axisymmetric modes; they appear and disappear at the same critical velocity. Instead, the transition to disordered waves and their disappearance when ramping down occur at different rotation velocities of the cylinders. Thus, the transition to stationary axisymmetric mode is supercritical while the transition to the Disordered Vortices mode is subcritical.

## b. Comparison with LSA results

We plot in figure 7.26 the critical Taylor number from experiments and from LSA as a function of the polymer elasticity. The dashed line  $ES = 0.672$  is the border between the potentially stable and unstable zones according to elasto-rotational Rayleigh criterion which predicts that the purely elastic instability (PEI) should appear on the right side of the dashed line. The instability modes observed on the left of this line should be related to the coupling between the rotation-induced and the elasticity-induced effects. They will be called elasto-rotational instability (ERI) modes. This phenomenon confirms the previous conclusion that the polymer viscosity is a source of instability in the elastic rotational flow.

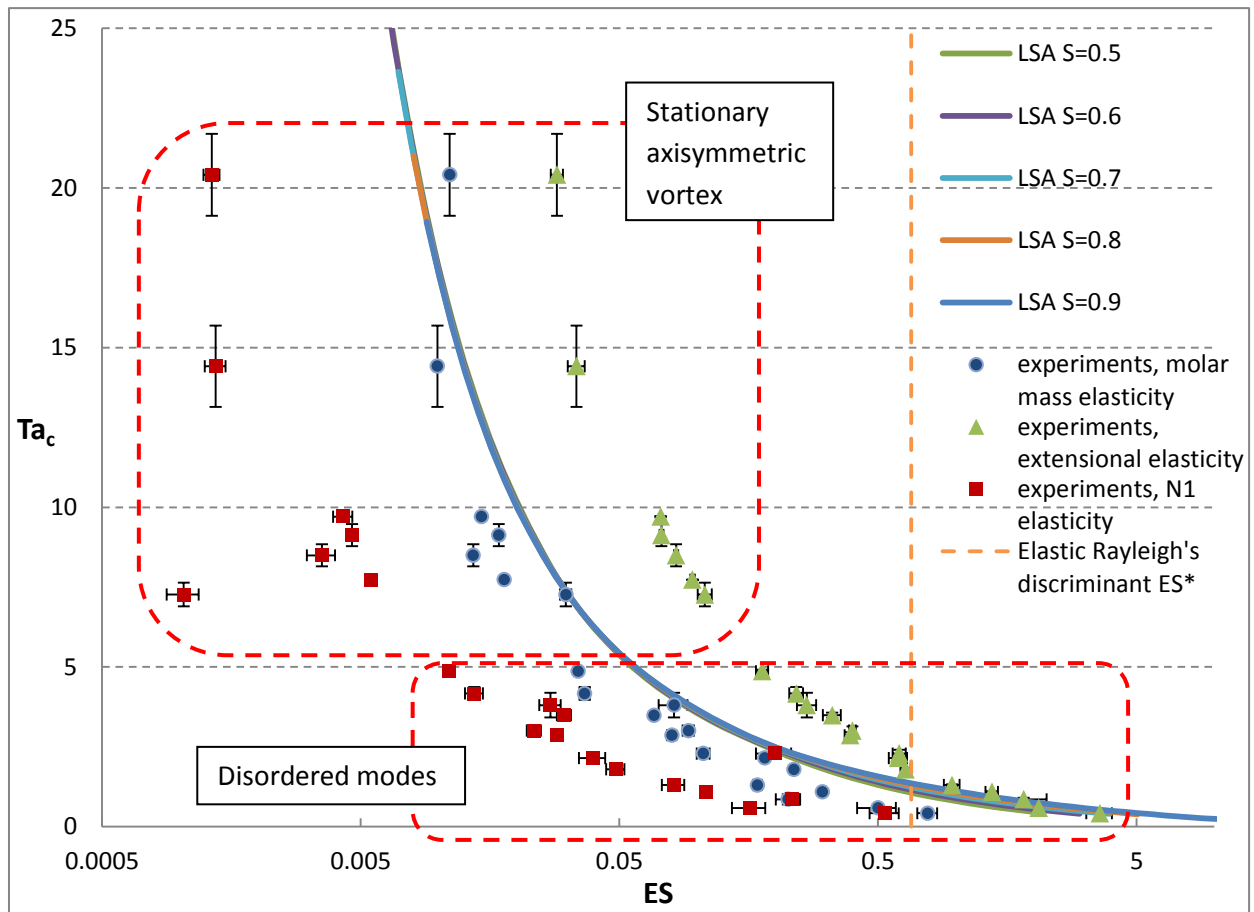


Figure 7.26: critical values of the transition from laminar flow to unstable flow on Keplerian regime. Solid lines – LSA critical curves for different  $S$ . Dashed line  $ES^* = 0.672$  is predicted by elasto-rotational Rayleigh discriminant. Solid points – experimental transient values, 3 colors present 3 different definitions of elasticity. Within each definition of elasticity, each point presents one solution tested. Dashed rectangular – group of different flow patterns.

Figure 7.26 shows that for every elasticity definition, all the critical points  $Ta_c(ES)$  form more or less one monotonically decreasing curve: for all definitions of elasticities,  $Ta_c$  decreases when  $ES$  increases. The solutions with large polymer elasticity  $ES$  require less shearing rate to be destabilized in the Keplerian rotation regime. This result is in good agreement with the LSA conclusion. Moreover, the polymer elasticity  $ES$  is the best coordinate appropriate to describe the polymer

elasticity in Keplerian regime. Among the 3 different definitions of elasticity, the molar mass elasticity  $E_m$  fits the best to LSA predictions.

The critical modes observed in the experiment can be classified into 2 groups (figure 7.27): stationary axisymmetric vortex mode for small values of  $ES$  and large values of  $Ta_c$ , and disordered modes for large values of the  $ES$  and small values of  $Ta_c$ . The disordered modes appear in form of disordered waves in space but with a definite frequency for intermediate values of  $ES$ , or in form of disordered waves with solitary vortices (indicated in figure 7.27). The LSA cannot predict the disordered modes which are nonlinear as they result from strong coupling between linear modes.

The value  $ES^*$  which is determined from the elasto-rotational Rayleigh discriminant lies on the right side of most of the experimental points. This suggests that these modes are driven both by the rotation and the elasticity effects. It is reasonable to assume that experiments with fluids of larger  $E$  would show purely elastic instability modes. The colored point lines separate the stationary axisymmetric mode and the oscillatory non-axisymmetric mode from LSA. These lines are situated near the edge of the experimental groups of stationary axisymmetric vortex and disordered modes. Considering the difficulty to estimate the elasticity of polymer solutions, the experimental critical modes correspond to the LSA predictions.

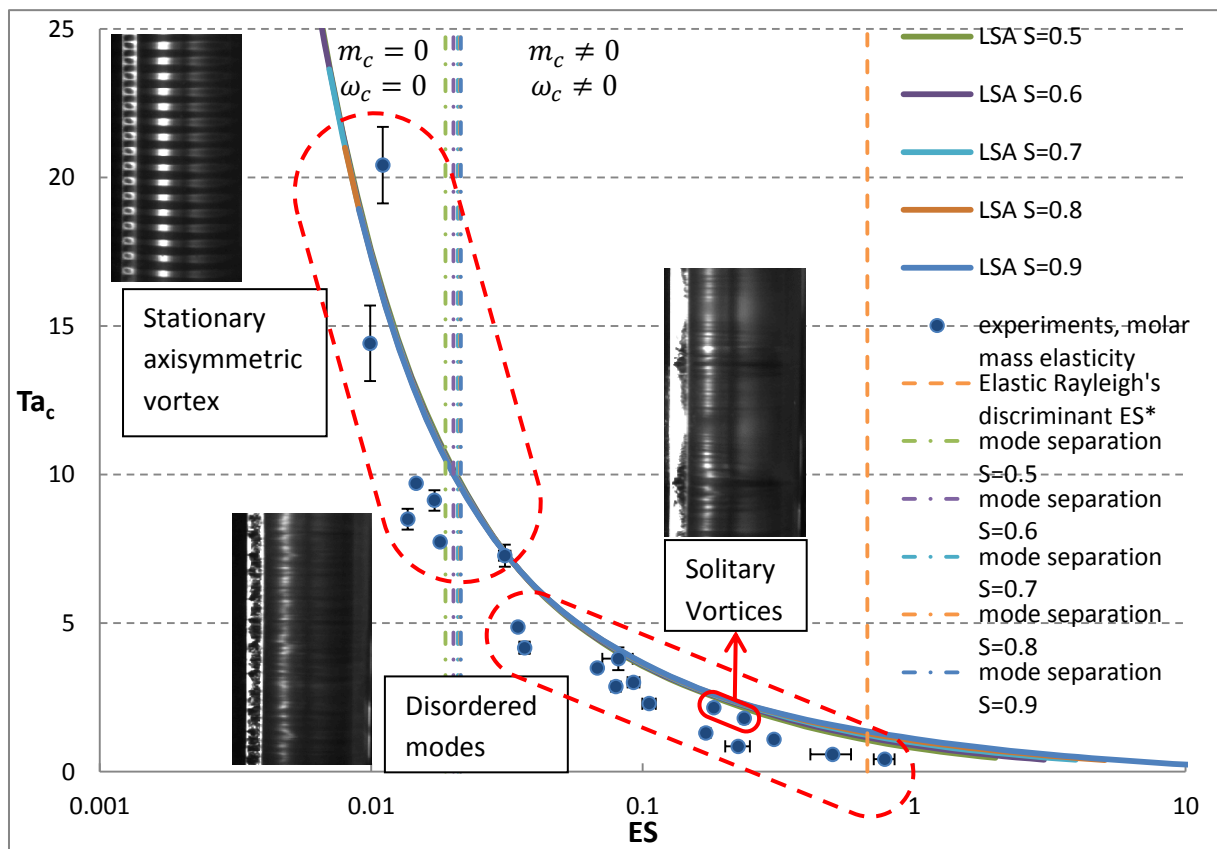


Figure 7.27: Comparison of the critical modes on Keplerian regime;  $E$  is defined with the molecular relaxation time. Solid lines – LSA critical curves for different  $S$ . Dashed line ( $ES^* = 0.672$ ) gives the separation between stable and unstable zones to elasticity driven perturbations. Solid points – experimental critical values. Dashed contour – different modes. Solid circle – location of the Solitary Vortices mode. Colored point lines separate the stationary axisymmetric mode and the oscillatory non-axisymmetric mode from LSA.

Then we nondimensionalize the experimental critical wave number  $k_c$  by  $q_c = 2\pi dk_c$  and compare it to the LSA predictions in figure 7.28 and compare the experimental critical angular velocity in the dimensionless form  $\omega_c$  and the LSA predictions of  $\omega_c/m$  in figure 7.29.

The experimental values of the axial wavenumber  $q_c$  follow the same trend as those obtained from the LSA: the axial wavenumber  $q_c$  decreases with  $ES$  and then remains steady around  $q_c \sim 4.5$  for  $ES > 0.03$ . The experimental  $\omega_c$  follows the trend predicted by LSA, where  $\omega_c$  is null for the stationary mode and almost constant for the disordered modes. However it is 10 times higher than the LSA prediction.

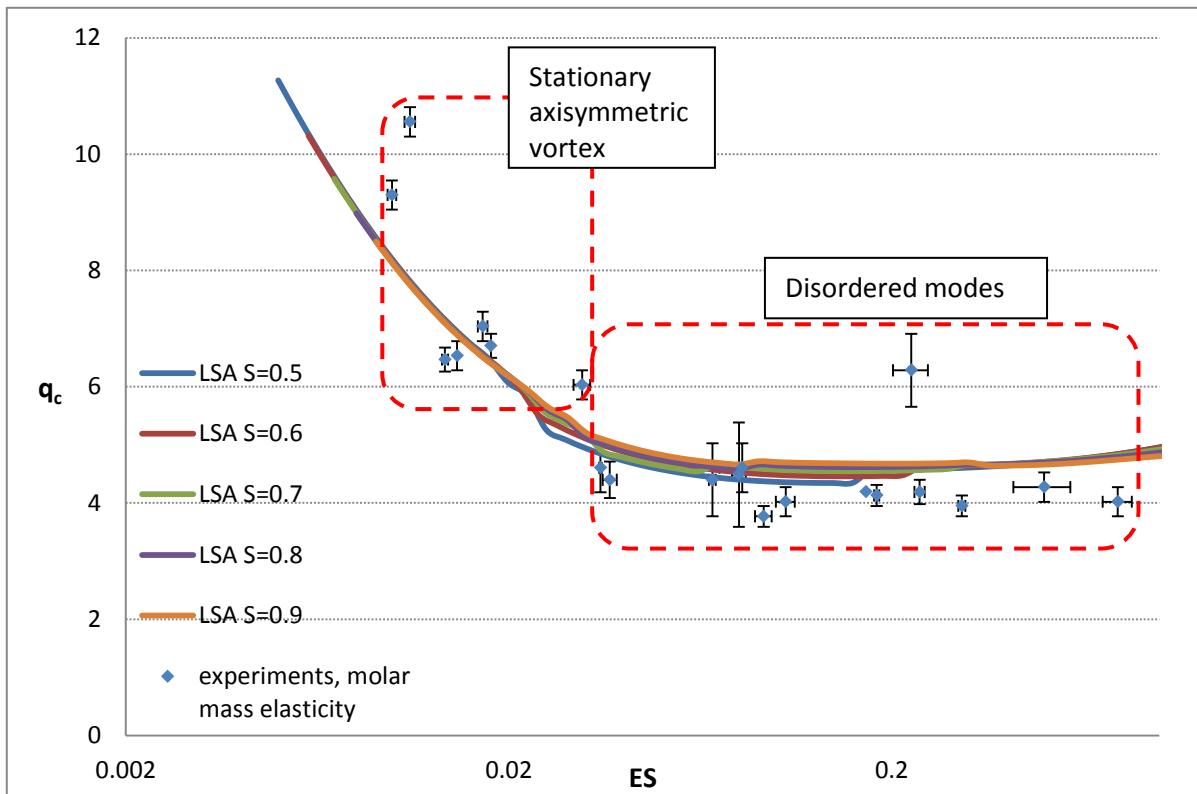


Figure 7.28: Variation of the critical axial wave number with  $ES$  defined by molecular relaxation time. Solid lines – LSA predictions for different  $S$ . Solid points – experimental critical wave numbers.

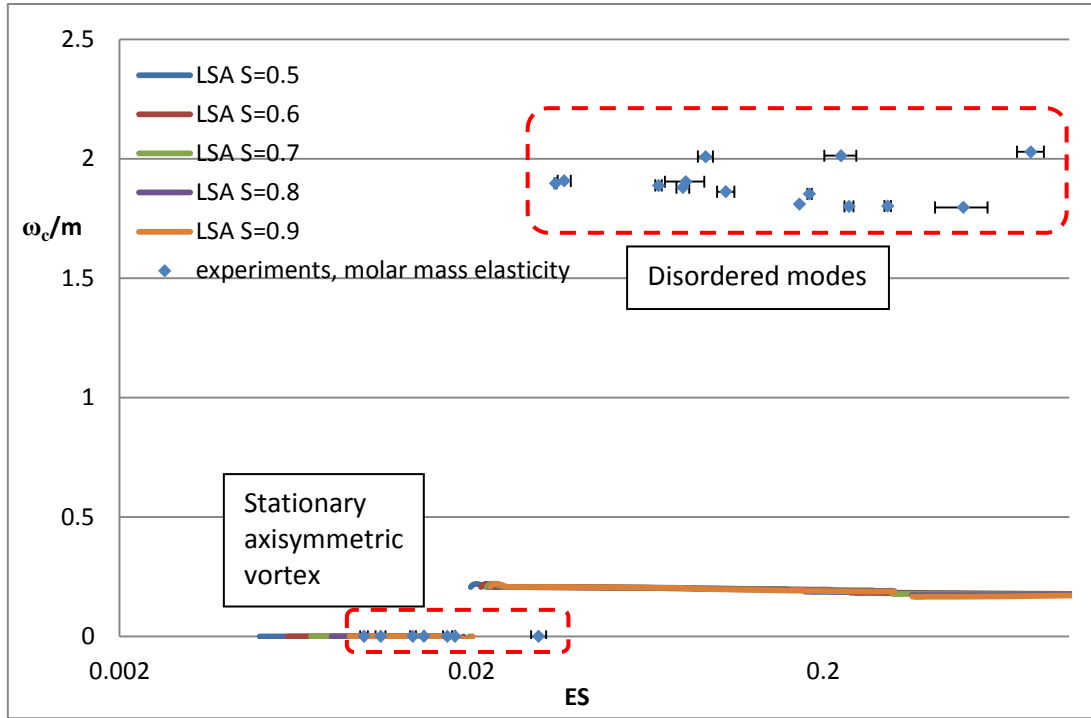


Figure 7.29: Variation of the critical frequency with  $ES$  defined by molecular relaxation time. Solid lines – LSA predictions for different  $S$ . Solid points – experimental critical angular frequency

## 7.2. The anti-Keplerian regime $\mu = \eta^{-3/2}$

In the Keplerian regime both centrifugal force and the elastic force contribute to the viscoelastic instability. In order to better understand the effects of the elastic force in the Keplerian regime, we have inversed the rotational velocities of the cylinders and studied the so called anti-Keplerian regime where  $\mu = \eta^{-3/2}$ . In our experimental geometry  $\eta = 0.8$ , we have  $\mu = \eta^{-3/2} = 1.398$ .

### 7.2.1. LSA results

To illustrate the LSA results, we present the theoretical critical curves  $Ta_c(E)$  for different  $m$  and for fixed value  $S = 0.7$  (figure 7.30). The most unstable mode for all values of  $E$  is the oscillatory axisymmetric mode ( $m = 0, \omega \neq 0$ ). The critical curves  $Ta_c(E)$  for different values of  $S$  are presented in figure 7.31: the threshold of the instability decreases with  $E$  for all values of  $S$  and becomes almost independent of  $S$  for  $E > 0.6$ . The critical curves  $Ta_c(ES)$  for different values of  $S$  are presented in figure 7.32 with the elasto-rotational Rayleigh discriminant  $ES^* = 3.451$ . The critical curves in the plane  $(Wi_c, Re_c)$  show the same trend (figure 7.33) as those of Ogilvie & Potter in the same regime for  $\eta = 0.95$  and  $S = 0.5$ . There is an elastic instability with a given threshold  $Wi_c(Re = 0) > 23$  (see chapter 9) which increases as the shear increases, i.e. the elastic instability is suppressed by the shear. The variations of the critical wavenumber  $q_c$  and the critical frequency  $\omega_c$  with the elasticity  $E$  for different  $S$  are shown in figure 7.34. The critical wavenumber has a very large value compared to the other cases investigated so far and especially with respect to the Newtonian case: the corresponding vortices should have small sizes compared to the gap width. Figure 7.35 illustrates the patterns of the few properties of the critical mode in the gap for  $S = 0.7$ ,  $E = 1$ ,  $Ta_c = 0.976$ ,  $m = 0$ ,  $q_c = 24.2$ ,  $\omega_c = 0.02$ . The critical modes are flattened and the

instability develops near the inner cylinder. Besides, the  $N_2$  variations are negligible in comparison with the  $N_1$  variation while the pressure variation is small, just as the case of  $\mu = \infty$ . So we can conclude that the anti-Keplerian regime and  $\mu = \infty$  regime share the same critical modes.

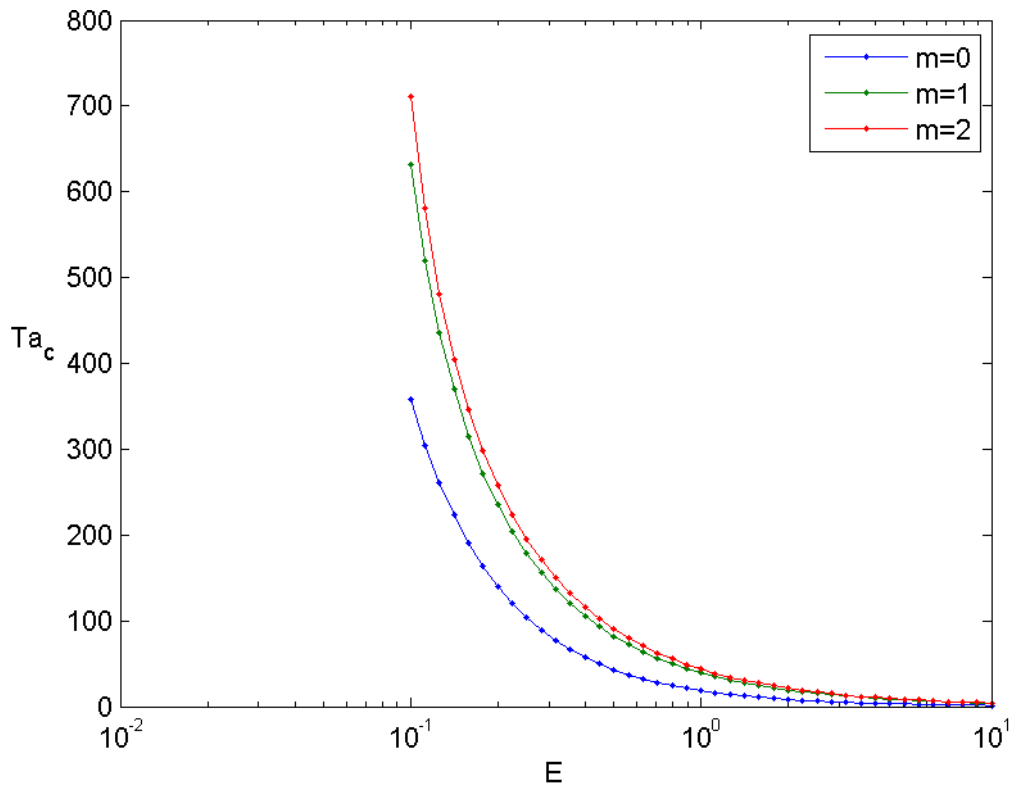


Figure 7.30: Critical curves  $Ta_c(E)$  for different  $m$  at fixed  $S = 0.7$ .

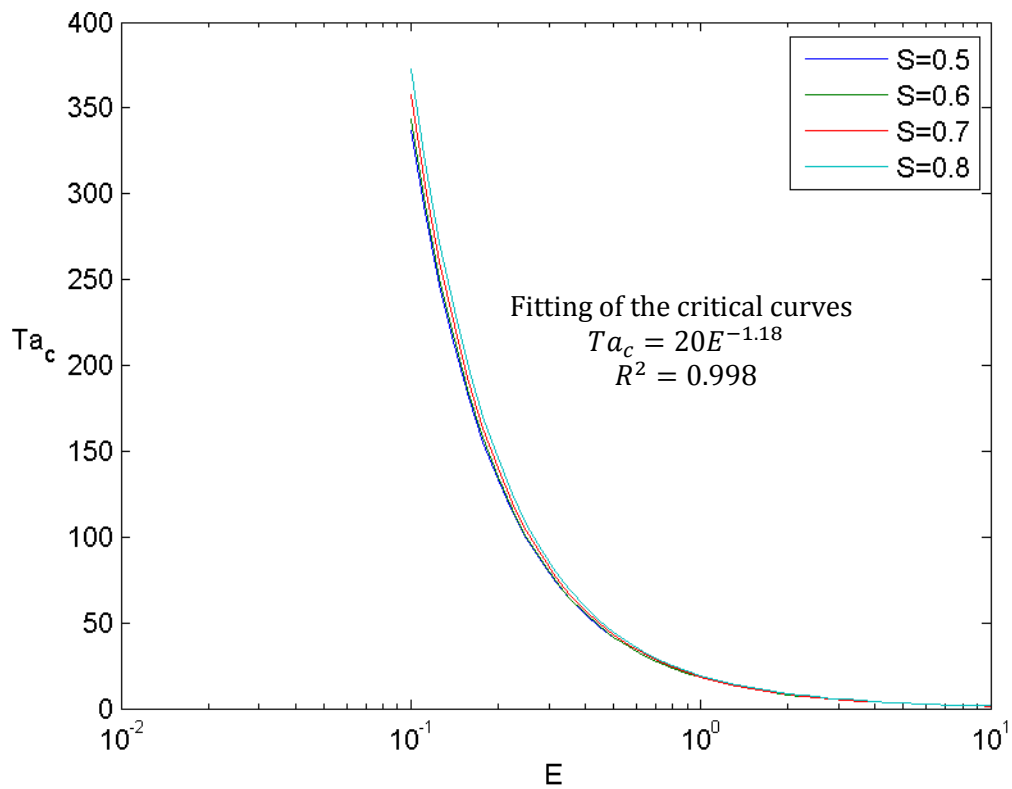


Figure 7.31: Critical curves  $Ta_c(E)$  for different  $S$ .

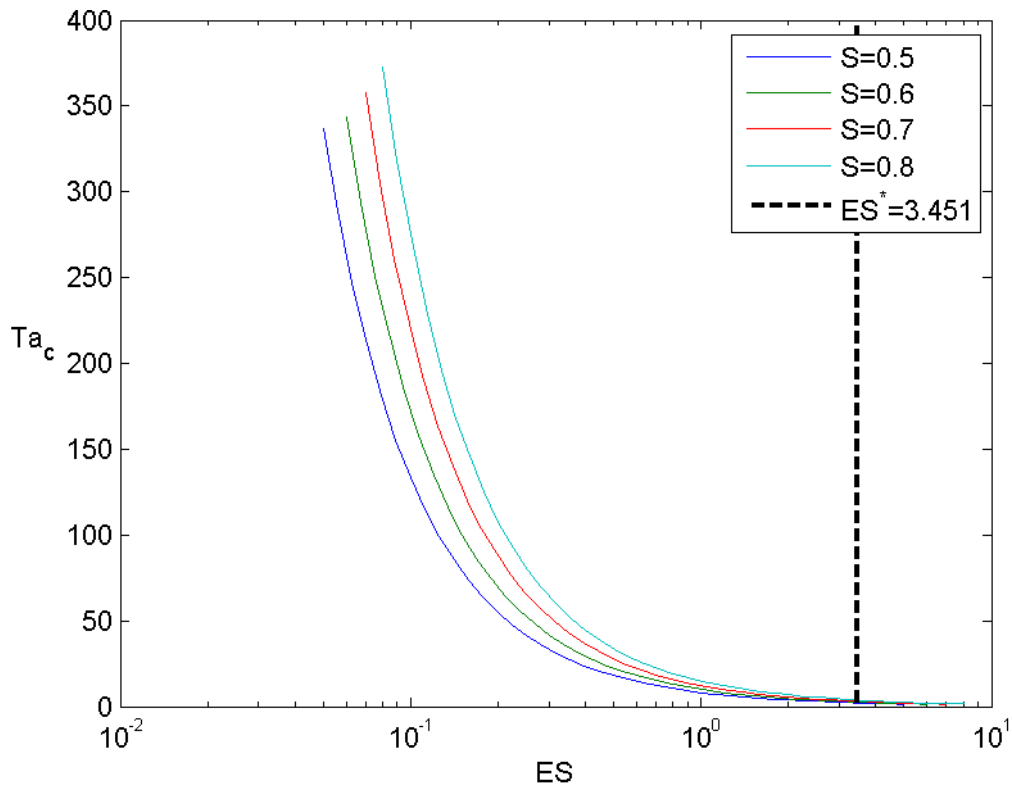


Figure 7.32: Critical curves  $Ta_c(ES)$  for different  $S$ . Dashed line represents the  $ES^* = 3.451$  from elasto-rotational Rayleigh discriminant.

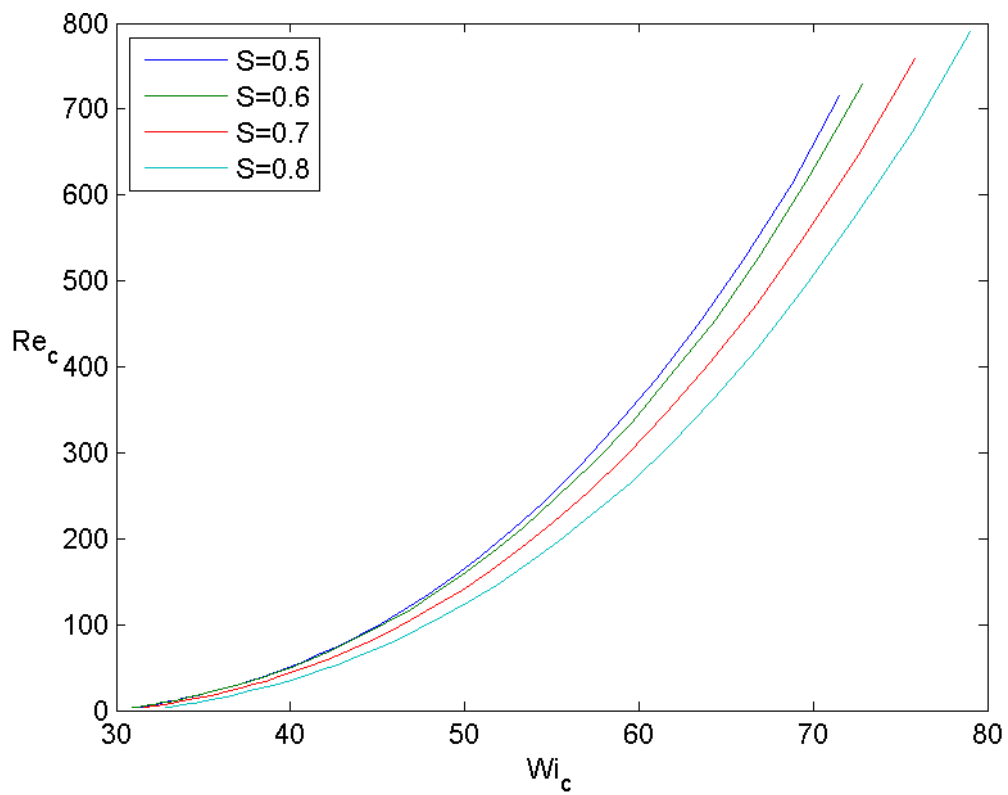


Figure 7.33: Critical curves  $Re_c(Wi_c)$  for different  $S$

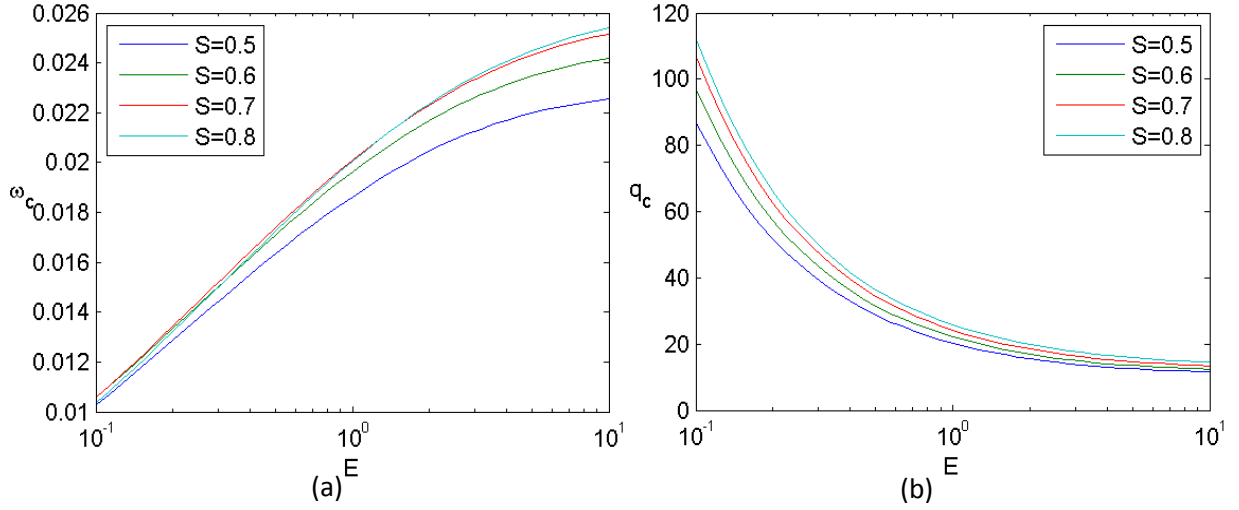


Figure 7.34: (a) The angular frequency  $\omega_c$  of the critical modes in respect to  $E$  for different  $S$  in anti-Keplerian regime. (b) The axial wave number  $q_c$  of the critical modes in respect to  $E$  for different  $S$ .

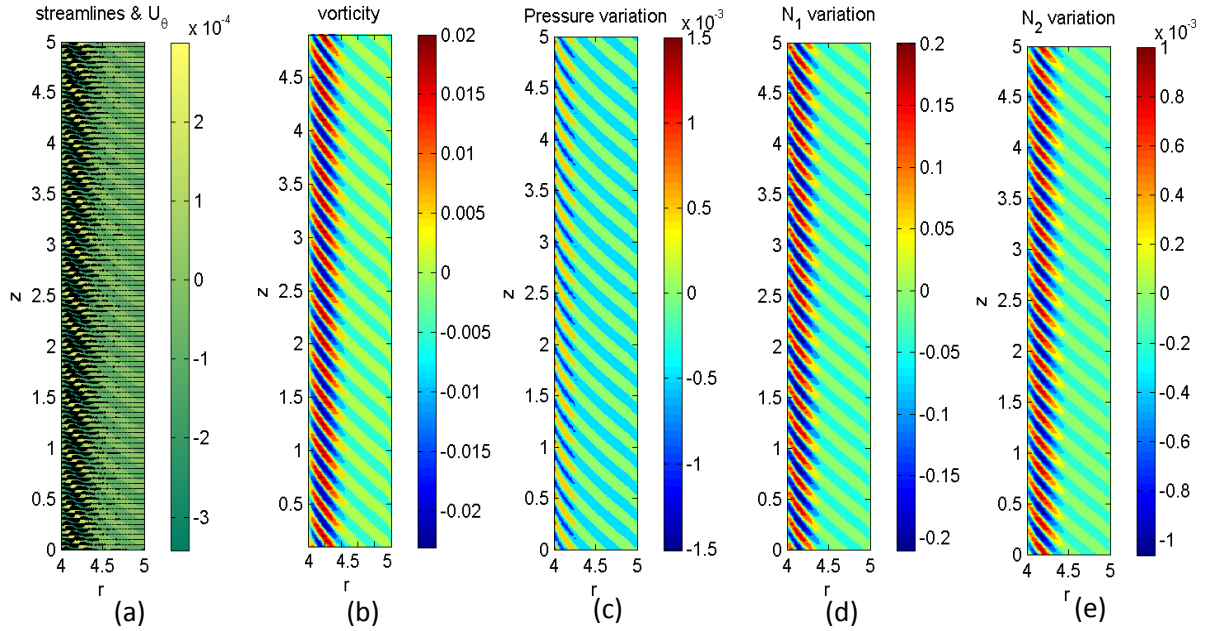


Figure 7.35: Pattern properties of the critical mode in the gap view for  $S = 0.7, E = 1, Ta_c = 0.976, m = 0, q_c = 24.2, \omega_c = 0.02$  in anti-Keplerian regime. (a) Black arrows represent the velocity field while the colors represent the azimuthal velocity  $V_{(r,z)}$  (b) the vorticity  $\omega_\theta$ , (c) the pressure variation, (d) the  $N_1$  variation. Color maps of (b, c, d) represent the relative amplitude.

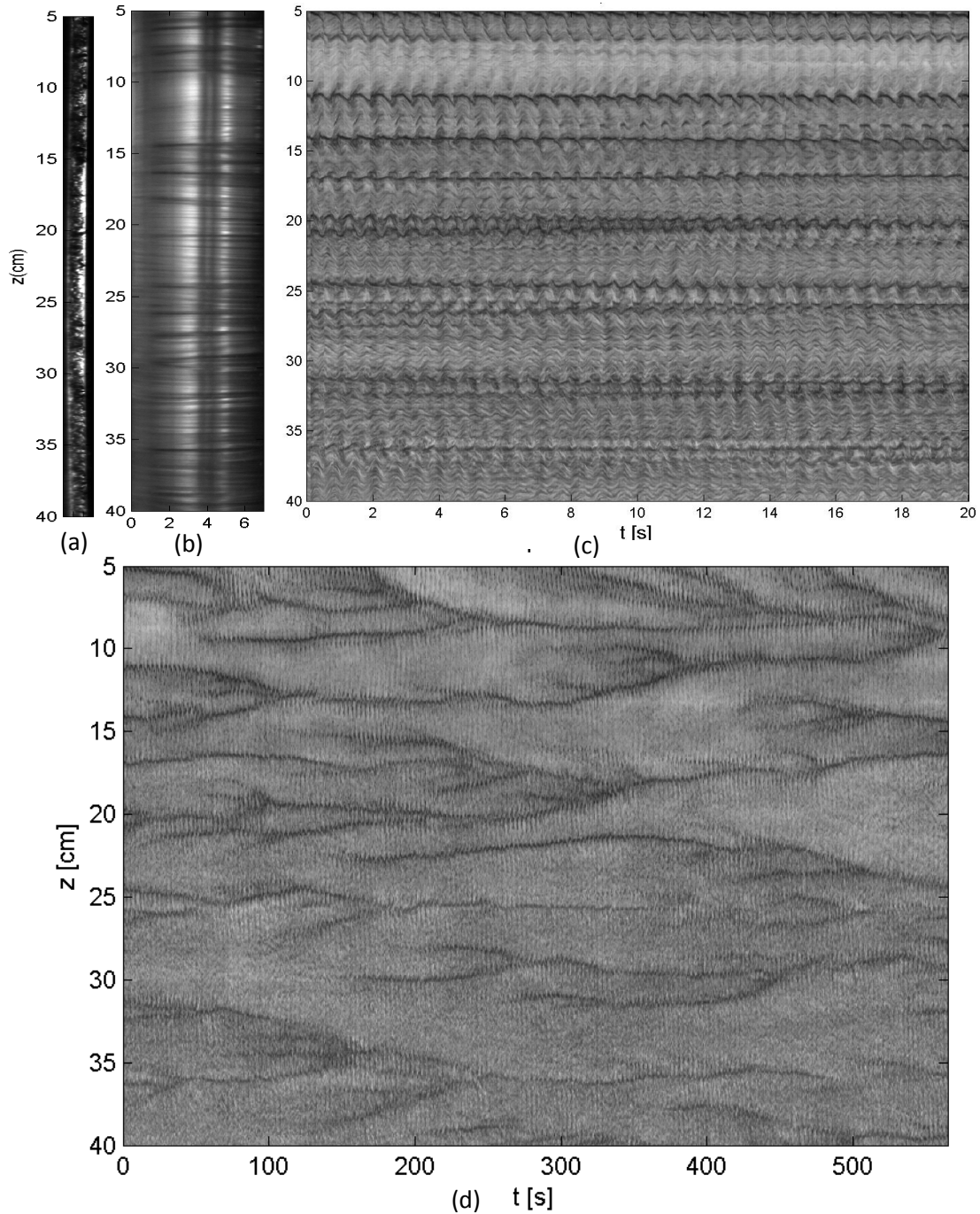
The anti-Keplerian regime bears some common behaviors with the rotation regime  $\mu = \infty$ : the critical curves  $Ta_c(E)$  or  $Re_c(Wi_c)$  have similar shapes even if the threshold of the elastic instability are different; the critical modes are oscillatory axisymmetric and the critical wavenumbers are very large corresponding to small vortices in the gap (Figure. 6.31, Figure. 7.35). This strong similarity indicates that the critical mode in the anti-Keplerian regime is a purely elastic mode.

## 7.2.2. Experimental results

We have realized experiments in the case of the anti-Keplerian regime for some solutions with viscosity ratio which were supposed to exhibit instability at acceptable values of shear rate.

### a. Flow patterns

The critical flow patterns and the spectra in space and time are illustrated in figure 7.36 for the solution with  $E_m = 0.34$  and  $S = 0.51$ . The flow patterns are disordered in space and in time (figure 7.36 c-d) and only frequencies of the cylinders' rotation are observed (figure 7.36 f). These patterns are similar to those observed in the case when  $\mu = \infty$  (figure 6.30).



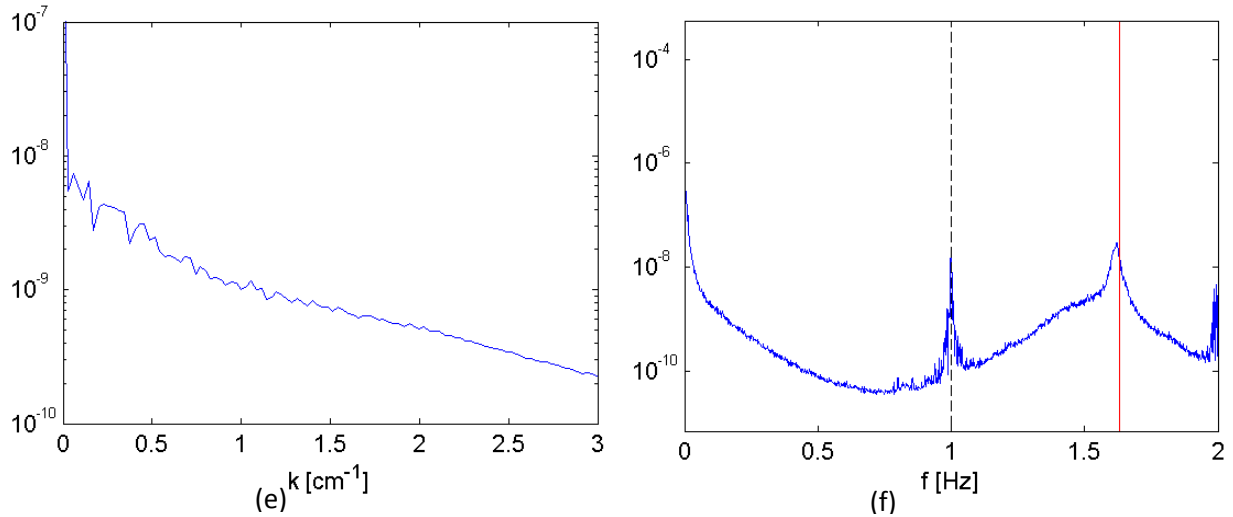


Figure 7.36: Flow patterns and space-time diagram in anti-Keplerian regime at  $Ta_c = 7.34$ ,  $E_m = 0.34$ ,  $S = 0.51$ . (a) Gap view (b) Front view by laser sheet (c) Space-time diagram of 20s (d) Longtime space-time diagram © space spectrum (f) time spectrum. Red dashed line – the frequency of the inner cylinder. Black dashed line – the flicker frequency of the spot light.

### **b. Comparison with LSA results**

From the LSA results, the best parameter for the characterization of the solution is the elasticity  $E$  and not the polymer elasticity  $ES$ . We have compared the experimental data with theoretical ones in figure 7.37. The theoretical results agree well with the experiment if one uses the extensional relaxation time  $\tau_e$  to define the elasticity. This situation was encountered also in the  $\mu = \infty$  regime.

In the anti-Keplerian regime the only viscoelastic solutions that could be destabilized have the viscosity ratio  $S$  limited in the interval  $[0.5, 0.7]$ .

The critical angular frequency and the critical axial wavenumbers of the experiments and LSA are compared in figure 7.38 and 7.39 with extensional elasticity. We can see that good agreement is obtained for  $q_c$  while the experimental  $\omega_c$  is distinct from the LSA prediction.

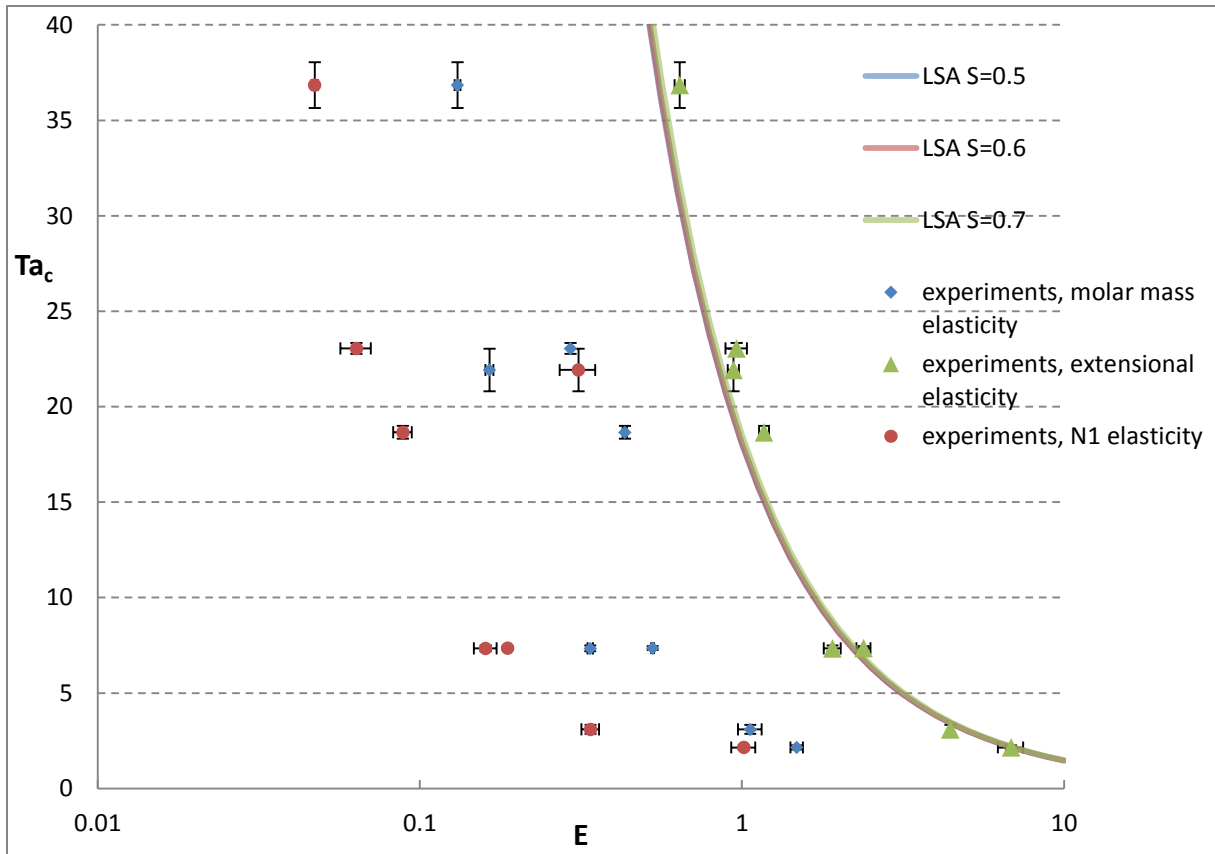


Figure 7.37: Critical values  $Ta_c(E)$  in the anti-Keplerian regime. Solid lines – LSA critical curves for different  $S$ . Solid points – experimental critical values, 3 colors present 3 different definitions of elasticity.

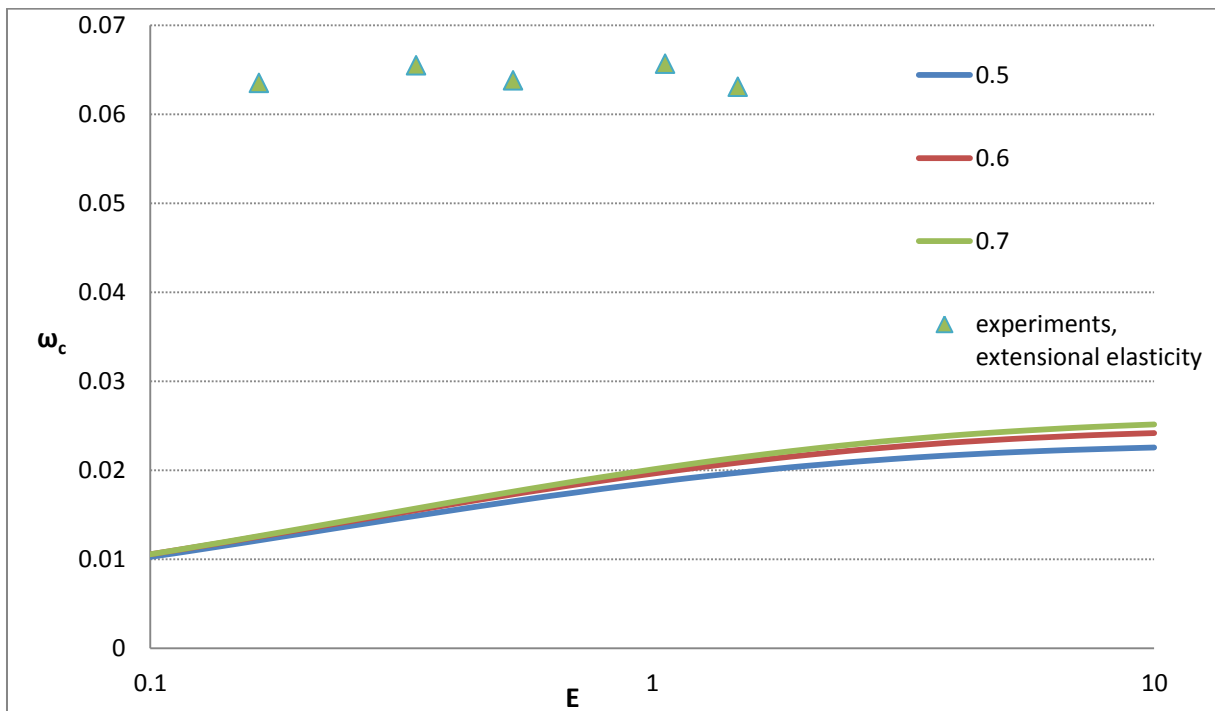


Figure 7.38: Critical values  $\omega_c(E)$  in the anti-Keplerian regime. Solid lines – LSA critical curves for different  $S$ . Solid points – experimental critical values defined by extensional elasticity.

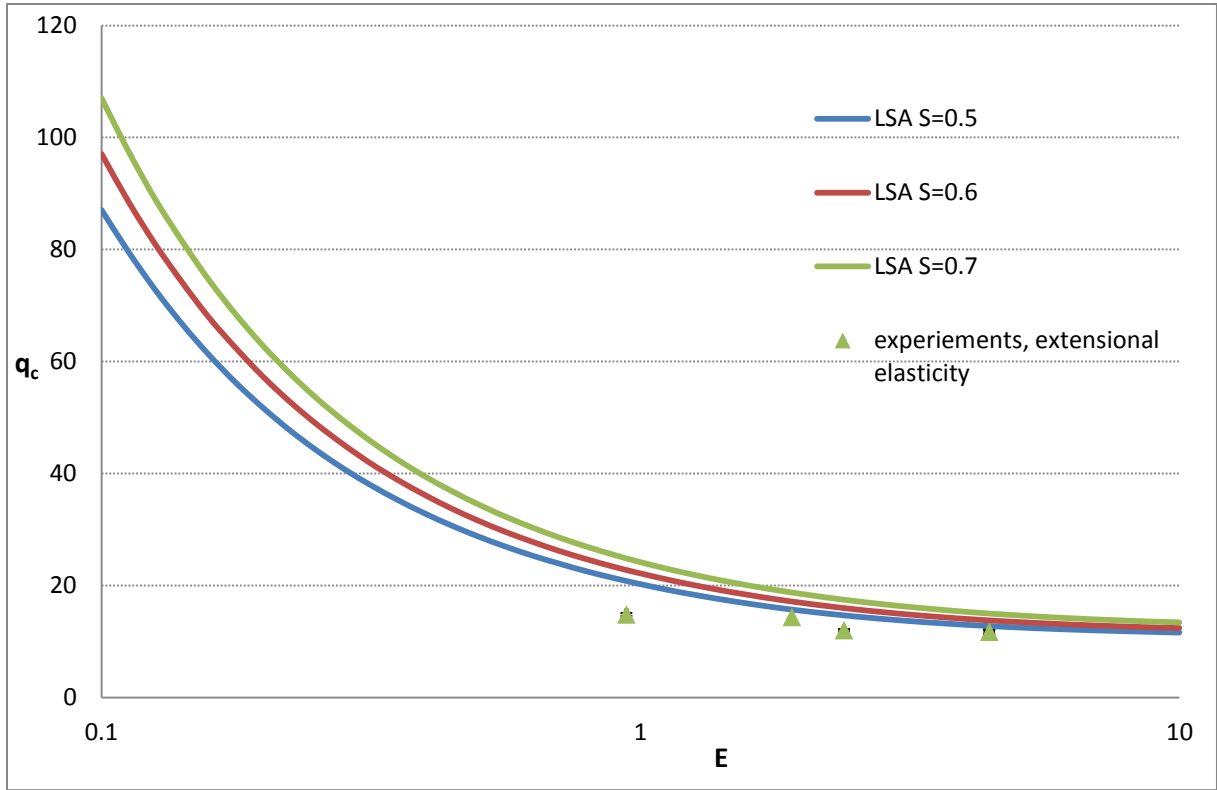


Figure 7.39: Critical values  $q_c(E)$  in the anti-Keplerian regime. Solid lines – LSA critical curves for different  $S$ . Solid points – experimental critical values defined by extensional elasticity.

### 7.3. Discussion of the VEI in the Keplerian rotation and MRI analogy

#### **a. Application of Rayleigh criterion and Velikhov-Chandrasekhar criterion**

The linear stability analysis and the experiments have shown the existence of critical modes in the zone where the elasto-rotational Rayleigh discriminant did not predict the instability i.e. for  $ES < 0.672$  for  $\eta = 0.8$ . The existence of this instability suggests that the polymer molecules in the liquid play the same role of tensile force as the magnetic field tension. The polymer analog of the magnetic field  $\vec{B}_{p3} = B_0 \vec{e}_z$  plays the role of the axial magnetic field required for the SMRI. In the quasi-Keplerian zone,  $\Phi_r(r) > 0$  while  $d\Omega/dr < 0$ , so that the Velikhov-Chandrasekhar criterion of the instability is satisfied. However the elasto-rotational instability (ERI) where  $\Phi_{er}(r) < 0$  is not analog of MRI. So that the MRI analog zone is determined by  $\Phi_r(r) > 0$ ,  $d\Omega/dr < 0$ ,  $\Phi_{er}(r) > 0$ .

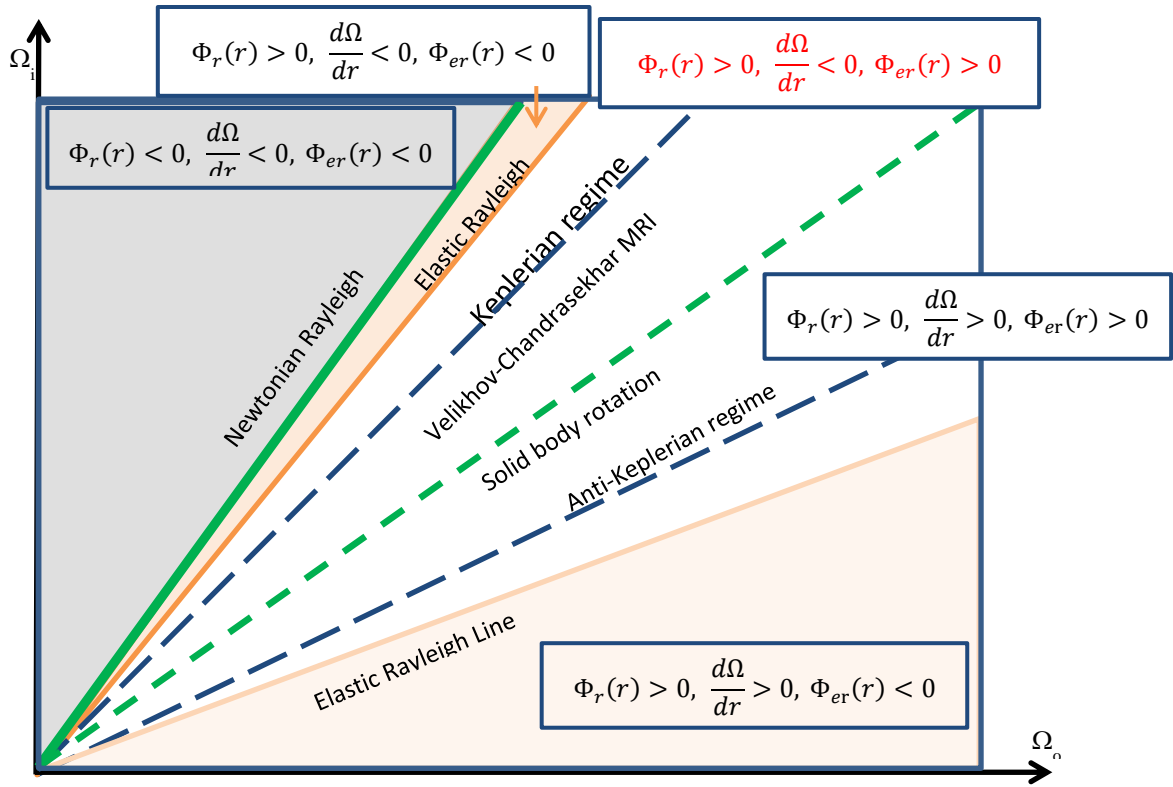


Figure 7.40: Application of the Velikhov-Chandrasekhar criterion for ERI.

**b. Condition for VEI analogs : axial field dominant or azimuthal field dominant**

The polymer analog of the magnetic field has three possibilities, two of which have non zero azimuthal components which depend on  $Wi$ . According to equation 3.29, the axial field will dominate over the azimuthal field if  $Wi \ll Wi^* \sim 0.76$ . In this case the destabilization of the viscoelastic flow in the Keplerian regime will lead to the VEI analog of the standard MRI (SMRI) which is an axisymmetric instability. Thus, the stationary axisymmetric modes which have been observed for small values of  $Wi$  are the analogs of the SMRI.

For  $Wi > Wi^*$ , both the axial and azimuthal fields are comparable and the destabilization will lead to ERI analog of the helical MRI (HMRI). We may conclude that the disordered waves mode which is the superposition of the counter-propagating waves is the analog of the HMRI.

For  $Wi \gg Wi^*$ , one may observe the purely elastic instability predicted by the elasto-rotational Rayleigh criterion which should be the analog of the similar Michael's criterion of MHD for the stability of conducting liquid in the azimuthal magnetic field [Michael1954] [Davidson2013]:

$$\Phi(r) - \frac{1}{\rho\mu_0 r^3} \frac{d}{dr} (rB_\theta)^2 > 0 \quad \text{and} \quad (\Omega r)^2 < B_\theta^2 \tag{7.1}$$

According to this criterion, the instability should be axisymmetric. We expect this instability in the extreme case of  $E \rightarrow \infty$  which corresponds to the purely elastic instability (see chapter 9). In the case of large but finite  $E$ , non-axisymmetric mode with  $m_c = 1$  is predicted by LSA. This may be analog of the azimuthal MRI (AMRI) which is a non-axisymmetric instability.

The figure 7.41 presents the experimental and LSA critical values  $Ta_c(ES)$  (figure 7.26) together with the criteria of  $Wi^*$  that separate VEI analog to different types of the MRI.

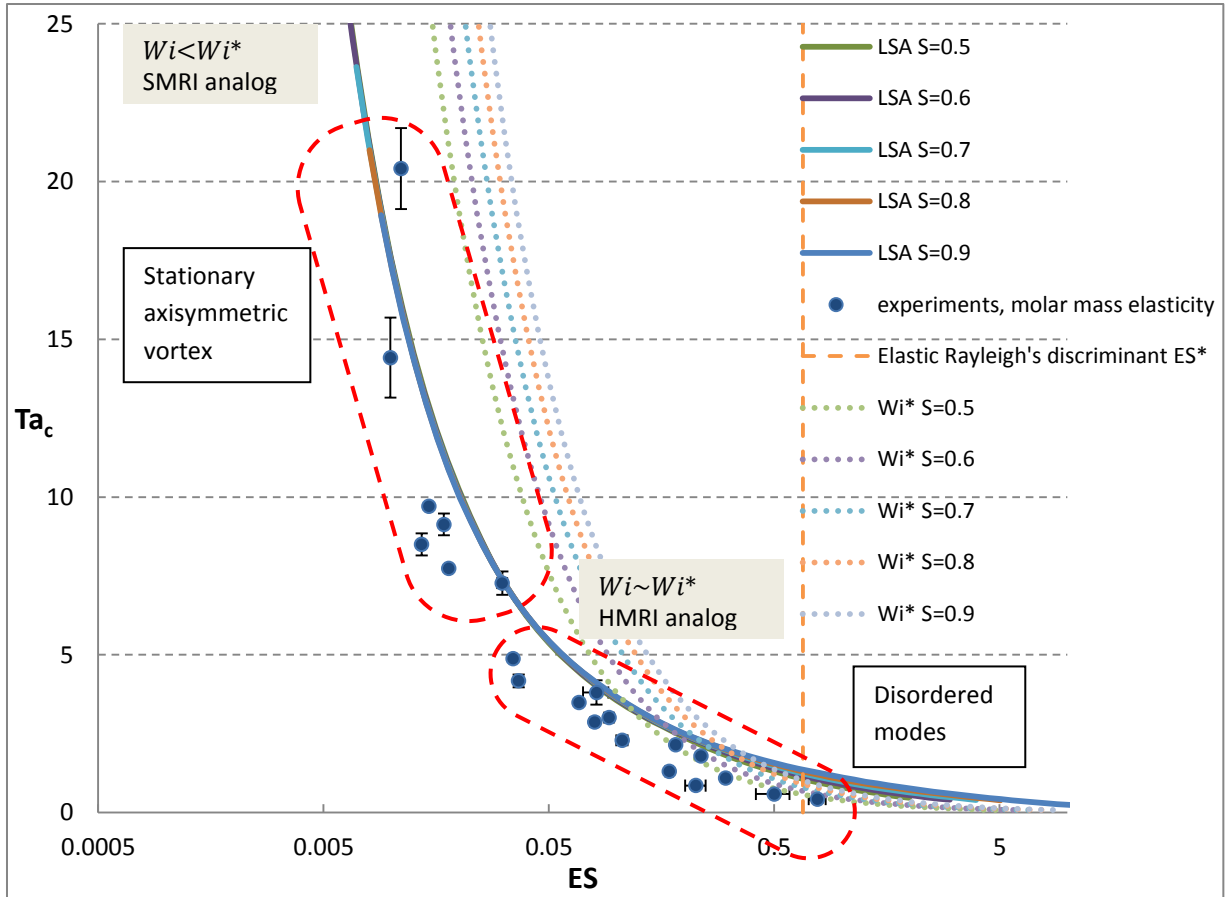


Figure 7.41: Critical values on Keplerian regime. Solid lines – LSA critical curves for different  $S$ . Dashed line  $ES^* = 0.672$  is predicted by elasto-rotational Rayleigh discriminant. Solid points – experimental transient values defined by molar mass elasticity. Dashed rectangular – group of different flow patterns. Colored point lines – criterion of  $Wi = Wi^*$  for different  $S$ .

### c. Alfvén waves

The characteristic polymeric analog of the magnetic field  $B_0 = \sqrt{\rho v_p / \tau}$  (see expression 3.23) suggests the existence of a characteristic velocity  $U_c = \sqrt{v_p / \tau}$  which is the analog of the Alfvén velocity defined as  $V_A = B / \sqrt{\rho \mu_0}$  in MHD. We shall call this characteristic velocity  $U_c$  the *polymeric Alfvén velocity*  $V_A^p$

$$V_A^p = \frac{B_0}{\sqrt{\rho}} = \sqrt{\frac{v_p}{\tau}} \quad 7.2$$

For a fixed polymeric viscosity ( $v_p$ ) of the solution, i.e. for a solution with a given elasticity, the polymer viscosity defines the polymeric Alfvén velocity. When scaled with the viscous diffusion velocity  $v/d$ , the dimensionless polymeric Alfvén velocity  $\hat{V}_A^p$  is

$$\hat{V}_A^p = \sqrt{\frac{S}{E}} \quad 7.3$$

If one uses the characteristic rotation velocity  $U_c^r = d\dot{\gamma}$ , one gets

$$\hat{V}_A^p = \frac{1}{Re} \sqrt{\frac{S}{E}} = \frac{\sqrt{ES}}{Wi} = \hat{B}_0 \quad 7.4$$

where  $\hat{B}_0$  is the dimensionless polymeric analog of the magnetic characteristic field  $B_0$ .

#### **d. Comparison with results of Ogilvie & Potter and experiments of Boldyrev**

Ogilvie & Potter [Ogilvie2008] performed the LSA for the only case of  $\eta = 0.95$  and  $S = 0.5$ , this case has been used to test our code. We have investigated the viscoelastic regime in more detail for the annular flow geometry with  $\eta = 0.8$  both in Keplerian and anti-Keplerian regimes ( $\mu = \eta^{3/2}, \mu = \eta^{-3/2}$ ) and with different values of viscosity ratio  $S$ .

In the Keplerian regime, Ogilvie & Potter predicted a critical mode in form of “ribbon” structure, we have not found this mode neither in the LSA nor in the experiment because of the difference in radius ratio  $\eta$ . Instead, we found stationary axisymmetric mode for small  $E$  and disordered waves mode which is a superposition of counter-propagating waves for intermediate  $E$  from LSA. For Ogilvie & Potter, no stationary axisymmetric mode was obtained because of the small gap and of the value of  $S = 0.5$ , so that no SMRI analog is observed.

Boldyrev et al. [Boldyrev2009] reported experimental observation of stationary axisymmetric modes ( $m = 0$ ) and helicoidal mode ( $m = 1$ ) in high molecular aqueous polymer solutions which were shear thinning in a cylindrical annulus with  $\eta = 0.903$  and viscosity ratio  $S \in \{0.983, 0.991, 0.995\}$ . These authors have observed helicoidal modes in the same range of the elasticity  $E$  as in our case of disordered waves mode, but they reported axisymmetric mode for large but finite values of  $E$  for which the LSA predicts the non-axisymmetric modes corresponding to the analog of HMRI.

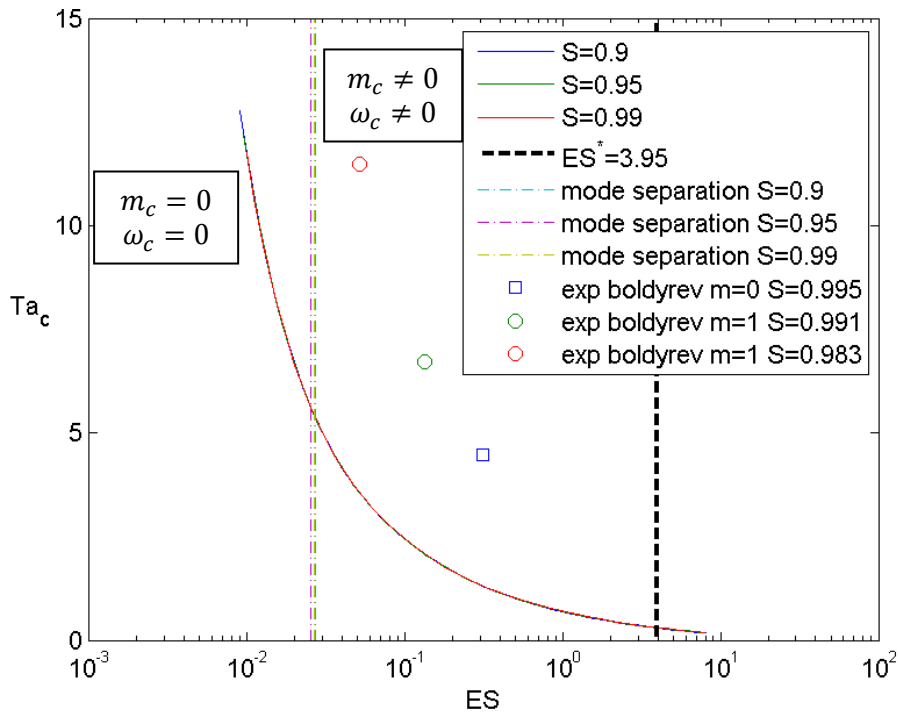


Figure 7.42 Threshold curve for the polymer solutions used in the experiment by Boldyrev et al. (2009) and corresponding experimental values for  $\eta = 0.903, S \in \{0.983, 0.991, 0.995\}$ .

We have performed the linear stability analysis with the conditions of the experiments of Boldyrev *et al.* ( $\eta = 0.903$ ) the critical curves are plotted in the figure 7.42. For weak values of  $ES$  the critical mode is axisymmetric and stationary while it is non-axisymmetric and oscillatory for large values of  $ES$ . The curve of the critical axial wavenumber is similar to the curve obtained for  $\eta = 0.8$  while the critical azimuthal wavenumber takes values from 0 to 3. The experimental points reported by Boldyrev *et al.* are located above the theoretical curve, moreover, the stationary axisymmetric mode is found in the zone of non-axisymmetric modes.

We have computed the critical modes for different values of viscosity ratio and elasticity and performed experiments with many solutions with well-controlled rheology. We have provided a more complete set of results of the VEI in Keplerian and anti-Keplerian regimes than previous studies. The experimental results are in good agreement with the LSA results so that the analogy between the VEI and the SMRI and HMRI is confirmed.

## 7.4. Conclusion

In this chapter we have studied theoretically and experimentally the viscoelastic instability in the Keplerian regime ( $\mu = \eta^{3/2}$ ) and the anti-Keplerian regime ( $\mu = \eta^{-3/2}$ ). The analogy between the VEI at different  $E$  and SMRI or HMRI has been established theoretically and confirmed experimentally with viscoelastic fluids

In the Keplerian regime, we have found a good agreement between the experimental and theoretical critical curves  $Ta_c(ES)$  if the elasticity is defined with the molecular relaxation time. We have observed two different modes in the Keplerian regime which are the Stationary and Axisymmetric vortex mode at small  $ES$  (analogy with SMRI) and the disordered modes at larger  $ES$  (analogy with HMRI). These two modes are different from the Taylor Vortex mode or the disordered vortices mode observed in the  $\mu = 0$  regime. The stationary axisymmetric mode is supercritical while the different disordered modes are subcritical. For large values of  $ES$ , the critical mode should be the purely elastic instability mode.

The anti-Keplerian regime is very similar to the  $\mu = \infty$  regime: critical modes are disordered vortices and the critical curves have the same shape and are parametrized by the elasticity  $E$  instead of the  $ES$ .



# Chapter 8: Viscoelastic instability in the intermediate regime of $\mu = \eta^3$

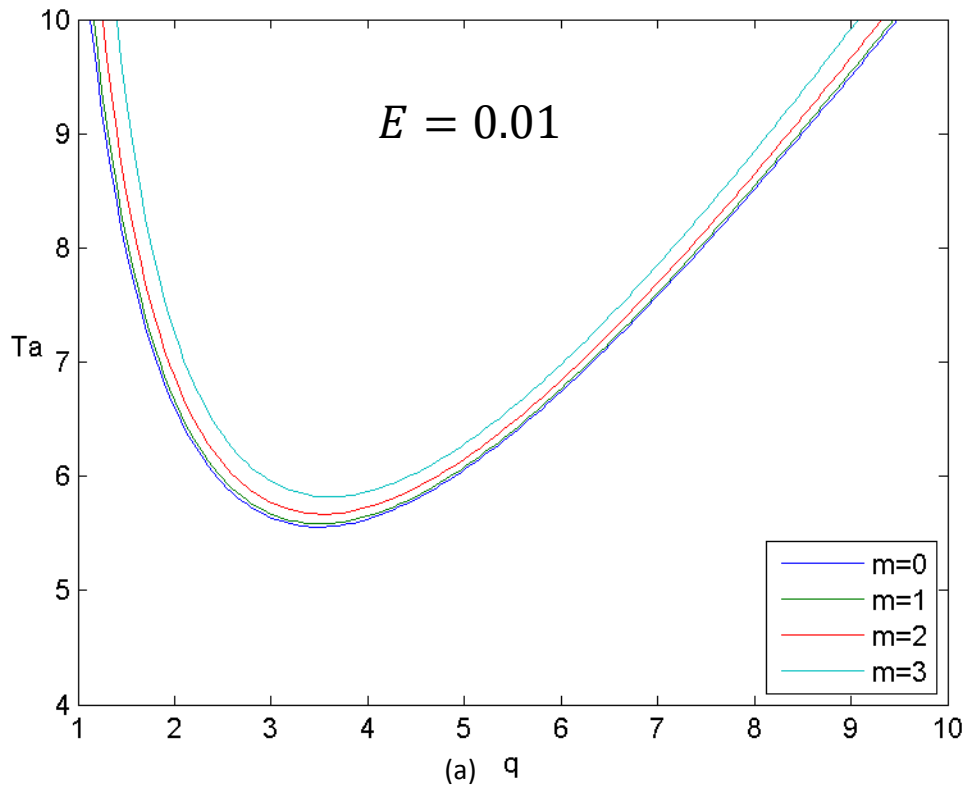
Following the theoretical analysis of Ogilvie-Potter [Ogilvie2008], we have analyzed the regime  $\mu = \eta^3$  where both the centrifugal force and the elasticity force intervene together as driving mechanisms of instability. This regime may be considered as an intermediate regime between the Keplerian regime and the inner cylinder rotating regime of  $\mu = 0$ . The study of Ogilvie-Potter was limited to  $\eta = 0.95$  and  $S = 0.5$ , we have investigated the case when  $\eta = 0.8$  and  $S \in [0.5, 0.8]$  corresponding to the experimental data.

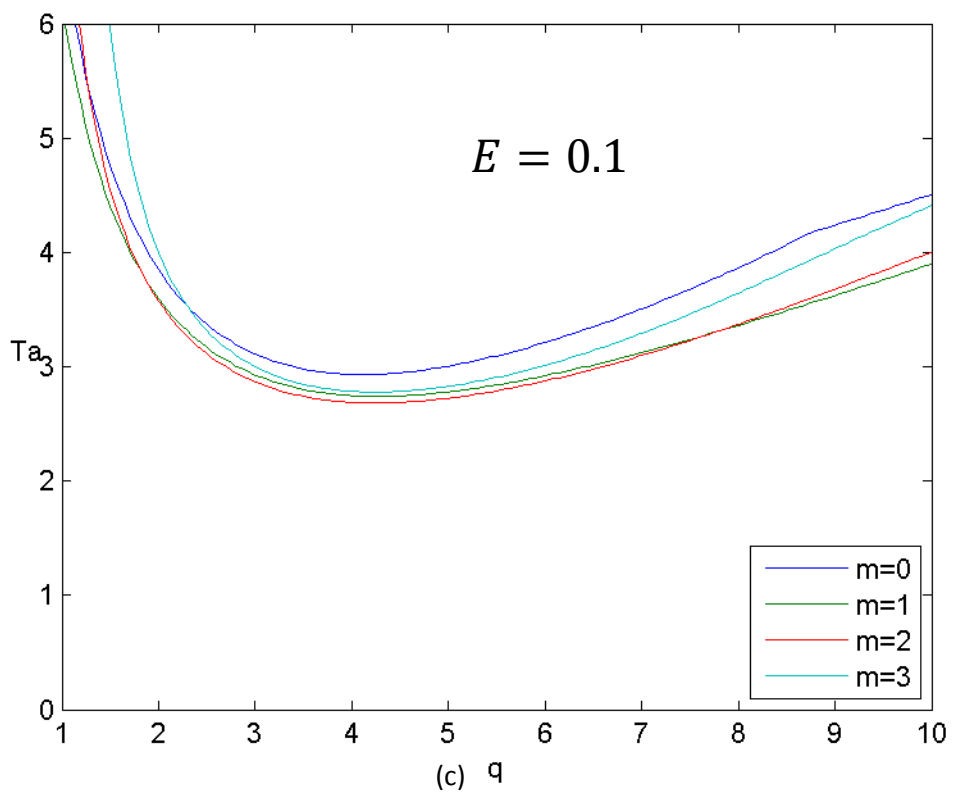
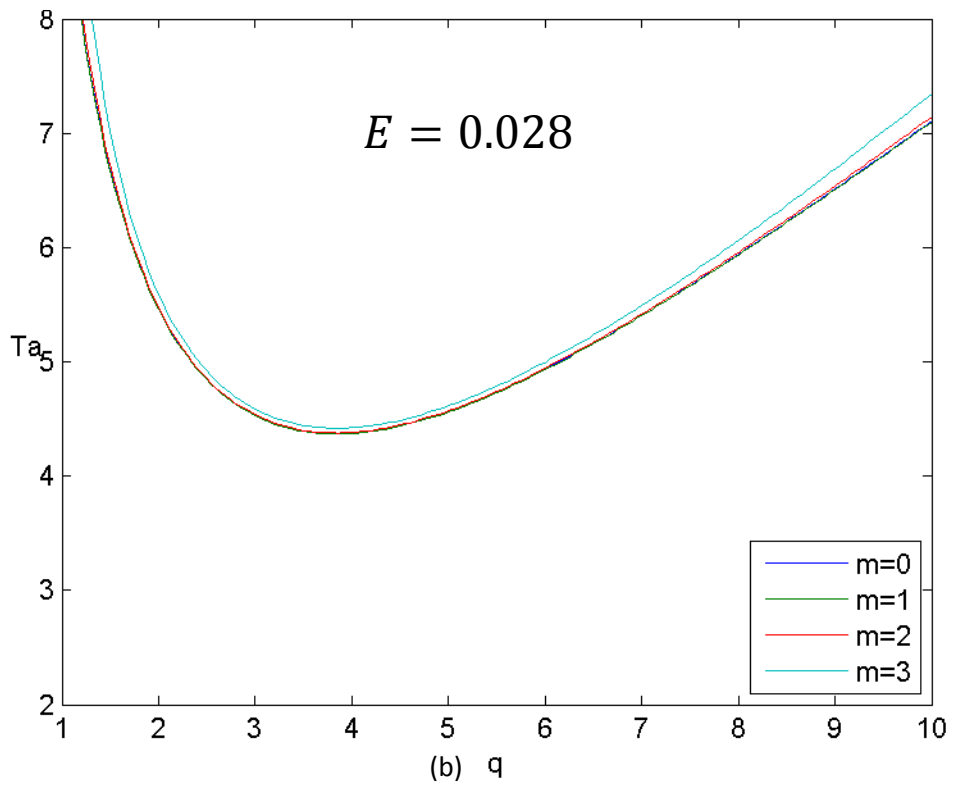
## 8.1. LSA results

According to Rayleigh stability criterion discussed in chapter 4, the Newtonian Couette flow in the intermediate rotation regime ( $\mu = \eta^3$ ) is unstable. In figure 4.1 the rotation line of  $\mu = \eta^3$  appears between  $\mu = 0$  and  $\mu = \eta^{3/2}$ . In the geometry of our experimental configuration  $\eta = 0.8$  we have  $\mu = 0.512$ .

### a. Marginal stability curves

The marginal stability curves  $Ta_c(q)$  are plotted in figure 8.1 for different values of the azimuthal wavenumber  $m$  and for  $E \in \{0.01, 0.028, 0.1, 1\}$  for fixed  $S = 0.7$ . For small  $E$  the marginal curves of different  $m$  are close to each other while for large  $E$  the bottom of the lowest marginal curve ( $m = 1$ ) is too flat to choose the critical wavenumber  $q_c \in [4.3, 5.8]$ .





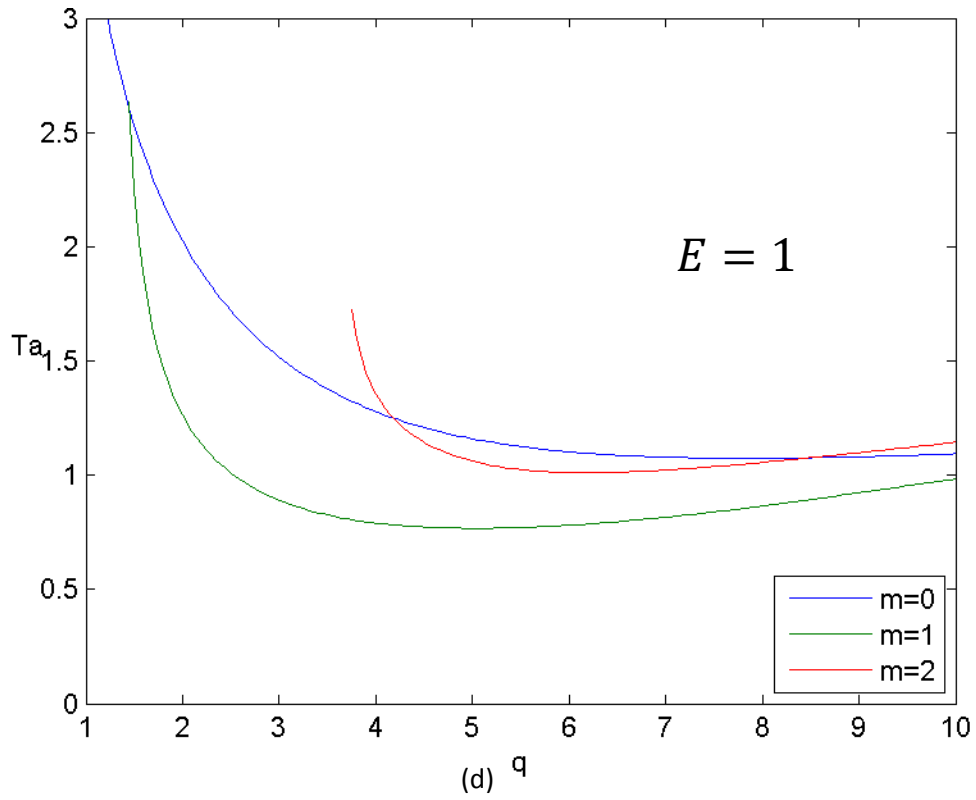


Figure 8.1: Marginal stability curves  $Ta_c(q)$  for different  $m$  for  $S = 0.7$  (a)  $E = 0.01$  (b)  $E = 0.028$  (c)  $E = 0.1$  (d)  $E = 1$  in regime  $\mu = \eta^3$ .

**b. Variation of the critical parameters with  $E$**

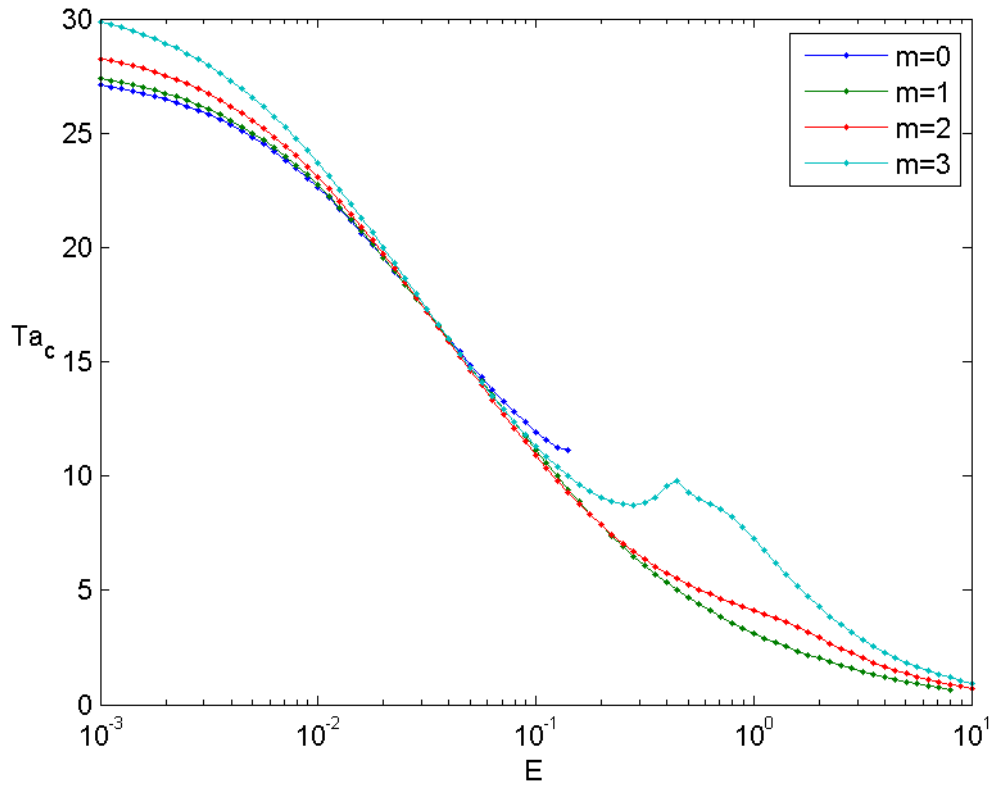
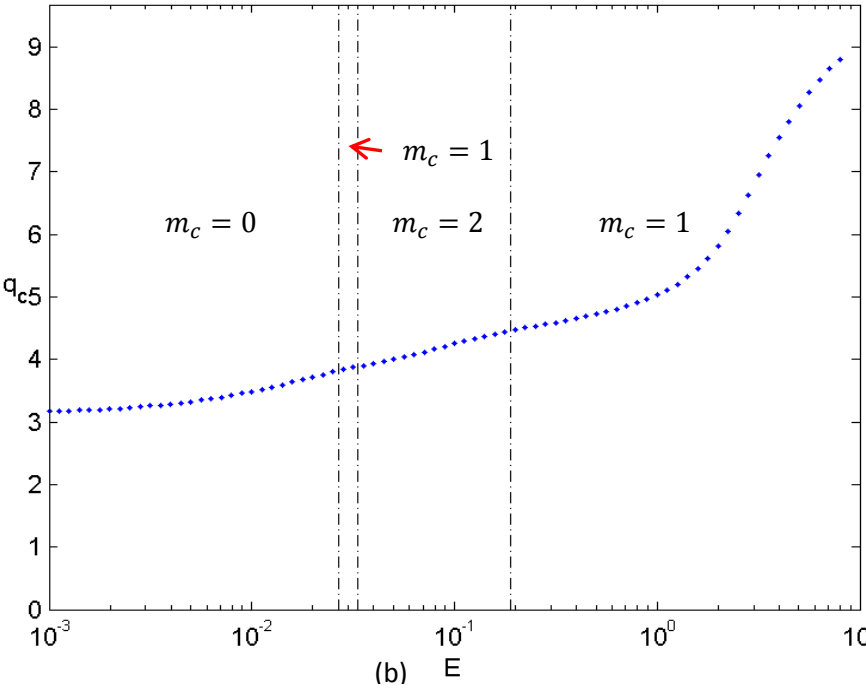
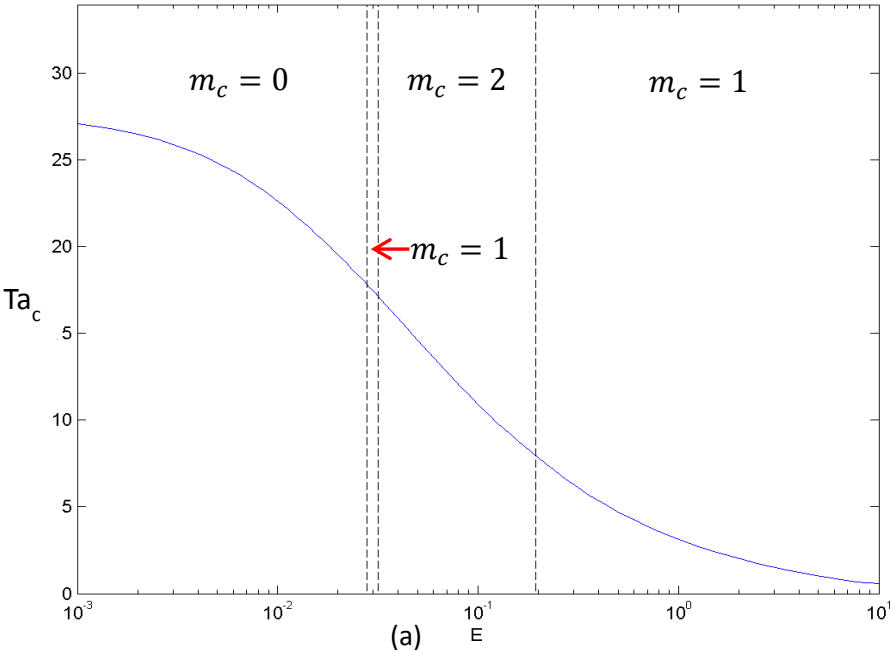


Figure 8.2: Critical curves,  $Ta_c(E)$  for different  $m$  for a solution with  $S = 0.7$  in regime  $\mu = \eta^3$ .

From the marginal stability curves, we illustrate the critical curves  $Ta_c(E)$  for different  $m$ . Taking  $S = 0.7$  as an example (figure 8.2), the critical curves for different  $m$  are close to each other and  $Ta_c$  decreases with  $E$ .

The critical curves corresponding to the lowest values of  $Ta_c(E)$  and to the critical wavenumbers  $q_c$  and frequency  $\omega_c$  are plotted in figure 8.3. At  $E = 0$ , the curves intersect the vertical axis at the value  $Ta_c = 27.77$  corresponding to the pure centrifugal instability. For very low values of  $E < 0.027$ , the critical modes are stationary axisymmetric modes and their wavenumber increases from  $q_c = 3.12$  very slowly with  $E$ . For values of  $E > 0.027$ , the critical modes are oscillatory non-axisymmetric modes ( $m_c \neq 0, \omega_c \neq 0$ ), their wavenumber increases linearly with  $E$  up to  $E \sim 1.5$ . For larger  $E$ , the critical wavenumber  $q_c$  increases sharply with  $E$  as the elasticity is dominant the centrifugal force.



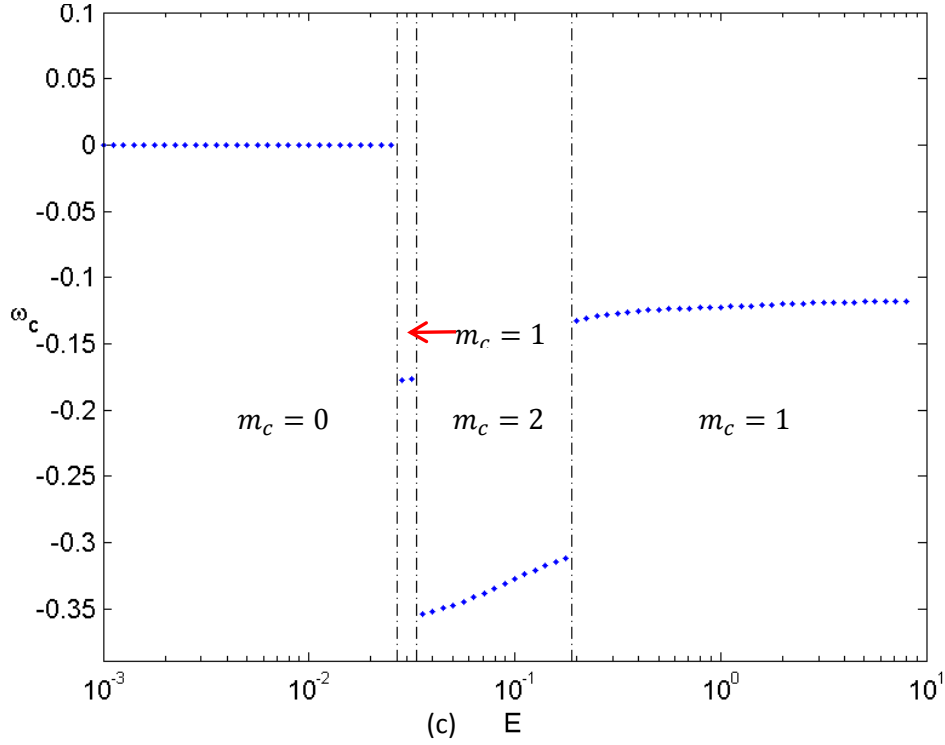


Figure 8.3: Variation of the critical parameters with  $E$  for  $S = 0.7$  in  $\mu = \eta^3$  regime: (a) Threshold  $Ta_c$ , (b) critical wavenumber  $q_c$ , (c) critical frequency  $\omega_c$ .

The non-axisymmetric modes depend on the elasticity  $E$ . There are three codimension 2 points, critical parameters of which are given in table 8.1.

$E$	$Ta_c$	$q_c$	$m_c$	$\omega_c$
0.027	18.1	3.80	0	0
		3.84	1	-0.178
0.034	16.9	3.88	1	-0.177
		3.90	2	-0.354
0.189	8.09	4.44	2	-0.312
		4.48	1	-0.132

Table 8.1: Codimension-two points for  $S = 0.7$  in the intermediate rotation regime  $\mu = \eta^3$ .

The cross-section  $(r, z)$  of flow patterns of the azimuthal component of the vorticity are shown in figure 8.4. More properties of these four flow patterns are shown from figure 8.5 to figure 8.8. The shape of the azimuthal vorticity distribution in the gap changes as the elasticity increases from stationary to nonaxisymmetric modes. The instability generates the second normal stress difference and the ratio  $N_2/N_1$  decreases with  $E$  suggesting that in the purely elastic modes, the first normal stress difference plays a crucial role while the second one should be neglected. This result should be verified in DNS.

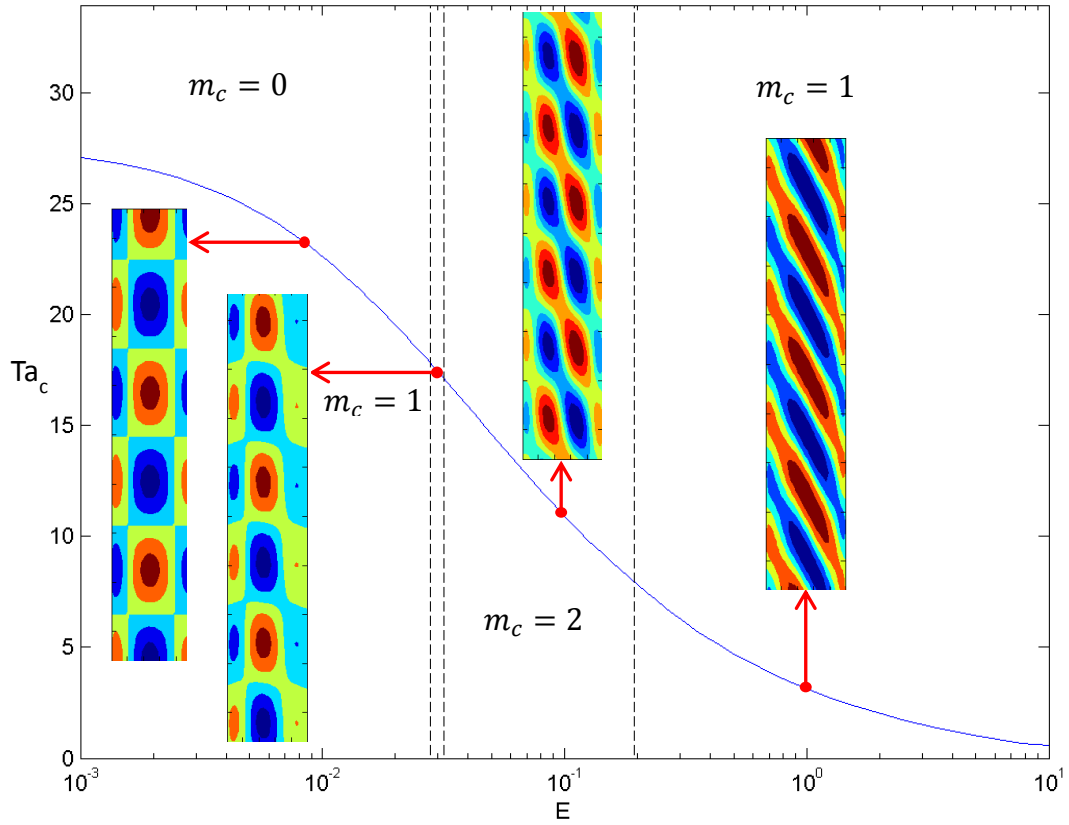


Figure 8.4: Cross-section  $(r, z)$  of the azimuthal component of the vorticity for  $S = 0.7$  in  $\mu = \eta^3$  regime.

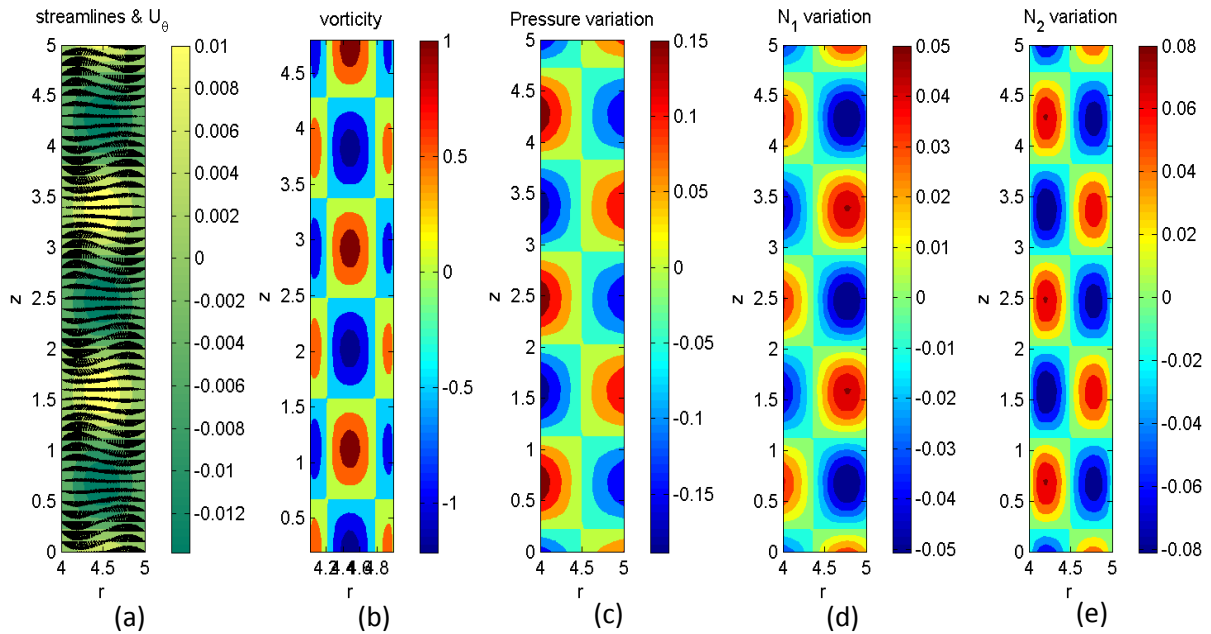


Figure 8.5: Critical mode for  $S = 0.7$ ,  $E = 0.01$ ,  $Ta_c = 86.6$  in  $\mu = \eta^3$  regime, with  $m = 0$ ,  $q_c = 3.49$ ,  $\omega_c = 0$ . (a) Black arrows represent the velocity field in  $(r, z)$  direction while the colors represent the azimuthal velocity  $V$  (b) the vorticity  $\omega_\theta$  (c) the pressure variation (d) the  $N_1$  variation (e) the  $N_2$  variation. Color maps of (b, c, d, e) represent the relative amplitude.

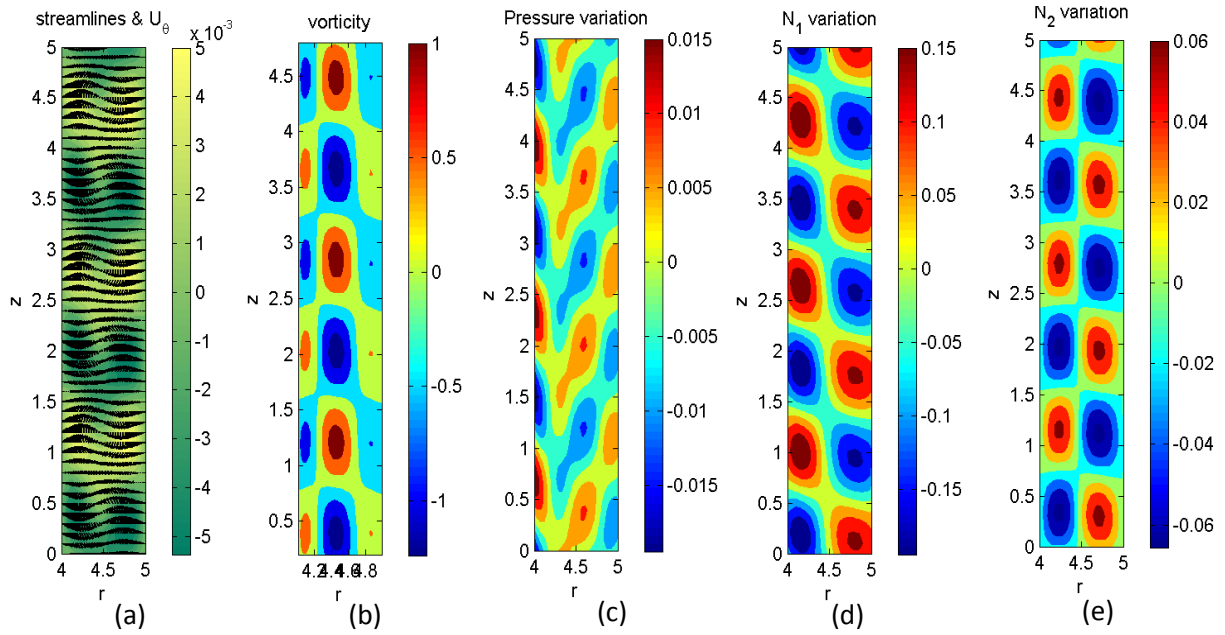


Figure 8.6: Critical mode for  $S = 0.7$ ,  $E = 0.028$ ,  $Ta_c = 52.4$  in  $\mu = \eta^3$  regime, with  $m = 1$ ,  $q_c = 3.84$ ,  $\omega_c = -0.178$ . (a) Black arrows represent the velocity field in  $(r, z)$  direction while the colors represent the azimuthal velocity  $V$  (b) the vorticity  $\omega_\theta$  (c) the pressure variation (d) the  $N_1$  variation (e) the  $N_2$  variation. Color maps of (b, c, d, e) represent the relative amplitude.

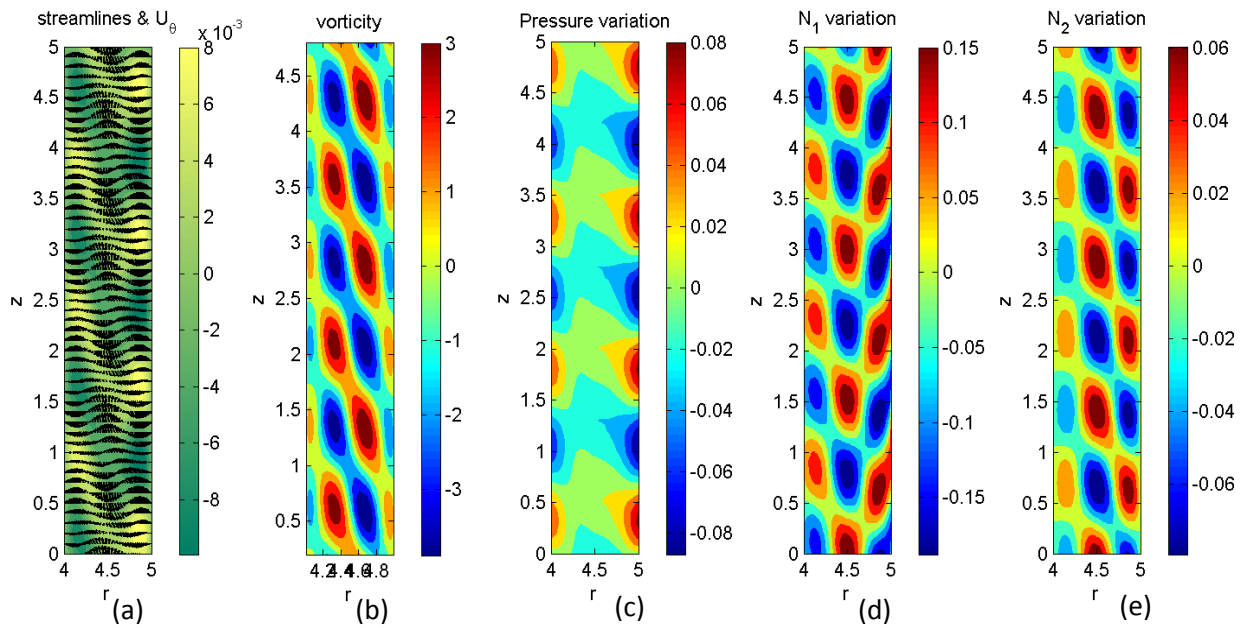


Figure 8.7: Critical mode for  $S = 0.7$ ,  $E = 0.1$ ,  $Ta_c = 32.2$  in  $\mu = \eta^3$  regime, with  $m = 2$ ,  $q_c = 4.25$ ,  $\omega_c = -0.327$ . (a) Black arrows represent the velocity field in  $(r, z)$  direction while the colors represent the azimuthal velocity  $V$  (b) the vorticity  $\omega_\theta$  (c) the pressure variation (d) the  $N_1$  variation (e) the  $N_2$  variation. Color maps of (b, c, d, e) represent the relative amplitude.

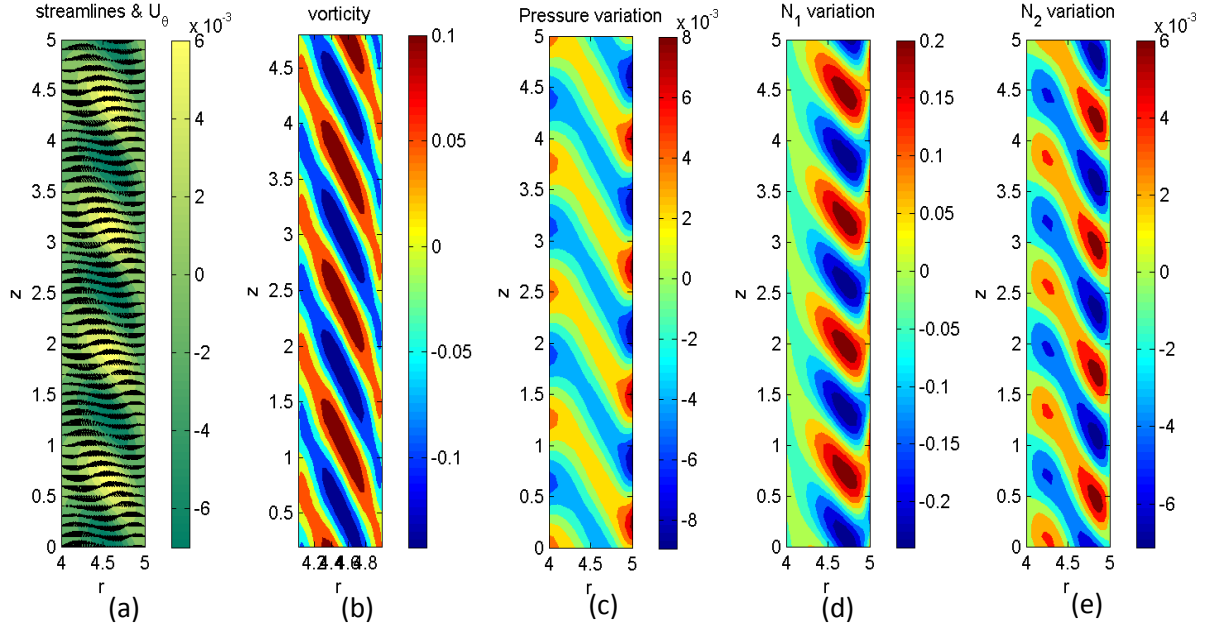


Figure 8.8: Critical mode for  $S = 0.7$ ,  $E = 1$ ,  $Ta_c = \text{in } \mu = \eta^3$  regime, with  $m = 1$ ,  $q_c = 5.03$ ,  $\omega_c = -0.122$ . (a) Black arrows represent the velocity field in  $(r, z)$  direction while the colors represent the azimuthal velocity  $V$  (b) the vorticity  $\omega_\theta$  (c) the pressure variation (d) the  $N_1$  variation (e) the  $N_2$  variation. Color maps of (b, c, d, e) represent the relative amplitude.

The comparison of the critical modes of the intermediate regime with the other regimes ( $\mu = 0$  regime, figure 6.3 – 6.7) and the Keplerian regime, figure 7.3 – 7.9) shows the similarity of critical modes and critical curves between the intermediate regime and the  $\mu = 0$  regime at small  $E$ : the critical modes are stationary axisymmetric modes (the Taylor Vortex) due to centrifugal force. While for large values of  $E$ , the intermediate regime yields results similar to those of the Keplerian regime.

### c. Effect of the viscosity ratio $S$ on the critical states

To complete the comparison the critical curves of  $Ta_c(ES)$  for different  $S$  are presented in figure 8.9. For  $ES < 0.08$ , different critical curves are merged into one curve, and for  $E > 0.08$ , the critical curves diverge slightly from each other and the viscosity ratio becomes stabilizing.

The variation of the critical curves  $Re_c(Wi_c)$  for different  $S$  is given in figure 8.10. The critical curves for different  $S$  cross the vertical axis of  $Wi_c = 0$  at the same point of  $Re_0 = 58.9$ . The critical curves decrease with  $Wi_c$  and cross the horizontal axis of  $Re_c = 0$  at different values of  $Wi_0$ , threshold of the elastic instability, which depend on the value of  $S$ .

The variation of  $Ta_c$  with the modified Weissenberg number  $K_c$  for different  $S$  (figure 8.11) shows that the curves start at the same point corresponding to the threshold of the pure centrifugal instability ( $K_c = 0$ ). Then they diverge as  $Wi_c$  increases. The different curves intersect all in the cross point  $K^* = 1.72, Ta_c^* = 5.6$ . Like in the Keplerian regime, this cross point separates state diagram into two zones in which the viscosity ratio plays opposite role: is destabilizing for  $K_c < K^*$  and stabilizing for  $K_c > K^*$ . The presence of the precise cross point is another evidence of the similarity between the intermediate regime and the Keplerian regime at large  $E$ . The colored dashed lines separate the stationary axisymmetric mode and the oscillatory non-axisymmetric mode.

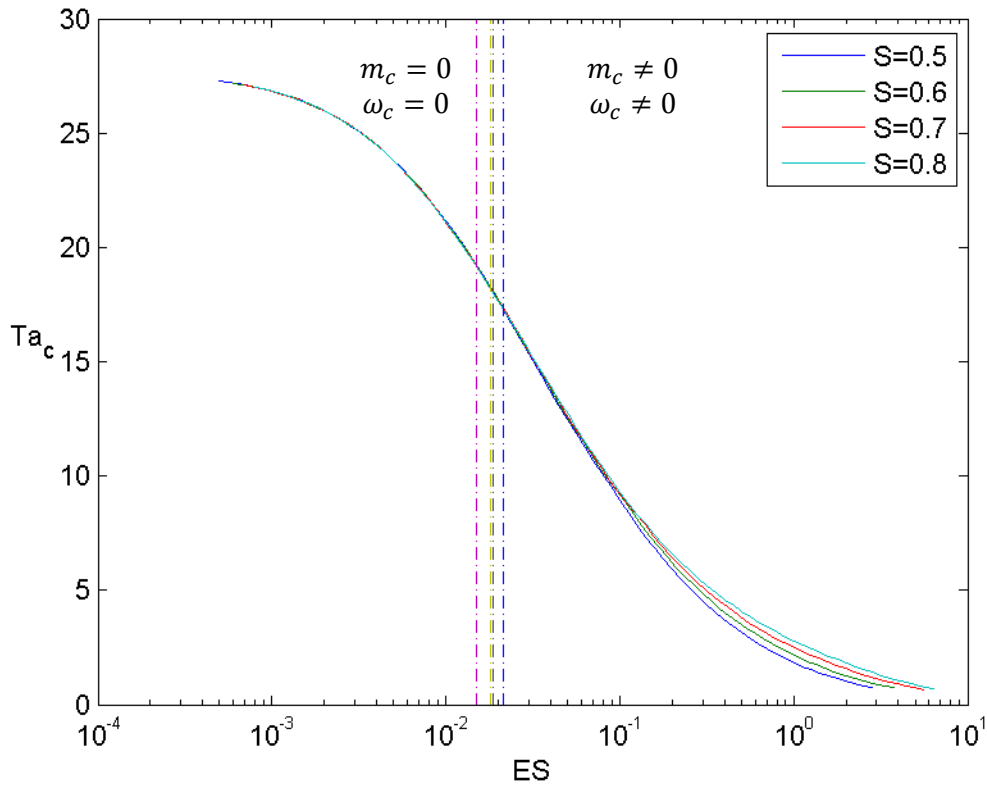


Figure 8.9: Critical curves  $Ta_c(ES)$  for different  $S$  in  $\mu = \eta^3$  regime. The colored dashed lines separate the stationary axisymmetric mode from the oscillatory non-axisymmetric mode by LSA.

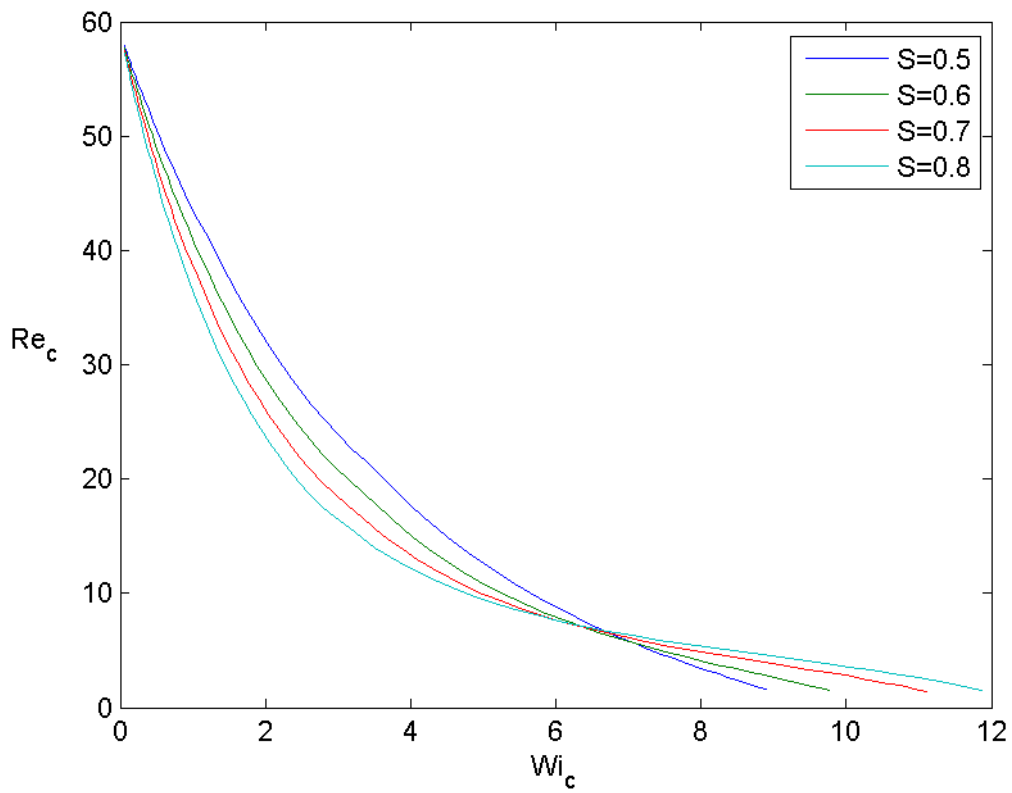


Figure 8.10: Critical curves,  $Re_c(Wi_c)$  for different  $S$  in  $\mu = \eta^3$  regime.

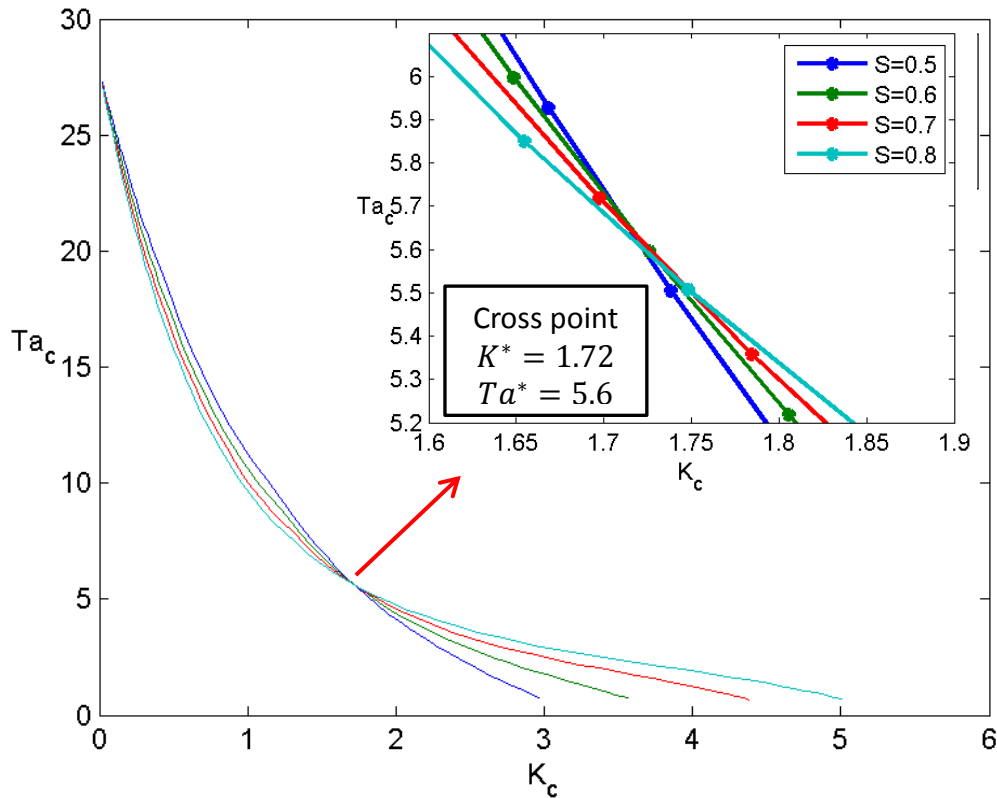


Figure 8.11: Critical curves,  $Ta_c(K_c)$  for different  $S$  in  $\mu = \eta^3$  regime.

## 8.2. Experimental results

In the experiment, five viscoelastic solutions have been tested in the intermediate regime  $\mu = \eta^3$ .

### a. Flow patterns

Among the five experimental points, we have observed 2 different unstable modes: the Ribbons mode at small  $ES$  (figure 8.12) and the Disordered Waves mode at large  $ES$  (figure 8.13). The Ribbons mode is the same mode observed in the  $\mu = 0$  regime while the Disordered Waves mode is the same mode observed in the Keplerian regime.

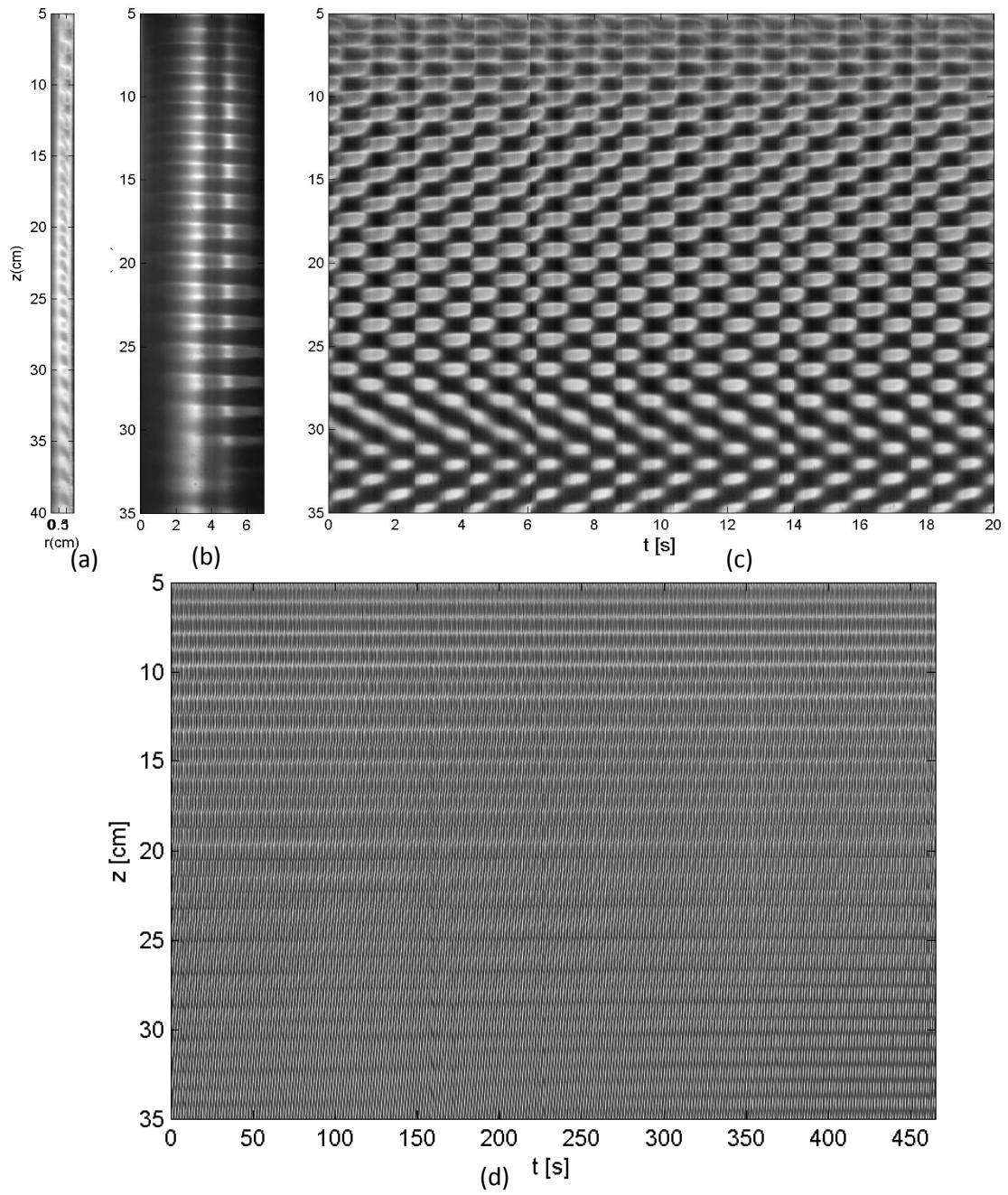


Figure 8.12: Flow patterns and space-time diagram of the Ribbons mode on  $\mu = \eta^3$  regime for  $Ta_c = 13.73$ ,  $E_m = 1.06$ ,  $S = 0.47$ . (a) Gap view (b) Front view by laser sheet (c) Space-time diagram. (d) Longtime space-time diagram.

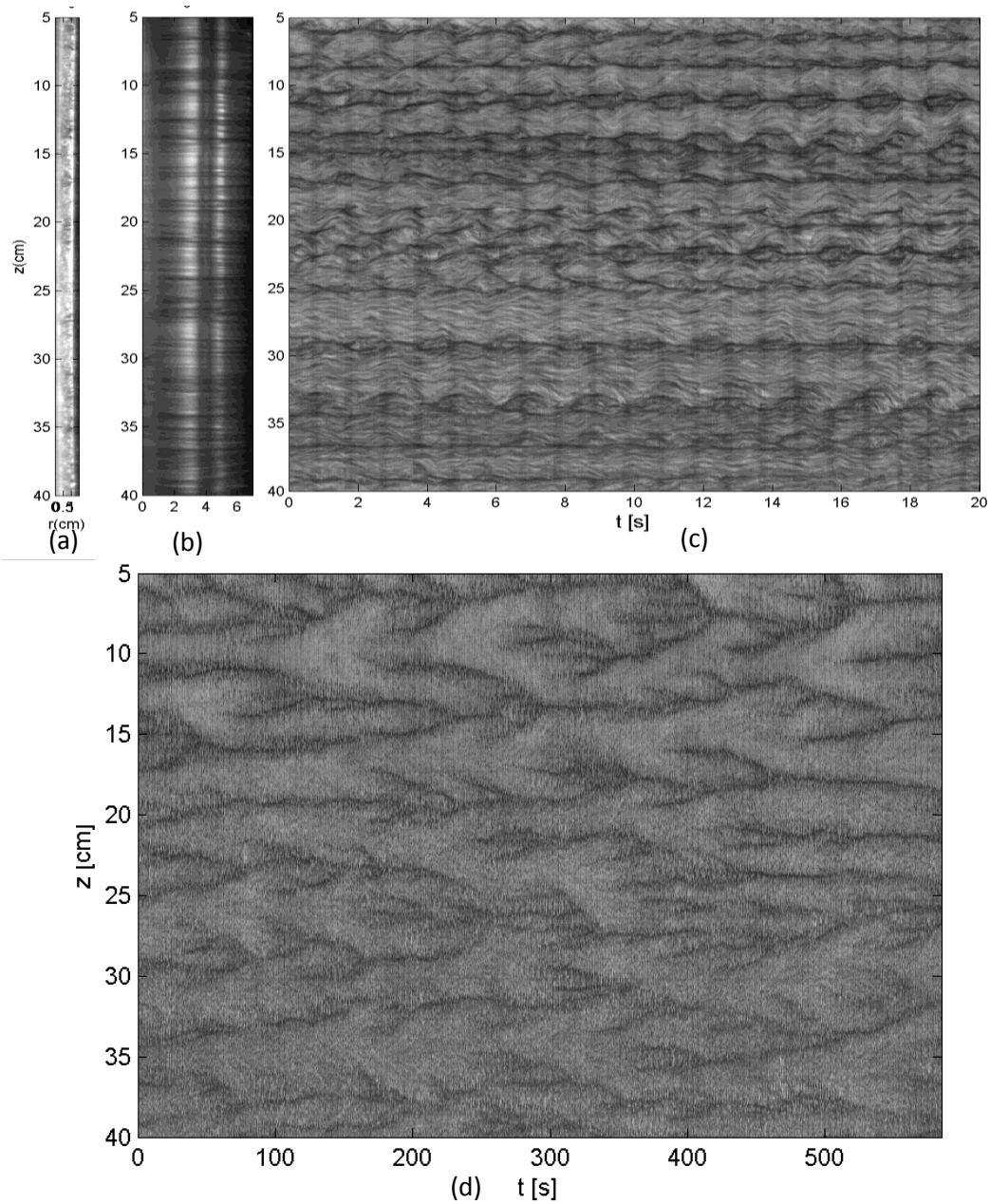


Figure 8.13: Flow patterns and space-time diagram of the Disordered Waves mode on  $\mu = \eta^3$  regime at  $Ta_c = 4.66$ ,  $E_m = 0.34$ ,  $S = 0.5$ . (a) Gap view (b) Front view by laser sheet (c) Space-time diagram. (d) Longtime space-time diagram.

To make sure that the unstable mode at large  $ES$  is the Disordered Waves mode not the Disordered Vortices mode, we plot also in figure 8.14 the transient space-time diagram from laminar flow to unstable flow and the Fourier spectrums related to this diagram. Counter propagating waves interact to form propagating ribbons and the disordered waves and the peak of the wave in the time spectrum is distinct from the rotating cylinders.

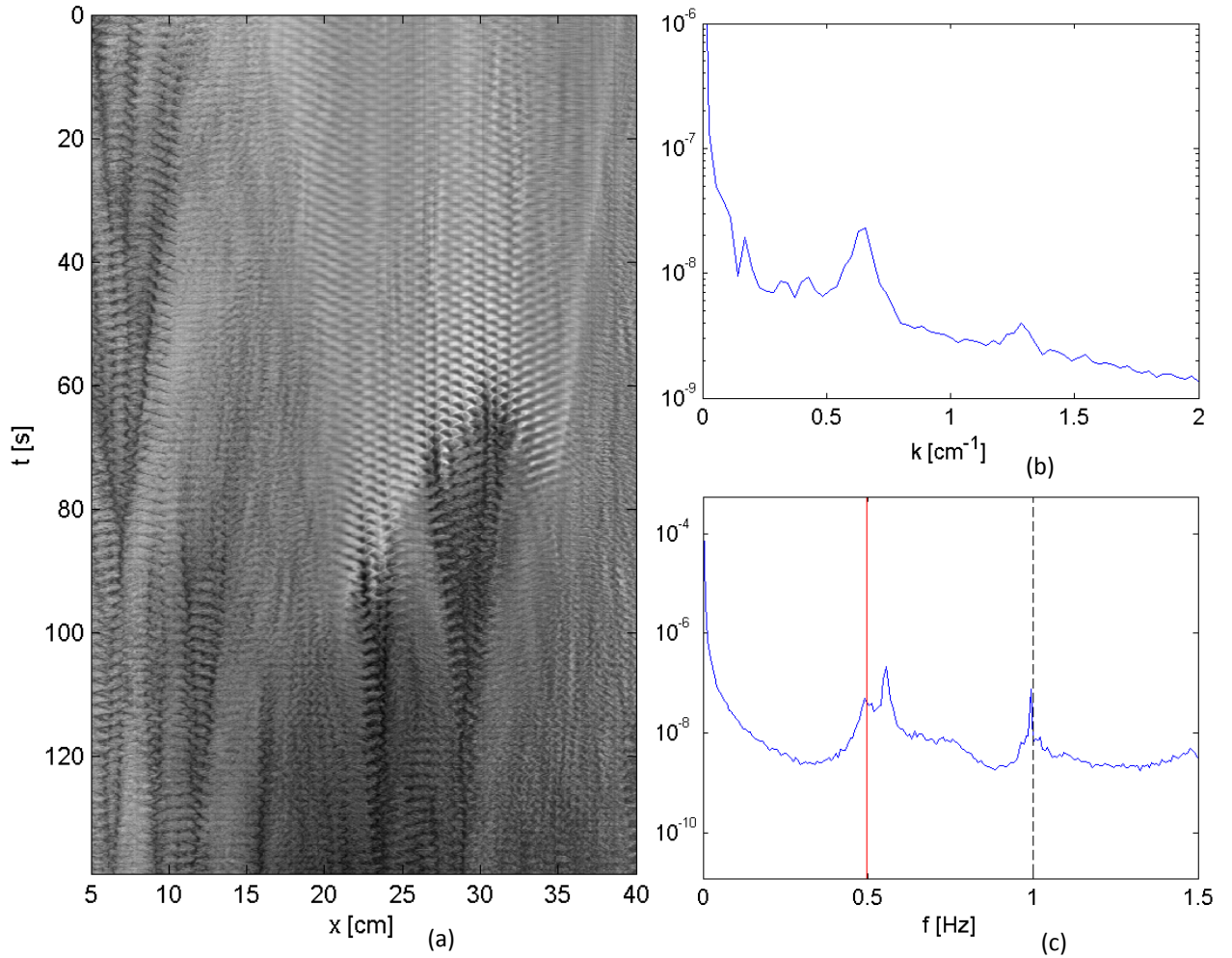


Figure 8.14: Transient space-time diagram and Fourier spectrums of the Disordered Waves mode on  $\mu = \eta^3$  regime at  $Ta_c = 4.66, E_m = 0.34, S = 0.5$ . (a) Space-time diagram (b) space spectrum (c) time spectrum. Red solid line – outer cylinder rotation frequency. Red dashed line – inner cylinder rotation frequency. Black dashed line – flicker frequency of the spot light.

### **b. Comparison with LSA results**

The experimental critical values  $Ta_c(ES)$  with  $E$  defined by three different relaxation times ( $\tau_e, \tau_m, \tau_{N1}$ ) are plotted together with the LSA critical curves (figure 8.15). We observe that the experimental critical points decrease with  $ES$  as predicted by the LSA critical curves. The LSA critical curves go through the three definitions of the elasticity: at small values of  $ES$ , the LSA critical curves are close to experimental points with  $E$  defined with  $N_1$  and at large  $ES$  the LSA critical curves are close to experimental points with  $E$  defined with the extensional relaxation time. The colored dashed lines separate the stationary axisymmetric mode from the oscillatory non-axisymmetric mode by LSA. It is difficult to say whether these mode separation lines correspond to the experiments or not because of the lack of experiments of stationary axisymmetric mode in small  $ES$ .

We resume the variation of the experimental  $\omega_c$  and  $q_c$  with  $ES$  defined by the molecular relaxation time together with the LSA predictions is shown in figure 8.16 and 8.17, though we have only tested five solutions in this regime. We can see that the experimental  $\omega_c$  and  $q_c$  follow the trend of the LSA prediction.

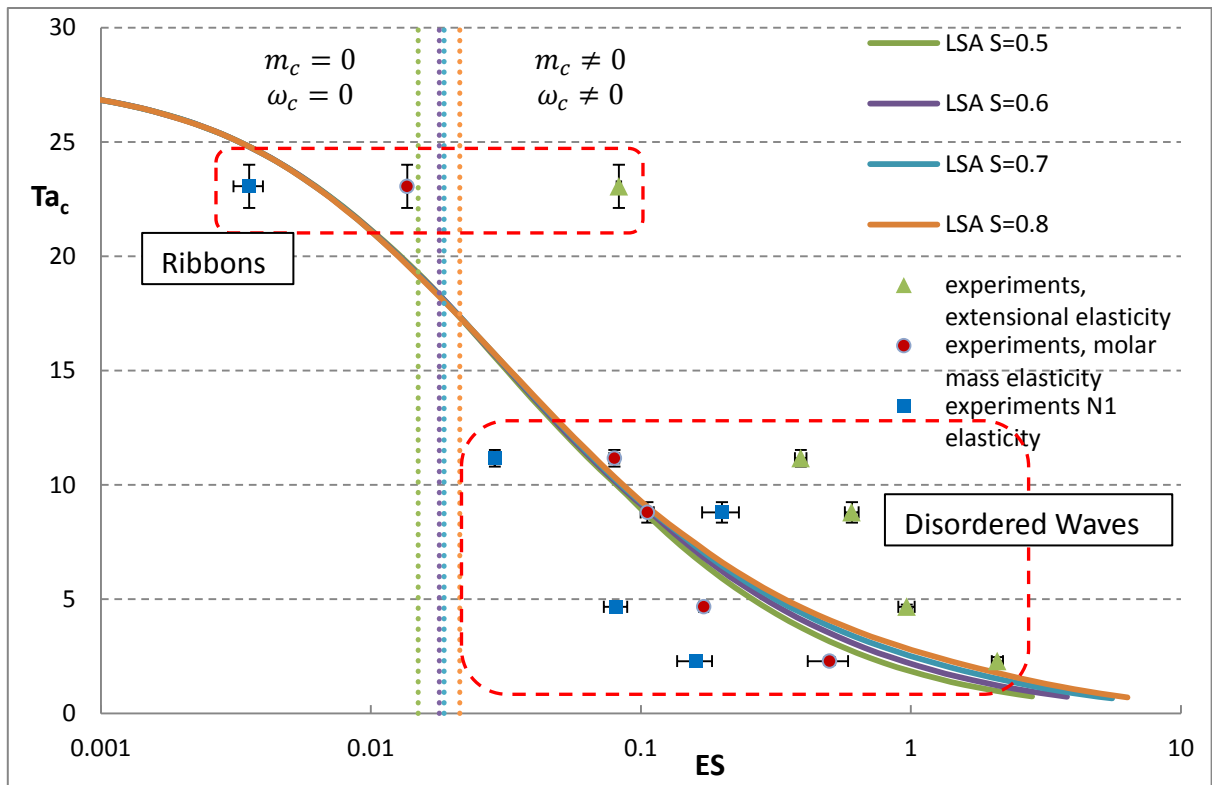


Figure 8.15: Variation of the critical values with  $ES$  on  $\mu = \eta^3$  regime. Solid lines – LSA critical curves for different  $S$ . Solid points – experimental transient values, 3 colors represent the 3 different definitions of elasticity. The colored dashed lines separate the stationary axisymmetric mode from the oscillatory non-axisymmetric mode by LSA.

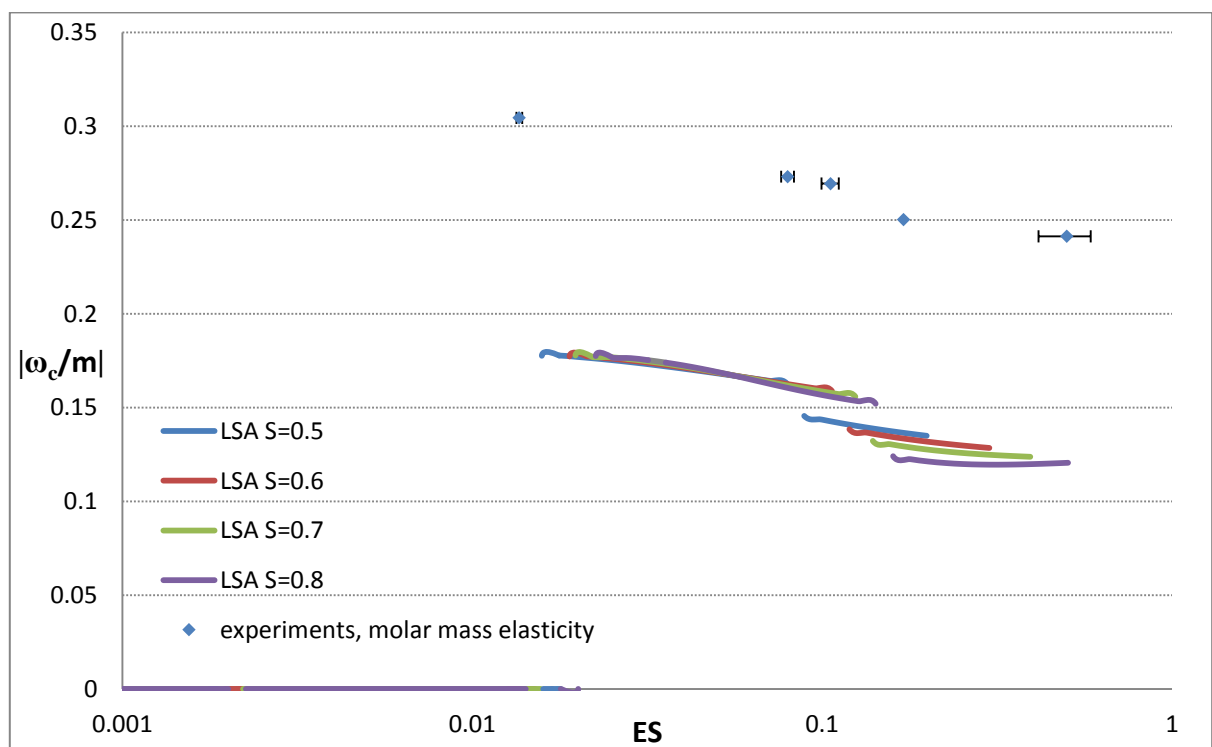


Figure 8.16: Variation of the critical angular velocity with  $ES$  defined by the molecular relaxation time. Solid lines – LSA predictions for different  $S$ . Solid points – experimental angular velocity.

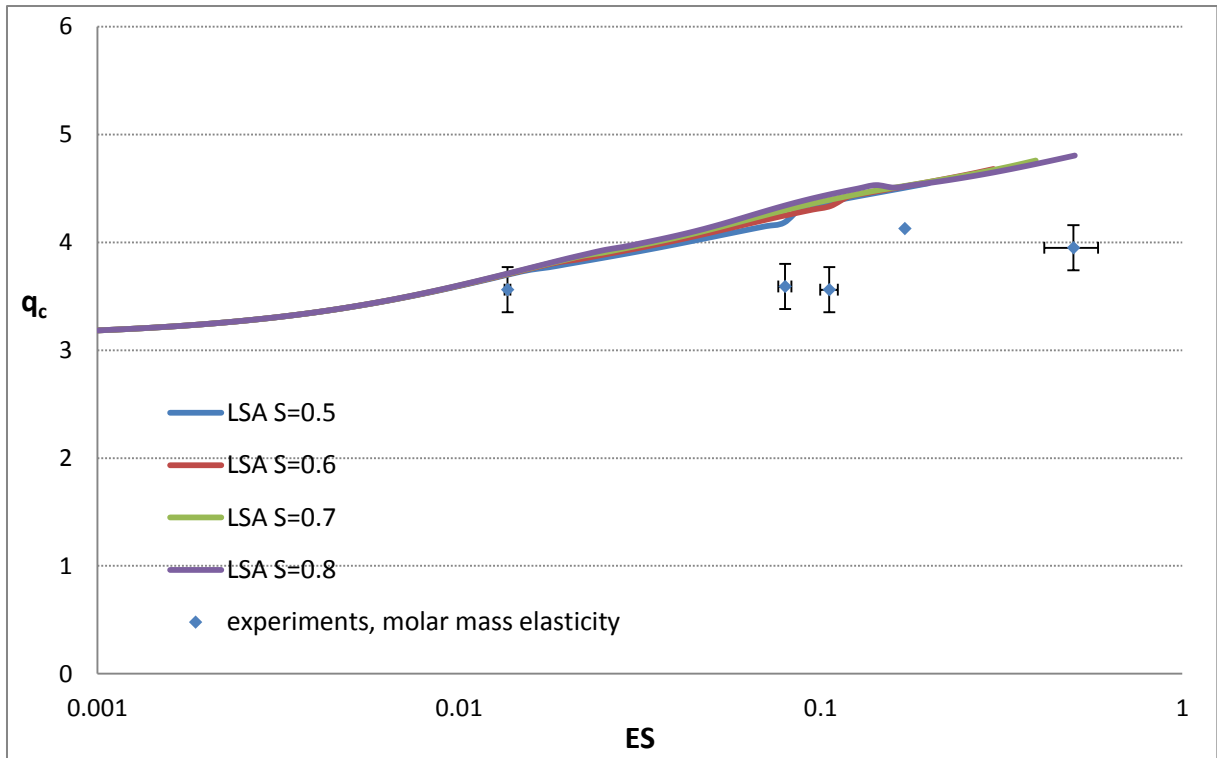


Figure 8.17: Variation of the critical axial wave number with  $ES$  defined by the molecular relaxation time. Solid lines – LSA predictions for different  $S$ . Solid points – experimental critical wave numbers.

### 8.3 Conclusion

To conclude the analysis of this intermediate regime of  $\mu = \eta^3$ , we have found that the viscoelastic instability in the  $\mu = \eta^3$  regime resembles the  $\mu = 0$  regime for small  $E$  while it resembles the Keplerian regime for large  $E$ . For very large values of the elasticity, the purely elasticity mode should be critical for small values of shear rate.



# Chapter 9: Pure elastic instability

---

In this chapter we revisit the special case of the purely elastic instability for all investigated regimes in the limit  $Re \rightarrow 0$  corresponding to  $E \rightarrow \infty$ . The goal is to search for the universal scaling between flow parameters to get a better description of the purely elastic instability.

In the limit of  $Re = 0$  and  $E = \infty$  with finite  $Wi = ERe$ , the dimensionless general equations 2.20 reduce to:

$$\begin{aligned} \nabla \cdot \vec{U} &= 0 \\ 0 &= -\nabla \Pi + \nabla \cdot \bar{T}^p + (1 - S)\nabla^2 \vec{U} \\ \bar{T}^p + Wi \left[ \frac{\partial \bar{T}^p}{\partial t} + \vec{U} \cdot \nabla \bar{T}^p - (\nabla \vec{U})^T \cdot \bar{T}^p - \bar{T}^p \cdot \nabla \vec{U} \right] &= S[\nabla \vec{U} + (\nabla \vec{U})^T] \end{aligned} \quad 9.1$$

## 9.1. LSA results

The purely elastic instability was first studied theoretically and experimentally by Larson et al. [Larson1990]. However their linear stability analysis is limited to the small gap limit. We have already recalculated the case of Larson et al. and similar critical curves are observed (see figure 4.8). Based on the equations 9.1 we calculated the critical Weissenberg number  $Wi_0$  and the corresponding critical wave numbers  $q_c$  and  $m_c$  and critical frequency  $\omega_c$  for different  $S$  and different rotational regimes.

### a. Marginal stability curves

The marginal stability curves  $Wi(q)$  are plotted in figure 9.1 for different  $m$  for  $S = 0.5$  and  $S = 0.8$ . For  $S = 0.5$  the lowest marginal curve  $m = 1$  possesses a clear minimum so that it is easy to determine a critical wavenumber  $q_c$ . For  $S = 0.8$ , the bottom of the marginal curve ( $m = 0$ ) is so flat that several axisymmetric modes of different  $q \in [12, 14.6]$  are critical. A similar result was obtained by Joo & Shaqfeh [Joo1992]. These modes may interact with each other and lead to more complex dynamics, analysis of which is beyond the framework of the LSA.

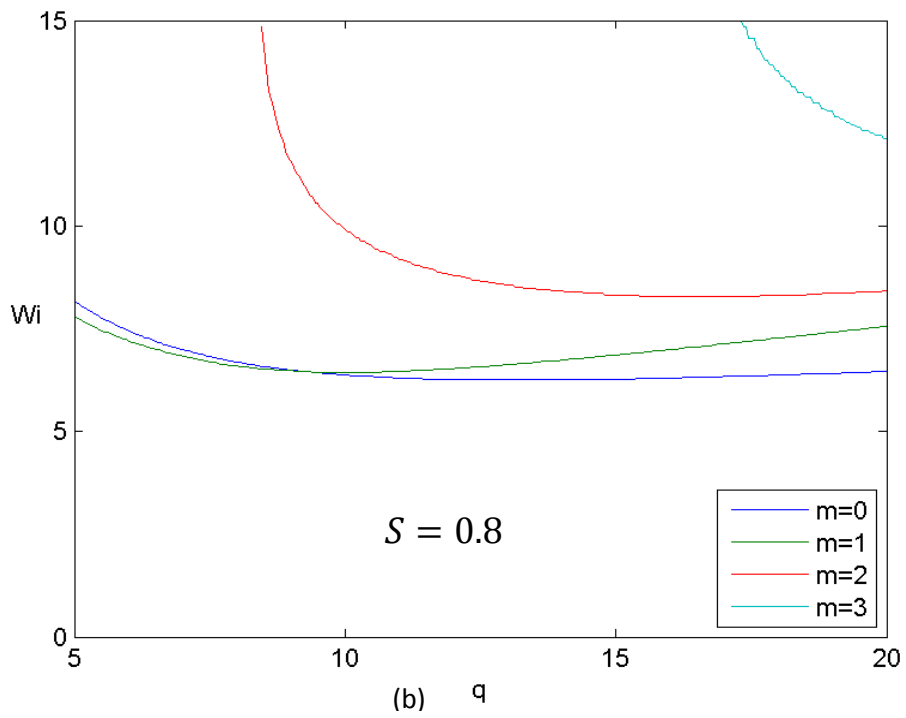
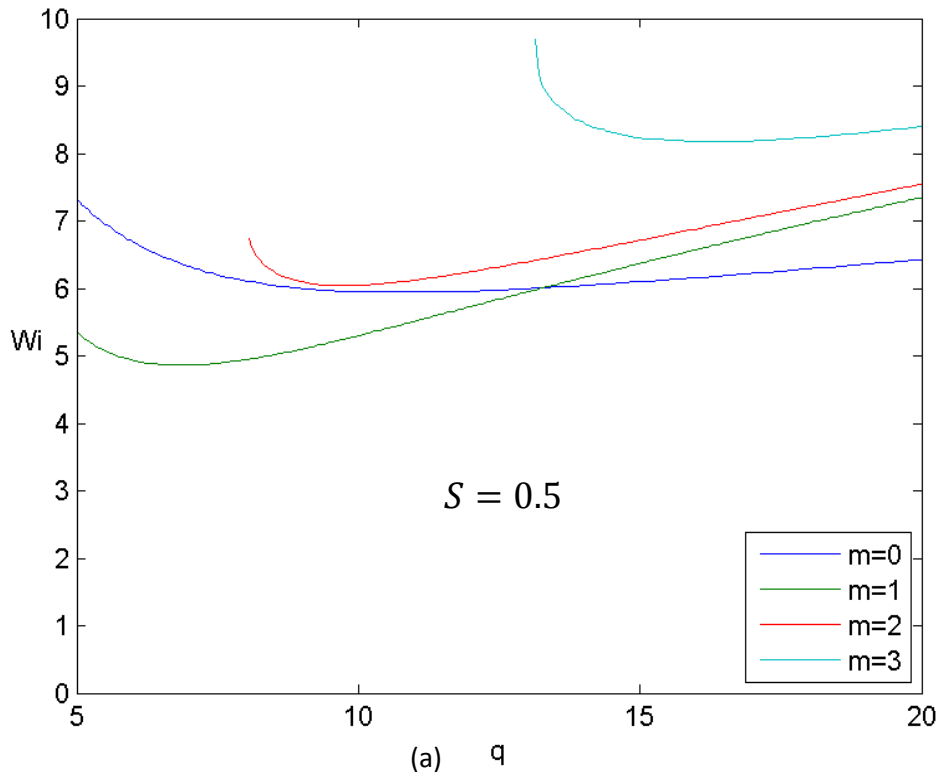


Figure 9.1: Marginal stability curves of the purely elastic limit in Keplerian regime for (a)  $S = 0.5$  and (b)  $S = 0.8$ .

b. Variation of the critical modes with  $S$

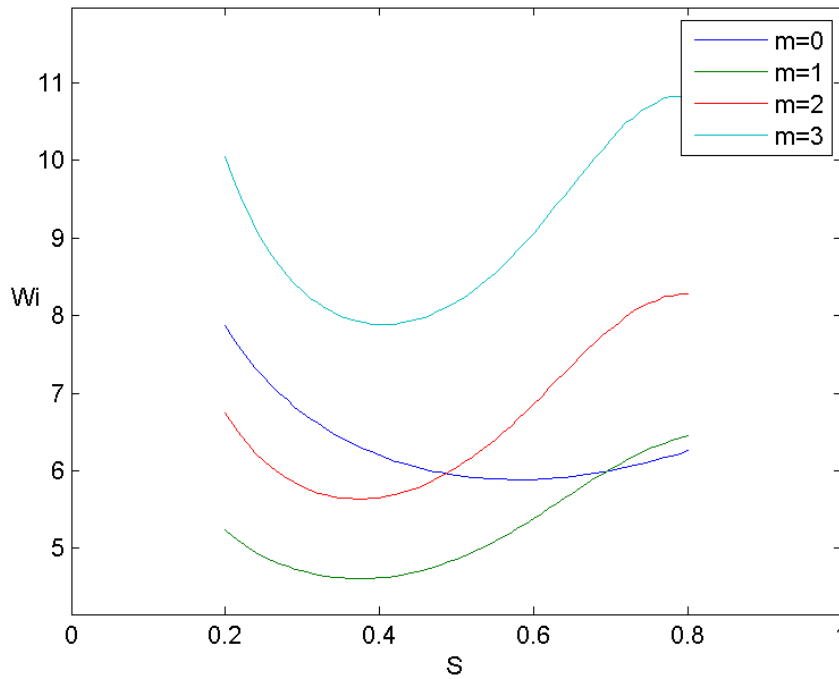


Figure 9.2: Critical curves  $Wi(S)$  for different  $m$  at  $q_c$  on Keplerian regime.

Taking the Keplerian regime as an example, we plot in figure 9.2 the critical curves of  $Wi(S)$  for different  $m$ . We observe that as  $S$  increases,  $Wi$  decreases to a minimal value of  $Wi$  for  $S < S_0$  and then increases for  $S > S_0$ . The value  $S_0$  yielding the minimum of  $Wi$  depends on  $m$ . The mode  $m = 1$  possesses the smallest  $Wi$  at  $S_0 = 0.375$  so that it is the most unstable mode for  $S < S_1$  with  $S_1 = 0.695$ . When  $S > S_1$ , the axisymmetric mode  $m = 0$  becomes most unstable. So in the Keplerian regime, the viscoelastic solution with a viscosity ratio  $S_0 = 0.375$  requires a minimal shear rate to generate a purely elastic instability in form of oscillating non axisymmetric modes. For solutions with  $S > 0.695$ , the critical modes are oscillatory axisymmetric. The point  $(S_1, Wi_1)$  is a codimension 2 point.

The variation with  $S$  of the smallest values of  $Wi$  which are the critical values of the purely elastic instability is shown in figure 9.3 for different rotational regimes. The critical curves are ordered from top to bottom  $Wi(\mu = \eta^{-3/2}) > Wi(\mu = \infty) > Wi(\mu = 0) > Wi(\mu = \eta^3) > Wi(\mu = \eta^{3/2})$ . These curves are similar to each other, meaning that they may not depend on the rotation rate. In particular, they share the same  $S_0 = 0.375$  for the minimum of  $Wi$  and the same abscissa  $S_1 = 0.695$  of the codimension 2 point which separates the non-axisymmetric mode and the axisymmetric mode.

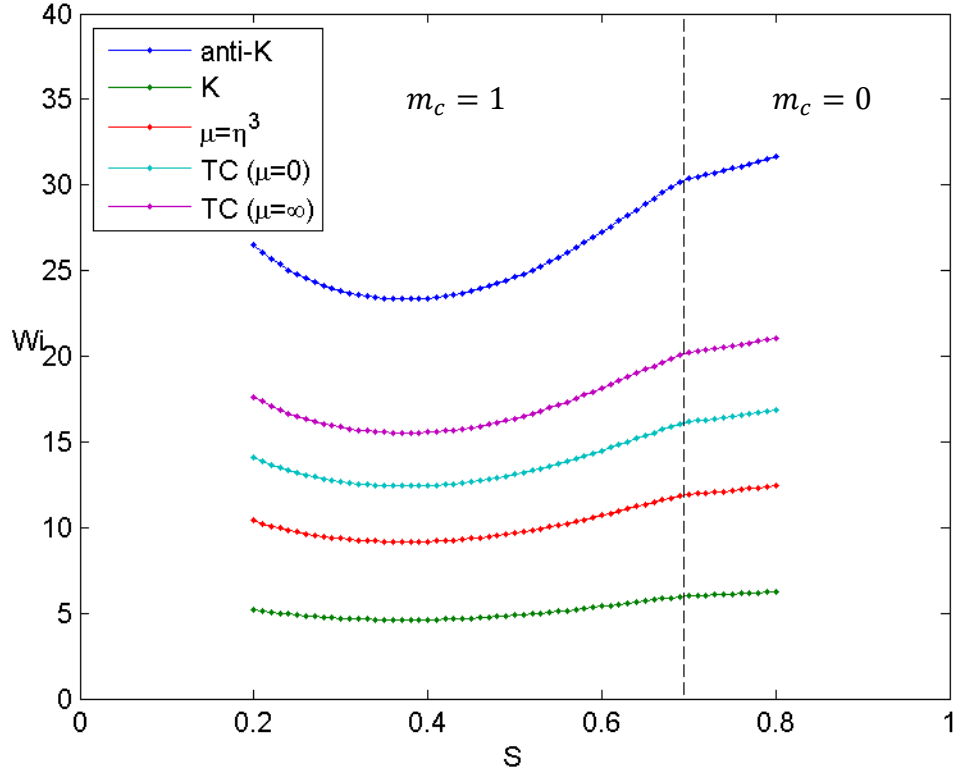
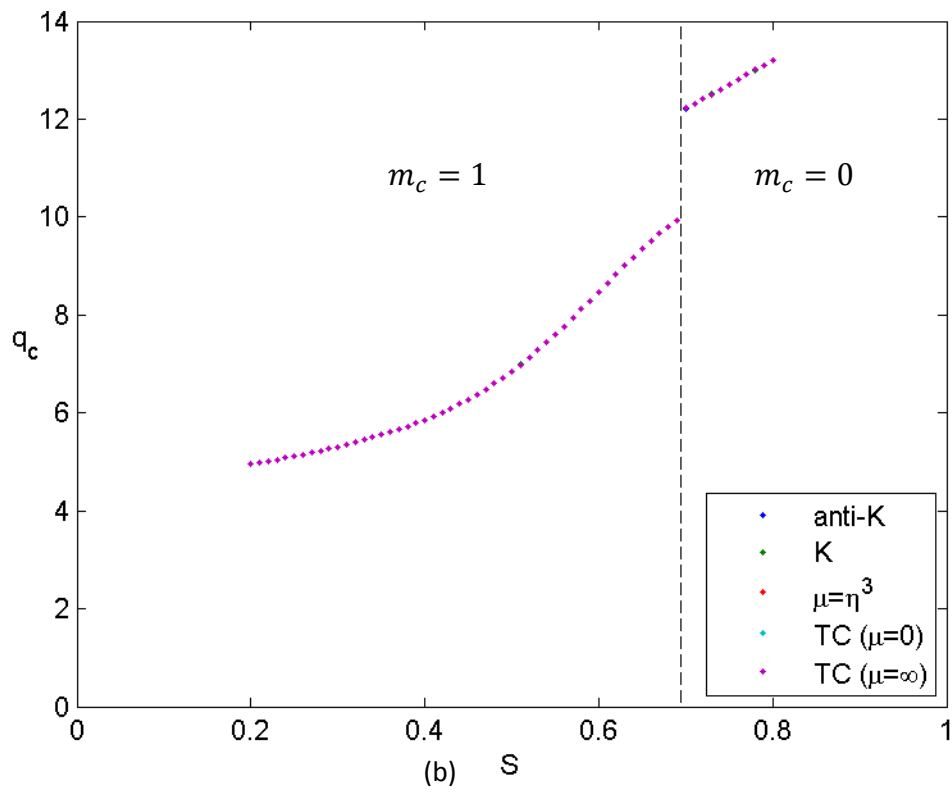
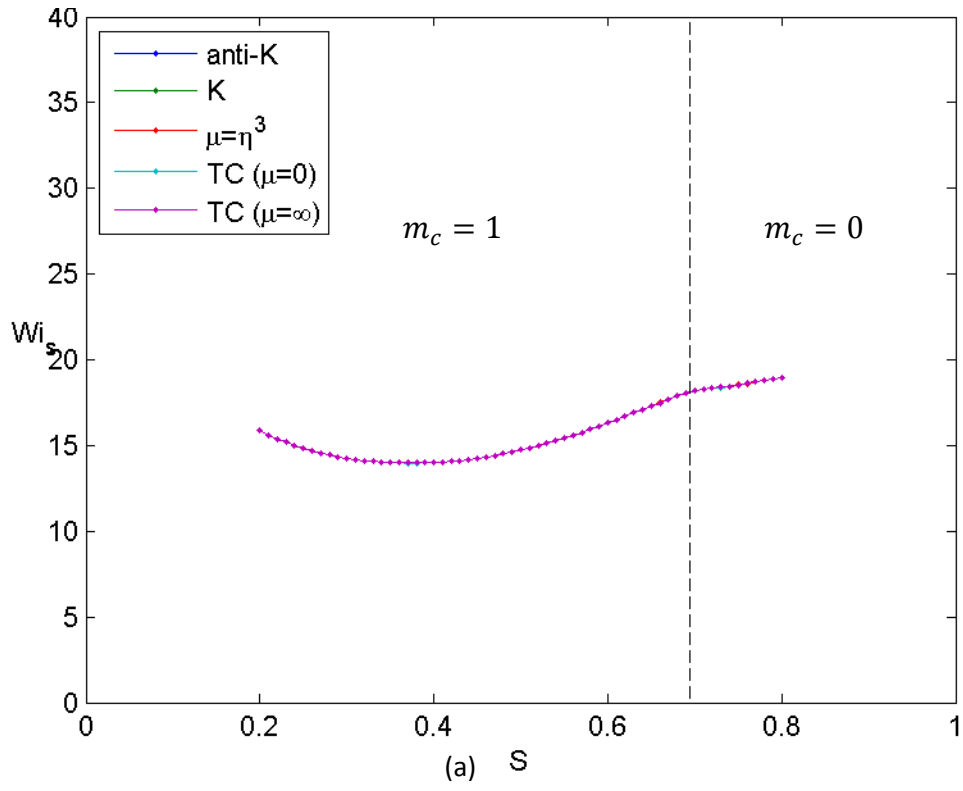


Figure 9.3: Critical curves  $Wi(S)$  for different rotation regimes.

This similarity suggests to search for an appropriate parametrization which may allow merging all these curves into one single curve. If we replace  $Wi$  by the shear Weissenberg number defined by  $Wi_s = \tau \dot{\gamma}$  with the shear rate defined at the mean radius i.e.  $\dot{\gamma} = |\Omega_i - \Omega_o|(R_i + R_o)/2d$ , then the critical curves of all the studied regimes collapse in to one same curve (figure 9.3), since the purely elastic instability is driven only by the elastic force and not by the inertial force. So the critical shear Weissenberg number  $Wi_s$  is independent to the rotational regimes. Besides, the critical wavenumber  $q_c$  is also independent when  $Re = 0$  for different regimes. In the codimension 2 point, the axial wavenumber pertains a discontinuity. Unlike the critical values  $Wi_s$  and  $q_c$ , which are represented by single curves (figure 9.4a-b), the critical angular frequency  $\omega_c$  changes for different rotational regimes (figure 9.4-c). In each regime, the variation of the critical frequency is quite small for each mode ( $m = 0$  and  $m = 1$ ). At the codimension 2 point, the frequency pertains a strong discontinuity.



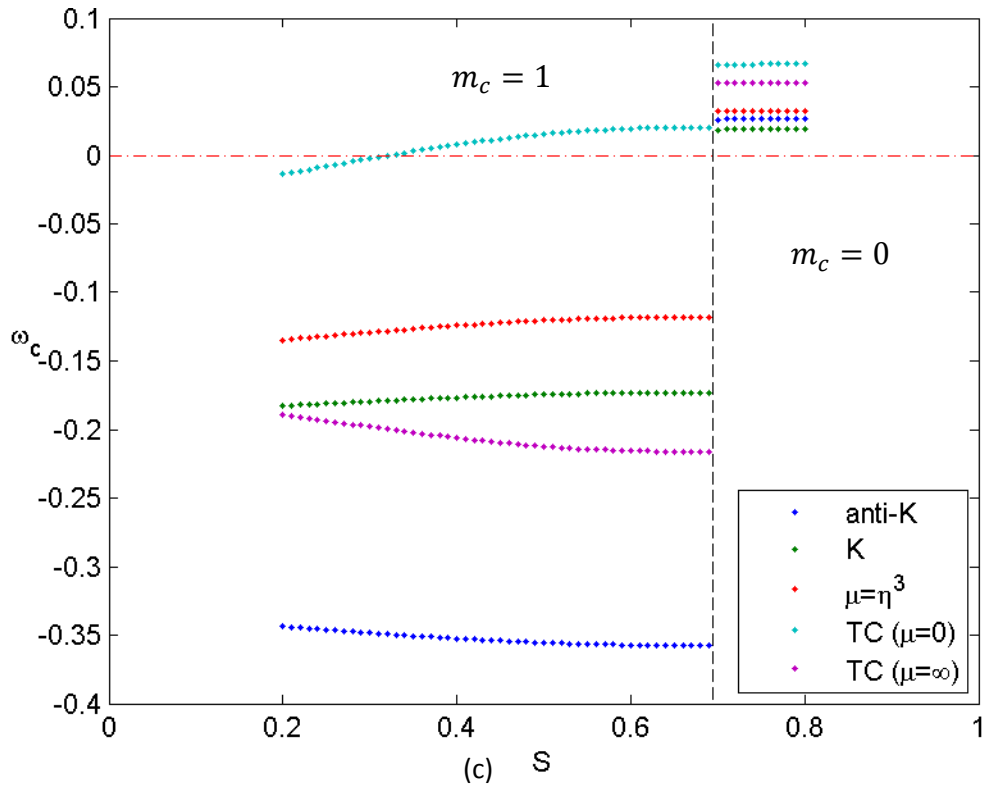


Figure 9.4: Variation of the critical parameters: (a)  $i_s(S)$ , (b)  $q_c(S)$ , (c)  $\omega_c(S)$ .

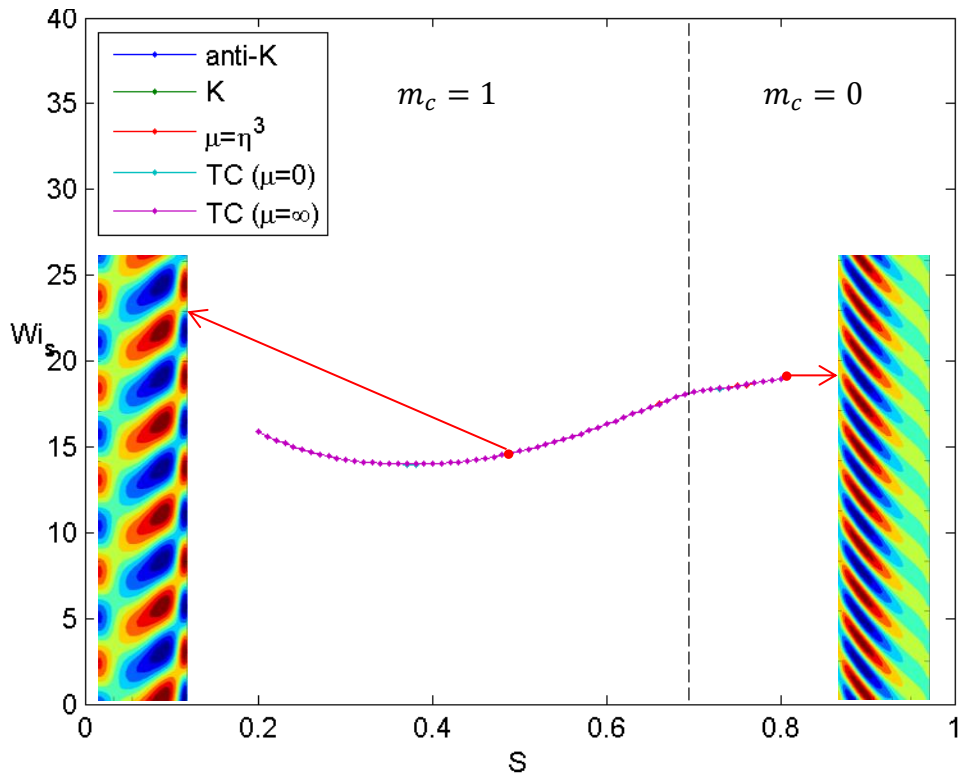


Figure 9.5: Azimuthal vorticity patterns in the gap.

In figure 9.5, we have represented the azimuthal vorticity component of the critical mode in the Keplerian rotation regime for  $S = 0.5$  and  $S = 0.8$ . All rotational regimes share the same critical

mode. Both types of the critical modes are flattened vortices. The non-axisymmetric mode  $m_c = 1$  are located near the outer cylinder while the axisymmetric mode  $m_c = 0$  is located near the inner cylinder. The critical dimensionless wavenumbers  $q_c$  of these modes are larger than  $\pi$ , this means that the critical vortices have size which is smaller than the gap width (figure 9.5).

## 9.2. Experimental results

Larson et al. have found the purely elastic instability in the experiments with polymer solution that had very long relaxation time. Estimated by the normal stress difference  $N_1$  their solutions has  $\tau_{N1} \sim 7.8s$  which is more than 20 times larger than our most elastic solution which has  $\tau_{N1} \sim 0.36s$ . So it is difficult for us to reach the purely elastic limit of  $E \rightarrow \infty$  as Larson et al. have done. However the previous discussion of the  $\mu = \infty$  regime and the anti-Keplerian regime showed that the purely elastic instability with limited  $E$  can be reached by rotating the outer cylinder much faster than the inner cylinder. We found that the experimental critical values defined by the extensional relaxation time  $E_e$  agree very well with the LSA predictions in these two regimes

We surmise the experimental  $Ta_c$  in respect to the extensional defined elasticity  $E_e$  of all the five studied regimes in figure 9.6. We see that for all regimes  $Ta_c$  decreases with  $E_e$  and at large  $E_e$  all points approach the horizontal axis  $Ta_c = 0$ .

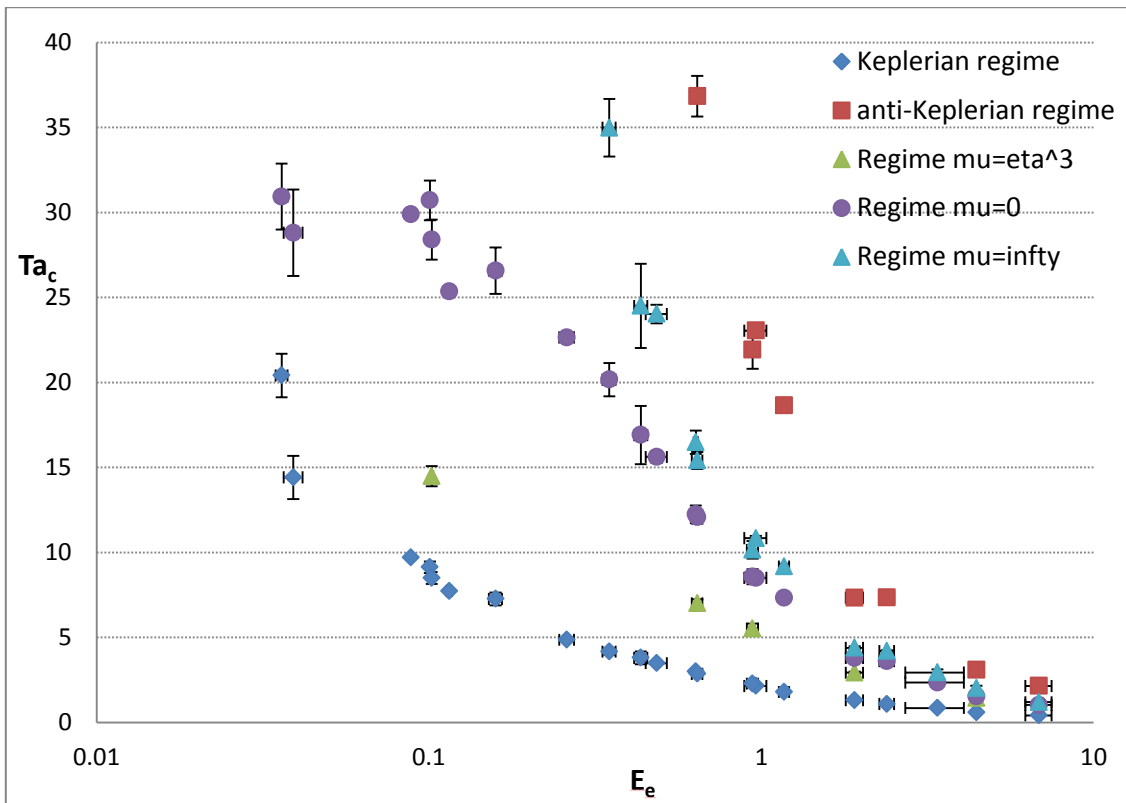


Figure 9.6: Experimental critical value  $Ta_c(E_e)$  of five rotational regimes.

The variation of the critical shear Weissenberg  $Wi_s$  for the five regimes both for experimental values and LSA values with  $E_e$  for  $S = 0.5$  is represented in figure 9.7. The specific value of  $S = 0.5$  is chosen to compare with the experimental points because this value fits better to the five most elastic solutions that are relatively close to the purely elastic limit. As  $E$  increases, both the

experimental and the LSA predicted  $Wi_s$  of all regimes converge to the critical  $Wi_s \approx 15$  of the purely elastic limit for  $S = 0.5$ .

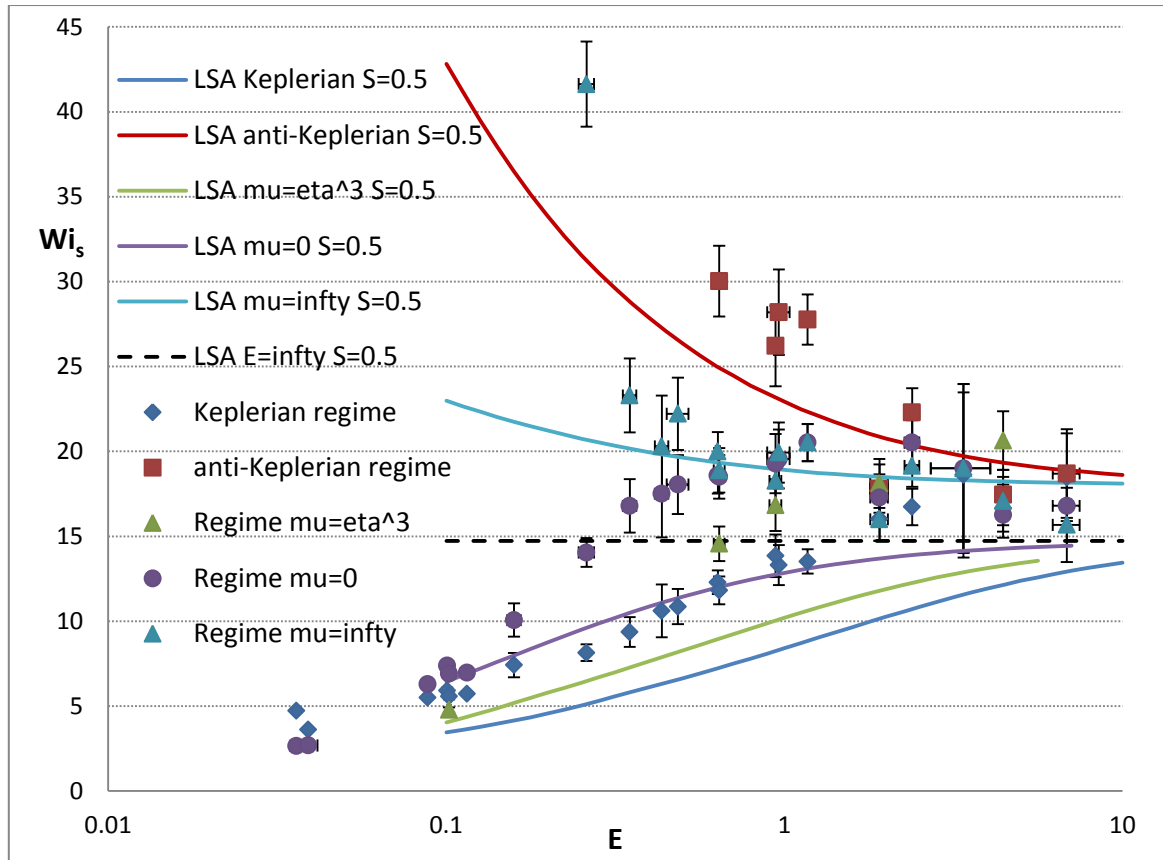


Figure 9.7: Experimental and LSA critical values  $Wi_s(E_e)$  of five regimes. Solid points: experimental critical values. Solid lines: LSA predictions of  $S = 0.5$ . Dashed black line: the LSA prediction of the  $Wi_s$  at  $S = 0.5$ .

The comparison of the experimental curve  $Wi_s(S)$  with the theoretical curve is given in figure 9.8. All the experimental points lie above, but close to the theoretical curve from LSA. The discrepancy between the theoretical and the experimental results is due to the fact that the experimental solutions in all regimes have finite elasticity.

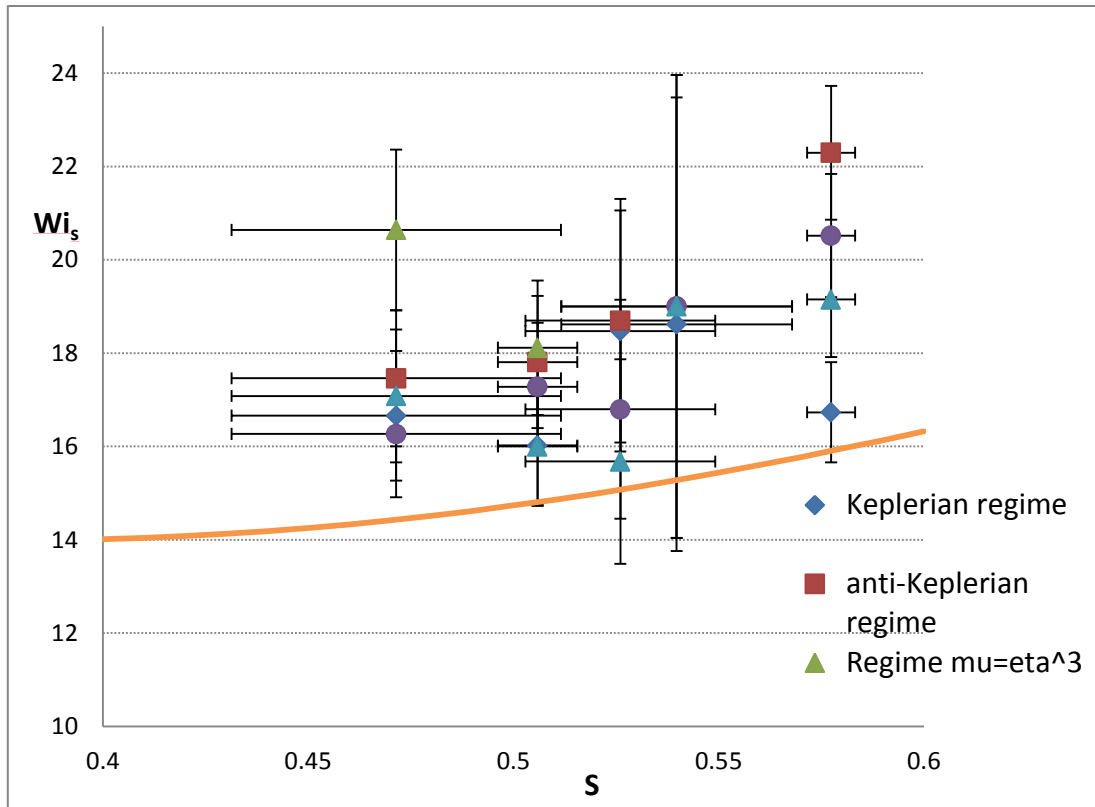


Figure 9.8: Experimental and LSA critical values  $Wi_s(S)$  of five regimes. Solid points: experimental critical values. Solid line: LSA prediction.

### 9.3. Conclusion

The stability of the infinite-elasticity solutions has allowed determining a unique critical curve  $Wi_s(S)$  for the pure elastic instability independent to rotational regimes. The pure elastic instability appears in form of the oscillatory non axisymmetric modes for values of  $S < 0.695$  while it appears in form of oscillatory axisymmetric modes for  $S > 0.695$ . The experimental data obtained in solutions with finite elasticity show a trend to a unique curve as the elasticity is increased large enough. The experimental investigation is worth of continuation especially with solutions of large elasticity ( $E \gg 10$ ).



# General conclusion

---

In this thesis the viscoelastic instability (VEI) of a polymer solution governed by the Oldroyd-B model is studied theoretically and experimentally in the Couette-Taylor system with different rotation regimes. The analogy between VEI and magnetorotational instability (MRI) is discussed theoretically so that the experiments of VEI may help in the deepening of the understanding of the MRI and the momentum transportation in accretion disks.

The rotational Rayleigh discriminant has been generalized to include the elasticity effects of the polymer solutions, the resulting elasto-rotational Rayleigh discriminant predicts that the elastic force enhances the centrifugal instability and induces the purely elastic instability in a circular Couette flow potentially stable to centrifugal perturbations. This elasto-rotational Rayleigh discriminant is analog of the Michael's criterion of instability of conducting fluids in the presence of an azimuthal magnetic field.

We have conducted linear stability analysis (LSA) based on the complete Oldroyd-B equations and experiments with polymer solutions of 1000ppm POE with various concentration of PEG (2.5% - 25%). The working solutions were thoroughly characterized by the rheology measurements to test the validity of the Oldroyd-B model. The viscosities and the relaxation times were measured by different methods. The viscosities  $\nu, \nu_s, \nu_p$  and the relaxation times  $\tau_e, \tau_m, \tau_{N1}$  were found to increase with the polyethylene glycol concentration in water  $C_{PEG}$  so that the elasticities  $E_e, E_m, E_{N1}$  increase with  $C_{PEG}$  while the viscosity ratio  $S$  decreases with  $C_{PEG}$ .

The LSA and experimental test were performed for the flow in the Couette-Taylor system with a radius ratio  $\eta = 0.8$ . The aspect ratio of the experimental setup was  $\Gamma = 45.7$  which is large enough to allow comparison with theoretical results obtained in the infinite aspect ratio.

In the case of the sole rotating inner cylinder ( $\mu = 0$ ), we have observed theoretically and experimentally three different critical modes from small  $E$  to large  $E$ : Taylor vortex mode, Ribbons mode and Disordered vortices. The Taylor vortex mode and the Ribbons mode are supercritical while the disordered modes occur via a subcritical transition. The threshold  $Ta_c$ , axial wavenumber  $q_c$  and angular frequency  $\omega_c$  of the critical modes show good agreement between experiments and LSA predictions. Qualitative agreements are also found between our experimental results and those of Baumert [Baumert1999], Groisman [Groisman1998] and Kelai [Kelai2011]. The viscosity ratio  $S$  is found to play opposite roles: destabilizing for small values of the elasticity and stabilizing for large values of the elasticity and in particular in the purely elastic regime.

In the Keplerian regime ( $\mu = \eta^{3/2}$ ), instability modes were predicted and observed in the zone where they were not predicted even by the elasto-rotational Rayleigh criterion. These modes appear in form of the stationary axisymmetric vortices for small values of  $ES$  (analog of SMRI) and in form of the disordered modes for large  $ES$  (analog of HMRI). These modes are different from the Taylor Vortex mode or the disordered vortices observed in the  $\mu = 0$  regime. Among the disordered modes solitary vortices appear for intermediate values of  $ES$ . The stationary axisymmetric mode is supercritical while the disordered modes are subcritical. For large values of the elasticity, the critical mode is the purely elastic instability mode. In this Keplerian regime, the polymer elasticity  $ES$

appears to be a better control parameter than  $E$ , in fact the critical curves  $Ta_c(ES)$  converge into a single curve for different  $S$ . This single curve fits the experimental thresholds of the critical modes when the elasticity is defined with the molecular relaxation time  $\tau_m$ .

Two other situations where there is no centrifugal instability in Newtonian flows have been investigated for the viscoelastic fluids. The case when only the outer cylinder is rotating ( $\mu = \infty$  regime) and the anti-Keplerian regime ( $\mu = \eta^{-3/2}$ ) in which the outer cylinder rotates faster than the inner one. The VEI occurs in form of axisymmetric and oscillatory modes. The LSA critical curves of the thresholds  $Ta_c(E)$  are independent to  $S$  and they fit perfectly the experimental critical values when the elasticity is defined with the extensional relaxation time.

In the intermediate regime of  $\mu = \eta^3$ , the VEI resembles the  $\mu = 0$  regime for small  $E$  while it resembles the Keplerian regime for large  $E$ .

In the limit of  $Re = 0$  and  $E \rightarrow \infty$  with finite  $Wi$ , a unique critical curve  $Wi_s(S)$  for the pure elastic instability for all rotational regimes is predicted by the LSA where the shear rate has been determined at the mean radius. The pure elastic instability appears in the form of the oscillatory non-axisymmetric modes for values of  $S < S_1$  while it appears in form of oscillatory axisymmetric modes for  $S > S_1$ . The experimental data obtained in solutions with finite elasticity show a trend to a unique curve as the elasticity is large enough. The experimental investigation is worth of continuation especially with solutions of large elasticity ( $E \gg 10$ ).

The present investigation of the VEI in Keplerian regime confirms the analogy between VEI at small elasticity and SMRI where the elastic force field is analog to the axial magnetic field that destabilizes accretion disks. Different types of MRI are distinct from each other by the form of magnetic field. The analysis of the polymer analog  $\vec{B}_p$  of the magnetic field, suggests that in Keplerian regime, the VEI is analog to the SMRI when  $Wi \ll Wi^*$ , while the VEI is analog to the HMRI when  $Wi \approx Wi^*$  and the VEI could be an analog to the AMRI or Michael instability when  $Wi \gg Wi^*$ . The stationary axisymmetric vortex mode is the analog to the SMRI while the disordered waves mode is the analog to the HMRI. Is the purely elastic mode at  $Wi \gg Wi^*$  and large  $E$  the analog of the AMRI remains an open issue to be investigated in forthcoming work.

This thesis was limited to the first instability modes of the viscoelastic flows both in the theoretical analysis and in the experiments. The behavior of some marginal curves and the existence of multiple codimension 2 points suggest the necessity of non-linear analysis to investigate the mode coupling. There is a need for DNS of the flow equations to compute the torque and the radial transport of the momentum. PIV measurements will permit to characterize in more details the critical modes, the higher instability modes and the turbulence in the Keplerian regime of the viscoelastic flows. Moreover, measurements of the torque on the cylinders will give complementary data on the momentum transportation in viscoelastic flows and bring a new break in the validation of the analogy between the VEI and MRI in accretion disks.

# List of references

---

- ANDERECK, C DAVID, LIU, SS & SWINNEY, HARRY L 1986 Flow regimes in a circular Couette system with independently rotating cylinders. *Journal of Fluid Mechanics* **164**, 155-183.
- AVGOUSTI, MARIOS & BERIS, ANTONY N 1993 Non-axisymmetric modes in viscoelastic Taylor-Couette flow. *Journal of Non-Newtonian Fluid Mechanics* **50** (2), 225-251.
- BALBUS, STEVEN A 2011 Fluid dynamics: A turbulent matter. *Nature* **470** (7335), 475-476.
- BALBUS, STEVEN A & HAWLEY, JOHN F 1991 A powerful local shear instability in weakly magnetized disks. i-linear analysis. ii-nonlinear evolution. *The Astrophysical Journal* **376**, 214-233.
- BALBUS, STEVEN A & HAWLEY, JOHN F 1998 Instability, turbulence, and enhanced transport in accretion disks. *Reviews of modern physics* **70** (1), 1.
- BALBUS, STEVEN A, 2009 Magnetorotational instability. *scholarpedia* **4**(7):2409 [http://www.scholarpedia.org/article/Magnetorotational\\_instability](http://www.scholarpedia.org/article/Magnetorotational_instability)
- BAUMERT, BRANDON MAX & MULLER, SUSAN J 1997 Flow regimes in model viscoelastic fluids in a circular Couette system with independently rotating cylinders. *Physics of Fluids (1994-present)* **9** (3), 566-586.
- BAUMERT, BRANDON MAX & MULLER, SUZAN J 1999 Axisymmetric and non-axisymmetric elastic and inertia-elastic instabilities in Taylor-Couette flow. *Journal of Non-Newtonian Fluid Mechanics* **83**, 33-69.
- BIRD, ROBERT BYRON, ARMSTRONG, ROBERT CALVIN, HASSAGER, OLE & CURTISS, CHARLES F 1977 *Dynamics of polymeric liquids*, , vol. 1. Wiley New York.
- BOLDYREV, STANISLAV, HUYNH, DON & PARIEV, VLADIMIR 2009 Analog of astrophysical magnetorotational instability in a Couette-Taylor flow of polymer fluids. *Physical Review E* **80** (6), 066310.
- CASSEN, PATRICK & MOOSMAN, ANN 1981 On the formation of protostellar disks. *Icarus* **48** (3), 353-376.
- CHANDRASEKHAR, S 1960 The stability of non-dissipative Couette flow in hydromagnetics. *Proceedings of the National Academy of Sciences of the United States of America* **46** (2), 253.
- CHILD, ADAM, KERSALÉ, EVY & HOLLERBACH, RAINER 2015 Nonaxisymmetric linear instability of cylindrical magnetohydrodynamic Taylor-Couette flow. *Physical Review E* **92** (3), 033011.
- CRUMEYROLLE, O, LATRACHE, N, MUTABAZI, I & EZERSKY, AB 2005 Instabilities with shear-thinning polymer solutions in the Couette-Taylor system. In *Journal of Physics: Conference Series*, , vol. 14, p. 78. IOP Publishing.
- DAVIDSON, PETER ALAN 2013 *Turbulence in rotating, stratified and electrically conducting fluids*. Cambridge University Press.
- DUBRULLE, B, MARIE, LOUIS, NORMAND, CH, RICHARD, D, HERSANT, F & ZAHN, J-P 2005 A hydrodynamic shear instability in stratified disks. *Astronomy & Astrophysics* **429** (1), 1-13.
- GROISMAN, ALEXANDER & STEINBERG, VICTOR 1997 Solitary vortex pairs in viscoelastic Couette flow. *Physical Review Letters* **78** (8), 1460.
- GROISMAN, ALEXANDER & STEINBERG, VICTOR 1998 Mechanism of elastic instability in Couette flow of polymer solutions: experiment. *Physics of Fluids (1994-present)* **10** (10), 2451-2463.

- HOLLERBACH, RAINER & RÜDIGER, GÜNTHER 2005 New type of magnetorotational instability in cylindrical Taylor-Couette flow. *Physical review letters* **95** (12), 124501.
- HOYLE, F 1960 The origin of the solar nebula. *Quarterly Journal of the Royal Astronomical Society* **1**, 28.
- HUISMAN, SANDER G, VAN DER VEEN, ROELAND CA, SUN, CHAO & LOHSE, DETLEF 2014 Multiple states in highly turbulent Taylor-Couette flow. *Nature communications* **5**.
- JI, HANTAO & BALBUS, STEVEN 2013 Angular momentum transport in astrophysics and in the lab. *Physics Today* **66** (8), 27-33.
- JI, HANTAO, BURIN, MICHAEL, SCHATMAN, ETHAN & GOODMAN, JEREMY 2006 Hydrodynamic turbulence cannot transport angular momentum effectively in astrophysical disks. *Nature* **444** (7117), 343-346.
- JOO, YONG LAK & SHAQFEH, ERIC SG 1992 The effects of inertia on the viscoelastic Dean and Taylor-Couette flow instabilities with application to coating flows. *Physics of Fluids A : Fluid Dynamics (1989-1993)* **4** (11), 2415-2431.
- KELAI, F 2011 *Etude expérimentale des instabilités viscoélastiques dans le système de Couette-Taylor*, Ph. D. thesis, University of Le Havre.
- KIRILLOV, OLEG N & STEFANI, FRANK 2013 Extending the range of the inductionless magnetorotational instability. *Physical review letters* **111** (6), 061103.
- KIRILLOV, OLEG N, STEFANI, FRANK & FUKUMOTO, YASUhide 2014 Local instabilities in magnetized rotational flows: a short-wavelength approach. *Journal of Fluid Mechanics* **760**, 591-633.
- KUPFERMAN, RAZ 1998 Simulation of viscoelastic fluids: Couette-Taylor flow. *Journal of Computational Physics* **147** (1), 22-59.
- LARSON, RONALD G, SHAQFEH, ERIC SG & MULLER, SUSAN J 1990 A purely elastic instability in Taylor-Couette flow. *Journal of Fluid Mechanics* **218**, 573-600.
- LATRACHE, NOUREDDINE, CRUMEYROLLE, OLIVIER & MUTABAZI, INNOCENT 2012 Transition to turbulence in a flow of a shear-thinning viscoelastic solution in a Taylor-Couette cell. *Physical Review E* **86** (5), 056305.
- MACKAY, MICHAEL E & BOGER, DAVID V 1987 An explanation of the rheological properties of Boger fluids. *Journal of non-newtonian fluid mechanics* **22** (2), 235-243.
- MAGDA, JJ & LARSON, RG 1988 A transition occurring in ideal elastic liquids during shear flow. *Journal of non-newtonian fluid mechanics* **30** (1), 1-19.
- MICHAEL, DH 1954 The stability of an incompressible electrically conducting fluid rotating about an axis when current flows parallel to the axis. *Mathematika* **1** (01), 45-50.
- OGILVIE, GORDON I & POTTER, ADRIAN T 2008 Magnetorotational-type instability in Couette-Taylor flow of a viscoelastic polymer liquid. *Physical review letters* **100** (7), 074503.
- OGILVIE, GORDON I & PROCTOR, MICHAEL RE 2003 On the relation between viscoelastic and magnetohydrodynamic flows and their instabilities. *Journal of Fluid Mechanics* **476**, 389-409.
- OLDROYD, JG 1950 On the formulation of rheological equations of state. In *Proceedings of the Royal Society of London A: Mathematical, Physical and Engineering Sciences*, , vol. 200, pp. 523-541. The Royal Society.
- PRINGLE, JE 1981 Accretion discs in astrophysics. *Annual review of astronomy and astrophysics* **19**, 137-162.
- SEILMAYER, MARTIN, GALINDO, VLADIMIR, GERBETH, GUNTER, GUNDRUM, THOMAS, STEFANI, FRANK, GELLERT, MARCUS, RÜDIGER, GÜNTHER, SCHULTZ, MANFRED &

- HOLLERBACH, RAINER 2014 Experimental evidence for non-axisymmetric magnetorotational instability in a rotating liquid metal exposed to an azimuthal magnetic field. *Physical review letters* **113** (2), 024505.
- SHAQFEH, ERIC SG 1996 Purely elastic instabilities in viscometric flows. *Annual Review of Fluid Mechanics* **28** (1), 129{185.
- STEFANI, FRANK, GERBETH, GUNTER, GUNDRUM, THOMAS, HOLLERBACH, RAINER, PRIEDE, J\_ANIS, RÜDIGER, GÜNTHER & SZKLARSKI, JACEK 2009 Helical magnetorotational instability in a Taylor-Couette flow with strongly reduced Ekman pumping. *Physical Review E* **80** (6), 066303.
- STEFANI, FRANK, GUNDRUM, THOMAS, GERBETH, GUNTER, RÜDIGER, GÜNTHER, SCHULTZ, MANFRED, SZKLARSKI, JACEK & HOLLERBACH, RAINER 2006 Experimental evidence for magnetorotational instability in a Taylor-Couette flow under the influence of a helical magnetic field. *Physical review letters* **97** (18), 184502.
- STEFANI, FRANK, GUNDRUM, THOMAS, GERBETH, GUNTER, RÜDIGER, GÜNTHER, SZKLARSKI, JACEK & HOLLERBACH, RAINER 2007 Experiments on the magneto-rotational instability in helical magnetic fields. *New Journal of Physics* **9** (8), 295.
- SWINNEY, HARRY L & GOLLUB, JERRY P 1981 Hydrodynamic instabilities and the transition to turbulence. *Hydrodynamic instabilities and the transition to turbulence* **1**.
- WOOLFSON, MICHAEL 2000 The origin and evolution of the solar system. *Astronomy & Geophysics* **41** (1), 1-12.



# List of tables and figures

---

## Tables

Table 3.1: Main control physical parameters of the viscoelastic Couette flow.

Table 3.2: Base flow characteristics in the Couette-Taylor system.

Table 6.1: Codimension-two point for  $S = 0.6$  in  $\mu = 0$  regime.

Table 7.1: Codimension-two points for  $S = 0.6$  in Keplerian regime.

Table 8.1: Codimension-two points for  $S = 0.7$  in the intermediate rotation regime  $\mu = \eta^3$ .

## Figures

Figure 1.1: The “dumbbell” model to explain the mechanism of the MRI proposed by Balbus.

Figure 1.2: (a) Shear thinning effect, (b) Weissenberg effect.

Figure 1.3: Photo of the purely elastic instability provided by Larson & Shaqfeh [Larson 1990].

Figure 1.4: “Dumbbell” model proposed by Larson & Shaqfeh [Larson 1990].

Figure 3.1: A scheme of the Couette-Taylor flow system.

Figure 3.2: The velocity of the base flow for five different rotation regimes for  $\eta = 0.8$ .

Figure 3.3: Radial profile of the pressure gradient for five rotation regimes for  $\eta = 0.8, ES = 1$ . Solid lines represent the Newtonian flows while dashed lines represent the viscoelastic flows.

Figure 3.4: Average shear rate: (a) traditional definition, (b) dynamic definition [Dubrulle 2015].

Figure 4.1: Stability diagram of the circular Couette flow according to circulation Rayleigh criterion.

Figure 4.2: Andereck’s diagram of Newtonian Couette-Taylor instabilities for different rotational regimes with  $\eta = 0.883$ ;  $R_i$  and  $R_o$  are the Reynolds numbers of the inner and outer cylinders respectively. The red line represents the condition of  $\Phi_r = 0$ . The flow in the positive  $\Phi_r$  zone is predicted to be stable Couette flow, all states were found in the region where  $\Phi_r < 0$ .

Figure 4.3: Rotational Rayleigh discriminant  $\Phi_r(r)$  and elasto-rotational Rayleigh discriminant  $\Phi_{er}(r)$  for flows with  $ES = 1$  in five rotation regimes.

Figure 4.4: Rotational epicyclic frequency  $\omega_{ep}^r$  and elasto-rotational epicyclic frequency  $\omega_{ep}^{er}$  with  $ES = 1$  for five regimes.

Figure 4.5: 3D plot of the neutral surface of the elastic Rayleigh discriminant.

Figure 4.6: Rayleigh lines for different  $ES$  on  $(\mu, \eta^2)$  diagram.

Figure 4.7: Critical polymer elasticity  $ES^*$  in respect to radius ratio  $\eta$  on Keplerian and anti-Keplerian regime.

Figure 4.8: Schematic stability diagram according to elasto-rotational Rayleigh discriminant.

Figure 4.9: Eigenvalues of the linear equation with the parameters of  $Re = 500$ ,  $Wi = 15$ ,  $\eta = 0.8$ ,  $S = 0.7$ ,  $m = 0$ ,  $q = 10$ , on Keplerian regime  $\mu = \eta^{3/2}$ .

Figure 4.10: Critical curves of the most unstable axisymmetric mode of the purely elastic instability when  $Re = 0$  and  $m = 0$  at the small gap limitation  $\eta \sim 1$ . (a) Results of Larson & Shaqfeh. (b) Our results. All syntaxes in both figures are defined by the way of Larson & Shaqfeh [Larson1990].

Figure 4.11: Critical curves  $Re_c - Wi_c$  represent 2 different instable modes: purely elastic mode and inertia-elastic mode.  $S = 0.8$ ,  $m = 0$ ,  $\eta \sim 1$ . (a) Results of Joo et al. (b) Our results.

Figure 4.12: Critical curves for different azimuthal wavenumber (denoted by  $\epsilon$  for figure (a),  $m$  for figure (b)) for a specific wavenumber  $q = 3.12$  for  $\nu_s/\nu_p = 3.76$ ,  $\eta = 0.95$ ,  $\mu = 0.5$  defined by Avgousti. (a) Results of Avgousti. (b) Our results.

Figure 4.13: (a) (b): Contours of the growth rate  $s$  optimized with respect to  $m$  and  $k$  on map of  $(Re, Wi)$  for Keplerian case at  $\eta = 0.95$ ,  $S = 0.5$ . (a) results of Ogilvie & Potter where the white line represents the critical curve; (b) our results where the white zone represent negative growth rate so that the separation line represents the critical curve. (c) (d) : Eigen function of the preferred mode on a specific set of  $(Re, Wi)$  along the critical curve for  $Re = 40$ . The azimuthal velocity perturbation is indicated by color scale. (c) results of Ogilvie & Potter (d) our results.

Figure 5.1: Experimental setup and its environment.

Figure 5.2: (a) Monomer of PEO and PEG (b) PEO sealed in a flacon.

Figure 5.3: (a) The shear stress rheometer (Anton Par MC300). (b) The plan-cone measuring cellule.

Figure 5.4: Solvent viscosity with respect to shear rates for PEG concentration from 2.5% to 25%.

Figure 5.5: Dynamic viscosity of working fluids of different PEG concentrations in respect to shear rate. Each PEG concentration is represented by one color in the diagram. Dashed lines – working range of experiments.

Figure 5.6: Total solution viscosity  $\rho\nu$ , polymer viscosity  $\rho\nu_p$  and solvent viscosity  $\rho\nu_s$  with respect to the PEG concentrations and their fitting curves for  $C_{PEO} = 1000$  ppm .

Figure 5.7: Viscosity ratio  $S$  with respect to PEG concentration.

Figure 5.8: The photo of extensional relaxation time and the principle of the measurement.

Figure 5.9: Variation of the filament diameter with the time, experimental data for a solution of 10% PEG and 1000 ppm PEO measured by CaBER .

Figure 5.10: Adjusted first normal stress difference  $N_1$  in respect to the shear rate  $\dot{\gamma}$ . The points in the red dashed rectangular are used to estimate  $\tau_{N1}$ .

Figure 5.11: Variation of the relaxation times  $\tau$  with PEG concentration.

Figure 5.12: Variation of the Elasticities  $E$  with the PEG concentration.

Figure 5.13: Variation of the Elasticities  $E$  with the viscosity ratio  $S$ .

Figure 6.1: Marginal curves  $Ta(q)$  for different  $m$  at chosen  $E$  for  $S = 0.6$ . Colored dashed lines indicate  $q_c$  and  $Ta_c$  for different  $m$  (a)  $E = 0.01, m_c = 0, \omega_c = 0$  (b)  $E = 0.1, m_c = 1, \omega_c < 0$  (c)  $E = 1, m_c = 1, \omega_c > 0$ .

Figure 6.2: Variation of the critical values of  $Ta_c$  with  $E$  for different  $m$  at fixed  $S = 0.6$ .

Figure 6.3: Variation of the critical parameters with the elasticity number  $E$  for  $S = 0.6$  in  $\mu = 0$  regime: a)  $a_c(E)$ ; b)  $q_c(E)$ ; c)  $\omega_c(E)$ . Loose dashed vertical line separates critical azimuthal wave numbers  $m_c$ . Dense vertical line separates the positive and negative angular frequency.

Figure 6.4: Color: Vorticity  $\omega_\theta$  of the critical modes in the gap for different values of the elasticity number  $E$  and for  $S = 0.6$  in  $\mu = 0$  regime. Solid line: critical curve  $a_c(E)$ .

Figure 6.5: Critical mode for  $S = 0.6, E = 0.01, Ta_c = 41.3$  on  $\mu = 0$ , with  $m = 0, q_c = 3.28, \omega_c = 0$ . (a) Black arrows represent the velocity field in  $(r, z)$  direction while the colors represent the azimuthal velocity  $V$  (b) the vorticity  $\omega_\theta$  (c) the pressure variation (d) the  $N_1$  variation © the  $N_2$  variation. Color maps of (b, c, d, e) represent the relative amplitude.

Figure 6.6: Critical mode for  $S = 0.6, E = 0.1, Ta_c = 27.2$  in  $\mu = 0$  regime, with  $m = 1, q_c = 4.37, \omega_c = -0.034$ . (a) Black arrows represent the velocity field in  $(r, z)$  direction while the colors represent the azimuthal velocity  $V$  (b) the vorticity  $\omega_\theta$  (c) the pressure variation (d) the  $N_1$  variation © the  $N_2$  variation. Color maps of (b, c, d, e) represent the relative amplitude.

Figure 6.7: Critical mode for  $S = 0.6, E = 1, Ta_c = 5.74$  in  $\mu = 0$  regime, with  $m = 1, q_c = 6.03, \omega_c = 0.014$ . (a) Black arrows represent the velocity field in  $(r, z)$  direction while the colors represent the azimuthal velocity  $V$  (b) the vorticity  $\omega_\theta$  (c) the pressure variation (d) the  $N_1$  variation © the  $N_2$  variation. Color maps of (b, c, d, e) represent the relative amplitude.

Figure 6.8: Critical curves  $Ta_c(E)$  for different  $S$  in  $\mu = 0$  regime.

Figure 6.9: Critical curves  $Ta_c(ES)$  for different  $S$  in  $\mu = 0$  regime.

Figure 6.10: Critical curves  $Re_c(Wi_c)$  at critical wave numbers for different  $S$  in  $\mu = 0$  regime.

Figure 6.11: Critical curves  $Ta_c(K_c)$  for different values of  $S$  in  $\mu = 0$  regime. The insert figure on the right top corner is a zoom in around the "intersection point".

Figure 6.12: Variation of the critical angular frequency  $\omega_c$  with  $ES$  for different  $S$  in  $\mu = 0$  regime.

Figure 6.13: Variation of the critical wave number  $q_c$  with  $E$  for different  $S$  in  $\mu = 0$  regime.

Figure 6.14: Critical mode of Taylor Vortex observed in a solution of 1000ppm PEO and 2.5% PEG ( $Ta_c = 28.8, E_m = 0.011, S = 0.87$ ) in  $\mu = 0$  regime: (a) gap view, (b) front view, (c) space-time diagram of the front view.

Figure 6.15: Critical mode of Ribbons at  $Ta_c = 28.4, E_m = 0.0168, S = 0.81$  in  $\mu = 0$  regime for a solution of 1000ppm PEO and 5% PEG. (a) gap view (b) front view (c) space-time diagram of the front view.

Figure 6.16: Demodulation of the space-time diagram of the Ribbons mode. (a) demodulated left wave (b) space-time diagram (c) demodulated right wave.

Figure 6.17: Critical mode of Disordered Vortices at  $Ta_c = 12.1, E_m = 0.131, S = 0.61$  in  $\mu = 0$  regime for a solution of 1000ppm PEO and 15% PEG. (a) gap view (b) front view (c) space-time diagram of 20s of the front view.

Figure 6.18: Space-time diagram of 600s for 3 different modes: (a) Taylor Vortex (b) Ribbons (c) Disordered vortices.

Figure 6.19: Fourier spectra of the Disordered Vortices for a solution of 1000ppm PEO and 15% PEG ( $Ta_c = 12.1, E_m = 0.131, S = 0.61$ ) in  $\mu = 0$  regime: (a) space spectrum (b) time spectrum. Red dashed line – the frequency of the inner cylinder. Black dashed line – the flicker frequency of the spot light.

Figure 6.20: Transition to Disordered Vortices for a solution of 1000ppm PEO and 15% PEG ( $Ta_c = 12.1, E_m = 0.131, S = 0.61$ ) in  $\mu = 0$  regime. (a) Space-time diagram of the transient state, (b) space spectrum, (c) time spectrum.

Figure 6.21: Variation of the critical values of  $Ta_c$  with the polymer elasticity  $ES$  in  $\mu = 0$  regime. Solid points represent experimental critical values, 3 colors correspond to 3 different definitions of elasticity. Within each definition of elasticity (see section 5.4), each point represents one tested solution. Continuous lines are the LSA critical curves for different  $S$ .

Figure 6.22: Variation of the critical values of  $Ta_c$  with the polymer elasticity  $ES$  defined by the mass molar relaxation time in  $\mu = 0$  regime. Solid points represent experimental critical values. Dashed rectangles are groups of different critical modes. Continuous lines are LSA critical curves for different values of  $S$ .

Figure 6.23: Variation of the critical angular frequency with  $ES$  defined with molecular relaxation time in  $\mu = 0$  regime. Solid points – experimental critical values. Dashed rectangles – groups of different critical modes. Continuous lines – theoretical critical angular frequencies for different  $S$ .

Figure 6.24: Dimensionless critical axial wave number  $q_c$  in  $\mu = 0$  regime. Solid lines – LSA critical wave numbers for different  $S$ . Solid points – experimental critical values. Dashed circle – group of different critical modes.

Figure 6.25: Critical values on regime of  $\mu = 0$ . Continuous lines – LSA critical curves. Solid points – experiments of Kelai. Open points – our experiments. Violet triangle – experiment of Baumert.

Figure 6.26: Marginal curves  $Ta(q)$  for different  $m$  at  $S = 0.7$  and  $E = 1$ .

Figure 6.27: Critical curves  $Ta_c(E)$  for different  $m$  at fixed  $S = 0.7$  in  $\mu = \infty$  regime.

Figure 6.28: Critical curves,  $Ta_c(E)$  for different  $S$  in  $\mu = \infty$  regime.

Figure 6.29: Critical curves  $Re_c(Wi_c)$  for different  $S$  in  $\mu = \infty$  regime.

Figure 6.30: Variation of the critical parameters with  $E$  for different values of  $S$  in  $\mu = \infty$  regime: (a) angular frequency  $\omega_c$  (b) axial wave number  $q_c$ .

Figure 6.31: Critical mode for  $S = 0.7, E = 1, Ta_c = 4.73$  on  $\mu = \infty$ , with  $m = 0, q_c = 14.4, \omega_c = 0.050$ . (a) Black arrows represent the velocity field in  $(r, z)$  direction while the colors represent the azimuthal velocity  $V$  (b) the vorticity  $\omega_\theta$  (c) the pressure variation (d) the  $N_1$  variation © the  $N_2$  variation. Color maps of (b, c, d, e) represent the relative amplitude.

Figure 6.32: Critical mode of Disordered Vortices at  $Ta_c = 15.4, E_m = 0.131, S = 0.61, \mu = \infty$  for a solution of 1000ppm PEO and 15% PEG. (a) gap view (b) front view (c) space-time diagram of 20s of the front view (d) long-time space-time diagram © space spectrum (f) time spectrum. Red dashed line – the frequency of the inner cylinder. Black dashed line – the flicker frequency of the spot light.

Figure 6.33: Critical values of the transition from laminar flow to unstable flow on regime of  $\mu = \infty$ . Solid lines – LSA critical curves for different  $S$ . Solid points – experimental transient values, 3 colors present 3 different definitions of elasticity. Within each definition of elasticity, each point present one solution tested.

Figure 6.34: Variation of the critical angular velocity  $\omega_c$  in  $\mu = \infty$  regime. solid points – experimental critical values for  $E$  defined by extensional relaxation time. Continuous lines – LSA critical curves for different  $S$ .

Figure 6.35: Variation of the critical axial wave number  $q_c$  with  $E$  in  $\mu = \infty$  regime. Solid points – experimental critical values for  $E$  defined by extensional relaxation time. Continuous lines – the LSA critical curves for different  $S$ .

Figure 6.36: Critical values on regime of  $\mu = \infty$ . Continuous lines – LSA critical curves. Blue circle – our experiments. Red triangle – experiments of Kelai. Violet squire – experiment of Baumert.

Figure 7.1: Marginal curves  $Ta(q)$  for different  $m$  at chosen  $E$ . (a)  $E = 0.01$  (b)  $E = 0.036$ , (c)  $E = 0.1$ , (d)  $E = 1$ .

Figure 7.2: Critical curves,  $Ta_c(E)$  for different  $m, S = 0.6$  on Keplerian regime.

Figure 7.3: Variation of the critical curve  $Ta_c(E)$  for  $S = 0.6$  on Keplerian regime. Black dashed lines separate critical azimuthal wave number  $m_c$ . Color maps – vorticity  $\omega_\theta$  in the gap plane  $(r, z)$ , where red represents positive values and blue represents negative values .

Figure 7.4: Variation of the critical frequency of the critical modes with  $E$  and  $S = 0.6$  in Keplerian regime. Dashed vertical lines separate different  $m_c$ .

Figure 7.5: Variation of the critical axial wavenumber  $q_c$  of the critical modes with  $E$  for  $S = 0.6$  on Keplerian regime. Dashed vertical lines separate different  $m_c$ .

Figure 7.6: Critical mode for  $S = 0.6, E = 0.01, Ta_c = 273$  in Keplerian regime, with  $m = 0, q_c = 10.3, \omega_c = 0$ . (a) Black arrows represent the velocity field in  $(r, z)$  direction while the colors represent the azimuthal velocity  $V$  (b) the vorticity  $\omega_\theta$  (c) the pressure variation (d) the  $N_1$  variation © the  $N_2$  variation. Color maps of (b, c, d, e) represent the relative amplitude.

Figure 7.7: Critical mode for  $S = 0.6$ ,  $E = 0.035$ ,  $Ta_c = 97.4$  in Keplerian regime, with  $m = 1$ ,  $q_c = 5.98$ ,  $\omega_c = -0.207$ . (a) Black arrows represent the velocity field in  $(r, z)$  direction while the colors represent the azimuthal velocity  $V$  (b) the vorticity  $\omega_\theta$  (c) the pressure variation (d) the  $N_1$  variation © the  $N_2$  variation. Color maps of (b, c, d, e) represent the relative amplitude.

Figure 7.8: Critical mode for  $S = 0.6$ ,  $E = 0.1$ ,  $Ta_c = 48.6$  in Keplerian regime, with  $m = 2$ ,  $q_c = 4.62$ ,  $\omega_c = -0.406$ . (a) Black arrows represent the velocity field in  $(r, z)$  direction while the colors represent the azimuthal velocity  $V$  (b) the vorticity  $\omega_\theta$  (c) the pressure variation (d) the  $N_1$  variation © the  $N_2$  variation. Color maps of (b, c, d, e) represent the relative amplitude.

Figure 7.9: Critical mode for  $S = 0.6$ ,  $E = 1$ ,  $Ta_c = 12.5$  in Keplerian regime, with  $m = 1$ ,  $q_c = 4.75$ ,  $\omega_c = -0.178$ . (a) Black arrows represent the velocity field in  $(r, z)$  direction while the colors represent the azimuthal velocity  $V$  (b) the vorticity  $\omega_\theta$  (c) the pressure variation (d) the  $N_1$  variation © the  $N_2$  variation. Color maps of (b, c, d, e) represent the relative amplitude.

Figure 7.10: Critical curves  $Ta_c(E)$  for different  $S$  in Keplerian regime.

Figure 7.11: Critical curves  $K_c(E)$  for different  $S$  in Keplerian regime.

Figure 7.12: Critical curves,  $Ta_c(ES)$  for different  $S$ : the vertical dashed line is the elasto Rayleigh line that separates the potential stable from the potentially unstable zone to the elasticity-induced perturbations.

Figure 7.13: Critical curves  $Ta_c(K_c)$  for different  $S$  in Keplerian regime.

Figure 7.14: Critical curves,  $Re_c(Wi_c)$  for different  $S$  in Keplerian regime.

Figure 7.15: Flow patterns and space-time diagram on Keplerian regime at  $Ta_c = 8.50$ ,  $E_m = 0.017$ ,  $S = 0.81$ . (a) Gap view by laser sheet, (b) Front view, (c) Space-time diagram. The space-time diagram seems wavy, however all the wavy frequencies are related to the rotational cylinders.

Figure 7.16: Fourier spectra of the space-time diagram on Keplerian regime at  $Ta_c = 8.50$ ,  $E_m = 0.017$ ,  $S = 0.81$ . (a) space spectrum, (b) time spectrum. Red lines – rotation frequencies of the inner and outer cylinder and the mean rotation of them. Green dashed line – a combination of frequencies of the cylinders ( $2\Omega_o - \Omega_i$ ). Black dashed line – flicker frequency of the spot light.

Figure 7.17: Comparison between the critical modes: (a) (b) Front view of the Taylor Vortex mode (a) and the Stationary and Axisymmetric mode (b); (c) (d) space-time diagram of 10 mins of the Taylor Vortex mode (c) and the Stationary and Axisymmetric mode (d).

Figure 7.18: Flow patterns and space-time diagram of the Disordered Waves mode on Keplerian regime at  $Ta_c = 2.86$ ,  $E_m = 0.13$ ,  $S = 0.61$ . (a) Gap view by laser sheet (b) Front view (c) Space-time diagram.

Figure 7.19: Fourier spectrums of the space-time diagram on Keplerian regime at  $Ta_c = 2.86$ ,  $E_m = 0.13$ ,  $S = 0.61$  (a) space spectrum (b) time spectrum. Red dashed line – the frequency of the inner cylinder. Black dashed line – the flicker frequency of the spot light. Green dashed line – the frequency difference of  $\Omega_o - \langle \omega \rangle$ .

Figure 7.20: Space-time diagram and Fourier spectra of the Disordered Waves mode on Keplerian regime at  $Ta_c = 2.86$ ,  $E_m = 0.13$ ,  $S = 0.61$  for a wave generated near the bottom endplate. (a) Space-time diagram (b) space spectrum (c) time spectrum. Red solid line – outer cylinder rotation frequency. Red dashed line – inner cylinder rotation frequency.

Figure 7.21: Demodulation of the zoom in space-time diagram of the transition.  $Ta_c = 2.86$ ,  $E_m = 0.13$ ,  $S = 0.61$ . (a) Space-time diagram of the transition (b) Demodulated waves.

Figure 7.22: Demodulation of the space-time diagram of the Disordered Waves mode.  $Ta_c = 2.86$ ,  $E_m = 0.13$ ,  $S = 0.61$ . (a) Demodulated left wave (b) Space-time diagram of the saturated flow (c) Demodulated right wave.

Figure 7.23: Comparison between the critical modes: (a) (b) longtime space-time diagram of Disordered Vortices mode (a) and Disordered Waves mode (b); (c) (d) transient space-time diagram of Disordered Vortices mode (c) and Disordered Waves mode (d).

Figure 7.24: Flow patterns and space-time diagram of the Solitary Vortices mode on Keplerian regime at  $Ta_c = 2.15$ ,  $E_m = 0.29$ ,  $S = 0.62$ . (a) Gap view by laser sheet (b) Front view (c) Space-time diagram. (d) long time space-time diagram. © space spectrum (f) time spectrum. Red line and dashed line – the frequency of the inner and outer cylinder. Black dashed line – the flicker frequency of the spot light. Green dashed line – the mean frequency  $\langle \omega \rangle$ .

Figure 7.25: Demodulation of the space-time diagram of the Solitary Vortices mode at  $Ta_c = 2.15$ ,  $E_m = 0.29$ ,  $S = 0.62$ . (a) Demodulated left wave (b) Space-time diagram (c) Demodulated right wave.

Figure 7.26: Critical values of the transition from laminar flow to unstable flow on Keplerian regime. Solid lines – LSA critical curves for different  $S$ . Dashed line  $ES^* = 0.672$  is predicted by elasto-rotational Rayleigh discriminant. Solid points – experimental transient values, 3 colors present 3 different definitions of elasticity. Within each definition of elasticity, each point present one solution tested. Dashed rectangular – group of different flow patterns.

Figure 7.27: Location of the Solitary Vortices mode on  $Ta_c(ES)$  on Keplerian regime;  $E$  is defined with the molecular relaxation time. Solid lines – LSA critical curves for different  $S$ . Dashed line ( $ES^* = 0.672$ ) gives the separation between stable and unstable zones to elasticity driven perturbations. Solid points – experimental critical values. Dashed circle – different modes. Solid circle – location of the Solitary Vortices mode. Colored point lines separate the stationary axisymmetric mode from the oscillatory non-axisymmetric mode by LSA.

Figure 7.28: Variation of the critical axial wave number with  $ES$  defined by molecular relaxation time. Solid lines – LSA predictions for different  $S$ . Solid points – experimental critical wave numbers.

Figure 7.29: Variation of the critical frequency with  $ES$  defined by molecular relaxation time. Solid lines – LSA predictions for different  $S$ . Solid points – experimental critical angular frequency.

Figure 7.30: Critical curves  $Ta_c(E)$  for different  $m$  at fixed  $S = 0.7$ .

Figure 7.31: Critical curves  $Ta_c(E)$  for different  $S$ .

Figure 7.32: Critical curves  $Ta_c(ES)$  for different  $S$ . Dashed line represents the  $ES^* = 3.451$  from elasto-rotational Rayleigh discriminant.

Figure 7.33: Critical curves  $Re_c(Wi_c)$  for different  $S$ .

Figure 7.34: (a) The angular frequency  $\omega$  of the critical modes in respect to  $E$  for different  $S$  in anti-Keplerian regime. (b) The axial wave number  $q$  of the critical modes in respect to  $E$  for different  $S$ .

Figure 7.35: Pattern properties of the critical mode in the gap view for  $S = 0.7, E = 1, Ta_c = 0.976, m_c = 0, q_c = 24.2, \omega_c = 0.02$  in anti-Keplerian regime. (a) Black arrows represent the velocity vectors of while the colors represent the azimuthal velocity  $V_{(r,z)}$  (b) the vorticity  $\omega_\theta$ , (c) the pressure variation, (d) the  $N_1$  variation. Color maps of (b, c, d) represents the relative amplitude.

Figure 7.36: Flow patterns and space-time diagram in anti-Keplerian regime at  $Ta_c = 7.34, E_m = 0.34, S = 0.51$ . (a) Gap view (b) Front view by laser sheet (c) Space-time diagram of 20s (d) Longtime space-time diagram © space spectrum (f) time spectrum. Red dashed line – the frequency of the inner cylinder. Black dashed line – the flicker frequency of the spot light.

Figure 7.37: Critical values  $Ta_c(E)$  in the anti-Keplerian regime. Solid lines – LSA critical curves for different  $S$ . Solid points – experimental critical values, 3 colors present 3 different definitions of elasticity.

Figure 7.38: Critical values  $\omega_c(E)$  in the anti-Keplerian regime. Solid lines – LSA critical curves for different  $S$ . Solid points – experimental critical values defined by extensional elasticity.

Figure 7.39: Critical values  $q_c(E)$  in the anti-Keplerian regime. Solid lines – LSA critical curves for different  $S$ . Solid points – experimental critical values defined by extensional elasticity.

Figure 7.40: Application of the Velikhov-Chandrasekhar criterion for ERI.

Figure 7.41: Critical values on Keplerian regime. Solid lines – LSA critical curves for different  $S$ . Dashed line  $ES^* = 0.672$  is predicted by elasto-rotational Rayleigh discriminant. Solid points – experimental transient values, 3 colors present 3 different definitions of elasticity. Dashed rectangular – group of different flow patterns. Colored point lines – criterion of  $Wi = Wi^*$  for different  $S$ .

Figure 7.42 Threshold curve for the polymer solutions used in the experiment by Boldyrev et al. (2009) and corresponding experimental values for  $\eta = 0.903, S \in \{0.983, 0.991, 0.995\}$ .

Figure 8.1: Marginal stability curves  $Ta_c(q)$  for different  $m$  for  $S = 0.7$  (a)  $E = 0.01$  (b)  $E = 0.028$  (c)  $E = 0.1$  (d)  $E = 1$  in regime  $\mu = \eta^3$ .

Figure 8.2: Critical curves,  $Ta_c(E)$  for different  $m$  for a solution with  $S = 0.7$  in regime  $\mu = \eta^3$ .

Figure 8.3: Variation of the critical parameters with  $E$  for  $S = 0.7$  in  $\mu = \eta^3$  regime: (a) Threshold  $Ta_c$ , (b) critical wavenumber  $q_c$ , (c) critical frequency  $\omega_c$ .

Figure 8.4: Cross-section  $(r, z)$  of the azimuthal component of the vorticity for  $S = 0.7$  in  $\mu = \eta^3$  regime.

Figure 8.5: Critical mode for  $S = 0.7$ ,  $E = 0.01$ ,  $Ta_c = 86.6$  in  $\mu = \eta^3$  regime, with  $m = 0$ ,  $q_c = 3.49$ ,  $\omega_c = 0$ . (a) Black arrows represent the velocity field in  $(r, z)$  direction while the colors represent the azimuthal velocity  $V$  (b) the vorticity  $\omega_\theta$  (c) the pressure variation (d) the  $N_1$  variation © the  $N_2$  variation. Color maps of (b, c, d, e) represent the relative amplitude.

Figure 8.6: Critical mode for  $S = 0.7$ ,  $E = 0.028$ ,  $Ta_c = 52.4$  in  $\mu = \eta^3$  regime, with  $m = 1$ ,  $q_c = 3.84$ ,  $\omega_c = -0.178$ . (a) Black arrows represent the velocity field in  $(r, z)$  direction while the colors represent the azimuthal velocity  $V$  (b) the vorticity  $\omega_\theta$  (c) the pressure variation (d) the  $N_1$  variation © the  $N_2$  variation. Color maps of (b, c, d, e) represent the relative amplitude.

Figure 8.7: Critical mode for  $S = 0.7$ ,  $E = 0.1$ ,  $Ta_c = 32.2$  in  $\mu = \eta^3$  regime, with  $m = 2$ ,  $q_c = 4.25$ ,  $\omega_c = -0.327$ . (a) Black arrows represent the velocity field in  $(r, z)$  direction while the colors represent the azimuthal velocity  $V$  (b) the vorticity  $\omega_\theta$  (c) the pressure variation (d) the  $N_1$  variation © the  $N_2$  variation. Color maps of (b, c, d, e) represent the relative amplitude.

Figure 8.8: Critical mode for  $S = 0.7$ ,  $E = 1$ ,  $Ta_c =$  in  $\mu = \eta^3$  regime, with  $m = 1$ ,  $q_c = 5.03$ ,  $\omega_c = -0.122$ . (a) Black arrows represent the velocity field in  $(r, z)$  direction while the colors represent the azimuthal velocity  $V$  (b) the vorticity  $\omega_\theta$  (c) the pressure variation (d) the  $N_1$  variation © the  $N_2$  variation. Color maps of (b, c, d, e) represent the relative amplitude.

Figure 8.9: Critical curves  $Ta_c(ES)$  for different  $S$  in  $\mu = \eta^3$  regime. The colored dashed lines separate the stationary axisymmetric mode from the oscillatory non-axisymmetric mode by LSA.

Figure 8.10: Critical curves,  $Re_c(Wi_c)$  for different  $S$  in  $\mu = \eta^3$  regime.

Figure 8.11: Critical curves,  $Ta_c(K_c)$  for different  $S$  in  $\mu = \eta^3$  regime.

Figure 8.12: Flow patterns and space-time diagram of the Ribbons mode on  $\mu = \eta^3$  regime for  $Ta_c = 13.73$ ,  $E_m = 1.06$ ,  $S = 0.47$ . (a) Gap view (b) Front view by laser sheet (c) Space-time diagram. (d) Longtime space-time diagram.

Figure 8.13: Flow patterns and space-time diagram of the Disordered Waves mode on  $\mu = \eta^3$  regime at  $Ta_c = 4.66$ ,  $E_m = 0.34$ ,  $S = 0.5$ . (a) Gap view (b) Front view by laser sheet (c) Space-time diagram. (d) Longtime space-time diagram.

Figure 8.14: Transient space-time diagram and Fourier spectrums of the Disordered Waves mode on  $\mu = \eta^3$  regime at  $Ta_c = 4.66$ ,  $E_m = 0.34$ ,  $S = 0.5$ . (a) Space-time diagram (b) space spectrum (c) time spectrum. Red solid line – outer cylinder rotation frequency. Red dashed line – inner cylinder rotation frequency. Black dashed line – flicker frequency of the spot light.

Figure 8.15: Variation of the critical values with  $ES$  on  $\mu = \eta^3$  regime. Solid lines – LSA critical curves for different  $S$ . Solid points – experimental transient values, 3 colors represent the 3 different definitions of elasticity. The colored dashed lines separate the stationary axisymmetric mode from the oscillatory non-axisymmetric mode by LSA.

Figure 8.16: Variation of the critical angular velocity with  $ES$  defined by the molecular relaxation time. Solid lines – LSA predictions for different  $S$ . Solid points – experimental angular velocity.

Figure 8.17: Variation of the critical axial wave number with  $ES$  defined by the molecular relaxation time. Solid lines – LSA predictions for different  $S$ . Solid points – experimental critical wave numbers.

Figure 9.1: Marginal stability curves of the purely elastic limit in Keplerian regime for (a)  $S = 0.5$  and (b)  $S = 0.8$ .

Figure 9.2: Critical curves  $Wi(S)$  for different  $m$  at  $q_c$  on Keplerian regime.

Figure 9.3: Critical curves  $Wi(S)$  for different rotation regimes.

Figure 9.4: Variation of the critical parameters: (a)  $i_s(S)$ , (b)  $q_c(S)$ , (c)  $\omega_c(S)$ .

Figure 9.5: Azimuthal vorticity patterns in the gap.

Figure 9.6: Experimental critical value  $Ta_c(E_e)$  of five rotational regimes.

Figure 9.7: Experimental and LSA critical values  $Wi_s(E_e)$  of five regimes. Solid points: experimental critical values. Solid lines: LSA predictions of  $S = 0.5$ . Dashed black line: the LSA prediction of the  $Wi_s$  at  $S = 0.5$ .

Figure 9.8: Experimental and LSA critical values  $Wi_s(S)$  of five regimes. Solid points: experimental critical values. Solid line: LSA prediction.

# Résumé

---

L'instabilité magnéto-rotationnelle (MRI) apparaît dans un écoulement dans des liquides conducteurs électriques en rotation différentielle en présence d'un champ magnétique, lorsque la vitesse angulaire décroît avec la distance de l'axe de rotation. Cette instabilité est considérée comme la clé pour comprendre la turbulence et le transport de moment cinétique angulaire dans les disques d'accrétion astrophysiques. A ce jour, il n'existe pas de observations directes de la MRI dans un écoulement képlérien. Selon Ogilvie et Proctor, l'instabilité viscoélastique (IVE) est analogue à la MRI : la force élastique due aux polymères joue le rôle de champ magnétique. Cette analogie est basée sur la ressemblance entre les équations des écoulements viscoélastiques du modèle d'Oldroyd-B et les équations de la magnéto-hydrodynamique (MHD). À la suite de cette analogie, il existe une seule expérience, mais avec une solution viscoélastique qui ne satisfait pas le modèle d'Oldroyd-B. Cette thèse est consacrée à une étude expérimentale et théorique afin de vérifier cette analogie dans un écoulement képlérien, et mieux comprendre l'origine du transport du moment dans les disques d'accrétion.

La première tâche a consisté à généraliser le discriminant de Rayleigh aux écoulements viscoélastiques. Le critère de Rayleigh généralisé (élasto-rotationnel) stipule qu'un écoulement viscoélastique est instable si la somme de discriminant de Rayleigh Newtonien et la stratification radiale de la différence du contrainant normal  $N_1$  est négative. La force élastique peut renforcer l'instabilité centrifuge ou induire elle-même l'instabilité purement élastique. Dans le régime képlérien, on peut avoir de l'instabilité purement élastique quand l'élasticité polymérique  $ES$  est supérieure à une valeur critique  $ES^*$  qui dépend du rapport des rayons. L'analogie de la MRI se trouve en dehors de la zone d'instabilité purement élastique. Le critère de Rayleigh elasto-rotationnel est analogue au critère d'instabilité de Michael pour de fluides de conducteurs électriques en présence d'un champ magnétique azimuthal.

Pour analyser l'IVE, nous avons effectué l'analyse de stabilité linéaire basée sur les équations complètes du modèle d'Oldroyd-B. Le problème de valeurs propres résultant a été résolu en utilisant un code numérique développé sur Matlab et en utilisant la méthode de collocation de Chebyshev. Le code a été validé par la comparaison avec les résultats disponibles dans la littérature.

Les expériences ont été réalisées dans un système de Couette-Taylor qui consiste en l'écoulement dans l'entrefer entre deux cylindres coaxiaux avec un rapport de rayon  $\eta = 0,8$ . Le rapport d'aspect du dispositif expérimental était  $\Gamma = 45,7$  qui est suffisamment grand pour comparer avec les résultats théoriques obtenus dans le rapport d'aspect infini. Nous avons utilisé des solutions aqueuses de 1000 ppm de polyoxyéthylène (POE) et de polyéthylène glycol (PEG) de concentration variable (2,5% - 25%). Les solutions ont été bien caractérisées par des tests rhéologiques pour s'assurer qu'elles correspondent au modèle d'Oldroyd-B. La viscosité de cisaillement de la solution polymère et du solvant de PEG sont mesurées par un rhéomètre de cisaillement. Ces deux viscosités augmentent avec la concentration de PEG tandis que le rapport de la viscosité polymérique et de la solution totale  $S$  diminue avec la concentration de PEG. Le temps de relaxation de la solution de polymère est estimé par trois méthodes différentes : mesure par un rhéomètre extensionnel (CABER) ; mesure par la première différence de contraintes normales  $N_1$ , détermination par la relation de ce temps avec la viscosité du polymère et la masse molaire. Pour la

plupart des solutions, les temps de relaxations et l'élasticité calculée avec ces temps de relaxation augmentent avec la concentration de PEG.

En tournant le cylindre intérieur et fixant le cylindre extérieur (régime  $\mu = 0$  où  $\mu$  est le rapport de vitesse entre le cylindre extérieur et intérieur), nous avons observé trois modes différents pour de solutions de petite à grande élasticité  $E$ : le vortex de Taylor, le mode rubans, et des tourbillons désordonnés. Le mode de vortex de Taylor est supercritique et les deux autres sont sous-critiques. Cette observation est en accord avec la prédiction de LSA qui dit que le mode critique est axisymétrique et stationnaire pour de faibles valeurs de  $E$  et non-axisymétrique et oscillant pour de grandes valeurs de  $E$ . Le mode des tourbillons désordonnés correspond à l'instabilité purement élastique. Pour de faibles valeurs de  $E$ , le seuil théorique et expérimental de l'instabilité  $Ta_c$  est quasiment constant et coïncide avec la valeur critique du fluide Newtonien. Ce seuil décroît rapidement quand  $E$  devient grand. Ceci confirme que l'élasticité renforce l'IVE. Le rapport de viscosité  $S$  joue deux rôles opposés: déstabilisant pour les petites valeurs de l'élasticité et de stabilisation pour les grandes valeurs de l'élasticité et en particulier dans le régime purement élastique. Le nombre d'onde critique et la fréquence critique sont aussi calculés par LSA et ils se trouvent en accord avec de l'expérience qualitativement. Des accords qualitatifs sont également observés entre nos résultats expérimentaux et ceux de la littérature.

En régime képlérien ( $\mu = \eta^{3/2}$ ), nous avons observé le mode de vortex axisymétrique et stationnaire pour de faibles valeurs de  $ES$  et le mode des ondes désordonnées pour de grandes valeurs de  $ES$ . Le mode de vortex axisymétrique est formé par des tourbillons aplatis avec une longueur d'onde axiale inférieure à la taille de l'entrefer; le mode des ondes désordonnées est formé par des ondes contra-propagatives. Parmi les modes désordonnés, des tourbillons solitaires apparaissent dans une petite plage de valeurs de  $ES$ . Le mode axisymétrique stationnaire est supercritique tandis que les modes désordonnés sont sous-critiques. Tous ces modes se trouvent dans la zone  $ES < ES^*$ , donc ils ne sont pas dus à l'instabilité purement élastique. En accord avec de l'expérience, la stabilité linéaire montre que le mode critique est axisymétrique et stationnaire pour de faibles valeurs de  $E$  et non-axisymétrique et oscillant pour de grandes valeurs de  $E$ . Le paramètre  $S$ , caractérisant l'élasticité polymérique, semble être le meilleur paramètre de contrôle que l'élasticité  $E$  en régime képlérien parce que toutes les courbes critiques  $Ta_c(ES)$  convergent en une courbe pour différentes valeurs de  $S$ . Et cette courbe correspond mieux aux seuils expérimentaux de l'instabilité lorsque le nombre élastique est défini avec le temps de relaxation déterminé par la masse molaire. La stabilité linéaire montre aussi que le rapport de viscosité  $S$  est une source déstabilisante quand le nombre de Weissenberg modifié  $K$  est petit et stabilisante quand  $K$  est grand.

En tournant seulement le cylindre extérieur (régime  $\mu = \infty$ ) ou en anti-képlérien ( $\mu = \eta^{-3/2}$ ), le cylindre extérieur tourne plus vite que l'intérieur, la force centrifuge n'est plus de source de l'instabilité, donc l'instabilité purement élastique est induite par la seule force élastique. Dans ces deux cas, nous avons observé quand même de l'instabilité avec de solution de grande élasticité en forme de mode désordonné dans le temps et dans l'espace. La stabilité linéaire prédit que le mode critique est axisymétrique et oscillant et elle montre que les courbes critiques de  $Ta_c(E)$  sont indépendantes de  $S$ . Ces courbes s'adaptent parfaitement aux valeurs critiques expérimentales lorsque l'élasticité est définie par le temps de relaxation extensionnel.

Dans un régime intermédiaire ( $\mu = \eta^3$ ) entre le régime  $\mu = 0$  et le régime képlérien, nous avons observé des modes critiques de différente nature: le mode de rubans qui est la même mode en régime  $\mu = 0$  est observé pour de faibles valeurs de  $E$  et le mode des ondes désordonnés qui est la même mode en régime képlérien est observé pour de grandes valeurs de  $E$ .

A la limite de très grande élasticité ( $E \rightarrow \infty$ ), nous avons trouvé une courbe critique unique  $Wi_s(S)$  de l'instabilité purement élastique pour tous les régimes de rotation dans la limite ( $Ta = 0$ ) où le nombre Weissenberg  $Wi_s$  est défini par le taux de cisaillement au milieu de l'entrefer. L'instabilité purement élastique apparaît sous la forme des modes non axisymétriques oscillatoires pour de  $S < S^*$  alors qu'elle apparaît sous forme de modes axisymétriques oscillatoires si  $S > S^*$ . Les données expérimentales obtenues avec les solutions de l'élasticité finie montrent une tendance à une courbe unique dès que l'élasticité devient assez grande.

Cette thèse a confirmé l'analogie entre l'IVE et la MRI standard (SMRI) en régime képlérien où les molécules de polymères jouent un rôle analogue à celui des lignes de champ magnétique axial qui déstabilise les disques d'accrétion. Différents types de MRI sont distincts les uns des autres par la forme du champ magnétique. L'analyse de l'analogie polymérique du champ magnétique montre que dans le régime képlérien, le mode de vortex axisymétrique de l'IVE est analogue à la SMRI quand  $Wi$  est inférieur à une valeur critique  $Wi^*$ , tandis que le mode désordonné est analogue à la MRI hélicoïdale (HMRI) lorsque  $Wi$  est en même ordre de  $Wi^*$ .

Cette thèse est limitée à l'étude théorique et expérimentale de la première instabilité du fluide viscoélastique. Le comportement de certaines courbes marginales et l'existence de multiples points de codimension 2 suggèrent la nécessité d'une analyse non linéaire pour étudier le couplage des modes. Les mesures de PIV permettront de caractériser en détail les modes critiques, les modes supérieurs d'instabilité plus élevés et la turbulence dans le régime de képlérien viscoélastique. La DNS permettra de calculer le couple et le transport du moment dans la direction radiale y compris sur les cylindres. Ces études devraient apporter de nouveaux arguments à la validation de l'analogie entre l'IVE et l'MRI pour une meilleure compréhension de la dynamique complexes des disques d'accrétion.

Key words: viscoelastic instability, magnetorotational instability, Keplerian flow, Taylor-Couette system, Oldroyd-B model, linear stability analysis, rheology.

## **Abstract**

This thesis is devoted to the verification of the analogy between the viscoelastic instability (VEI) and the magnetorotational instability (MRI) in a Keplerian flow, in order to get better understanding of the momentum transportation in accretion disks.

The elasto-rotational Rayleigh discriminant is deduced to clarify the role of the elasticity in the VEI. The linear stability analysis (LSA) with Oldroyd-B model is performed to predict critical parameters of viscoelastic modes, and it reveals the influence of the elasticity, polymer viscosity on the VEI. Experiments with well controlled aqueous solutions of polyoxyethylene (POE) and polyethylene glycol (PEG) are conducted. We have observed supercritical stationary axisymmetric mode with solutions of small elasticity and subcritical disordered modes with solutions of large elasticity. Both the flow patterns and the critical values of these modes are in good agreement with the LSA predictions. According to the analogy, the stationary axisymmetric mode is likely the analog of the standard MRI while the disordered mode is likely the analog of the helical MRI.

The thesis contains also theoretical and experimental results with four other rotation regimes and the limit case of infinite elasticity.

Mots clés: instabilité viscoélastique, instabilité magnéto-rotationnel, écoulement képlérien, système de Couette-Taylor, model d'Oldroyd-B, analyse de stabilité linéaire, rhéologie.

## **Résumé**

Cette thèse est consacrée à la vérification de l'analogie entre l'instabilité viscoélastique (VEI) et l'instabilité magnéto-rotationnel (MRI) dans un écoulement képlérien, afin de mieux comprendre le transport du moment dans les disques d'accrétion.

Le discriminant de Rayleigh élasto-rotationnel est établi pour clarifier le rôle de l'élasticité dans le VEI. L'analyse de stabilité linéaire (LSA) avec le modèle d'Oldroyd-B est effectuée pour prédire les paramètres critiques des modes viscoélastiques. Il fait apparaître également l'influence de l'élasticité, la viscosité polymérique et d'autres paramètres de contrôle pour le VEI. Des expériences bien contrôlées avec des solutions aqueuses de polyoxyéthylène (POE) et de polyéthylène glycol (PEG) sont effectuées. Nous avons observé le mode stationnaire axisymétrique supercritique avec des solutions de faible élasticité et modes désordonnés sous-critiques avec des solutions de grande élasticité. Les formes et les valeurs critiques de ces modes sont en bon accord avec les prédictions théoriques de LSA. Selon l'analogie, le mode axisymétrique stationnaire est probablement l'analogue de MRI standard, tandis que le mode désordonné est probable que l'analogue de MRI hélicoïdale.

La thèse contient aussi des résultats théoriques expérimentaux sur quatre autres régimes de rotation et un cas de limite d'élasticité infinie.